

Progress in Structures

Part 1

Edited by
Xingang Zhou, Mingjin Chu,
Jinming Liu, Shuying Qu and Haitao Fan

Progress in Structures

Edited by
Xingang Zhou
Mingjin Chu
Jinming Liu
Shuying Qu
Haitao Fan

Progress in Structures

Selected, peer reviewed papers from the
2nd International Conference on
Civil Engineering, Architecture and Building Materials
(CEABM 2012),
May 25-27, 2012, Yantai, China

Edited by

**Xingang Zhou, Mingjin Chu, Jinming Liu,
Shuying Qu and Haitao Fan**



Copyright © 2012 Trans Tech Publications Ltd, Switzerland

All rights reserved. No part of the contents of this publication may be reproduced or transmitted in any form or by any means without the written permission of the publisher.

Trans Tech Publications Ltd
Kreuzstrasse 10
CH-8635 Durnten-Zurich
Switzerland
<http://www.ttp.net>

Volumes 166-169 of
Applied Mechanics and Materials *4-vol.-set*
ISSN 1662-7490

Full text available online at <http://www.scientific.net>

Distributed worldwide by

Trans Tech Publications Ltd
Kreuzstrasse 10
CH-8635 Durnten-Zurich
Switzerland

Fax: +41 (44) 922 10 33
e-mail: sales@ttp.net

and in the Americas by

Trans Tech Publications Inc.
PO Box 699, May Street
Enfield, NH 03748
USA

Phone: +1 (603) 632-7377
Fax: +1 (603) 632-5611
e-mail: sales-usa@ttp.net

Preface

The International Conference on Civil Engineering, Architecture and Building Materials provides a forum for accessing to the most up-to-date and authoritative knowledge from both industrial and academic worlds, sharing best practice in this exciting field of Civil Engineering, Architecture and Building Materials. The first CEABM was successfully taken place in Haikou, China, June 18-20, 2011. Following the success of the inaugural conference, the 2nd CEABM was held in Yantai, China, from 25 to 27 May 2012, organized by School of Civil Engineering of Yantai University, College of Civil and Architecture Engineering of Guizhou University and Hainan Society of Theoretical and Applied Mechanics. This conference was organized in four simultaneous tracks: “Progress in Civil Engineering”, “Progress in Structures”, “Advanced Building Materials and Sustainable Architecture” and “Sustainable Environment and Transportation”. All papers included in this collection had undergone the careful peer-review by the experts of international and domestic of China before it is selected for publications.

We would like to express our sincere appreciations to all the authors for their papers and presentations in this conference. We wish to thank the members of the scientific committees and invited referees for their assistance in reviewing the abstracts and full papers. We are grateful to all the invited speakers who came to share their knowledge with us. We hope that this book will not only provide the readers a broad overview of the latest advances but also provide the researchers a valuable summary and reference in this field. Finally, thanks are also given to Trans Tech Publications for producing this volume.

The Organizing Committee of CEABM 2012

Organized by:

School of Civil Engineering, Yantai University

College of Civil and Architecture Engineering, Guizhou University

Hainan Society of Theoretical and Applied Mechanics

Conference Organization

Chairman

Prof. Hongnan Li, Dalian University of Technology, China

Co-Chairmen

Prof. Xingang Zhou, Yantai University, China

Prof. Chaohe Chen, South China University of Technology, China

Prof. Yong Huang, Guizhou University, China

International Scientific Committee

Prof. Longsheng Bao, Shenyang Jianzhu University, China

Prof. Tai Bao, Guizhou University, China

Prof. Wenbo Bao, Shenyang University of Technology, China

Prof. Chaohe Chen, South China University of Technology, China

Prof. Wanlin Cao, Beijing University of Technology, China

Dr. Mingjin Chu, Yantai University, China

Prof. Changyu Cui, Harbin Institute of Technology, China

Prof. Zhiheng Deng, Guangxi University, China

Prof. Shengguo Ding, Guizhou University, China

Prof. Xiuli Du, Beijing University of Technology, China

Prof. Ping Feng, Tianjing University, China

Dr. Peng Feng, Tsinghua University, China
Prof. Yaojun Ge, Tongji University, China
Prof. Linhai Hang, Tsinghua University, China
Prof. Yong Huang, Guizhou University, China
Prof. Zhihong Huang, Guizhou University, China
Prof. Weiliang Jin, Zhejiang University, China
Prof. Guoqiang Li, Tongji University, China
Prof. Qiusheng Li, City University of Hong Kong
Prof. Hongnan Li, Dalian University of Technology, China
Prof. Zhengliang Li, Chongqing University, China
Prof. Zhengnong Li, Hunan University, China
Prof. Lijuan Li, Guangdong University of Technology, China
Prof. Aiqun Li, Southeast University, China
Prof. Hui Li, Harbin Institute of Technology, China
Prof. Shirong Li, Yangzhou University, China
Prof. Guangfan Li, Hainan University, China
Prof. Feng Liu, Guangdong University of Technology, China
Prof. Tianqing Ling, Chongqing Jiaotong University, China
Prof. Xinzheng Lu, Tsinghua University, China
Prof. Jianguo Nie, Tsinghua University, China
Academician Prof. Wei Sun, Southeast University, China
Dr. Yongbo Shao, Yantai University, China
Prof. Yaozong Shi, Highway Survey and Design Institute of Hainan Province
Prof. Jinfeng Wang, Huaqiao University, China
Prof. Bo Wu, South China University of Technology, China
Prof. Hong Wang, Guizhou University, China
Prof. Lai Wang, Shandong University of Science and Technology
Prof. Yan Xiao, Hunan University, China
Prof. Shilang Xu, Zhejiang University, China

Senior Engineer. Jianxin Xu, China Communications Water Transportation
Planning and Design Institute Co., Ltd

Prof. Shanhua Xu, Xi'an Univ. of Architecture and Tech., China

Prof. Tao Xie, Guizhou University, China

Prof. Zhixin Yan, Lanzhou University, China

Dr. Zhenjun Yang, The University of Manchester, UK

Prof. Lieping Ye, Tsinghua University, China

Prof. Tiejun Zhao, Qingdao Technological University, China

Prof. Xingang Zhou, Yantai University, China

Prof. Jiru Zhang, Wuhan University of Technology, China

Prof. Chuangbin Zhou, Wuhan University, China

Prof. Xuejun Zhou, Shandong Jianzhu University, China

Dr. Ahmed Sarhan, Malaya University, Malaysia

Dr. Gui Wang, The University of Queensland, Australia

Dr. Scott T. SMITH, Hong Kong University, Hong Kong

Dr. Sreenivasan M, SR Technical University, IN

Dr. Tianjian Ji, The University of Manchester, UK

Prof. Abdul Amir H. Kadhum, Malaysia

Prof. A. Kaveh, Iran University of Science & Technology, Iran

Prof. Aftab Mufti, University of Manitoba, Canada

Prof. Antoine E. Naaman, University of Michigan, USA

Prof. Ayman Mosallam, Univ of California Irvine, USA

Prof. B. H. V. Topping, Heriot-Watt University, Edinburgh, UK

Prof. Chao Hsun Haung, National Taipei University of Technology, Taiwan

Prof. Chiew Sing-Ping, Nanyang Technological University, Singapore

Prof. Carlos Aquino, Ritsumeikan University, Japan

Prof. David Hui, University of New Orleans, USA

Prof. Hamid Ronagh, The University of Queensland, Australia

Prof. Han-Bin Ge, Meiju University, Japan

Prof. I. E. Harik, University of Kentucky, USA
Prof. J. H. Bungey, University of Liverpool, Liverpool, UK
Prof. Jian-Fei Chen, the University of Edinburgh, UK
Prof. Jongwook Park, Sungkyunkwan University, Korea
Prof. Katsuyuki Kida, Kyushu University, JP
Prof. Ken-ichi Manabe, Tokyo Metropolitan University, Japan
Prof. Kum-Gil Sung, Inha University, Korea
Prof. Kyung-Man Moon, Korea Maritime University, Korea
Prof. K. J. Bathe, Massachusetts Institute of Technology, USA
Prof. Kang Seok Lee, Chonnam National University, South Korea
Prof. Lau Hieng Ho, Curtin University of Technology, Malaysia
Prof. Luciano Feo, University of Salerno, Italy
Prof. Lawrence C. Bank, University of Wisconsin-Madison, USA
Prof. Marcus M.K. Lee, the University of Southampton, UK
Prof. Mark G Stewart, The University of Newcastle, Australia
Prof. M. N. Soutsos, University of Liverpool, Liverpool, UK
Prof. Nangkula Utaberta, The National University of Malaysia
Prof. Ramiro Sofronie, University of Bucharest, Romania
Prof. R. Sri Ravindra rajah, University of Technology, Australia
Prof. Tim Ibell, University of Bath, UK
Prof. Tamon UEDA, Hokkaido University, Japan
Prof. TAN Kang-Hai, Nanyang Technological University, Singapore
Prof. Tan Kiang Hwee, National University of Singapore
Prof. Wen-Hsiang Hsieh, National Formosa University, Australia
Prof. Zhi-Shen Wu, Ibaraki University, Japan
Prof. Zong Woo Geem, iGlobal University, USA

Conference Secretary

Dr. Mingjin Chu, Yantai University, China

Table of Contents

Preface and Conference Organization

Chapter 1: Structural Engineering

Test Research on the Behaviors of Steel Bar Truss and Concrete Superimposed Floor Slabs Y.X. Li, L. Jiang, Z.Q. Yu, J. Li and Y.W. Li	3
A Taylor Series Integration Method with Coupling in Structural Dynamics Z.Y. Guo	9
Optimization Design of Core Thickness of Exterior Frame and Core Hybrid Structures in High-Rise Buildings S.Y. Zhang, W.W. Zhao and H.H. Wang	14
Mean Wind Pressure Field on the Typical Large-Span Roof Structures F.H. Li, M. Gu, Z.H. Ni and S.Z. Shen	19
Explosion Resistance Investigation into Sandwich Structure of Steel Fiber Reinforced Concrete Support Plate X.W. Wang	25
Failure-Mode Based Coupled Shear Wall Optimization Design S.S. Zheng, Q. Xu and Z.Q. Li	29
Experimental Tests on Composite Beam with Various Slab Systems A. Saggaff, M.M. Tahir, N. Jamaluddin, P.N. Shek and C.S. Tan	33
Experiment on a Concrete Filled Steel Tubular Arch with Corrugated Steel Webs Subjected to Spatial Loading J. Gao, J.Z. Su and B.C. Chen	37
Research on Steel Beam-Column Joints of Concrete Filled Steel Tube M. Li, Y. Liu, Z.Z. Sun, Y.F. Liu and J.F. Du	43
Structural Optimization of Transmission Line of Steel Poles L. Qin, Y.N. Luo and P. Huang	48
Analysis of Storey Damage Effect Factors of SRC Frame-RC Core Tube Hybrid Structure under Cyclic Loading S.S. Zheng, W. Yang, Q.L. Tao and Y. Hu	52
A Multiaxial Damage Statistic Constitutive Model for Concrete S.S. Zheng, W.Y. Li, Q.L. Tao and Y. Fan	56
Influence of Various Inclinations of Webs on Anti-Torsion Characteristic of Steel-Concrete Composite Box Girder X.H. Hu	60
Contrastive Finite Analysis of SRC Frame under Cyclic Loading Base on Macroscopic and Microscopic Element S.S. Zheng, W. Wang, P.J. Hou and M. Xie	64
A New Method Tracing Load-Deflection Equilibrium Path of a Doubly Nonlinear Truss S.T. Liu and Q.L. Long	68
Study on the Constitutive Model of Composite Materials in Elastic-Plastic Stage H.C. Qin and J.L. Wang	73
Experimental Study of Blind Bolted Joints to Concrete-Filled Thin-Walled Steel Tubular Columns under Cyclic Loading J.F. Wang, X.Y. Chen and H.T. Hou	78
Frame Column of the Limit Value of Axial Compression Ratio of Z.N. Tong	83
Experimental Study on the Behavior of Two-Way Concrete Slab under Furnace Loading Z.N. Yang and Y.L. Dong	88
Natural Element Method for Material and Geometrical Bi-Nonlinear Problems D.H. Ding, Q. Zhang and J.Q. Xiao	93
FEM Analysis on Seismic Behavior of Hybrid Coupled Wall System with Steel Boundary Elements Y. Shi, M.Z. Su and A.L. Song	98

Dynamic Characteristic Analysis on Experiment of Suspended-Span Structures in Water S.R. Zuo and J.X. Yang	104
Experimental Research on Hysteretic Behavior of Top-Seat Angles Beam-Column Connections X.W. Wang and D. Han	110
Applied Research on CL Structural System in the Construction of Affordable Housing Y.H. Hao, T.S. Jin and K.X. Zhao	114
Complex Genetic Algorithm for Structure Shape Optimization Design of Mixed Discrete Variables C.Y. Zhu, J.Y. Liu, H.Y. Liu and X.Z. Wang	118
Test Study on Anti-Sliding Coefficient of Friction-Type High-Strength Bolt Connectors H.N. Xing, X.P. Zhang, Z.L. Liu and L.Q. Jin	123
Projective Geometry on the Structure of Geometric Composition Analysis Application X.Z. Song, M.L. Lu and T. Qin	127
Research and Application of Pre-Stressed Concrete Composite Slabs J.S. Zhang, H.H. Nie, Y.L. Yang and Y. Yao	131
Wind-Induced Dynamic Analysis of the Flat Tensegrity Structures in Time Domain C.J. Lu, X.D. Wang and S.N. Lu	140
The Doubly Nonlinear Limit Load Analysis of Space Grid Structure C. Xi and Y.H. Hao	144
Dynamic Analysis of Gravity Platform's Marine Riser under Wave Load X. Wang, Y.B. Wang and N. Liu	150
Experimental Research and Calculation Analysis on Shear Crack Load of Steel Reinforced Concrete T-Shaped Columns J.T. Li, X.G. Zhang and Z.P. Chen	154
Elastoplastic Analysis of Structure Composed of Columns Based on the Basic Equation System Y. Li	159
Preliminary Study on Dynamic Progressive Collapse Analysis of Spatial Composite Frames with Concrete-Filled Steel Tubular Columns X.Y. Zhou, J.X. Wang and W.D. Wang	164
Rigidity Test Research of Rigid and Flexible Flange Connection in Substation Frameworks H.B. Li, J.F. Yang, Y.L. Peng and X.M. Han	168
Finite Element Analysis on Exterior Joint of Reinforced Concrete Frame Structure C.M. Wei, D.L. Shao, H. Su and Q. Zhao	172
Study on Bonding Properties of Bamboo-Steel Interface under Static Load J.L. Zhang, Y.F. Du, Z.M. Yan and Y.S. Li	176
Constant Amplitude Fatigue Calculative Method of Welded Hollow Spherical Joint with Cross-Board in Steel Plate-Type Grid Structure J.F. Jiao, H.G. Lei, H. Wu and Y. Liu	180
Research Progress and Prospect on Self-Drilling Screw Connection Shear Capacity L.F. Lu, Y.P. Zhang, W.Q. Fang and D.H. Yang	187
Free Vibration Analysis for Step Tubular Structures of Tall Buildings Supported on Elastic Foundation Soil Z.Y. Xiao, Y. Gong and Y.Q. Gong	194
Numerical Simulation Analysis on Shear Bearing Capacity Experiments of Cold-Formed Steel Self-Drilling Screws Connection L.F. Lu, G.Y. Huang, W.Q. Fang and D.H. Yang	200
Design and Analysis on Fan-Shape Four Pyramid Grid with Single Point Supporting K. Li and J. Ji	207
Calculation and Design Analysis of Grid with Six-Point Supporting K. Li, J. Ji and Y. Li	211
Test on Hybrid Connection for Steel Bars in Concrete Y. Tian, P. Feng, Z.H. Zhou, L.P. Ye and B.L. Wan	215
Parameters Analysis of Re-Centring SMA Damper Based on SAP2000 Y.H. Ling and H.H. Ling	219
A Simplified Prediction on Deflection of Web-Core Sandwich Beam in Weak Direction Y.B. Shao	226

Experimental Study on Elastic Modulus of Combined Aggregate Concrete Y.K. Zhang, L. Hui and S.S. Zhao	230
Wind Pressure Distribution on a Large-Span Roof Structure Q.H. Wang, B.Q. Shi and L.L. Zhang	234
Study of Bearing Capacity for Vertical Stiffener Joint with Concrete-Filled Square Steel Tube and Steel Beam S. Wang, Q. Zhu, J.H. Zhao and D.F. Zhang	239
Mode I Fracture Toughness of a Tri-Layered Beam with Interfacial Crack S.C. Her and W.B. Su	245
Theoretical and Experimental Study on Structural Dynamics Analysis Based on Electrical Circuit Analogy Method G. Li, P. Chen and Y.W. Hao	249
Lamb Wave Scattering Induced by a Rectangular Hole F.L. Feng and C. Lu	254
Finite Element Analysis of External Prestressing Beams Made of Strain Hardening Material A. Atta	259
Research on Horizontal Bearing Capacity of High-Rise RC Shear Wall Arranged High-Strength Steel in Boundary Concealed Columns Z.B. Li, H.M. Zhang, H. Ma, E.W. Guo and W.J. Wang	269
Experiment Study on Dynamic Characteristics of Unbounded Prestressed Concrete Beams F.G. Li and R. Li	273
The Influence of Static Response of Super Tall Building Mega-Frame Structure Caused by Changes of Frame Rigidities X.D. Xie, X. Wang and L. Qin	277
Research of Mechanical Influence of Initial Imperfections on Beam String Structure Y.S. Qi and S.H. Liu	282
Finite Element Analysis on Concrete Filled Steel Tubular Concrete Beam Joints under Cyclic Loading by OPENSEES Q.J. Chen, J.L. Guo, J. Cai, A. He, X.L. Tang and C. Yang	287
Axial Ultimate Capacity of Partially Encased Composite Columns G.T. Zhao and C. Feng	292
Fluctuating Pressure Correlativity Analysis on the Cantilevered Roof of a Stadium H.Y. Zhang, Z.H. Chen and F. Chen	296
Inelastic Dynamic Analysis of Steel Structure Using Force Analogy Method S.Q. Song and G. Li	304
Influence of Axial Load Level on Performance of Resist Impact on Tubular T-Joint H. Qu	310
Influence Analysis of Mortar Elastic Modulus to CRTS III Slab Track Vertical Dynamic Response Z.P. Zeng, X.S. Wang, W.R. Chen and G.C. Long	314
Finite Element Analysis on Circular Steel Tube Composite Column Filled with Steel Reinforced Concrete Y.F. Xu, X. Yang, X. Wang and S.Y. Bai	318
Experimental Investigation of Cold-Formed Steel Tubes Subjected to Web Crippling H.L. Peng, F. Zhou and L.W. Tong	322
Analysis of Slab and Beam's Moment Influenced by Stiffness Ratio H.X. Chen	329
On the Use of GB50018 and AISI Specifications to Estimate the Load-Carrying Capacity of Cold-Formed Steel Lipped Channel Columns D.F. Sun	333
The Research Status and Prospect of Passive Energy Dissipation Technology in Fields of Structural Engineering M. Chen and G.J. He	338
Shaking Table Model Test of Steel Frame Structure Y.S. Cao, Y.L. Zhao and J. Li	343
Modal Analysis of Tensioned Membrane Structure of Umbrella-Shaped J. Zheng, C.W. Huang and Y. Zhang	349

About One Way of Optimization of the Thick-Walled Shells V.I. Andreev	354
Reinforcing Design of the Crane Girder in a Factory L.L. Yu and L. Xu	359
Optimization of Yield Shear Coefficient for Parallel Base Isolation System Q. Rong and Y. Sheng	363
Vertical Isolation Research of Rubber Bearing in Series with Disk Spring Q. Rong and Y. Sheng	367
The FEM Analysis of Size Effect on Prism Concrete Specimens with Different Lengths under Loads of Axial Compression E.W. Guo, Z.B. Li, H. Ma, W.J. Wang and Y.P. Xie	371
Numerical Analysis of Composite Wind Turbine Blade Considering Failure Behavior M. Wang, R.X. Bai and Y.A. Shen	375
Research on the Ultimate Bearing Capacity for Steel Tubular Transmission Tower's Joints with Annular Plate B.H. Lv, Z.Q. Chen, H. Li, S.Q. Guan, X.L. Li and L. Zhang	379
The Behavior of Column during Constrained Buckling Process X.G. Wu, B.L. Zheng, P.F. He and S.G. Liu	385
Dynamic Characteristics Analysis of Large Space Shear Wall L.J. Zhou, J.Z. He and J. Huang	400
Topology Optimization of Building Structures Considering Wind Loading J.W. Tang, Y.M. Xie and P. Felicetti	405
Study on Analysis and Design of Structure Transfer Storey in Business-Living Building C.Y. Zhang, G.S. Bian, N. Liu and L. Sa	409
Research on Key Issues in Design of Outer-Plated Steel-Concrete Continuous Composite Beams L.H. Chen, F. Xiao and Q.L. Jin	414
Experimental Study on Post-Anchoring Pulling-Out Bearing Capacity of Inorganic Materials in Concrete Test Cubes S.Q. Cui, L.P. Jiang, B. Cheng and T. Wang	420
Research on Auxiliary Pile Group's Impact to Foundation Pit's Horizontal Displacement and Analysis on Pile Group's Equivalent B.S. Xu, R.C. Liu, M. Gong and Z.Y. Zeng	426
Experimental Study of Defects in Cast-<i>In-Situ</i> Bored Piles and its Application for Superdeep Defect Treatment Z.W. Wang	434
Research on the Working Performance of Dowel Bar during Horizontal Installation Errors P. Peng, B. Tian and K.M. Niu	441
Experimental Research on Frame Structure of Light Steel Temporary Buildings X.F. Cai, Y.C. Ma, Z. Zhang, J.Z. Zhou and L. Xue	450
The Second Order Elastic-Plastic Analysis of Plane Steel Frame Structures with Semi-Rigid Connections X.B. Hu and P. Zhou	454
Analysis on the Interfacial Dilatancy Effect in Anchorage Zone of Grouted Bolts Y. Guo, G.Y. Zhu, X.L. Jiang and Z.F. Song	459
Eccentrically Braced Steel Frame Design Theory and Application Research in China C.R. Zhao, C. Wei and Y.Y. Zhang	463
Method Study for Finite Element Modeling of Large Oil Storage Tanks Q. Ge, F. Xiong and X.Y. Peng	471
Experimental Investigation and Nonlinear Finite Element Analysis of U-Shaped Steel-Concrete Composite Beam W.H. Li and F.H. Zhao	477
Numerical Analysis of Negative Skin Friction for Pile under Surface Loading by Particle Flow Code F.X. Zhou and Y.M. Lai	482
Dynamic Response Analysis of Steel Rope Impact on Asymmetric Twin Tower Building with Large Bases Q.F. Wang, J. Yao, H.M. Wang and C.L. Guo	487

Optimization of Cold-Formed Channel Sections Using Imperialist Competitive Algorithm R. Kohandel, B. Abdi, P.N. Shek, M.M. Tahir and A.B.H. Kueh	493
Optimum Design of Pile Raft Foundation on Pile-Soil Interaction S.J. Wu, Z.M. Xiong and Y.G. Xu	497
The Analysis and Application Research on the Space Work of Portal Frame X.W. Zhang, Z.M. Xiong and N.N. Su	501
A Foundation Study of the Economic Analysis of Isolated Framework Structure K. Wang, Z.M. Xiong and N. Peng	505
Finite Element Analysis on Medium-Speed Mill-Foundation Coupled System M.Z. Yang, Z.F. Peng, F. Liu, Y.L. Peng and X.L. Sun	510
Finite Element Analysis of the Pull-Out Specimens of Steel Reinforced Lightweight Concrete J.W. Zhang and S.H. Guo	514
Modeling for Initial Post-Buckling Analysis of Laminated Plates and Shells by FEM C.S. Han, H.M. Zhang and Z.L. Cheng	520
Study on Load-Carrying Performance of Short Axially-Loaded Column with Gusset Plate between Double Cold-Formed Thin-Walled C Steel M. Chen and Y. Sun	526
Vibration Test and Analysis on Medium-Speed Mill-Foundation Coupled System B. Xu, Z.F. Peng, F. Liu, Y.L. Peng and F.J. Zhang	530
A Study of the Partially Prestressed Tendons RPC Concrete Pole Connection Design Y.Z. Ju, D.X. Yu and W. Dehong	534
Exposure Test of FRP-Reinforced Concrete Structure in Temperate Marine Tide Zone M.J. Chu, Z.J. Sun, H.C. Cui and K. Zhang	538
The Alternation Story-Height Truss Lateral-Load-Resisting System and its Simplified Analytical Method Y.J. He, X.H. Zhou and C.C. Yang	543
The Multi-Objective Optimization under Random Loads X.J. Wang, X.A. Zhang and Y. Lian	548
Static Behavior Study for Latticed Concrete-Filled Steel Tubular Wind Turbine Tower Joints B. Li, M. Qiao and C.Y. Gao	553
Experimental Study of Pile Foundation Dynamic Testing Used in the Anchor Rod Nondestructive Testing L.W. Zhang, W. Shi, Y.N. Zou and D.S. Zhu	559
Experimental Study on the Static Performance of Joints in the Castellated Portal Frame of Light-Weight Steel Y.S. Su, S.F. Zheng, Q.L. Li and J.Y. Quan	563
The FEM Analysis of Reinforced Concrete Beam-Slab-Column Joints Z.B. Li, P.Z. Zhao, H. Ma, K. Song and C. Wang	569
Simplify Analysis on Anti-Continuity Collapsed Frame Structure of Isolation Bearings and Non-Isolation Bearings S.W. Duan and D. Lu	574
Structural Design Optimization for a Case of a High-Rise Comprehensive Building A.F. Shao, L.X. Zhang and H.Z. Kang	579
Experimental Investigation on Vertical Tension Property of Laminated Rubber Bearings Z.Q. Zhang, S.C. Chen, W.M. Yan and X.X. Ren	583
Finite Element Model Updating of a Steel Jacket Scale Model Z.G. Li, Y.C. Li, S.Q. Wang and B. Yang	588
Research and Application of the Combined of SWMM and Tank Model G.Q. Sang, S.L. Cao and Z.B. Wei	593
The Effect of Joint Working Mode between Steel Wires on Local Bending Stress of Stay-Cable H. Li and G. Zheng	600
Experiment Study on Static Mechanical Behavior of Plain Steel Plate-Light Weight Concrete Hollow Composite Decks Y. Yang, B.L. Xu, S.S. Zeng and J.Y. Xue	604

Study on Static Design Methods of Plain Steel Plate-Light Weight Concrete Hollow Composite Decks Y. Yang, K. An, S.S. Zeng and J.Y. Xue	610
Nonlinear Finite Element Analysis of Layered Steel Fiber Reinforced Concrete Beam H. Jing and Y.Q. Li	616
Analysis on High Rates of Scaling and Salt Accumulation of 600MW Supercritical once-through Boiler X.N. Zhang, X.M. Li and C.M. Li	620
Study on Isolated Layer Mechanics Character of Combined Base Isolated Structure Based on Axial Forces Redistribute F.Y. Zhang, M. Gu, Y. Song and S. Xu	627
Bond Capacity of FRP Plate Depending on the Retrofit Methods and Shear Key Locations S.Y. Seo and S.J. Yoon	632
Development and some Prospects of the Shaft Lining Structure L.L. Wu, Y.G. Lian, Y.X. Kong, Y.J. Ma, B. Jiang, Y. Li and Y.Y. Li	636
Displacement-Based Seismic Design Method of Steel Moment Frame Q. Zhang, Y.F. Yue and E. Xiong	640
Static Strenght of Doubler Plate Reinforced Tubular K-Joints under Bending Load W.N. Sui, X.L. Zhang, G.C. Li and X. Bai	645
Finite Element Analysis of Axially Loaded Column Plated Column Base Z.G. Fang, J.P. Hao, J.J. Shi and W.H. Zhong	649
Test Research on Cast-<i>In-Situ</i> Concrete Pipe Piles under Lateral Load Z.T. Ma, Y.P. Wang and S.J. Liang	653
Experimental Investigation on Four Types of Steel Plate Shear Walls F. Li, S. Li, G.N. Wu and D. Wang	657
Experimental Study on Shear Behavior of Hybrid Fiber Reinforced High Performance Concrete Deep Beams S.B. Liu and L. Xu	664
Taper Roll Contour Design for Edge Drop Control of Non-Oriented Electrical Steel on Tandem Cold Rolling Mill G.H. Yang, J. Zhang, H.B. Li, J.G. Cao and S.H. Jia	670
Effective Stiffness of Rectangular Confined Concrete Columns with Continuous Compound Spiral Hoop W. Li, L. Jiang and L.Z. Sun	674
Analysis of Hybrid Effect of Two Hybrid Fiber CGFRP Bar and its Mechanical Properties X.S. Xu, S.L. Dong and X.D. Xu	680
Research Based on Relationship between Micro-Structural Damage and Intensity Attenuation Laws of Water-Bearing Limestone S.X. Liu, C.W. Liu, Y. Kang and D. Yang	684
Integral Space Concrete Roof Structure System Optimization Research K.C. Zhao, J.C. Zhao and M. Jiang	690
Bearing Capacity Analysis of Square Concrete-Filled Steel Tubular Column Based on RC Column with Spiral Stirrup T.C. Wang, C. Du and H.L. Zhao	694
Investigation on Dynamic Response of Steel Tower Structure under Time-History Wind Load J.W. Chen and L. Li	699
Experimental Research on Ceramsite Concrete Beams C. Du, W.L. Tian, X.W. Wang and D.J. Wang	708
Pull-Out Strength of Headed Bar According to the Lateral Confinement Effect of Reinforced Concrete Beam-Column Joint S.J. Yoon and S.Y. Seo	712
Performance Analysis of GFRP/Steel Composite Box Beams Y.Y. Li, Y.L. Wang and J.P. Ou	716
Numerical Analysis and Optimization on Dynamic Performance of Large Turbo Generator Frame Foundation B.S. Wang, D.H. Cao, Y.W. Yang, C.X. Xu and H.J. Qian	720

The Large Deflection of the Orthotropic and Rectangular Membrane under the External Distributed Load	
L. Jun, Z. Zhoulian, L. Changjiang, S. Weiju, Y.H. Zhang and H. Zeng	725
Shaking Table Test on Unreinforced Stone Masonry Pagoda	
F. Zhu, F.L. Wang, X.J. Sun and Y. Zhao	730
Research on Performance-Based Design Method of RC Structure	
H.T. Wan and J.W. Zhang	734
Influence of the Initial Imperfection on the Buckling of Steel Member Wrapped by Carbon Fibre	
P. Niu, G. Yang, C.F. Jin and X. Li	738
Five Developed Cylinder Reticulated Shell ANSYS Parametric Modelings	
X.Y. Lu, Z.D. Wang, X.W. Zhao and W. Chao	743
Parametric Modeling of Six Typical Double Primary Ribs Reticulated Dome	
X.Y. Lu, W. Chao, S.Y. Chen and Z.D. Wang	747
Seismic Performance Evaluation on Eccentrically Brace Steel Frame by Capacity Spectrum Method	
S. Yongkang and W. Zhengzhong	752
Excel Programming and Application for Concrete Filled Steel Tubular Structures	
F. Wang and X.R. Pan	756
Bearing Capacity Analysis on Slotted End Plate Connection Joints of Different Types	
R.H. Qiang, M.Z. Su, J. Yang and J. Cui	764
Calculation & Analysis on Integral Mound-Lifting System of Shear Wall Construction in High-Rise Building	
F. Wang and Y.S. Zeng	770
On the Influence of the Elastic Medium Stiffness in the Buckling Behavior of Compressed Beams on Elastic Foundation	
F. de Angelis and D. Cancellara	776
The Parametric Design Method of the Globoid Cam Based on the Software of ProEngineer	
Q.L. Liu, A. Tsai, S.F. Yao and E. Wang	784
Experimental Study on Vertical Base-Isolated System with Disk Spring	
Y. Zhao, J. Su and M. Lu	788
Simplified Calculation Analysis in Parallel Composite Isolation Structures	
W. Sun, Y. Yuan and N.H. Chen	793
Deformation-Based Nonlinear Finite Element Analysis of Steel High Performance Concrete Structural Walls	
M. Kaize	797
A New Type of Pile – Long with Cushion-Short without Cushion Rigid Pile	
M.F. Zhang, G.H. Yang and E.Q. Wang	803
Analysis of Cable Force Loss of Prestressing Structure during Tension Construction	
X. Zhao and H.Q. Fang	809
Research on Behavior of Composite Joints Consisting of Concrete and Steel	
J.J. Men, Z.F. Guo and Q.X. Shi	815
The Research on the Improved Genetic Algorithm and Optimized Based on the Random Functional Analysis	
Z.B. Xia, Z.X. Cao and K.F. Zhang	819
Analysis of Elasticity Solution of Bi-Direction Functionally Graded Piezoelectric Beam Subject to Voltage	
Y.Z. Yang	824
Bond Performance in Machined Reinforcing Bar for Reinforced Concrete	
C. Bosco and F. Tondolo	828
Monotonic Performance of Lightweight Concrete Shear Walls	
X.L. Yang, H.L. Wang and Q.C. Ren	832
Experimental Research on Full-Scale Reinforced Concrete Columns with Strong Confinement under Concentric Compression	
W.J. Zhang, B. Zhang, Z.B. Li, J. Wang and W.J. Wang	836

Chapter 1: Structural Engineering

Three-Stage Approach for Unrestrained Simply Supported RC Slabs under Uniformly Distributed Load J.X. Liu and K.H. Tan	845
A Finite Element Model for Simulating Out-of-Plane Behavior of Masonry Infilled RC Frames C.H. Zhai, J.C. Kong and X.H. Wang	849
Experiment for Attaching Force of a Suction Fan on Various Concrete Wall Surfaces B.J. Lim, Y.B. Ham and C.D. Park	853
Behaviour of Concrete Filled Steel Tube Reinforced Concrete (CFSTRC) Stub Columns: Experiments Y.J. Li, Q.X. Ren and F.Y. Liao	859
Optimization Simulations of Support System by Composite Soil-Nail Retaining Structure J.H. Huang, G. Song and E.X. Song	863
The Numerical Simulation for Wind Pressure on the Roof of Rhombic Plane and Saddle-Shaped Building C.H. Wang and J.F. Wu	869
Research of Two-Way Curved Arch Bridge Reinforced by BFRP B.R. Huo and X.D. Zhang	873
Multi-Storey Reinforced Concrete Frame Structure Earthquake Response Analysis C.H. Wang and J.F. Wu	877
Axial Compression Test of RC Columns Consolidation with BFRP B.R. Huo and X.D. Zhang	881
Numerical Investigation on Structural Behaviour and Curling Influence of Aluminum Alloy Bolted Connections T.S. Kim, Y.H. Jo and Y.C. Choi	885
Simplified Calculation Model of Analyzing Fiber Plasterboards Filled with Concrete Core Columns with Different Spacings Q.Z. Ma, X.L. Jiang and B.K. Zhang	890
Temperature Evolution and Optimization of Hot Extrusion Process for Al-Zn-Mg-Cu Aluminium Alloy Based on FEM Simulation L. Xu, G.Z. Dai, X.M. Huang, J.W. Zhao, J. Han and J. Gao	896
The Contrast Studies on High-Strength Bolts in Slip-Critical Connections between the Chinese and American Steel Structure Design Codes C. Huang and W.L. Pu	902
Nonlinear Analysis on Square Steel Tube Filled with Steel Reinforced High Strength Concrete Subjected to Bi-Compression Bending Load W. Ouyang	908
Experimental Research on Mechanical Properties of Sandwich Wall Panels with Bamboo Shear Connection M. Wang	914
Experimental Studies on Seismic Performance of High Strength Reinforced Concrete Columns W.X. Yang, Q.X. Shi and H.X. Sun	919
Influence Line Analysis of the Plane Trusses Based on EXCEL M.B. Zhao	927
FEM Analysis of Composite Structures for Plate-Cone Reticulated Shell X. Wang	931
Application of Finite Element Method for Nonlinear Analysis in Reinforced Concrete Structures M.R. Zhou	935
Geometrically Nonlinear Analysis Based on the Simple Truss D. Wi and Z.D. Li	939
Finite Element Static Analysis for Frame of Material Conveyor Base on ANSYS Y. Xie, G.P. Li and J.R. Fan	944

Chapter 2: Monitoring and Control of Structures

Fault Diagnosis System of Rolling Bearing Based on Wavelet Analysis L.N. Wang, H.B. Wang, Y.H. Cai and S.L. Wang	951
Investigation on Line-Shape Control Technology G.C. Yan and Z.X. Ma	956
The Comparative Analysis and Research of the Correction Model on Troposphere Delay C.L. Dong	960
Flexural Strength Evaluation of one-Way Void Deck Plate Slab with Polystyrene Foam S.H. Kim and S.U. Hong	964
Piezoelectric Impedance Based Elastic Modulus Monitoring for Concrete during Curing Z.G. Guo and Z. Sun	969
Knowledge Sharing in Quality Management L.L. Zhang, Y. Shang, H. Luo and Y. Shi	974
Seismic Behavior Analysis of Beam-Column Joints of Steel Structure Semirigid Y. Ge and G. Su	978
Damage Detection of Simply Supported Beam under Effect of Moving Load by Hilbert-Huang Transform H.B. Liu and H.H. Nguyen	984
Creep Prediction Model for Concrete Made of Crushed Clay Bricks as Coarse Aggregate S.I. Ahmad and S. Roy	994
Research on the Application of the Infrared Thermal Image Method in Detection of Concrete Density of Concrete-Filled Steel Tube R. Xu, D. Jiang and X. Lu	998
Steel Pip Corrosion Forecasting Based on Support Vector Machine G.Y. Ma	1002
Analysis of Influence of Raft Stiffness on Tall Building Interaction System X.Z. Sun and L. Wu	1007
The Study on Reconstruction Patterns of Urban Village by Game Theory - With Hohhot as an Example X.Q. Zhao, Y.P. Bai and J. Meng	1014
Analysis on Strength, Stiffness and Stability for Shippment Structure of Hull Subsection Q.D. Zeng and M.H. Qiao	1019
Study on the Crack in Concrete Flange of Outer-Plated Steel-Concrete Continuous Composite Beams L.H. Chen, Q.L. Jin and H. Si	1023
Strength Analysis of the Construction Generated Soil Serving as Filling Material for the Consolidation Piles L. Chen	1029
Elastic Local Buckling Strength of Tapered H-Shaped Cantilever Beams K. Yoshizawa and K. Ikarashi	1033
Analysis of the Fire-Resistance of Suspen Dome Structure Z.L. Zong, Y.F. He and S.G. Li	1040
Research on Combined Numerical Integral Algorithms in Structure Seismic Hybrid Testing X.J. Cai, S.Z. Tian and X.F. Wang	1045
Strength of Square CFT Stub Columns with Slender Sections Z.H. Lu, Y.G. Zhao and Z.W. Yu	1050
Frame of Monitoring Warning System for High Rocky Slope H. Jin	1054
Test Research on Seismic Performance of Column H.T. Wan and P. Li	1058
Nonlinear Finite Element Analysis of Interior Beam-Column Joints in Reinforced Concrete Frame H.J. Zhao, H.T. Fan and Z.X. Wang	1062
Robust Control for Uncertain Structural System Based on LMI Z.B. Gao	1067
Vibration Fault Analysis in Screw Compressor and Foundation Y.M. Zhou, Z.M. Song, H.F. Zhao and S.Y. Mi	1072
Identification Method Research of the Compressed Beam Elastic Buckling Load L. Du and F.C. Li	1076

Experimental Study on Flexural and Fatigue Property of Steel Fiber Reinforced Prestressed Concrete Slab S.Y. Wang, J. Hou and B. Huang	1083
Study on Explosion Resistance Performance of Injected Fluid Structure C. Zhang, W. Wu and Y. Li	1087
Research on Signal Transmission Property of Wireless Sensor Networks for Test System J. Sun, C.F. Zhu and J.L. Zhao	1091
Structural Safety Alarming Based on Signal Energy by Using Wavelet Packet Transform Z.G. Jiang and B. Chen	1097
Performance Degradation Assessment of a Beam Structure by Using Wavelet Packet Energy Z.G. Jiang and B. Chen	1102
Investigation into the Elastic-Plastic Ultimate Load-Carrying Capacity of Suspen-Dome F. Li, J. Niu and L.R. Ding	1108
Study of Hybrid Method on Beam Crack Evaluation C. Du, S. Li, Y.Y. Li and Z.T. Du	1113
Analysis of Steel Braced Frame Structure Response Encountered Higher Seismic Intensity M. Li, Y.F. Liu, L.G. Jia, Y. Liu and J. Du	1117
Crack Formation and Strength of Fire Damaged Concrete Beam W. Srisoros, K. Kaewpetch, P. Ariyasuk and A. Chokcharoenmahasarn	1121
Appraisal Parameters of Corrosion Damage of Aged Aluminum Alloy Material Y.H. Zhang, Q. Zhang, X.L. Chang, C.G. Yue, S.Y. Zhang and W.L. Liu	1127
An Alternative Method of Estimating Piping Construction Projects K.S. Lee and J.Y. Choi	1131
Numerical Analysis of Top Ring Beam for Foundation Pit H.Y. Xu	1137
Temperature Field Calculation of Mass Concrete Anchor H.T. Wan and L.M. Zhao	1141
Experimental Research on Damage Detection of Concrete Structures Based on Piezoelectric Smart Aggregates Y.Y. Meng, S. Yan and W. Sun	1145
Study on Accumulated Ductility Coefficient of Concrete Filled Steel Tubular Columns Based on Experimental Results P.Z. Xu, X. Wu, N. Zhang, H.J. Zhang and H.S. Xing	1152
Finite Element Investigation on Ultimate Strength of Bolted Connections W. Elleithy and C.K. Lim	1157
Optimal Sensors Placement Based on Modal Strain Energy H.B. Zheng, Q.S. Yan, J.L. Hu and Z. Chen	1164
A Multi-Hierarchical Damage Identification Method for Jacket Platform Using BP Neural Network X.Y. Chen, S.S. Dong and F.S. Liu	1170
Damage Identification of Arch Bridge Based on Curvature Mode Wavelet Analysis D.Q. Guan, X.L. Zhong and H.W. Ying	1176
Deformation Monitoring Data De-Noise Processing Based on Wavelet Packet Y.M. Yang, Z.G. Wang, Y.Y. Gao and F.P. Gao	1180
Mechanism and Dynamic Behavior of a Novel Hydraulic Force Pulse Generator Z.L. Yong, G.X. Wang and J.M. Yuan	1187
Sensibility Analysis on the Shearing Strength Parameters of Sliding Surface Y.J. Zhang, L. Zhao, A. Li and C.L. Zhang	1196
Experimental Study of Two-Dimensional Elastic Thin Plate Damage Identification Method Based on Modal Curvature D.H. Xie, H.W. Tang and R.S. Pan	1202
Finite Element Based Fatigue Life Evaluation of Anthropogenic CO₂ Pipeline Containing an Inner Defect Q. Wen, Q. Jin and J. Zhou	1207
Research on Plate Damage Detection by Two-Dimensional Wavelet Analysis D.Q. Guan, X.Q. Xiao and X.L. Zhong	1212

Evaluation of the Bearing Capacity of the Concrete Pier Exposed to the Freeze-Thaw Cycles Z.Y. Li	1216
The Analysis on the Deformation Prediction of Pile-Anchor Retaining Structure in Deep Foundation Pit in Kunming Y.H. Chen and Y.W. Wang	1222
Numerical Analysis to Influence of Different Roller Loads for Low Subgrade Connecting J.Y. Yuan, Y.Y. Tu, T. Cheng, D.B. Zhang, Z.H. Wu and J. Xiang	1226
A Study on the State Recognition of Frame Structure Based on the Maximum Lyapunov Exponent J. Yang, J.T. Zhou, J.X. Yang and Y. Chen	1230
Hybrid Control for Seismological Nonlinear Structures on Liapunov's Theory Y. Pan and T. Zhao	1237
Experimental Study about Testing Masonry Shear Strength with Drilled Core Method S.Q. Cui, X.W. Kong, X. Wang and M.L. Yang	1241
The Bearing Capacity Analysis of Wedge Cross-Section Based on Ansys Z.G. Li, Y. Guo and Y.J. Bi	1245
A Theoretical Study on Knowledge Discovery Technique for Structural Health Monitoring J. Li and J. Deng	1250
Study on Damage Identification of the Simply Supported Beam Employ the Difference of Deflection Influence Line under Symmetrically Load Y. Liu, X. Wang and F.X. Zhou	1254
Study on a New Foundation Stiffness Calculation Model Y.J. Ma, B. Yan and J. Zhang	1258
Damage Detection Analysis of Simple Beams Based on Strain Mode X. Guo, J.Q. Wu and K. Ma	1262
Damage Identification Method Research Based on the Change Rate of Strain Mode S.W. Wang and Y.M. Zhou	1267
Numerical Modeling and Feedback Analysis of Failure and Deformation of Soldier Pile Walls in Two Adjacent Deep Pits Z. Xing and W.X. Fu	1272
Experimental Study on Fatigue Crack Propagation of through-Thickness Crack under Out-of-Plane Bending X.C. Ju and T. Kazuo	1277
Failure Modes for Single-Layer Reticulated Domes under Oblique Impact D.Z. Wang, F. Fan, J.W. Dai, X.D. Zhi, Z. Cao and X.L. Du	1284
The Seismic Behavior and Failure Form in Structure of Frame-Shear Wall of High-Rise Concrete Residential Building X.Y. Liu and H.H. Dong	1290
A New Abnormal Index Based on Frequency Change for Structural Health Monitoring Y.S. Song, Z.G. Sun and N.Z. Zhao	1295
Experimental Research on Bending Property of GFRP Monopole Communication Tower Z.R. Shen and L. Xu	1299
Experimental Investigation on Wide-Span Cold-Formed Steel Roof Truss System S. Mohammad, M.M. Tahir, C.S. Tan and P.N. Shek	1304
Monitoring Strain Study of Cylinder Caisson Based on Fiber Grating Sensing Technology Y.H. Chen and J. Zhou	1308
Time-Delay Analysis for Active Controlled Structure System Y. Sheng, Q. Rong and Y. Pan	1312
Experimental Research on the Ductility of High Performance Concrete Beams Y.W. Yun, Q. Luo, I.Y. Jang, S.S. Sun and J.W. Zhang	1316
Numerical Analysis on Seismic Performance of Beam-Column Joint in the Added-Layers Steel Structure Y.P. Chu, Y. Yao, H.J. Wang and Y.J. Deng	1321
Compressive Strength Reduction of Concrete Subjected to Hydrostatic Compression J.Z. Lu, L. Chen, X. Zhu, N. Xu and G. Lin	1325
Field Experiment Study on the Bearing Characteristics of Squeezed Branch Pile in Loess Area W. Cui and Z.J. Wang	1329

Experimental Study on the Bearing Capacity and Ductility of High Strength Concrete Columns Wrapped with CFRP Cloth Z.J. Hu and Y. Xu	1333
Impact Evaluation of Mud Cake Thickness on Shearing Strength at Cement-Formation Interface J. Gu, B.L. Yang, Y.J. Yang, C. Ma, J.B. He and K. Li	1337
Nonlinear Reduction Analysis of Defects on Reticulated Shell Structure Bearing Capacity X. Tu, Y.Y. Wu, G.L. Xie and L. Zeng	1341
Analysis of Principal Component - Application of SVM Model in Prediction of Ultimate Bearing Capacity of Static Pressure Pipe Pile J.B. Zhao, C. Xu and H. Guo	1345
Analysis of Kinematic Behavior on Landslide Groundwater at K144 Section along Da-Yu Highway H. Wang, Q.C. Wang, X.L. Xu and Q. Wu	1353
Vibration Control Device and its Performance under Wind Load in High-Rise Buildings Z.H. Dong and J.Y. Yuan	1358
Dynamic Responses and Failure Modes of T-Shaped Concrete-Filled Steel Tube Core Columns under the Blast Loads Y.F. Xu, A. Wang and S.Y. Bai	1362
Application of Support Vector Machine in Springback Forecasting for Steel Structure J.G. Chen and Z.G. Li	1366
Finite Element Modeling for Health Monitoring and Condition Assessment of Large-Span Steel Roof Unloading Process Y.X. Liang, X.L. Wang and H.M. Zhong	1370
Dynamic Stability Analysis of Big Span Steel Tubular Truss D.Y. Pan	1375
Experimental Investigation on Temperature Distribution of Reinforced Concrete Beam D.F. Zhao, Z.K. You and D.D. Liu	1379
Experimental Study on Seismic Behaviors of Improved Composite Steel Staggered Truss Structures H.D. Ran, W. Xv and M.Z. Su	1383
Evaluation of the Vulnerability Index for Unreinforced Masonry Structures F. Djaalali, M. Bensaibi and N. Bourahla	1387
Bond Behaviour between Recycled Aggregate Concrete and Corroded Steel Rebars B. Lei	1391
Crack Width Calculation of Steel Reinforced Concrete Beams Considering the Bond-Slip C. Xiu Li, D.J. Shen, P.L. He, X.F. Dong and H.F. Zhang	1395
Structure Observation & Identification Considering Soil-Structure Interaction of Story Stiffness and Damping Ratio of 8-Story Steel Encased Reinforce Concrete Structure by Microtremor J. Ren, K. Morita and J.S. Pan	1399
Bearing Capacity of Fastener Steel Tube Full Hall Formwork Support Base on Stability of Pressed Pole with Multiple Point Restraint against Rotation Z.R. Lu, X.M. Sui and Z.H. Chen	1404
Damage Detection of Reinforced Concrete Beams by Wavelet Analysis G. Xue	1416
Experimental Study on Shear Behavior of Combined Aggregate Concrete Beams Y.K. Zhang, H. Liu and Z.Z. Song	1422
Study on Inhibition Effect of Extractives on Building Bamboo's Termite Prevention W.X. Peng, F.J. Wu, L. Cui, Q. Xue and D.C. Qin	1426
Model of Identifying Deflexion of Oil Storage Tank W.B. Liu	1429
The Research of Pore Water Pressure Effect on the Slope Safety Factor Based on Flac H.B. Liu, L.H. Zhang and D.H. Lin	1433
The Assessment Method and Application of Indirect Detection H.B. Chen, L. Wang, S.X. Gao and X.J. Tong	1437
Experimental Research on Structure and Performance of Joints in Cold-Rolled Rectangular Hollow Sections S.D. Hu, J. Zhang, L.X. Li and Q.M. Chang	1441

Cumulative Damage Investigation of Research Status and Problem Analysis of RC Structure	
P.L. Zhang	1446
Experimental Research on Ductility and Bearing Capacity of T-Shaped Columns with HRB500 Reinforcement	
Y.Y. Li, J.L. Qiao and J.X. Zhang	1450
Elasticity Damage and Plastic Analyses of Masonry	
W.F. Zhang and H. Wang	1454
Research on Judging Key Components for Collapse of Space Structures	
T.C. Wang, J. Kang, Z.P. Li and H.L. Zhao	1459
Research on Fault Diagnosis Method of the Aircraft Flap System Based on Weighted Fuzzy Petri Net	
Q.H. Xu, C. Jing and Y.M. Xu	1465
Determination of the Complex Moduli of Viscoelastic Materials by a Free-Vibration Method	
Y.C. Li and J.H. Liang	1471
Temperature Forecasting System of Cement Decomposing Furnace Based on Grey System Theory	
X.L. Liu and Y. Kun	1475
Analysis of Soil Disturbance Caused by Pipe Jacking Construction	
Y. Sun and Z.L. Xu	1480
A Method of Damage Identification for Shear Buildings	
F. Li and J.L. Wang	1484
Dynamic Response and Failure Mode Analysis on Light-Weight Steel Columns under Blast Loads	
S. Yan, L. Liu, P. Li, Z.Q. Xin and B.X. Qi	1489
Static Analysis of a Meteorological Tower under Lateral Loads	
Z.B. Su and S.N. Sun	1498
Experimental Study on the Flexural Behavior of SRHSHPC Beam	
S.S. Zheng, S.S. Zhu, P.J. Hou and S.L. Che	1502
Study on the Damage Law of SRC Frame-RC Core Wall Hybrid Structure Storey Affected by Component Damage	
S.S. Zheng, L.F. Sun, Q.L. Tao and Y. Hu	1506
Steady State Response of Compressible Fractional Derivative Viscoelastic Thick-Walled Cylinder	
L.C. Liu, L. Yu and H.X. Yu	1510
 Chapter 3: Structural Rehabilitation, Retrofitting and Strengthening	
Nonlinear Analysis of R.C Beams Strengthened with CFRP	
W.S. Li and K. Wang	1517
Experimental Study on the Splitting Tensile Strength of Recycled Concrete Made of Brick and Tile	
H. Wang and A.L. Zhai	1521
Research on the Rehabilitation of the Ancient City Wall of the Wuchang Uprising Gate	
Z. Sun	1526
Experimental Studies on the Bonding Failure between CFRP and Concrete in RC Two-Way Slabs Strengthened with CFRP Strips	
W.B. Sun, J. Zhao and Y. Jiang	1530
Fatigue Life Prediction of Corroded RC Beams Strengthened with CFRP under Repeated Loads	
L. Song and Z.W. Yu	1534
Improved Computing Method for Row Number of Bend-up Bars in Reinforced Concrete Beams	
L.P. Cai	1540
Analysis on Rationality of Deformation Resistance Structural Component Ring Beam	
L.W. You and W.S. Liu	1544

Calculation Method Investigation on Jacketing Reinforcement of RC Eccentric Compressive Column Subjected to Fire J.J. Guo, Y. Lu and P.X. Li	1548
Research on Stress Increase of Unbonded Tendons at Ultimate in Prestressed Concrete Continuous Beams X.D. Wang, W.Z. Zheng and Y. Wang	1554
Study of Strain Monitoring in a Construction of House Rectification B. Yuan, C.Y. Cai and S.T. Huang	1558
Experimental Study on Confinement Effectiveness of Different CFRP Hybridized Methods in Retrofitting Shear Deficient HSC Columns S.Y. Wang, H.C. Cao, W. Lu and Y. Liu	1565
Investigation on Vibration Reduction Effects of a New Vibration Isolation Module for Pier Foundation Z.X. Ma, W.P. Xie and G.C. Yan	1574
Experimental Research on the Performance of Fiber Reinforced Plasterboard Filled with Concrete under Eccentric Axial Load X.L. Huan and C.L. Li	1578
Optimal Placement of Triaxial Accelerometers Using Modal Kinetic Energy Method T.H. Yi, X. Wang and H.N. Li	1583
Contrast Experiment of Common Crack Repair Method and Comprehensive New Repair Technology Research Z.Q. Li, N.R. Bu and X.H. Cong	1587
Research on the Short-Time Deflection of Concrete Beams Reinforced with 500MPa Steel Bars Z.H. Li and X.Z. Su	1592
Experimental Study on the Shear Properties of Concrete Column Repaired by CFRP X.G. Cui, Z.W. Wang, N. Ma and Z.L. Yu	1598
Electrochemical Behavior of Carbon Steel in Neutral Chloride Solution Adding Amine-Carboxylate Based Corrosion Inhibitor Z.Y. Liu, X.L. Li, W.J. Lan and B.H. Wu	1603
Nonlinear Numerical Simulation Analysis on Mechanical Behavior of High-Strength Concrete Beams Reinforced by HRBF500 Steel L.J. Liu, X.G. Ye, X. Chong, Q. Jiang and L.L. Xie	1607
Experimental Study on Flexural Behaviors of Steel Reinforced Recycled Coarse Aggregate Concrete Beams W.Y. Qin, Y.L. Chen and Z.P. Chen	1614
Laboratory Tests on the Improvement of Strength of Silt Using Microbes Z.Y. Xu, S.J. Wan and Y.R. Ma	1620
The Filler Application of Light Weight Aggregate Concrete in Double-Curved Arch Bridge Reinforcement Y. Zhang and B. Li	1626
Effective Parameters on Strength of Fibre Reinforced Soil A. Chegenizadeh and H. Nikraz	1630
Studies on the Changes in the Parameters Stability of Hinge Joint Concrete Block Slope Y.Q. Zhang, Y.N. Mi, L. Wang, J.T. Zhao, Z.G. Wang and X. Shao	1639
Lean Duplex Stainless Steel Tubular Members Strengthened with CFRP Plate Subjected to Web Crippling S.M.Z. Islam and B. Young	1644
Flexural Fatigue Performance of RC Beams Strengthened with Hybrid Fiber Sheets X.J. Chen, X.E. Zhu, Z. Yang and M.X. Dai	1657
Study and Practice of Controlling Anchorage Force Loss of Prestressed Anchor Rope G.R. Lu, Q.B. Wang, X.J. Li and L.G. Wang	1663
Study on Formulation of PU Resin for Pipeline Lining Rehabilitation Technology S.J. Zhang, R. Wang, C.Q. Ma, X.Z. Yin and D. Yan	1669
Research on the Renovation and Re-Use Design of Historic Buildings Y.H. Xu	1674
The Finite-Element Analysis for CFRP and Steel Bar Strain in the Strengthened Concrete Slab X.G. Cui, J.W. Ding, Y. Yang and Y.F. Liu	1679

Research on Optimization Design for Reinforcing Method of Irregular Cross-Section Arch X.Y. Chen, B. Liao and J. Li	1684
---	------

Chapter 3: Structural Rehabilitation, Retrofitting and Strengthening

Analysis on Seismic Performance of Frame Columns Reinforced with Wing Walls X.Z. Zhang, R.H. Wang and W. Hu	1691
The Study on Bond and Anchorage Behavior of RC Flexural Members with Inorganic Adhesive Powder X.G. Zhou, H. Fang, J.Y. Yan and P. Zhu	1696
Research on Shearing Performance of RC Beams Strengthened with Steel Wire-Polymer Mortar C.Y. Zhao, S.M. Huang, Q.L. Yao and Y.J. Chen	1702
Distributed Hybrid Vibration Absorbers for Shock and Forced Vibrations L. Chen	1709
Experimental Research Treatment Measures of Joint on Paper Cellular Wallboard X. Miao, Y. Yao, Y.P. Chu, Y.J. Deng and Q.D. Han	1713
Displacement Based Approach for the Seismic Retrofitting of a RC Existing Building Designed for only Gravitational Loads D. Cancellara, F. de Angelis and V. Pasquino	1718
Experimental Evaluation of Lightweight AAC Masonry Wall Prisms with Ferrocement Layers in Compression and Flexure M. Abdel Mooty, A. Hendam, E. Fahmy, M. Abou Zeid and M. Haroun	1730
The Flexural Performance of Pre-Damaged Reinforced Concrete Beam Strengthened with CFRP in Seawater Environment Y.T. Wang, X.L. Du, F.X. Jiang and W. Zhang	1736
Strain-Based Fatigue Analysis of RC Beams Strengthened with FRP Laminates L.H. Huang, Y.J. Li, T.Q. Li and Q.X. Wang	1740
Research on Restoring Force Model of High Strength Concrete-Filled Steel Tubular Columns K.Z. Ma	1746
Study on Stress Increment of Externally Strengthened Prestressed Box Beams R.X. Wang, X.S. Chen, R. Guo and Q.R. Li	1752
Behaviors of Void Slab with GFRP Reinforcement S.H. Kim	1756
Design Method and Research of Adding Layers and Reinforcement of a Steel Structure S.Y. Wang, C.C. Du and J. Zhu	1760
Bond of Corroded Reinforcement in Concrete Wrapped with CFRP X.D. Dai, X. Kou and N. Cai	1765
FEM Analysis on the Fatigue Properties of Reinforced Concrete Beams Strengthened with CFRP Y. Wang, Y.N. Shen and J. Ma	1769
Cement Based Material with Crystal-Growth Ability under Long Term Aggressive Medium Impact S. Bohus and R. Drochytka	1773
Experimental Study on Replaceable Hybrid Coupling Beams T. Wang, X. Guo, X. He, C. Duan and Y. Du	1779
Properties Research on Concrete Laminated Beam Combined with GRC Enhanced Reinforcement Template J.F. Tian, Q.H. Wang and J.Z. Dong	1785
Bearing Capacity of Beams Strengthened by Common Methods Considering Strain Lag Effect S.M. Liu and Q.Y. Liu	1789
The Experimental Study on the Size Effects of Reinforced Concrete Members with Eccentric Compression F. Feng, J. Zhao and A. Lu	1793
Flexural Tests of Fiber-Reinforced-Concrete Beams Reinforced with FRP Rebars H.C. Qu, H.Y. Li and X. Zhang	1797

Influence of Reinforcing Steel Post-Capping Strength Deterioration on Collapse Resistance Capacity of a Single-Storey RC Planar Frame J.P. Han and J.P. Yang	1801
Numerical Simulation about Reinforced Concrete Beams Strengthened by Bolting Steel Plates X.S. Gao, D.H. Huo, S.H. Lv and X. Zhao	1807
Seismic Performance of Masonry Buildings Retrofitted by Pre-Cast RC Panels T. Wang, X. Chen, W.F. Li and Q.S. Miao	1811
Characteristics and Influencing Factors of Deflection in Concrete Beams Reinforced with FRP Bars X.S. Xu, H.D. Zhang and X.D. Xu	1818
Investigation of Effects of Baffle Configuration on the Performance of a Fixed-Cone Valve by Gas-Liquid Two-Phase Model W.L. Wei, B. Lv, Y.L. Liu and X.F. Yang	1824
Load-Deflection Analysis of RC Beams Strengthened with External CFRP Sheets X.Y. Lin, Y. Li and Z. Yan	1830

Chapter 4: Reliability and Durability of Structures

The Formation and Control of Laves Phase in K418 and 42CrMo Dissimilar Metal Laser Weld M. Pang, C.Z. Liu, G.H. Xu and J.H. Ma	1839
Probability-Based Durability Analysis of Structural Concrete under Chloride Salt Environment W.H. Shi, Z.W. Yu, Y.C. Kuang and C.B. He	1843
Analytical Investigation of Progressive Collapse Resistance Mechanism in Steel Moment Frame with Fiber Model C.Q. Liu and Z.Y. Mei	1848
The Interval Estimation about Confidence of the Reliability Index Z.M. Li, X.J. Kou and J.Y. Huang	1854
A Survey of Sulfate Resistance Test Methods X.J. Li and J. Zhang	1859
Reliability Analysis of Foundation Pit Directly Based on Field Information H.W. Zheng, H.Y. Wang, Z.G. Song and J. Cao	1863
Structural System Reliability Analysis for a Self-Anchored Suspension Bridge B.C. Yu and S.Y. Li	1868
Reliability Simulation Combining Kriging and Monte Carlo Radius-outside Importance Sampling in Space Structure Latch Q. Gong, J.G. Zhang and D. Su	1872
Reliability Assessment on Pipeline with Axial Surface Crack Z.X. Wang, X. Li and R.F. Zhang	1879
Aging Effect on Corrosion Damage Evolution Behavior of Fuse-Head Used for Electric Explosive Device Y.H. Zhang, Q. Zhang, X.L. Chang, C.G. Yue, S.Y. Zhang and W.L. Liu	1883
Life Prediction of Aluminum Alloy Structure Subjected to Corrosion Fatigue and Corrosion Damage Y.H. Zhang, Q. Zhang, X.L. Chang, C.G. Yue, S.Y. Zhang and W.L. Liu	1887
Analysis and Prevent Measure for Common Housing Construction Crack S.J. Yang and H. Wang	1891
A Practical Computing Method for Residual Area of Rebar Cross-Sections under Carbonation Induced Corrosion X.G. Wang and D.M. Zhong	1895
Reliability Model of Fatigue Damage Evolvement of Semi-Rigid Road Base Material S.Y. Wang, Z.C. Lai, G.S. Liu and X.J. Yang	1900
Effect of Alkali on the Impact Toughness of Adhesively Bonded Joints M. You, C.Z. Mei, W.J. Liu, J.R. Hu and L. Wu	1904
Research on the Non-Probabilistic Reliability Based on Interval Model A.R. Zhang and X. Liu	1908

Matrix Algorithm for Reliability of Structure in Generalized Random Space X.J. Liu, X.J. Li, W.H. Shi and Y.C. Kuang	1913
Fuzzy Reliability Analysis of Geocell Protective Slope Stability G.Y. Wang and Y. Han	1917
Investigation of Numerical Modeling for Concrete Corroded by Chloride Ion Diffusion W.J. Song, J. Dong, Y. Bai, F. Dong and W.Z. Sun	1922
A Discuss on Basing Half-Cell Potential Method for Estimating Steel Corrosion Rate in Concrete X.E. Zhu and M.X. Dai	1926
Characterization of Surface Crack Using Surface Waves S.C. Her and S.T. Lin	1931
Research on Chloride Diffusion Model in Pre-Stressed Concrete with Sulfate Attack R.G. Liu, J. Li and H. Li	1935
Reliability Analysis of Flexural Concrete Member Based on the Randomness of Pitting Y.L. Ma, Z.J. Li and Z. Zhao	1941
Influence of Boundary and Initial Condition on Durability of Concrete Structures Exposed to Chloride Environment X.G. Zhou and F. Zhao	1946
Reliability Assessment under Combinations of Snow Load Effect: The Lightweight Steel Structures with Gabled Frames and Components Designs Y.C. Cao, M. Liu, Y.Q. Wang and Y.N. Zhang	1954
The Accuracy Comparison of Assessing the Amount of Steel Corrosion in Concrete with Several Different Algorithms P.J. Cheng	1958
Influence of Cracks Parameters on Bearing Capacity for Prestressed Concrete Box Girder Z.N. Zhang	1963
Study on the Deformation and Stability of Building Foundations in Mining Subsidence Areas H.B. Chai	1967
Reliability Analysis of Different Concrete Strength RC Beams Reinforced by CFRP S. Chen, Y. Tao and S.H. Zhao	1971
Reliability Analysis on Construction Course of Open Caisson Structure J.C. Zhang and J. Yang	1976
Corrosion Properties of Rebar Welded Joints L.Y. Tang, Q.H. Xiao and S.Y. Zhang	1981
An Experimental Corrosion Investigation of Coupling Chloride Ions with Stray Current for Reinforced Concrete M. Chen, K. Wang, Q. Wu and Z. Qin	1987

Chapter 5: Seismic Engineering

Discussion on the Accuracy of Approximate Spring-Dashpot Artificial Boundary in Fluid-Saturated Porous Media Z.H. Wang, Y.M. Gai and C.G. Zhao	1997
Seismic Damage Analysis of SRHSHPC Frame Beams B. Wang, S. Zheng and F. Yu	2001
Numerical Analysis of Free Field under Horizontal Seismic Excitations S.L. Chen, C.Y. Cui and Z.T. Wang	2005
The Theoretical Solutions of Several Integrations in Relation with the Plane Wave Functions W.P. Shi and C.H. Li	2009
Analysis on Characters of Cross-Fault Tunnel under Action of Earthquake Q. Wang, G. Chen and E.D. Guo	2016
Investigation and Analysis on Seismic Damage of Historic Timber Structures Caused by Wenchuan Earthquake in Zhaozhua Ancient City L. Cheng, H.T. Liu, X.W. Zhu and B. Jia	2020

Dynamic Response of the Taizang Tower before and after Reinforcement under Seismic Load	
J.Q. Liu, Y.Y. Chao and C.C. Chen	2024
The Application and Study of Urban Seismic Shelters for Evacuation Based on GIS	
X.Y. Zhang and Z.T. Wang	2028
Study on the Floor Damage Model of Hybrid Structure under Seismic Excitation	
S.S. Zheng, W.P. Cao, Q.L. Tao and P.J. Hou	2033
Research on the Space Layout of Urban Seismic Disaster Prevention	
Q.Q. Zhao, W. Wang, C.F. Liu and X.R. Liu	2037
Seismic Fragility Analysis of SRC Frame Structures	
S.S. Zheng, W.B. Li, Q. Li and F. Wang	2042
Seismic Behavior of Reinforced Concrete Frame Columns with Different Volumetric Percentage of Stirrups	
S.S. Zheng, Y.H. Yan, Q.L. Tao and W.Y. Li	2046
Seismic Response Analysis for Tunnel Conveying Water under Traveling Waves Excitation	
J.Y. Liu, C.C. Xia and S.N. Sun	2050
Economic Losses Research of Seismic Damage Based on Grey Correlation and Genetic Neural Network	
X.Z. Li, Z.T. Wang and X.D. Guo	2054
A Direct Time-Domian Integral Method and its Implementation Based on Matlab	
M.S. Rong, T. Lu and B.D. Liu	2060
Research on the Stiffness Optimization of the Reinforced Concrete's Shear Wall Structure Based on the Earthquake Response Spectrum	
M.N. Zhang and Y.Y. Li	2066
Information Entropy Method for Evaluating Regional Earthquake Relative Disaster-Carrying Capability	
J. Liu, J.Y. Su, W. Wang and D.H. Ma	2070
Prediction of Seismic Casualties Based on Urban Land Types	
D.K. Zhao, J.Y. Su, W. Wang and D.H. Ma	2074
Analysis on the Mechanism for Baseline Drift of near-Fault Accelerograms	
Y.S. Wang and X.J. Li	2078
Evaluation of Seismic Behavior on Steel Frames with TSW Semi-Rigid Connections under the Nonlinear Time History Analysis	
M. Najdian and M. Izadnia	2083
Application of Seismic Isolation Designing Method Based on China Building Seismic Code	
X.M. Dong, Y.M. Wang, P.P. Guo and M.W. Li	2088
Analysis of Seismic Response of the Single Tower Cable-Stayed Bridge with Seismicity Mitigation and Energy Dissipation Devices	
J.X. Yang and Y. Zhang	2092
Stochastic Response Analysis and Reliability Evaluation of Nonlinear Structures under Earthquake	
Z.J. Liu and X. Fang	2100
Analysis of Seismic Response Influence of High Rise Building Nearby Subway Station in Soft Site	
H. Long, G.X. Chen and H.Y. Zhuang	2105
Advances in Seismic Research of Long-Distance Transportation Pipes	
T.Y. Hao	2112
Analysis of Different Seismic Response between Low and High Stories of Buildings	
K. Xia, L.X. Zhang, J.P. Liu and L. Dong	2115
The Model of Bounds on Seismic Responses	
J.L. Wang	2120
Seismic Response Research on Oil Pipeline with Corrosion Defects	
H.B. Qi, Q.S. Wang, L.L. Wang and X.D. Wu	2124
In Situ Test Methods in Bachu-Jiashi Earthquake Liquefied Evaluation	
Z.Y. Li, Y.R. Li and L.W. Chen	2128
Lateral Seismic Action on Gravity Retaining Wall along the Height	
H.M. Liu, X.X. Tao and X.Y. Zhou	2132

Seismic Response Analysis on Flat L-Shaped Frame Structure Based on FEM H.M. Wang, L. Cao, J. Yao and Z.L. Wang	2138
Seismic Strengthening Technology and Durability Analysis of Ancient Masonry Pagodas C. Wang and J.L. Yuan	2143
Earth-Rock Dam's Seismic Vulnerability Analysis of Mianyang City in the Wenchuan Ms8.0 Earthquake H.A. Liang, L.P. Jing, Y.Q. Li and C.H. Liu	2151
Seismic Analysis of the Single-Layered Cylindrical Grid Shell C. Shen, C.W. Huang and Y.L. Gao	2159
Study on Seismic Performance of Reinforced Concrete Masonry High-Rise Building X.J. Sun, H. Zhang, D.G. Lu and F.L. Wang	2164
Seismic Response Analysis of Subway Station in Tianjin Soft Soil Area D.J. Yang and Y. Li	2171
The Research on Hysteretic Energy in the Equivalent System Schemes between Multi Degree of Freedom System and Single Degree of Freedom System M.Q. Sheng and Y. Liu	2177
Analysis of Seismic Factors to Tunnels in the Earthquake Y. Zou, L.P. Jing, H.F. Sun and Y.Q. Li	2182
A Review on Long-Term Evaluation of Occurrence Probability for Subduction-Zone Earthquakes in Eastern Japan Z.R. Tao, X.X. Tao and W. Jiang	2190
Present Research and Prospect of Seismic Fragility for Steel-Concrete Mixed Structures Y.B. Liu, F. Chen and J.B. Liu	2197
Seismic Response Analysis of the Transfer Station in Transportation Junction Considering the Effect of the Pile and Soil Y. Guan, X.L. Jiang and Y.P. Zhang	2202
Analysis of the Seismic Performance of RC Frame Structures with Different Types of Bracings Z.X. Wang, H.T. Fan and H.J. Zhao	2209
Automatic Detection of Damage Level of Structures under the Severe Earthquake Using Sensor Network H. Ikeda, T. Kawaguchi and K. Oguni	2216
Dynamic Response of Ceiling System with Light Steel Furring and Gypsum Board under Severe Earthquake D.Z. Wang and J.W. Dai	2221
Experimental Study of Viscoelastic Dampers under Large Deformation G. Zhao, P. Pan, J.R. Qian and J.S. Lin	2226
Collapse Modes of a Double-Layer Space Truss Subjected to Multi-Dimensional Earthquakes X.H. Huang, Z.D. Xu and M.F. Yang	2234
Review of Anti-Seismic Capability Study of Storey-Adding Structure X. Xi, S.Y. Qu and C. Sun	2238
Seismic Dynamic Response Study of Wuhan Changjiang River Tunnel B.C. Dong and T.L. Shu	2243
Probabilistic Assessment of Soil Liquefaction by Using Seismic Chinese Code S. Vongchavalitkul and S. Kumpangta	2248
Comparative Analysis of Several Common Quasi-Statics Methods for Tunnel Seismic Soil Pressure Calculation T.F. Deng, Y. Gui and F.S. Nie	2253
Response of Transmission Lines under Three-Dimensional Seismic Excitations L. Tian, H.N. Li and W.M. Wang	2259
Analysis of Sample Survey of Rural Houses in Five Regions of Gansu and Earthquake Damage Prediction T.G. Zhou and C.M. Pan	2265
Spectrum Analysis of Isolated Vertical Seismic Response Storage Tanks J.F. Hao, J.H. Gao, Y. Liu and G.D. Liu	2270
Seismic Isolation Response and Parameter Influence Analysis of Nuclear Power Plant during Great Earthquake W.G. Liu, R.D. Wang, L. Hua and W.F. He	2275

Behaviour of Colliding Multi-Storey Buildings under Earthquake Excitation Considering Soil-Structure Interaction	
S. Mahmoud, A. Abd-Elhameed and R. Jankowski	2283
Normally Used Structural System Types of Guangzhou Country Residential Buildings and their Antiseismic Performance Analysis	
F. Wang and Z.J. Chen	2293
Study on Effects of Sea Ice on Nonlinear Seismic Responses of Single-Column Pier Subject to Different Types of Earthquakes	
F.Q. Qi and B. Song	2298
Comprehensive Method of Seismic Damage Assessment of Reinforced Concrete Structures Based on CPM	
C.F. Liu, J.Y. Su, X.D. Guo and W. Wang	2304
Regional Short-Term Earthquake Prediction Model Based on BP Neural Network	
W.S. Hu, H. Wang and H.L. Nie	2309
Estimation of the Liquefaction's Risk of a Soil Deposit under Seismic Solicitations: Petrochemical Zone of Skikda City	
S. Badreddine and K. Fillali	2315
Estimation of Direction of Wavefront Propagation and Apparent Velocity Using Earthquake Signals Recorded in Small-Size Dense Seismic Arrays	
P. Liu, H. Ma, X.W. Zhang, X.Y. Sun, F. Cao and L.L. Yu	2321
Research on Seismic Behaviour Factor of CBSF	
C. Li, J.F. Yang and Q. Gu	2326
Research on Inelastic Response Spectra for Asymmetric Plan Systems Subjected to Bi-Directional Earthquake Motions	
F. Wang, H.N. Li and T.H. Yi	2332
Displacement-Based Lateral Stiffness Design for Multi-Storey Structures Subject to Earthquake Motions	
F. Wang, H.N. Li and T.H. Yi	2337
Study on Change of Seismic Safety of RC Frame Building in Wenchuan County Town	
D. Wu and Y. Xiong	2341
Comparison of Base Shear Force Method in the Seismic Design Codes of China, America and Europe	
Z.N. Jiang and Z.H. Zhao	2345
The Parameter Study of Instantaneous Spectrum of Spatially Varying Ground Motion	
H.G. Chen, Y.M. Li, W. Zhang and Z.Q. Wu	2353
Influence of Ground Motion Spectral Shape on Nonlinear Responses of a 3-Storey RC Frame	
J.P. Han and Y. Luo	2358
The Analysis of Cantilever on Catastrophe to Irregular High-Rise Structure in Earthquake	
J.H. Zhang, Z.M. Xiong, Z.Q. Chen and L.B. Kong	2364
Seismic Response of a Viaduct under near-Fault Earthquakes	
Y.J. Chen, Y.B. Zhang, W.M. Yan and Y. Li	2368
Seismic Performance Study on Steel Frame Structures with Integral Panel	
H.T. Hou, M.L. Wu, M. Liu and Q. Ma	2373
Settlement Analysis of Soft Ground Replacement under Earthquake	
Z. Liu, S.H. An, R.H. Yuan and F. Li	2379
Three-Dimensional Elastic-Plastic Dynamic Interaction of Earth Dam and Intermountain Basin	
Y.Q. Li, L.P. Jing, H.A. Liang, C.H. Liu and Y. Zou	2383
Seismic Fragility Analysis of Reinforced Concrete Frames within Service Life	
N.J. Wang, J.M. Wang and W.T. Jiang	2391
Experimental Study on Shear Strength of Gravel Silty Clay from a Post-Earthquake High Slope	
P. Yang, Z.Y. Zhu, Y. Mo, B. Teng and Z.Y. Zou	2395
The Operation Platform Connection Styles' Influences on the Seismic Behavior of Thermal Power Plant Frame-Bent Structure	
G.L. Bai, S. Niu and B.P. Du	2400

The Response of the Bi-Directional Beam String Structure under Vertical Seismic Considering Supporting Frame X.R. Chen, J.B. Liu and W.Q. Wang	2404
An Ensemble of Ground Motions Simulation Based on Discrete Stationary Wavelet Transform Q. Bai, L.H. Fu, W.B. Bao, S.J. Jin and D.S. Zhang	2408
The Shaking Table Test and Analysis of Seismic Performance for Brick Mixes Structures of Traditional Folk Dwelling C.H. Li, H.Q. Li, J.B. Ji, Y.Q. Fu and F.F. Li	2412
Influence of Non-Uniform Movements and Soft Soil on Seismic Responses S. Hai	2419
Study on Performance-Based Seismic Evaluation and Strengthening for RC Damaged Structures Q.M. Gao and B. Wang	2423
Numerical Analysis of Seismic Behavior of Masonry Walls Confined by Precast Tie-Columns W.W. Luo, Y.M. Li, N.N. Zheng and N. Chen	2429
Seismic Design of High Rise Building in Shenyang R. Qin	2436
Key Issues of Using High Strength Steels in Seismic Structures and some Recent Progress G.Q. Li, Y.B. Wang, S.W. Chen and F.F. Sun	2444
Attenuation of Hysteretic Energy Spectra of Strong Ground Motion M.S. Gong, J. Sun and L.L. Xie	2453
Studies on Seismic Performance Test of Precast Prestressing Shear Wall R.R. Fu, Z.C. Liu, Q.L. Yin and K. Su	2457
The Seismic Performance Analysis of Steel Frame Adding the Viscoelastic Dampers Y.L. Wang, J.S. Lei, F.H. Zheng and K.L. Zhai	2461
Research on Numerical Simulation of Smart Base Isolation System with MR Damper (I) W.Q. Fu, F. Chen, D.H. Yu and Y.H. An	2467
Research on Longitudinal Seismic Calculation Theory of Single-Story Factory Building H. Ning, X.Y. Lv and Y.J. Wang	2471
Analysis of Guojuanyan Debris Flow Formation and Kinetic Parameters in Hongkou Village, Dujiangyan of Sichuan Province Post Earthquake S. Yang, J. Wang, X.J. Ji and H.L. Pan	2478
The Evaluation of Lithology Effects on Wenchuan Seismic Landslides M. Han and X.Y. Fan	2483
Seismic Response Analysis of Large Liquid Storage Tanks Y. Zhang and Y.H. Guan	2490
Analyzing Seismic Destructive Effect to the Submarine Rock and Soil Layers According to Submarine Seismic Records B.H. Zhang and H.S. Tian	2494
Pseudo-Dynamic Test on the Anti-Seismic Performance of Turbine Generator Foundation T.J. Qu, K. Xiang, X.J. Yin and X.Y. Shao	2507
Research on Numerical Simulation of Smart Base Isolation System with MR Damper(II) W.Q. Fu, F. Chen and H.M. Wang	2513
Near-Fault Baseline Correction Method and Application in Wenchuan Earthquake X.B. Peng, X.J. Peng and W.L. Yang	2517
Seismic Performance Evaluation of Village Buildings in Wenzhou K.J. Yang, W. Li and J.W. Yin	2522
Research on Methodology of Seismicity Delineating Zones in Different Areas of China M.S. Rong, Y. Yang and D.D. Xu	2528

Chapter 6: Disaster Prevention and Mitigation

Search of the Most Dangerous in Slide Slope Stability Analysis Based on Genetic Algorithm K. Wang, C.M. Wang, F. Qi and C.C. Niu	2535
Effect to Fire Countermeasures in the Process of Energy Policy Adjustment X.X. Ge	2539

Effects of Water and Thermal Contact Resistance on the Temperature Field of Concrete Filled Steel Tubular Columns	
J.S. Han, X.T. Wang and Q.W. Sun	2543
Research on Safety Assessment Theories and Application of the Internal Force Envelope Method in the Health Monitoring of Large	
J.T. Zhou, J. Song and Z.L. Yi	2548
The Mechanical Performance Analysis of Steel Truss in the Fire and Damage Assessment after Fire	
J. Zeng, Q. Yiang, B. Zhao and D.D. Liu	2555
Application of the Comprehensive Geophysical Prospecting Techniques in Hidden Trouble Detection of Tailings Dam	
H.Y. Ju, J.Q. Zhao, J.H. Li, B. Xu and C.T. Luo	2562
Study on Retaining Work of the Engineering Landslide	
F.Y. Qin, J.S. Tu and Q.Y. Ge	2566
Emergency Evacuation from a Multi-Room Compartment	
J.F. Liu and W.F. Yuan	2570

Chapter 6: Disaster Prevention and Mitigation

Modelling of Crowd Behaviour in Emergency Evacuation	
J.F. Liu and W.F. Yuan	2581
Travel Time Reliability for Rescue and Recovery after Disaster	
S.M. Fang and H. Wakabayashi	2591
The Review and Prospects of the Study on Chinese Geological Disaster	
J. Wang, S. Yang, X.J. Ji and G.Q. Ou	2597
Lahar Risk-Division of Changbai Moutian Region, China	
J. Sheng, L.H. Wan, H. Lv and Z.H. Wen	2601
Effect of Stirrup Ratio on Seismic Behavior of Cross-Shaped Columns with HRB500 Reinforcement	
Y.Y. Li, X. Rong and J.X. Zhang	2605
Study on Safety Evaluation for Construction Sites Based on Fuzzy-AHP and Grey Correlation Analysis	
Z.W. Zhong, Z.J. Liu, L.L. Mu and X.L. Kang	2609
Experimental Investigation on Dynamic Response of Spherical Explosion Vessel in Sludge	
D.Y. Chen and Y. Jun	2615
Blast Experiment Research on Safe Extent of Framed Glass Subjected to Small Priming Charge Explosion	
P. Ting, T. Liu, Q. Jiang and F. Gao	2619
Fiber Optic Inclinometer for Landslide Monitoring	
F. Li, W.T. Zhang, F. Li and Y.L. Du	2623
Flood Damage to Rural Buildings Result from Foundation Scour and Scour Protection Strategy	
Y.J. Liu, X.T. Ma and Y.M. Sun	2627
3D Building Modeling and Indoor Fire Event Representation in CityGML	
S.N. Ren, J.H. Mao, L. Ye and X.F. Liu	2631
Types of Hidden Safety Trouble for Existing Buildings in Shanghai and Solving Measures	
X.L. Yan	2637
Research on Urban Storm Flood Processes under Two Measures: Detention Pond and Retention Pond	
G.Q. Sang, S.L. Cao, Z.B. Wei and C.Q. Zheng	2643
The Analysis of Influencing Factors on the Number of Storms	
B.H. Wang, Z.J. Wang and S.L. Chen	2649
Study on the Techniques of Responders Dealing with Hazardouse Materials Accidents	
K.S. Wang	2654
Simulation Research on the Member Removal Method of the Typical Construction in Collapse Accident	
X. Chen	2658

Landslide Hazard Divisions of Shaanxi Province H.J. Ji and Y. Ji	2663
The Causes of Geological Disasters in Chongqing Expressway Mechanism and Treatment Research H.P. Li, R.X. Shan and Z.L. Yan	2669
Studied on Establishing Urban-Rural Disaster Prevention System Z.T. Wang, X.Y. Zang and P. Wang	2676
Study on Construction Risk Analysis and Risk Counter-Measures of River-Crossing Tunnel of Large-Diameter Metro J. Hu, H. Zeng and X.B. Wang	2680
Wireless Sensor Networks for Fire Detection in the Library Environment J. Liu, Y. Tian and H. Qi	2684
Evaluation of Lining Damage Caused by Fire in Tunnels Y.L. An	2688
Analysis of Failure Probability of a Potential Landslide in Northwest China Y. Hong, Q. Xu and K.Q. He	2692
Effects of Ice Thickness on the Aerodynamic Characteristics of Crescent Shape Iced Conductors D. Yan, W.J. Lou, M.F. Huang and W. Lin	2696
Analysis of Fire Resistance Response of Double Shell Structure under Specific Fire Scenarios X. Chen	2704
The Discussion on Fire Load Maximum of Building J.P. Wang	2709
Analysis on Influencing Factors of the Moment that Slider Begins to Slide for Sliding Base-Isolated System M. Sun, Y.G. Zhang and Y. Niu	2713
Constitutive Model of Shallow Landslides Catastrophe Theory under the Heavy Rainfall S.G. Cheng and H. Zheng	2718
Study to Catastrophe Mechanism of Bedding Rock Slope Burst S.G. Cheng and H. Zheng	2722
Numerical Simulation and Analysis of Compartment Fire in Subway Train B.S. Zhang and S.X. Lu	2726
Research on Mobile Water Spray Device Reducing the Temperature of Metro Fire Y. Li and L.X. Dong	2731
Theory of Unload-Load Response Ratio and its Application in Debris Landslide Forecast W.G. Chen, K.Q. He and J. Zhang	2735
Sluice Risk Consequence's Evaluation Based on Principal Component Analysis Method H.Y. Zheng, D.L. Zhuang, L.S. Xu, Z.F. Long and D.W. Yang	2740
Different Control Schemes Study on Landslide with Underground Crossing Pipeline C.D. Li, X.L. Hu, L.Q. Wang and Q.T. Liu	2744
PSInSAR Technology Research and its Application on Landslide Monitoring P.F. Tu, L. Xia, H.T. Li and S.C. Wu	2751
Research on Security Facilities for Mountainous Countryside Based on the Characteristics of Security Needs L.Y. Wei, K.Z. Jiang, S.B. Ma and Y.J. Zheng	2757
Geometrically Nonlinear Analysis of Composite Girder Cable-Stayed Bridge with Three Towers in Completion Stage Z.G. Zhou, F. Wang and L.H. Deng	2761
Analysis of Collapse Behavior for Demolition of Brick Walls C.W. Liao and T.L. Chiang	2765
Debris Flow Hazards and its Mitigation Works in Xianbuleng Gully, Jinchuan County, Sichuan Province, China J.F. Liu, Y. You and X.C. Chen	2769
Catastrophe Theory Analysis of Rock Mass Dynamic Destabilization Y. Zhang, D.J. Hu and L. Xue	2774

Deformation and Failure of Guantianba Landslide, in the Reservoir of Xiangjiaba Hydropower Station	
H.C. Zheng, J.B. Wei, W.X. Fu and Y.L. Cui	2782
Application of Real-Time Monitoring and Data Web Sharing to Landslides	
H.D. Wang, Q.L. Le, X.Y. Yang and Y.L. Gao	2787
Research of Experiment for Slope under Ice Disaster	
B. Huang, C.A. Zheng and W.L. Chao	2794
Stability Analysis of Side Slopes under Disasters of Ice and Snow	
C.A. Zheng and W.L. Chao	2799
The Experimental Study on Extinguishing Cooking Oil Fires by Water Mist	
J. Chen	2804
Risk Assessment of Field-Scale Flood Disaster Based on Combined Remote Sensing and Hydrological Dynamics Model	
J. Zhang and G.B. Ma	2810
Study on Four-Color Early Warning Mechanism of Collapse Hazards in Subsea Tunnel	
Y.G. Xue, S.C. Li, M.X. Su, D.H. Qiu and H. Tian	2814
Review of Landslide Monitoring	
Z.F. Song and X.P. Xin	2821

Chapter 7: Computational Mechanics

Relationship between Bending Solutions of FGM Timoshenko Beams and those of Homogenous Euler-Bernoulli Beams	
S.R. Li, Z.Q. Wan and P. Zhang	2831
Fracture Analysis of the Spiral Ribbed Pre-Stressed Steel Wire during Pre-Stretching	
Y.Q. Sun, L. Wu, Z. Wang, J. Li and Y. Zhang	2837
Preliminary Analysis on Wall Beam Force Algorithms under the Action of Vertical Load	
Y.S. Gao and Y. Sha	2841
Damage Evolution of the Interphase on C/SiC Composites with CZM Method	
Y.J. Chang, Z. Li and K.S. Zhang	2847
Proposed Calculation Formula of Shear Connectors in UHPFRC-NSC Composite Structure	
Y.H. Guo and Z.Q. Wang	2851
Stability Analysis of a Prey-Predator Model by Using Homotopy Analysis Method	
H.Y. Cao	2855
Prediction of Longitudinal Compression Strength for a 2.5D-C/SiC Composite Based on Laminate Theory	
Y.J. Chang, G.Q. Jiao and K.S. Zhang	2859
Comparison of Calculation Method on Bi-Directional Shearing Capacity of RC Framed Columns	
C. Du, R. Guo, M.J. Zhou and C.L. Zhang	2863
Shear Locking Analysis of Plate Bending by Using Meshless Local Radial Point Interpolation Method	
P. Xia and K.X. Wei	2867
Wavelet Multi-Scale Solution for Deflection of Thin Rectangular Plates under Temperature	
Y.C. Wang, K.L. Ren, Y. Dong and M.G. Wu	2871
An ANSYS-Based Approach for Nonlinear Dynamic Stability Analysis	
S.P. Lu and Q.Y. Zeng	2876
Analysis and Simulation of Elastic-Plastic Fracture Parameters at Crack Tip under Biaxial Loading and Uniaxial Loading	
Z.X. Wang and R. Liu	2883
Numerical Study on Shearing Properties of Profiled Steel Sheets	
J. Zheng, B. Chen, H.J. Xu and Y.L. Yang	2887
The Mechanical Properties Analysis of Rutting Resistance Road Based on ANSYS	
J.J. Li, Y.Q. Wang and J.G. Qiao	2892
Effect of Temperature on the Thermal Stress in the Single Lap Joint	
M. You, C.J. Chen, H.Z. Yu, C.Z. Mei and M. Li	2896

The Effects of Applied Axial Stress on Lateral Bearing-Load Capacity for Fully Grouted Reinforced Concrete Masonry Shear Walls Y. Zhao, F.L. Wang and F. Zhu	2900
Strain Analysis of Four-Tube Concrete-Filled Steel Tubular Columns B.W. Chen, R. He and Y. Cao	2906
Curvature Ductility of Concrete Element under High Strain-Rates Z. Syed, P. Mendis, N. Lam and T. Ngo	2910
Strain Gauge Based on Graphene Y.J. Ren and C.F. Zhu	2918
Calculation on the Vertical Cracking Load of Adaptive-Slit Shear Walls M.J. Chu, Y. Zhang and Z.J. Sun	2924
Analysis of Failure Mode and Propagation for Crack in Uniaxial Compression Y.Z. Sun, X.X. Zhai and J.M. Liu	2929
Analysis of the Mechanical Behavior of Short Tube Columns Filled with Concrete by Different Contact Surface Conditions T.W. Fan	2933
Mechanical Properties of Wood-Polymer Composite Prepared by <i>In-Situ</i> Polymerization of Methyl Methacrylate and Styrene Y.F. Li, D.W. Gong, X.Y. Dong and Z.B. Liu	2938
Mechanical Properties of New Cold-Formed Flange-Closed Welding Section Members S. Wu	2942
Test Research on Flexural and Shear Properties of Bamboo Plywood W.Q. Wu, S. Chen and X.Y. Ma	2951
Rock Mechanics Parameters Calculation of the Fractured Rock Based on the Effective Media Theory with Well Logging Y.Z. Zhang	2958
Experimental Study on Engineering Mechanical Properties of Beryllium L.J. He, D.M. Xu, J.M. Zhong, N. Hu, Z.H. Wang, B.S. Sun, Z. Li, J.K. Zhang, F. Li and H.L. Kang	2962
The Basic Characteristics of RAC and Mechanical Properties from Experimental C. Gao, Z. Pan, S.X. Gao, B.C. Yu and H.F. Mao	2966
The Optimized White Differential Equation of GM(1,1) Based on the Original Grey Differential Equation R. Zhou, J.J. Li and Y. Chen	2971
Research on Hydrodynamic Performance of Front-Mounted Water Separation Propeller F. Feng, X. Chang, X.R. Cheng and X.Y. Qi	2976
Experimental Research on Dependencies of Mechanical Property of Elastomeric Isolator with Lower Hardness and Parameters Analysis C.Y. Shen, Y.H. Ma, X.Z. Zhuang, Y.Y. Chen and S.B. Wang	2982
Numerical Study of Stress Intensity Factor in Notched Specimens Using Extended Finite Element Method G. Chen, T. Xu, Q. Xu and L. Bu	2995
Finite Element Model Updating for Unsymmetrical Damping System with Genetic Algorithm B.Q. Zhang, G.P. Chen and Q.T. Guo	2999
Study on Twin Shear Strength Theory S.J. Jin, Z.P. Wang and Z.X. Liu	3004
CFD Simulation of Prediction of Pressure Drop in Venturi Scrubber M. Ali, C.Q. Yan, Z.N. Sun, J.J. Wang and K. Mehboob	3008
Applying Condition of Kirsch's Stress Solution for Plate with Central Hole in the Engineering S.Q. Su and Y.Q. Che	3012
Study on the Mechanical Property of Concrete Materials under High Temperature (Fire) M.L. Ou, W.J. Cao and L.M. Jiang	3018
On an Extension of Hilbert Inequality B.J. Sun	3023
On a Refinement of Hardy-Hilbert Inequality B.J. Sun	3027

Research on the Calculation Method of Stress in Retaining Wall Based on Elasticity Theory L.B. Dang and L.B. Fu	3031
Analytic Solution of Single Span Beam under Non Uniform Load Q.X. Feng and C. Qu	3035
Research on the Calculation Model of Concrete Bending Member in Freeze-Thaw & Corrosion Environment Y. Sha and Y.S. Gao	3039
Error Analysis of Superposition Method in Bearing Capacity Calculation L.Y. Chen	3044
The Analysis of Pecan Picking Mechanism Based on the Vibration X.L. Li and W.B. Yao	3048
Study on Linear Calculation Method for the Refracturing Total Stress Field W.C. Zhao, T.T. Wang, C.Y. Sun, Y. Liu and C.P. Yang	3052
Experimental Study of Droplet Size Distribution Produced by a Multi-Orifice Effervescent Atomizer F. Xu, W. Dong and L. Qiang	3056
Analysis of Sliding Cable Element X.R. Fu, C. Luo, J.S. Ju, X.G. Jiang and G. Tian	3060
Analysis of Stress Distribution of Externally Pre-Stressed Beams under Transverse Loads P. Zhang, D. Shen and S.R. Li	3065
The Water Depth Effect on Ship Pressure Distribution and Surface Wave T. Miao, Z.H. Zhang, C. Wang, J.B. Liu and J.N. Gu	3071
New Exact Solutions to Variable Coefficient KP Equation J.Y. Yin	3075
A Modified Spectral Conjugate Gradient Methods with the New Line Search Condition M.J. Ma, Y. Su, H.T. Hua and Y. Zhang	3079
The Study on J-Integral of Composite Laminated Plate Crack Propagation Problem D. Zhao, Y. Zhao, X.R. Fu and W.J. Wang	3083
Mechanical Property Analysis on Joints of Steel Secondary Beam Inserted in Reinforced Concrete Frame Girder Q. Yu, J.L. Xu and X.Z. Zhao	3087
Analysis of Small Non-Sand Concrete Pile Grouting Pressure Based on Unified Strength Theory H.F. Tong	3095
Calculation of Different Stages Reinforced Concrete Beam Bending Stiffness X.Y. Guo	3100
Different Techniques Comparison in Biomechanical Analysis of Ping Pong B.J. Mao	3106
Study on Moment-Curvature Hysteresis Relationship of Reinforced Concrete Shear Walls G.Q. Zhou and F.M. Xia	3110
Numerical Study of Joint Behaviour for Robustness Assessment M.A. Gizejowski, L. Kwasniewski, B. Saleh and M. Balcerzak	3114
The Mechanical Response Analysis of the Frame Structure with the Interval Parameters Taken into Account F.B. Meng, S.Y. Qu, W.P. Shi and C.L. Li	3118
An Influence Analysis of Second-Order Effect to the Vibration Control of Piezoelectric Beam by the Spline Finite Point Method S.B. Li, L.J. Jiang, C.X. Gu and R. Qin	3124
The Influence of Process Force on the Wall Thickness H.D. Wen, X.T. Xiao, L.G. Tan, Y. Chen and K. Zhang	3131
Bending Solution of Plates on Winkler Foundation by Element-Free Galerkin Method Based on Mindlin Plate Theory M.Y. Xu, J.D. Sun, S.Q. Cui and L. Shi	3136
Study on Flexural Toughness and Crack Path Prediction for Polymer-Modified Concrete Q.Y. Cao, T.Y. Hao and W. Sun	3142
Experimental Verification of a Full-Size Buckling Restrained Brace L. Liu, C. Liu and X.J. Yin	3147

Thermal Stress Analysis of a Certain Concrete Wind Cover Y.N. Zhang and S.P. Zhao	3151
Correct Wavelet-Based Multilevel Numerical Method of Local Solution of Boundary Problems of Structural Analysis P.A. Akimov and M.L. Mozgaleva	3155
Tests of Buckling-Restrained Braces Using Low-Yield Point Steel as Core Material H. Yan, P. Pan, Y.Q. Wang, T. Makino and X. Qi	3159
Implementation Procedures of Parallel Preconditioning with Sparse Matrix Based on FEM G.L. Ji, Y.D. Feng, W.K. Cui and L.G. Lu	3166
Experimental Research on Mechanical Properties of Fundamental Frame Units in Multi-Ribbed Composite Wallboard Y.F. Yue and D. Zhao	3174
Study on Bending-Torsional Coupling Vibration of Intermediate Axis X.S. Yao and C.L. Zheng	3180
Mechanical Behavior of Concrete-Filled Double Steel Tubular Columns under Axial Compression Load X. Wang	3184
Study on the Influence of M Value to Internal Force and Deformation for Transverse Bent of High-Piled Wharf J.S. Gui, Z.G. Li and B. Zhang	3189
Hybrid Trefftz Finite Element Analysis of Orthotropic Potential Problem K.Y. Wang and P.C. Li	3193
A Correction Algorithm of Aberration of Light for Spacecraft Attitude Determination System B.H. Li, X.J. Chen, Y. Pang and B.Q. Xi	3197
A Simple Approach to Modeling the Failure of Flawed Polyester Textile with the Application of the Concepts for Fracture Mechanics G.N. Liu, H.D. Zhao, H.Z. Wang, S.C. Wang and M.H. Zhao	3202
Study of the Mechanical Behaviors of Fabric Made of Polyester Fibers in the Corrosive Ozone Gas Environment G.N. Liu, H.D. Zhao, W. Yang, S.C. Wang and M.H. Zhao	3206
Comparison Theorems for the Multi-Dimensional Backward Doubly Stochastic Differential Equations B.Y. Han	3210
Mechanical Capacity Analysis of Large Diameter Prestressed Concrete Cylinder Pipe (PCCP) Y.L. Wang, Y.Q. Bi and X.J. Zhou	3214
Constitutive Theory of Elastoplastic Coupled with Damage of Anisotropic Concrete J.Q. Xiao, Q. Zhang and D.H. Ding	3220
Capture of 2-D Crack Growth Path by the Polygonal Numerical Manifold Method H.H. Zhang	3224
Travelling Wave Solutions of Nonlinear Evolution Equation by Using an Auxiliary Elliptic Equation Method C.H. Xiang	3228
Mechanical Research on Bond-Slip Behaviors of Recycled Aggregate Concrete-Filled Square Steel Tubes J.T. Li, J.J. Xu, Z.P. Chen, Y. Li and Y. Liang	3233
Element Free Galerkin Formulation of Composite Beams with Longitudinal and Transverse Partial Interactions D. Ahmad, A.Y. Mohd Yassin and A. Kueh	3237
Damage Identification in Composite Plate Using an Inverse Optimization Procedure G. Sun, X.H. Cai and W.Q. Zhong	3241
Comparisons of AR Model and Wavelet Analysis Model W.F. Zhang, D. Xie, J. Ji and Y.C. Liu	3246
The Variation of the Stress Intensity Factor of Welded Flange-Blotwed Connection Y.P. Sun and Z.L. Teng	3250
Analytical Formulation on the Mechanical Behavior of Anchorage Interface for Full-Length Bonded Bolt B. Liu, L. Huang and D.Y. Li	3254

End Effects of Symplectic Solution to Stokes Flow in a Rectangular Cavity S.H. He, L.X. Zhang and L. Cao	3258
A Nonstandard Finite Difference Scheme for the Reaction Diffusion Equation M.D. Liu	3265
Mechanical Behavior Study on Connections of Multibarrel Tube-Confined Concrete Column with Steel Beam L.Y. Xu	3269
Dynamic Mechanical Behavior of Concrete under Uniaxial Stress T.X. Li, Y. Zhang and L.H. Jiang	3273
Strain Analysis of Composite Frame Joints with Double Side Penetrated Diaphragms M. Tong	3277
III-Posedness and Regularization Method for Nonlinear Identification Equations in Time Domain X.Z. Xie, F. Zhang, Y. Li and Y. Tan	3282
Calculation of Shear Capacity of Steel and Concrete Composite Beams Strengthened with FRP J.F. Liang, Z.P. Yang, J.B. Wang and J.P. Li	3290
Application Development of Tensile Value with Prestressing Cramp Iron F.X. Zeng	3294
Shear Capacity Analysis of SRHSC Frame Joints S.S. Zheng, X. Han, Q.L. Tao and W. Wang	3298
Shear Calculation of the Interface in SRHSHPC Beam S.S. Zheng, N. Zhou, Q.L. Tao and F. Wang	3302
A Method of Determining Dynamic Stability Critical Length of Construction Member Q. Sun and C.C. Guan	3306
Shear Resistant Strength Analysis of Construction Formwork Concrete Shear Wall Y.D. Liang, Z.G. Sun, J.Z. Jiang, G.C. Chi and Y. Jiang	3311
Practical Calculation Method of Force Method - Layered Force Method X.Z. Song, M.L. Lu and R.C. Jin	3317
Experimental Study on Basic Mechanical Properties of Recycled Concrete Made of Brick and Tile L.J. Xie, A.L. Zhai, C.H. Wang, C.L. Ji and S.J. Chen	3323
The Analysis of ZF6 AT Based on the Expansion Lever Method J.J. Li and J.H. Li	3329
Fine Stress Analysis and Strength Prediction of Joints in Axial Shear J.M. Liu and Y. Hong	3333
Mechanical Behavior of Single-Lap Adhesive Joints with Reinforced Pins J.M. Liu and W.X. Zhu	3338
Residual Stress Research of Cold-Formed Thin-Wall Steel Members Using the Finite Element Method H.C. Liu	3343
An Inverse Eigenvalue Problem for Star Spring-Mass System X. Tian and C.X. Li	3348
Uncertain Out-of-Plane Behavior of Composite Plates due to Spatially Random Material Properties H.C. Noh and D.W. Seo	3352
Brief Introduction of Residual Thrust Method and its Improvement Z.F. Song and X.M. Xu	3358
Scattering of SH Wave on Periodic Cracks in an Infinite Plane of Piezoelectric/Piezomagnetic Composite Materials W. Shi and L.X. Ma	3364
Catastrophe Model of Elastic Compression Pole Buckling Z.Q. Wang, Y. Du and F. Liu	3369
Analysis on Parameters Influencing Max. Stress of Inner Rubber of Elastomeric Bearing C.Y. Shen, Y.H. Ma, X.Z. Zhuang, Y.Y. Chen and S.B. Wang	3374
Identification of Local Time-Varying Systems Based on Dynamic Response Sensitivity K. Zhang, H. Li, Z.D. Duan and S.S. Law	3379

Flexural Behavior of SRC Columns under Axial and Bilateral Loading S.A. Zhang, Z.Z. Zhao and X.G. He	3383
Simplified Method for Elastic Distortional Buckling Stress of Cold-Formed Thin-Wall Steel Members Y. Zhao, W.M. Yan and C. Yu	3391
An Inverse Mode Problems for Simply Connected Central Symmetric Spring-Mass Systems X. Tian and C.X. Li	3399
Frame - Shear Wall Structures Subjected to Vertical Deformation and the Shrinkage and Creep of Concrete Relations L. Pan and L.W. Zhang	3403

CHAPTER 1:

Structural Engineering

Test research on the behaviors of steel bar truss and concrete superimposed floor slabs

Yongxing Li^{1,a}, Lu Jiang^{2,b}, Zhiqiang Yu^{2,c}, Jie Li^{3,d}, Yongwei Li^{4,e}

¹School of Civil Engineering, Xi'an University of Arch. & Tech. Xi'an, Shannxi, 710055, China

²Baosteel Construction System Integration Co. Ltd. Shanghai, 201900, China

³College of Civil Engineering, Tongji University. Shanghai, 200092, China

⁴Shaanxi Construction Engineering Group Construction Machinery Co. Ltd. Xi'an, Shannxi, 710032, China

^alyx2220@163.com, ^bjianglulujiang@163.com, ^c13524276419@qq.com

^dtongjilijie@163.com, ^e514050964@qq.com

Keywords: steel truss, superimposed slab, bearing capacities, temporary support

Abstract. Tests on two simple supported steel bar truss and concrete superimposed floor slabs have been carried out to study their mechanic behavior and bearing capacities. The one is prefabricated steel truss concrete slab without temporary support in the mid-span to simulate its mechanic status in construction stage, the other is superimposed board (prefabricated + post-cast layer) in use phase. Test results show that the deformation of the prefabricated steel truss concrete slab in construction stage meets the requirement of the Code, and the slab is mainly controlled by deflection instead of cracks; Performance of superimposed board is excellent in use stage; and the steel bar is elastic in both stages during the tests.

Introduction

The steel bar truss in steel bar truss and concrete superimposed floor slabs consists of a upper chord bar, two bottom chord bar and some inclined web members, which are automatic welding formed in the factory. The concrete casting of the steel truss superimposed slab is divided into two phases. Firstly, pouring the concrete to form the prefabricated slab in the factory or construction site. Secondly, after the strength of the concrete is well, casting the concrete on the prefabricated slab which is already carried on the structure in construction site, finally the whole composite board is formed. In construction stage, prefabricated slab lapping on the steel or concrete structural beams, the steel bar truss and concrete slab work together as beam members, which are able to bear the vertical load above the slab without the temporary support across the span, and the upper floor doesn't transfer vertical loads to the lower floor. In normal use, the steel trusses are distributed as steel of slabs, which can afford service loads.

Steel bar truss concrete superimposed floor slabs are widely used in abroad. However, few filed applications are available in China. This kind of floor has four obvious advantages in construction stage, including no formwork system, no temporary support across the span, no field welding operation and less amount of concrete in site. There is no need to use suspended ceiling and to make fire protection and anticorrosion, and the surface of prefabricated slabs can be directly treated with lacquer putty. The whole production process is industrialization, mechanization and high production efficiency. Meanwhile, the superimposed slab collaborates well with the assembly of steel structural residence, whose construction speed is very fast.

Since the 1920s, composite structure has developed a lot [1,2]. In abroad, studies of concrete composite beam and slab structure is mainly focus on normal section strength subjected to bending members, shear strengths between concrete composition plane and bearing capacities of composite beams, etc. But few consider the effect of secondary load of concrete composite flexural members in construction stage [3,4,5,6]. In China, researches concentrate on bearing performance and shear performance of concrete composite bending members under ultimate loads [7,8], as well as mechanical behavior of concrete composite slab considering the effect of secondary loading. Chinese concrete structure design code (GBJ 10-89) provides calculation formulas of normal section strength, oblique section strength and shear strength between concrete composition plane for concrete composite flexural members, as well as the checking formula of mechanical behavior in use stage. Paper [9] has carried out tests on the mechanical behavior of steel bar truss concrete composite floor slab, but the span of floor is short. It is short of test research on the properties of larger span steel bar truss concrete composite floor slab with no temporary support in construction in domestic. This paper conducts a test on two specimens of steel bar truss superimposed floor slabs with no temporary support across the single span, getting the system's ultimate bearing capacity and mechanical property by measuring the deflection of slabs and stress of steel bar truss, and observing the crack distribution patterns of the slabs.

Test scheme

Design and production of specimens. There are two specimens in the test, the details of which are shown in figure 1 and figure 2. And the steel truss is 90mm high. Table.1 shows the specific sizes of specimens. Table.2 and 3 give the floor sizes of superimposed slabs and concrete material properties respectively.

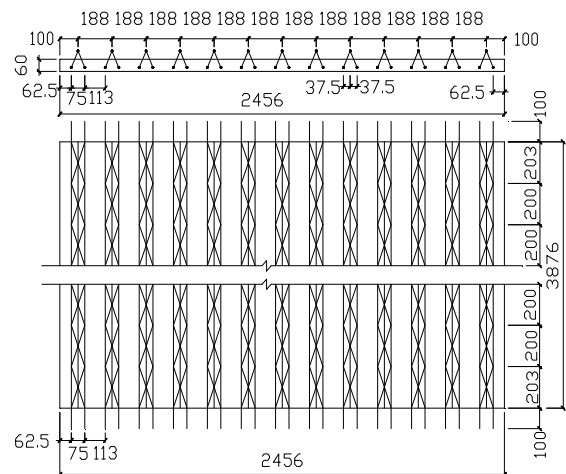
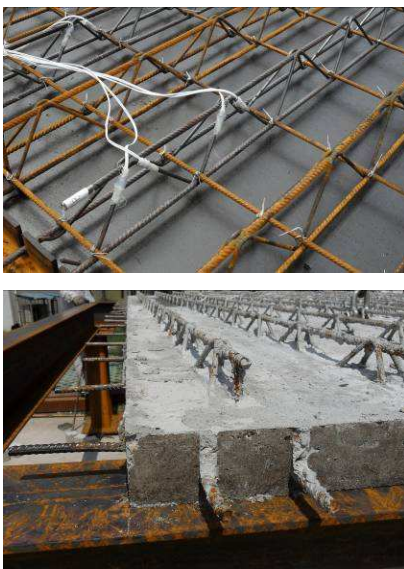


Fig.1. Local figure of the superimposed floor slab Fig. 2. Arrangement plan of steel bar truss

Table 1 Details of steel bar truss

Steel bar truss	upper chord	down chord	web member	distributing bar
diameter [mm]	10	10	6	8
spacing [mm]	188	75 /113	200	200
length [mm]	3876	4006	128	2656
steel type	G550	G550	HRB400	HRB400

Table 2 Sizes of concrete slab

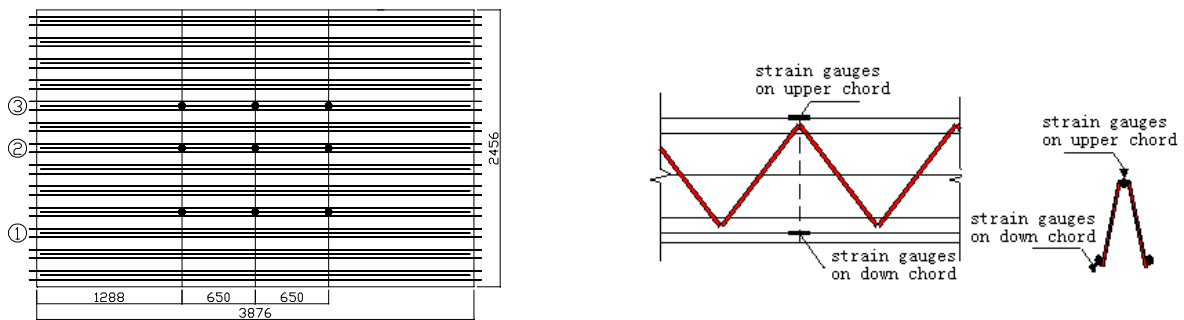
length [mm]	Width [mm]	thickness of prefabricated layer [mm]	thickness of superimposed layer [mm]
3876	2456	60	60

Table 3 Material properties of concrete

numbering	Layers of concrete	f_c [N/mm ²]	f_t [N/mm ²]	E_c [N/mm ²]
DB1	prefabricated layer	25.7	2.32	32246
DB2	prefabricated layer	29.1	2.51	33361
	superimposed layer	18.277	1.87	28820

The prefabricated slab use 60 mm thick concrete poured once. However, the steel truss concrete superimposed slabs point two poured process: first pour 60mm thick concrete to form prefabricated plate, then pouring 60mm thick concrete of composite layer after the strength of prefabricated concrete reached 100%.

Testing scheme. Arranging the strain gauges on upper chords, down chords and inclined web members of steel bar truss before the prefabricated slab is produced and monitoring strains of steel bars in the whole process of the test (see figure 3 & figure 4). Reserve the wire interface of strain gauge when pouring concrete and making label. In the experiment, simulating service loads on the floor by adding sands manually. Fig.3 and fig.4 give the arrangement plans of strain gauges on upper chords, down chords and webs in steel bar truss. Each steel bar truss has five measuring points of strain gauge across the span, three in the chords and the other in web members for details.



(a) Arrangement plan of strain gauges points on upper and down chords

(b) Arrangement details of measuring on upper and down chords

Fig. 3. Arrangement plan of strain gauges in chords of steel bar truss

There are complementary displacement meters at the two sides of the board since the width of slab is large. The arrangement of displacement meters is shown in fig. 5.

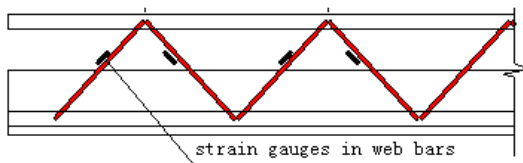


Fig. 4. Arrangement plan of strain gauges in web bars

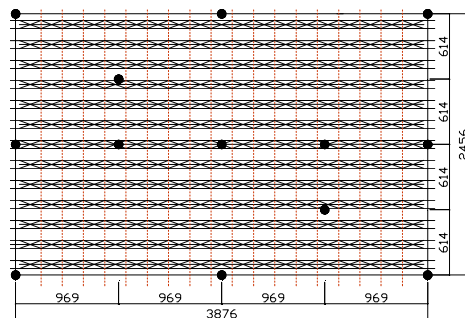


Fig. 5. Arrangement of displacement meters of DB1, DB2 floor slabs

Capturing crack by the naked eye with light, then using the crack visualizer measure cracks in the test. The bottom surface of slabs is white-washed and drawn rectangular grids, spacing of which is 100 mm.

Test device is seen in fig. 6. In order to simulate uniform load on the floor in the experiment, piling sand uniformly on the slab first, adding sand bags later, which have gaps among each other. Fig.7 shows the loading schematic diagram of floor slabs.



Fig. 6. Test devices of floor slabs

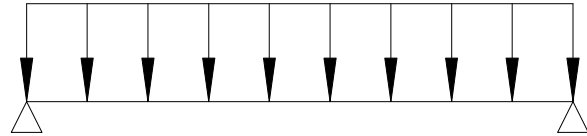


Fig. 7. Loading schematic diagram of floor slabs

Test phenomena and results

Test phenomena. Piling sands uniformly on the surface of prefabricated slabs to simulate concrete load of post-cast layer (1.5kN/m^2 for specific) and live load in construction stage. When the load is 3.0kN/m^2 , there appear tiny cracks at the direction perpendicular to long span in the mid-span, and the deflection is 16.5mm. When the load reached 4.5kN/m^2 , the cracks in mid-span expand towards both sides of the plate, and the edge of plate also has cracks, whose widest width is 0.15mm. The deflection is visible. Fig.8 shows the cracks on the surface of prefabricated floors, whose distribution under construction load is similar to the expected distribution of cracks on the one-way slab. It indicates that the cracks are not the control factors to the prefabricated slab in construction stage as the width of cracks are very small.

The loading method in serviceability stage is similar to the one using in the construction stage. There are no cracks on the superimposed slab when the applied load reaching 2.0kN/m^2 , which is the code required data. As the load adding to 4.0kN/m^2 , there appear micro-cracks at the direction perpendicular to long span in the mid-span and the deflection is not obvious. Then the cracks in mid-span expand towards both sides of the plate with the load increasing. When the load reached 10.0kN/m^2 , the biggest crack is 0.2mm wide and the deflection is still small. Fig.9 shows the cracks on the surface of composite floors. There are no cracks on the interface between prefabricated and composite layers, which indicates that the bond behavior between them is good for the linking action by the truss bars.

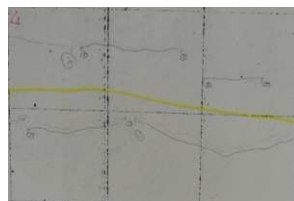
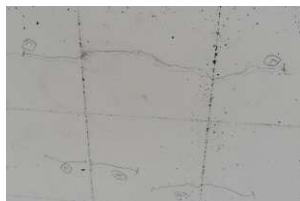


Fig. 8. Cracks of prefabricated slab Fig. 9. Cracks of superimposed slab

Test results. Table 4 gives the deflections of steel truss prefabricated slabs in construction stage. It's concluded from table 4 and experimental phenomena that the deflection of prefabricated floor is less than 20mm, which is the required minimum values of codes, and the width of crack is small under the loads of self-weight of post-casting layer concrete and construction load, which shows its

bearing capacity is more than 6.0kN/m^2 . As a result, the limit state of prefabricated slab is controlled by deflection rather than bearing capacity and cracks under construction loads. Fig.10 gives the load- strain curves of truss bars in prefabricated slabs, in which the web's strain is small and the chord's strain is big, and the compressive strain in upper chord is two times as the tensional strain in bottom chord. The results of strain measurements indicate that all the steel bars are still elastic. The upper chord bars of prefabricated slabs mainly bearing compression, which shows that steel truss playing an important role in the prefabricated slabs. The load-deflection curve of mid-span is shown in Fig.11. The relationship between deflection and load is basically linear, which explain that slab is still elastic.

Table 4 Deflection of prefabricated slab

Load [kN/m^2]	3.0	4.5	6.0
DB1 deflection in mid-span [mm]	6.545	16.413	46.701

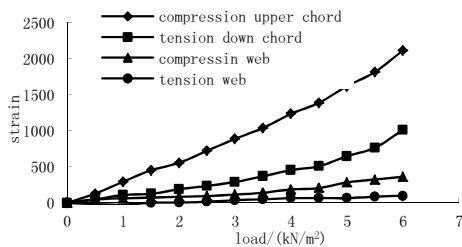


Fig. 10. Load- strain curves of truss bars in DB1 slab

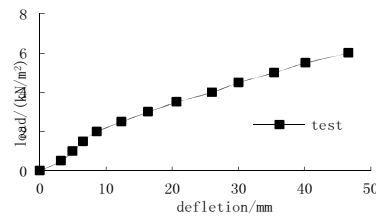


Fig. 11. Mid-span load-deflection curve of DB1 slab

Table 5 shows the deflection of steel truss composite slab in serviceability state. From table 5 and above experimental phenomena, it can conclude that both the deflection and crack of composite floor under normal use loads are small and the slab's bearing capacity is more than 11.0kN/m^2 , which meet standard requirements. The load-strain curves of steel bar are shown in fig.12, in which the web's strain is small and the chord's strain is big, and the tensional strain in bottom chord is four times as the compressive strain in upper chord. All the curves are linear liking the ones under construction loads. Steel bars are elastic in normal use, which is proven by the strain measuring results. The concrete of composite layer bear compression and the bottom bars of steel truss bear tension in superimposed floor. Fig.13 gives mid-span load-deflection curve of superimposed slab. There is a linear relationship between them, which indicates that the composite floor is still elastic and can be optimized in practical use.

Table 5 Deflection of steel bar truss and concrete superimposed floor slabs

live load [kN/m^2]	2.0	4.0	11.0
DB2 deflection in mid-span [mm]	2.490	6.285	26.475

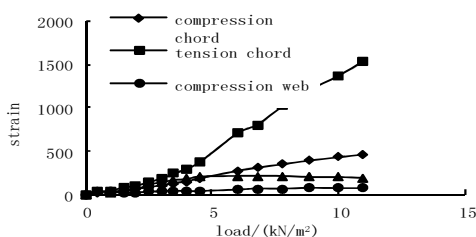


Fig. 12. Steel bar load-strain curve of DB2 slab

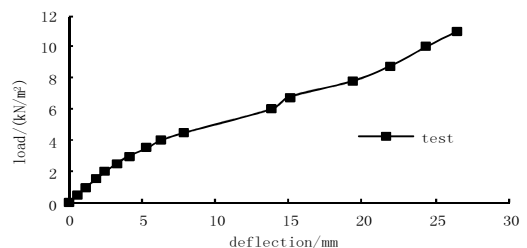


Fig.13. Mid-span load-deflection curve of DB2 slab

Conclusions

Conclusions are obtained from the test research on two specimens of steel bar truss and concrete superimposed floor slabs as follows:

(1) In construction phase, the behavior of prefabricated slab under loads of self-weight and construction live load is controlled by the deflection instead of cracks and bearing capacity, and its strength, deflection and cracks can satisfy the code requirements.

(2) In serviceability state, both the cracks and deflection of composite floor are small and its bearing capacity is large, all of which meet the standard requirements.

(3) Steel bar truss concrete composite slab system can cooperate very well with the assembly structure, particularly in steel structure. This kind of floor has many advantages, such as rapid construction speed, good comprehensive economical benefit, no need to use suspended ceiling and to make fire protection and anticorrosion, energy conservation and environmental protection. It is worth popularizing and applying in practical engineering.

References

- [1] Zhou Wanghua. Modern concrete composite structure [J]. China Architecture & Building Press, 1998.
- [2] Zhao Shunbo, Zhang Xinzong. Concrete composite structure design principle and application [M]. China WaterPower Press, 2001.
- [3] Zhou Wanghua. Design method study of the whole assembly beam slab abroad [J]. Architectural technology communication (Building Structure), 1980, (2): 35 - 41.
- [4] R. H. Evans and A. S. Parker. Behavior of Prestressed Concrete Composite beams [J], ACI, 1995, 51(5):861-878
- [5] Branson, Dan E. Deformation of Concrete Structures [M], McGraw-Hill, 1977.
- [6] British concrete structure specifications (CPI10) [S]. 1976.
- [7] Nie Jianguo, Chen Bilei, Chen Ge. Experimental study on shear behavior of R.C. laminated slabs [J]. Industrial Construction, 2003, 55 (12) : 43-46.
- [8] Ye Xianguo, Hua Hegui, Experimental study on connections of superimposed slabs [J]. Industrial Construction, 2010, 12 (1): 59-63.
- [9] Liu Yi. Performance research of steel bar truss and concrete composite slab [D]. Master degree thesis of Zhejiang university, Hangzhou, 2006.3.

A Taylor Series Integration Method with Coupling in Structural Dynamics

Zeying Guo

School of Engineering, Shanxi Normal University, Linfen, Shanxi, 041004, China

gzeying@126.com

Keywords: Structural dynamics, Coupling, Taylor series, Implicit method, Stability, Accuracy

Abstract. Based on the coupled precise time integration method and basic assumptions of constant average acceleration method in Newmark family, implicit series solution of structural dynamic equation is put forward by introducing the Taylor series expansion. Relevant time step integration formulas were designed. Stability and accuracy of the method were analyzed. Stability analyses show that the coupling implicit method is stable when damping ratio is equal to 0, and is conditionally stable when damping ratio are other values. The results show that the accuracy of the algorithm can be controlled by choosing the number of truncation order of Taylor series expansion and is better than that of traditional scheme with the increase of time step. Number examples are given to demonstrate the validity of the proposed method.

Introduction

Step-by-step integration method in time domain is effective in structural dynamic equation solution. The precise integration method (PIM) solves the time step integration for the time-invariant system first [1]. For such a problem, precise integration gives a highly precise numerical result, which approaches the full computer precise. Renewal precise time step integration method (RPTSIM) [2] and Gauss precise time-integration method [3,4] are improvement of precise integration method. Newmark-renewal precise time step integration method is put forward [5,6].

Inverse matrix solution is avoided in Newmark-renewal precise time step integration method, while loading values of three time points are need to be calculated. If the load is arbitrary, the values of every time points are difficult to get which will affect the accuracy of time step integration method. Therefore, based on the coupled precise time integration method and basic assumptions of constant average acceleration method in Newmark family, implicit series solution of structural dynamic equation is put forward by introducing the Taylor series expansion.

Implicit Taylor Series Integration Method with Coupling

Equations of motion for a multi-degree of freedom (MDOF) system often appear in matrix form as

$$M\ddot{x} + C\dot{x} + Kx = F \quad (1)$$

Where M , C , K are the mass, damping and stiffness matrices respectively. x , \dot{x} , \ddot{x} are the displacement, velocity and acceleration vectors respectively. F is the dynamic load. Time of earthquake action is divided into some time interval Δt .

Basic assumptions of Constant average acceleration method are

$$\ddot{\mathbf{x}}_{i+1} = \frac{2}{\Delta t}(\dot{\mathbf{x}}_{i+1} - \mathbf{x}_i) - \ddot{\mathbf{x}}_i \quad (2)$$

$$\mathbf{x}_{i+1} = \mathbf{x}_i + \Delta t \dot{\mathbf{x}}_i + \frac{1}{4} \Delta t^2 (\ddot{\mathbf{x}}_{i+1} + \ddot{\mathbf{x}}_i) \quad (3)$$

Where $\ddot{\mathbf{x}}_i, \dot{\mathbf{x}}_i, \mathbf{x}_i$ are the acceleration, velocity and displacement vectors at time t_i and $\ddot{\mathbf{x}}_{i+1}, \dot{\mathbf{x}}_{i+1}, \mathbf{x}_{i+1}$ are the same vectors at time t_{i+1} respectively. Δt is a small but constant time step.

Substituting Eq.2 into Eq. 1 at time t_{i+1} , and the equation can be simplified as

$$\dot{\mathbf{x}} = \mathbf{H}\mathbf{x} + \mathbf{P} \quad (4)$$

in which

$$\mathbf{H} = -\left(\frac{2}{\Delta t} \mathbf{M} + \mathbf{C}\right)^{-1} \mathbf{K} \quad \mathbf{P} = \left(\frac{2}{\Delta t} \mathbf{M} + \mathbf{C}\right)^{-1} \left(\frac{2}{\Delta t} \mathbf{M}\dot{\mathbf{x}}_i + \mathbf{M}\ddot{\mathbf{x}}_i + \mathbf{F}_{i+1}\right)$$

By dispersing numerical value, Eq.4 gives

$$\mathbf{x}_{i+1} = \mathbf{T}\mathbf{x}_i + \int_{t_i}^{t_{i+1}} \exp(\mathbf{H}(t_{i+1} - t'))\mathbf{P}(t')dt' \quad (5)$$

The solution accuracy of Eq.5 is mainly decided by the integral calculation because the precise computation of exponential matrix $\mathbf{T} = \exp(\mathbf{H}\Delta t)$ approaches the full computer precise. Taylor series solution [7] is adopted to solve the integral calculation. Only the loading at points of time step boundary are needed which can improve the solution accuracy. The loading within the time interval $[t_i, t_{i+1}]$ is often simulated by an analytical function. If the loading is piecewise linear, one may express it in terms of time-invariant vectors as $\mathbf{P}(t') = \mathbf{P}_0 + \mathbf{P}_1(t' - t_i)$

Suppose $t' - t_i = s$, Substituting the Taylor series expansion into the integral term of Eq.5, the integral solution can be expressed as

$$\begin{aligned} \int_{t_i}^{t_{i+1}} \exp(\mathbf{H}(t_{i+1} - t'))\mathbf{P}(t')dt' &= \int_0^{\Delta t} \exp(\mathbf{H}(\Delta t - s)) \cdot (\mathbf{P}_0 + \mathbf{P}_1 \cdot s) ds \\ &= \mathbf{T}(\Delta t) \cdot \sum_{l=0}^{\infty} \left(\frac{(-\mathbf{H})^l}{l!} \frac{\Delta t^{l+1}}{l+1} \mathbf{P}_0 + \frac{(-\mathbf{H})^l}{l!} \frac{\Delta t^{l+2}}{l+2} \mathbf{P}_1 \right) \end{aligned} \quad (6)$$

Step-by-step integration formulas are

$$\mathbf{x}_{i+1} = \mathbf{T}(\Delta t)\mathbf{x}_i + \mathbf{T}(\Delta t) \cdot \sum_{l=0}^{\infty} \left(\frac{(-\mathbf{H})^l}{l!} \frac{\Delta t^{l+1}}{l+1} \mathbf{P}_0 + \frac{(-\mathbf{H})^l}{l!} \frac{\Delta t^{l+2}}{l+2} \mathbf{P}_1 \right) \quad (7)$$

$$\dot{x}_{i+1} = -\left(\frac{2}{\Delta t} M + C\right)^{-1} Kx_{i+1} + \left(\frac{2}{\Delta t} M + C\right)^{-1} \left(\frac{2}{\Delta t} M\dot{x}_i + M\ddot{x}_i + F_{i+1}\right) \quad (8)$$

$$\ddot{x}_{i+1} = -M^{-1}C\dot{x}_{i+1} - M^{-1}Kx_{i+1} + M^{-1}F(t_{i+1}) \quad (9)$$

From Eq.7 to Eq.9, it can be found the solution accuracy is controlled freely by the truncation order l of the Taylor series expansion.

Stability of the Proposed Method

In order to investigate the stability of a direct integration scheme, one has to check if the spectral radius ρ of the integration transformation matrix A for a single-DOF (SDOF) system is less than or equal to unity [7,8]. The formulas of a single-DOF (SDOF) system are

$$x_{i+1} = T(\Delta t)x_i + T(\Delta t) \cdot \sum_{l=0}^{\infty} \left(\frac{(-h)^l}{l!} \frac{\Delta t^{l+1}}{l+1} p_0 + \frac{(-h)^l}{l!} \frac{\Delta t^{l+2}}{l+2} p_1\right) \quad (10)$$

$$\dot{x}_{i+1} = hx_{i+1} + p_{i+1} \quad (11)$$

$$\ddot{x}_{i+1} = -2\zeta\omega\dot{x}_{i+1} - \omega^2 x_{i+1} + f_{i+1} \quad (12)$$

in which

$$T = \exp(h \cdot \Delta t) = \left(\exp\left(h \cdot \frac{\Delta t}{2^N}\right)\right)^{2^N} = \left(\exp\left(-\frac{\Omega^2}{2 + 2\zeta\Omega}\right) \frac{1}{2^N}\right)^{2^N}$$

$$h = -\frac{\omega\Omega}{2 + 2\zeta\Omega} \quad p_{i+1} = \frac{1}{1 + \zeta\Omega} \dot{x}_i + \frac{\Delta t}{2 + 2\zeta\Omega} \ddot{x}_i + \frac{\Delta t}{2m + c\Delta t} f_{i+1}$$

According to the implicit method above, every item of the transformation matrix A for an SDOF system can be written as

$$\begin{aligned} a_{11} &= T, & a_{12} &= \frac{Te}{1 + \zeta\Omega}, & a_{13} &= \frac{Te}{2 + 2\zeta\Omega}, & e &= \sum_{l=0}^{\infty} \left(\frac{(-h)^l}{l!} \frac{\Delta t^l}{l+1}\right) \\ a_{21} &= -\frac{T\Omega^2}{2 + 2\zeta\Omega}, & a_{22} &= \frac{2 + 2\zeta\Omega - Te\Omega^2}{2(1 + \zeta\Omega)^2}, & a_{23} &= \frac{2 + 2\zeta\Omega - Te\Omega^2}{(2 + 2\zeta\Omega)^2} \\ a_{31} &= -\frac{T\Omega^2}{1 + \zeta\Omega}, & a_{32} &= -\frac{2\zeta\Omega + 2\zeta^2\Omega^2 + Te\Omega^2}{(1 + \zeta\Omega)^2}, & a_{33} &= \frac{-4\zeta\Omega - 4\zeta\Omega^2 + Te\zeta\Omega^3 - Te\Omega^2}{2(1 + \zeta\Omega)^2} \end{aligned}$$

in which Ω ($\Omega = \omega\Delta t$) is sampling-frequency [8] and ξ ($\xi = c/2m\omega$) is damping ratio.

According to the theory of arithmetic stability, integration formulas are stable when spectral radius $\rho(A)$ of transformation matrix (A) satisfies $\rho(A) = \max|\lambda_i| \leq 1$, in which λ_i are eigenvalues of matrix A . The truncation order l is equal to 4 and the curves of $\rho(A)$ to Ω are found through developing program when ξ is adopted different value, which are presented in Fig.1.

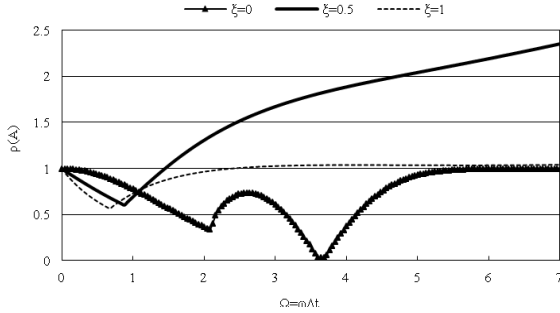


Fig.1 Spectral radius ρ of transform matrix against sampling-frequency Ω

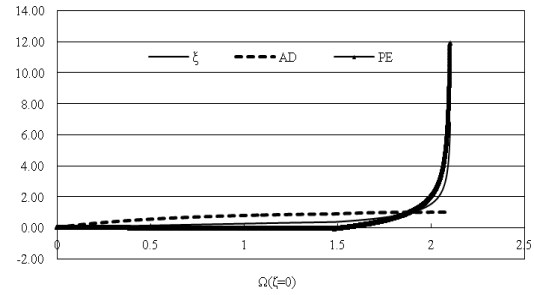


Fig.2 Algorithmic damping ratio $\bar{\zeta}$, amplitude decay AD and period elongation PE against Ω

Fig.1 shows that the method is stable because spectral radius $\rho(A)$ of transformation matrix is less than unity when damping ratio equal to 0. But spectral radius is found having the area of more than unity when damping ratio is equal to 0.5 or 1.0. Therefore, the method is conditionally stable in total.

Accuracy of the method

More precise method of accuracy is to analyze amplitude decay (AD) and period elongation (PE) produced by algorithmic damping $\bar{\zeta}$. Amplitude decay AD and period elongation PE are all related to eigenvalues of matrix A . According to reference [9]

$$PE = \Omega / \bar{\Omega} - 1 \quad AD = 1 - \exp(-2\pi\bar{\zeta})$$

$$\bar{\zeta} = -\ln(A_2) / (2\bar{\Omega}) \quad \bar{\Omega} = \bar{\omega}\Delta t = \arctg\sqrt{A_2 / A_1^2 - 1} \quad \Omega = \omega\Delta t \quad \omega = \Delta t / T_p$$

A_1 is the mark and A_2 is determinant of matrix A . $\bar{\zeta}$, AD and PE are all related to Ω . The truncation order l is four and the curves of $\bar{\zeta}$, AD and PE against Ω are found through developing program when algorithmic damping ξ is adopted different value, which are presented in Fig.2.

From Fig.2, it is observed that when undamped case ($\zeta = 0$) with truncation order l is equal to 4, the algorithmic damping $\bar{\zeta}$. Amplitude decay AD and period elongation PE are extremely small at small time interval, which show the precise accuracy of the method.

Numerical Example

The equations of motion for a two-degree of freedom system [2] are given by

$$\begin{bmatrix} 2 & 0 \\ 0 & 1 \end{bmatrix} \begin{bmatrix} \ddot{x}_1 \\ \ddot{x}_2 \end{bmatrix} + \begin{bmatrix} 1.2 & -0.4 \\ -0.4 & 0.6 \end{bmatrix} \begin{bmatrix} \dot{x}_1 \\ \dot{x}_2 \end{bmatrix} + \begin{bmatrix} 6 & -2 \\ -2 & 4 \end{bmatrix} \begin{bmatrix} x_1 \\ x_2 \end{bmatrix} = \begin{bmatrix} 0 \\ 10 \end{bmatrix} f(t)$$

$$\begin{bmatrix} x_1 \\ x_2 \end{bmatrix}_{t=0} = \begin{bmatrix} 0 \\ 0 \end{bmatrix}, \quad \begin{bmatrix} \dot{x}_1 \\ \dot{x}_2 \end{bmatrix}_{t=0} = \begin{bmatrix} 0 \\ 0 \end{bmatrix} \quad f(t) = \begin{cases} \sin(\pi t), & 0 \leq t \leq 1.0 \\ 0, & 0 \end{cases}$$

Table 1 shows the displacement response x_2 for $0 \leq t \leq 1.0$ computed by three methods. As loading values of RPTSIM are need to be calculated in every time interval, there will be greater calculation error with the increase of time step. As for the proposed method, only the loading values at points of time step boundary are needed which can improve the solution accuracy. Table 1 shows that with the increase of time step Δt , calculation accuracy of proposed scheme is better than that of traditional method such as constant average acceleration method in Newmark family. At the beginning of time domain, dynamic response values are far more than the exact solution because the proposed method has a certain transcendedce.

Table 1 Displacement response x_2 of two-degree of freedom system

scheme	Δt		0.2s	0.4s	0.6s	0.8s	1.0s
Exact solution		x_2	0.0395484	0.282357	0.8000647	1.48989	0.0395484
RPTSIM (tolerance%)	0.05	x_2	0.0279666(29.29)	0.241084(14.6)	0.729910(8.83)	1.409350(5.41)	2.04726(2.8)
	0.2	x_2	0.0094277(76.16)	0.138504(51.0)	0.525889(34.3)	1.146850(23.0)	1.81469(29.2)
The proposed method (tolerance%)	0.05	x_2	0.0405030(0.10)	0.281213(0.41)	0.790127(1.31)	1.461040(1.94)	2.05383(2.49)
	0.2	x_2	0.0541474(36.9)	0.290529(2.89)	0.761920(4.84)	1.360780(8.67)	1.86557(11.4)
Constant average acceleration method (tolerance%)	0.05	x_2	0.0404560(2.29)	0.282682(0.12)	0.798644(0.25)	1.484640(0.35)	2.09838(0.37)
	0.2	x_2	0.0535154(35.3)	0.287420(0.12)	0.769670(3.87)	1.408170(5.49)	1.98257(5.87)

Conclusion

Implicit series solution with coupling of structural dynamic equation is put forward by introducing the Taylor series expansion, which based on the coupled precise time integration method and basic assumptions of constant average acceleration method in Newmark family. The results of stability analyses show that the coupling implicit method is stable when damping ratio is equal to 0, and is conditionally stable when damping ratio are other values. The results show that the accuracy of the algorithm can be controlled by choosing the truncation order of Taylor series expansion and is better than that of traditional scheme with the increase of time step.

Acknowledgements

The work described here has been supported by Doctoral Scientific Research Foundation of Shanxi Normal University of China with Grant Number 833093.

References

- [1] Wanxie Zhong. J. of Comput. and Appl. Math. Vol.163(2004),p.59
- [2] Mengfu Wang, Xiyuan Zhou. Acta Mech. Sinica Vol.36(2004),p.19,in Chinese.
- [3] Mengfu Wang, Xiyuan Zhou. Eng. Mech. Vol.21(2004),p.13,in Chinese.
- [4] Mengfu Wang, F.T.K.Au. Comput. and Struc. Vol. 84(2006),p.779
- [5] Zeying Guo, Qingning Li, Shoujun Zhang. Proceedings of the Ninth International Symposium on Structural Engineering for Young Experts Beijing, Shanghai, China, (2006),p.180
- [6] Zeying Guo, Qingning Li, Shoujun Eng. Mech. Vol. 24(2007),p.13, in Chinese.
- [7] Jinqiao Li, Jianhua Yu. J. of Sichuan University (Engineering Science Edition). Vol.34(2002),p.2,in Chinese.
- [8] Huanchun Sun, Naisi Qu, Jiahao Lin. Higher computational structural dynamics(Dalian University of Technology Press, Dalian (1992),in Chinese.

Optimization Design of Core Thickness of Exterior Frame and Core Hybrid Structures in High-rise Buildings

Shuyun Zhang^{1, a}, Wenwei Zhao^{1, b} and Haihua Wang^{1, c}

¹ Xi'an University of Science and Technology, Xi'an 710054, China

^axazhshy@126.com, ^b821610686@qq.com, ^c751458426@qq.com

Keywords: exterior frame and core hybrid structures, core thickness, seismic response analysis, optimization design.

Abstract. Considering core thickness is important issue to performance of exterior frame and core hybrid structure in high-rise buildings, seismic response analysis is conducted by response spectrum method for finite element models with different core thickness. The optimization design of core thickness of hybrid Structures on the basis of the seismic response is studied, the core thicknesses are chosen as design variables, the objective function about core volume is adopted, some specification requirements such as deformation, the ratio of lateral stiffness to gravity, storey shear to gravity, storey shear of exterior frame, axial compression ratio of column and wall limb, bearing capacity of structural member and core construction are regarded as restricting conditions, the optimal mathematical model is established for reflecting integrity dynamic properties of hybrid structure. The ANSYS software is used for optimizing tool, the hybrid structures optimization design are made through different initial values for verifying convergence of optimization method, the optimal result show that the performances of hybrid structure are improved, the internal forces are reduced and the ratios of inner force born by exterior frames are increased in the optimal scheme.

Introduction

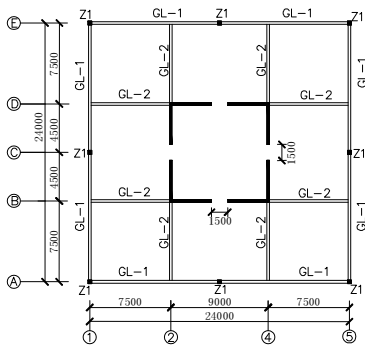
Hybrid structures in high-rise buildings have grown rapidly in recent years, especially exterior frame and core hybrid structures are used widely. However, there are different views on the performance at home and abroad [1,2], such as single seismic defense line of hybrid structures is particularly prominent, the reinforced concrete core is higher relative stiffness and less strength than the exterior frame. Reasonable stiffness ratio between the two substructures under earthquake action is the basis of ensuring the second seismic defense line, core thickness is one of the main factors affecting stiffness ratio of hybrid structure.

Structural optimal design is a new technology in the past three decades that mathematics, mechanics and engineering design methods can be combined. According to all constraints, in a given material and structural type and loading condition the mathematical model of structural optimization is proposed, and then the model are solved with optimization principle and method. Designer who passively check the program in previous can actively select design scheme by optimal design, as a result, the plan meeting the requirements of economic and security would be obtained where the material distribution is the most reasonable state.

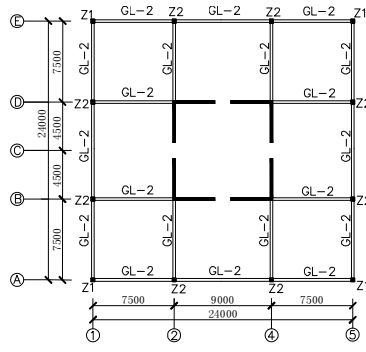
The goal of this paper is to study the optimal design problem of core thickness of hybrid Structures in high-rise buildings on the basis of structural seismic response by finite element analysis.

Effect of the core thickness on structural performance

Hybrid structure example. A 30-storey composite frame and reinforced concrete core hybrid structures in high-rise buildings is used as a numerical example in this paper[3], the total height is 109 m, the core thickness in 1 to 6 floor is 700mm, the core thickness in 7 to10 floor is 600mm, the core thickness in 11 to 30 floor is 400mm. The structure plane of the example building is shown in Fig. 1. The 3-D finite element analysis have been completed by ANSYS software, in which beams and



(a) structure plane of 1 to 2 layers



(b) structure plane of rest layers

Fig.1 Hybrid structure plane

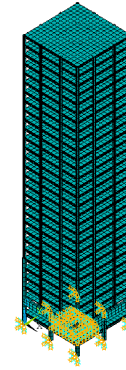


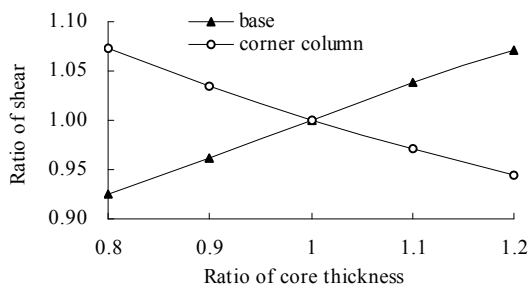
Fig.2 Finite element model

columns are simulated by three nodes Timoshenko space beam element, shear wall and floor are simulated by eight nodes curved shell element, sections of SRC member are defined by user, Two-dimensional eight-node elements are used to simulate different materials section that obey the plane section assumption, the finite element model is shown in Fig. 2.

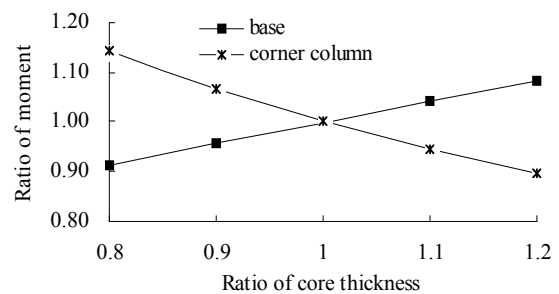
Seismic response analysis. The earthquake classification is the first group; the characteristic period of ground motion is 0.35 s; the design basic acceleration of ground motion is 0.20g; the seismic fortification intensity is 8 degrees; the modal damping ratio of 0.04 is assumed. The seismic responses are numerical calculated by response spectrum method, modal analysis shown that natural frequencies of vibration are separated by more recent, thus complete quadratic combination (CQC) method is applied to combine 30 modes[4]. Four models response under earthquake action are obtained, in which core thickness of 0.8 times and 0.9 times and 1.1 times and 1.2 times in example were taken. The structural performances are list in table 1, the displacements and story drift ratios are nonlinear reduce with the increase of core thickness, the floor of the maximum of story drift ratios move up, the base shear and base overturning moment increase with core thickness. For such hybrid structure, the shears borne by the exterior frame are larger at middle floors, the shears of corner column at 15 floor are analyzed, the variation trend of column inner force with core thickness is shown in Fig.3, the shears of corner column at 15 floor are decrease with core thickness, the relationship between moment of corner column and core thickness at 1 floor are same law, it is concluded that the inner forces of exterior frame will be lessen as the core thickness increase.

Table 1 The main performance of hybrid structure with core thickness

Ratio of core thickness	0.8	0.9	1	1.1	1.2
Top displacement[mm]	56.9	55.2	53.7	52.4	51.3
The maximum of story drift ratios	1/1541	1/1587	1/1629	1/1660	1/1700
Base shear [kN]	5445	5669	5892	6114	6316
Base overturning moment [kN·m]	621301	650807	679638	707897	735373



(a) Ratio of shear in corner column at 15 floor



(b) Ratio of corner in column moment at 1 floor

Fig.3 Variation trend of column inner force with core thickness

The thick core can reduce the structural displacement during earthquake and will inevitably lead to bear more internal force in whole structure, moreover, the ratios of inner forces borne by the exterior frame are relatively less, the core will bear more inner forces, thus it can make more obvious shortcomings of hybrid structure, therefore, how to select the core thickness is issues with practical significance, in which the structure has less earthquake effects and meet the seismic requirements.

Mathematical model of structural optimization

This optimization problem can be described as the following mathematical model:

$$\begin{aligned}
 \text{Find:} \quad & X = (x_1, x_2, \dots, x_n)^T \\
 & F(x_1, x_2, \dots, x_n) \rightarrow \min \\
 \text{Subject to} \quad & g_i(x) = g_i(x_1, x_2, \dots, x_n) \leq 0 \quad (i = 1, 2, \dots, m) \\
 & h_j(x) = h_j(x_1, x_2, \dots, x_n) = 0 \quad (j = m + 1, m + 2, \dots, p)
 \end{aligned} \tag{1}$$

Eq.1 is common expression for optimization problem, where $X = (x_1, x_2, \dots, x_n)^T$ is design variables, $F(x)$ is objective function that is a function of design variables. $g_i(x)$ and $h_j(x)$ are state variables. We can see that structural optimization is extreme value problem of objective function where criteria method or mathematical programming can be used, usually mathematical programming. The application of structural optimization is limited by reason of time-consuming computation involved writing programs. Finite element technology provides an effective analytical tool for structural optimization, the combination of finite element analysis and optimization methods promote the application of structural optimization.

Optimization model of hybrid structure

Design variables. The thickness of core-RC are taken as the design variables, in view of load distribution and internal force distribution are varying along the height of the hybrid structure, core thicknesses are theoretically different in each layer, however, we must taken into account construction demands, in general, several thickness along the height are set. In this paper three thicknesses are taken as design variables that are expressed as $H = (h_1, h_2, h_3)^T$, where h_1 is the core thickness at 1 to 6 layers, h_2 is the core thickness at 7 to 10 layers, h_3 is the core thickness at 11 to 30 layers.

Objective function. In general, we wishes to reduce the internal force of structure under earthquake, thin core could induce the exterior frame to bear more internal forces and reduce the structural weight, as a result of the engineering cost is reduced. The weight of core-RC is the objective function to be minimized, further simplified as the volume of core-RC, the objective function is expressed as Eq.2.

Constraint conditions. The constraint conditions include deformation limit, overall stability, bearing capacity, member ductility, and construction requirements[5].

In conclusion, this optimal design problem can be described as the following nonlinear programming problem: find $H = (h_1, h_2, h_3)^T$ such that

$$\text{Min} \quad VOL(h) = F(h_1, h_2, h_3). \tag{2}$$

$$\text{S.T.} \quad \max(\Delta u_i / h_i) \leq 1/800. \tag{3}$$

$$EJ_d = \frac{11qH^4}{120u} \geq 1.4H^2 \sum_{i=1}^n G_i. \tag{4}$$

$$V_{Eki} \geq \lambda \sum_{j=i}^n G_j. \tag{5}$$

$$\mu_{c,\max} \leq [\mu_c]. \tag{6}$$

$$\mu_{w,\max} \leq [\mu_w]. \tag{7}$$

$$\varepsilon_{c,\max} \leq 0.003; \varepsilon_{s,\max} \leq \varepsilon_y. \tag{8}$$

$$h_i \geq [h_{\min}] \quad (i = 1, 2, 3). \tag{9}$$

$$h_1 \geq h_2 \geq h_3. \tag{10}$$

This is optimization model for the nonlinear programming problem with constraints.

Eq.3 is deformation limit Where Δu_i are storey drift on each floor; h_i are floor height on each floor.

Eq.4 is the ratio of stiffness to weight influencing structural stable[6], where EJ_d is equivalent elastic stiffness along one principal axis, in which the structural stiffness is converted to the equivalent of vertical cantilever with the equal principle of the top displacement under inverted triangular load; q is the maximum of inverted triangular load; u is the top displacement under inverted triangular load; H is building height; G_i is representative value of gravity load at floor i .

For long period structures, the seismic response may not be correctly estimated by response spectrum method, Eq.5 is the specification limits that the ratio of characteristic shear value to representative value of gravity load must be meet [6], where V_{Eki} is shear characteristic value under earthquake at floor i ; λ is horizontal seismic shear coefficient; G_j is representative value of gravity load at floor j .

Eqs.6 and Eqs.7 are the upper limit for axial compression ratio of column or shear wall set by code for seismic design of buildings ($[\mu_c]$ or $[\mu_w]$), for controlling structure of the ductility, where $\mu_{c,\max}$ is the maximum axial compression ratio for SRC column; $\mu_{w,\max}$ is the maximum axial compression ratio for shear wall.

Eq.8 is the bearing capacity limits for SRC column, where $\epsilon_{c,\max}$ is the maximum concrete compressive strain at the extreme outer compressive fiber in section; $\epsilon_{s,\max}$ is the maximum concrete tensile strain at the extreme outer tensile fiber; ϵ_y is the steel yield strain. Eq.9 and Eq.10 are construction requirements.

Optimization application to hybrid structure

Optimization process. The ANSYS software is used for optimizing tool by written analysis file of APDL language, the sub-problem method is adopt[7], the optimization design are applied to the aforementioned example of hybrid structures. The load combination is the sum of 1.2 times load effect of weight representative value and 1.3 times load effect of horizontal earthquake action characteristic value. For verifying convergence of optimization method, three optimization designs are made through different initial values, the optimal results are very close, the proposed optimal algorithm is uniform convergence, the optimal result with different initial values are list in table 3.

Table 2 Optimal results with different initial values

Optimal design order	Initial values		Optimal results		Iteration number
	Core thickness [mm]	Core volume [m ³]	Core thickness [mm]	Core volume [m ³]	
1	(400,200,200)	857	(402,365,246)	1035	13
2	(700,600,400)	1721	(406,402,245)	1052	16
3	(900,800,800)	3474	(402,364,251)	1044	21

Optimal scheme. It should not be advocated to obtain the optimal solution only considered the minimum of objective function, the optimal project is determined through the comprehensive consideration of the benefit of objective function and structural response with design variables. For the hybrid structure example under frequently occurred earthquake, the optimization results show that the core thickness is in the range of 400~500mm at 1 to 6 layers and 350~450mm at 7 to 10 layers and 250~300mm at 11 to 30 layers, so the framework and concrete cylinder two substructure reasonable share the internal force, the material is able to make full use.

If the core of example structure are 700mm, 600mm, and 400mm, after optimization design, core are 500mm, 400mm, and 300mm in optimal scheme, the inter forces of whole hybrid structure are reduced, the proportions of core borne by the exterior frames are decrease, thus the frames will bear more inter forces, the performance of two sub-structures are improved, the seismic response before and after optimization is list in table 3.

Table 3 Comparison of seismic response before and after optimization

Items	Initial state	Optimal state
Core thickness[mm]	(700,600,400)	(500,400,300)
Top displacement[mm]	53.8	59
The maximum of story drift ratios	1/1544	1/1413
Base shear [kN]	9722	8448
Base overturning moment [kN·m]	894319	784232
The maximum ratio of shear borne by frame	14.3%	18.5%
The maximum ratio of shear borne by core	95%	93%
Axial force of corner column at 1 floor [kN]	2542	2719
Moment of corner column at 1 floor [kN·m]	268	322
The maximum shear of frame column[kN]	62	76

Conclusions

Based on seismic response analysis and optimization design for core thickness of hybrid structure, some conclusions can be drawn:

(1) Seismic responses of hybrid structure with different the core thickness had studied, the thick core can reduce the structural displacement and will inevitably lead to bear more internal forces while the hybrid structure under earthquake action, moreover, the ratios of inter forces borne by the exterior frame are relatively less, thus it can make more obvious shortcomings of hybrid structure.

(2) The optimization model of hybrid structure for the appropriate core thickness is made based on the structural dynamic performance, the optimal solutions are gotten by the ANSYS software, the optimization design make the design scheme reasonable and avoid to repeat design.

(3) Optimal algorithm convergence are checked with different initial values, the results show that the objective function can fell rapidly in the first few iteration and eventually converge, the Calculating time is in withstand range with practical application value.

Acknowledgements

This scientific research program is funded by the Nation Nature Science foundation of china (Grant NO.50578129) and by Shaanxi Provincial Education Commission (Program NO. 2010JK669).

References

- [1] Peifu Xu, Cuikun Wang, Congzhen Xiao: Building structure, Vol. 39 (9) (2009), p. 28 (in Chinese)
- [2] Dasui Wang, Jianlong Zhou: Journal of Building Structure, Vol. 31 (6) (2010), p. 62 (in Chinese)
- [3] Peifu XU, Yantao XUE, cong-zhen XIAO, et al: Building Structure, Vol. 35(5) (2005), p. 3 (in Chinese)
- [4] Anil k. Chopra: Dynamic of Structures : Theory and Applications to Earthquake Engineering (Tsinghua University Press, Beijing 2005)
- [5] Ministry of Construction, P.R.C: GB50011-2010, Code for Seismic Design of buildings (China Architecture & Building Press, Beijing 2001) (in Chinese).
- [6] Ministry of Construction, P.R.C: *JGJ 3-2010, Technical specification for concrete structure of tall buildings* (China Architecture & Building Press, Beijing 2010) (in Chinese).
- [7] Xia-sa Studio. *New Classical ANSYS & Workbench Tutorial* (Publishing House of Electronic Industry, Beijing 2004) (in Chinese).

Mean wind pressure field on the typical large-span roof structures

Fanghui Li^{1,a}, Ming Gu^{2,b}, Zhenhua Ni^{3,c}, and Shizhao Shen^{4,d}

¹School of Architectural Engineering, Heilongjiang University, China

²State Key Laboratory of Disaster Reduction in Civil Engineering, China

³ Department of Civil Engineering, Shantou University, China

⁴ School of Civil Engineering, Harbin Institute of Technology, China

^afhli_2000@163.com, ^bminggu@tongji.edu.cn, ^czhni@stu.edu.cn, ^dszshen@hit.edu.cn

Keywords: wind pressure; large-span roof; wind tunnel test; dome; pitched roof

Abstract. The wind tunnel tests of some typical large roofs, including a saddle roof, pitched roof and domes, are carried out with various terrains which cover suburban and urban exposures. The wind pressure data of roofs are obtained by using the synchronous multi-pressure scanning technique. The wind pressure coefficient and local shape factors of the wind load was investigated. The effects of various terrains on wind pressures of roofs are discussed. From the results, we can see mean pressures of these roofs exposed to the mean pressures exposed to the suburban terrain are 2 or 3 times those exposed to the urban terrain. And the terrains are no directly influence to the wind pressure shape factors.

Introduction

The shape of the large space roof structure changes in diversity. Because it's existing the phenomenon that the turbulence and airflow are separated in the atmospheric boundary layer and heavy attached and so on. Leading to the roof surface fluctuation wind pressure field with spatio-temporal complexity, fluctuating randomness has a non-Gauss feature. For the structure with complex shape and surrounding environment, the wind load on the roof can not acquired according to the load code or the standard, wind tunnel text provides a very effective tool. Using the wind pressure data measured simultaneously by wind tunnel test, can study the influence of characteristics of wind pressure, wind angle, landforms type or other factors on the partial area of the roof in-depth. With the span increasing and use of lightweight materials, roof becoming the wind sensitive structure. Large space roof structure free vibration characteristics shows a very narrow frequency band that gathered a large number of mode, lead to fluctuation wind-induced response resonate excited the sensitivity increases. The traditional mode superposition method to calculate wind-induced response reflects the participation of multi mode. In the design process, the dynamic wind loads of structure treated with the static wind loads. To ensure the structure design safety by a simple static analysis to estimate the wind-induced response, many countries' load code use the gust load factor method to determine the wind load of structure. However, this method applies to the determination of horizontal loads on the high-rise building, and it's possible failing on roof structure. The large space roof structure mainly be acted on vertical wind load and the contribution may be very small relative to the horizontal wind load. At this time, gust load factor method has limitations and can't provide useful information. This paper focus the mean wind load distributions on the typical large span roof, further more, can be advance practicality design method for the low rise roofs based on this research.

Wind tunnel test

The rigid models of saddle roof with enclosing wall under different terrain conditions were made at a scale of 1/50. The prototype diagonal distance is 40m, its lowest height is 8 m and its top height is 16 m. The 81 pressure taps were distributed over the inside and outside surface of the model. The wind

characteristic was achieved by a combination of turbulence generating spires, and roughness elements along the wind tunnel floor upstream of the model. Wind pressure time series at the pressure taps distributed over the saddle roof were measured simultaneously. Fig.1 shows the arrangement of the taps distributed over the roof. The photograph of the saddle roof model in wind tunnel is shown in Fig.2. The test of the saddle roof was carried out in the TJ-2 atmospheric boundary wind tunnel of the State Key Laboratory for Disaster Reduction in Civil Engineering at Tongji University, China. The TJ-2 wind tunnel is a boundary layer tunnel of closed-circuit type. The working section of the tunnel is 3m wide, 2.5m high and 15 m long. The wind pressures were measured substantially simultaneously with the sampling frequency of 312.5 Hz by using the DSM-3000 data acquisition system. And wind tunnel test of the pitched roof and dome with rise-span ratio of 0.1 and 0.2 were carried out in the Shantou University. The Fig.3 and Fig.4 shows the wind tunnel model of pitched roof in the B category and D category respectively. The Fig.5 and Fig.6 gives the test model of the dome with rise-span ratio 0.1 of the B and D categories.

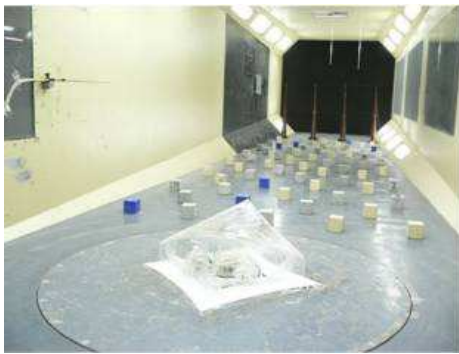


Fig.1 Wind tunnel model of saddle roof

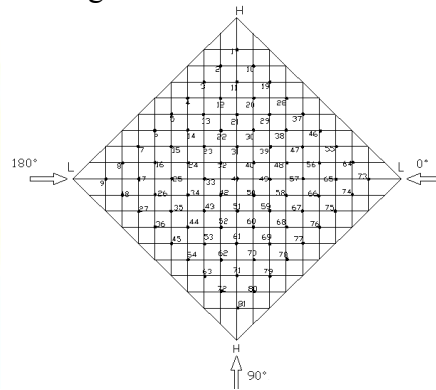


Fig.2 Arrangement of pressure taps



Fig.3 Testing model of B category in wind tunnel

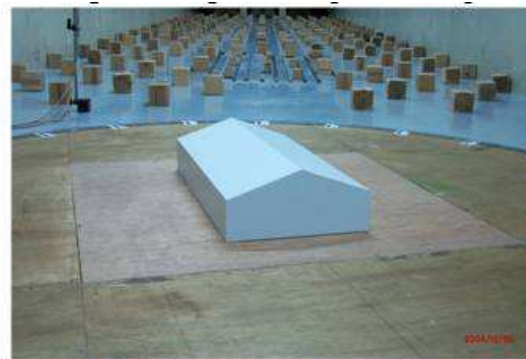


Fig.4 Testing model of D category in wind tunnel



Fig.5 Testing model dome with rise-span ratio of 0.1 of B category

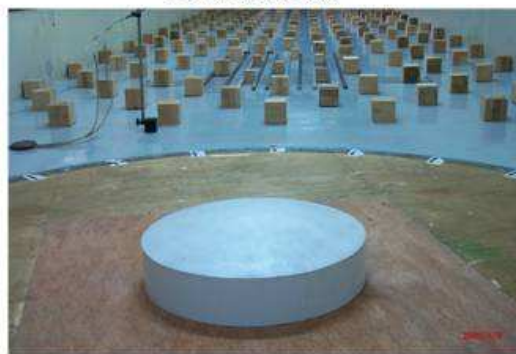


Fig.6 Testing model dome with rise-span ratio of 0.1 of D category

Mean wind pressure field expressions

Wind pressure coefficients

The wind pressure shape factor μ_{si} of the i -th pressure tap are defined as

$$\mu_{pi} = \frac{p_i - p_\infty}{0.5\rho V^2} \tag{1}$$

The p_i represents the time evolution of the i -th pressure tap, p_∞ the reference value of pressure, V is reference wind velocity.

Wind pressure shape factors

With the wind pressure data which are measured simultaneously in a wind tunnel test, the wind pressure shape factor μ_{si} of the i -th pressure tap are defined as

$$\mu_{si} = \frac{p_i - p_\infty}{0.5\rho V^2} \cdot (z_{r\alpha} / z_i)^{2\alpha} \tag{2}$$

The p_i represents the time evolution of the i -th pressure tap, p_∞ the reference value of pressure, V is reference wind velocity, $z_{r\alpha}$ is reference high, z_i is the high of the i -th tap, α is surface roughness index.

Mean wind pressure coefficient distributions

This part focuses on the influence of the terrain category on the mean wind pressure coefficient. The wind pressure coefficient on the saddle roof in the B and D category for 0° wind direction is shown in Fig.7. The Fig.8 shows the wind pressure coefficient on the pitched roof in the B and D category for 0° wind direction. The table 1 gives the detail values of the coefficient on the pitched roof for the 90° wind direction. From comparison of the figures and table, we can see, the value of the wind pressure coefficients on the saddle roof and pitched roof in the D category is 2 or 3 times those exposed to the B category.

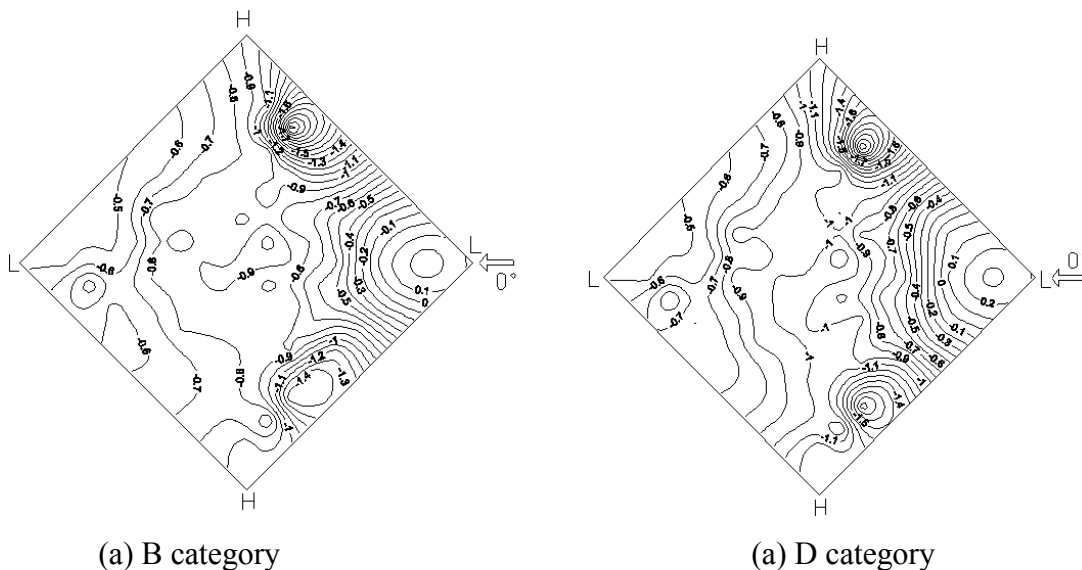


Fig 7: Distribution of shape factors on saddle roof in exposure categories B and D for 0° wind direction

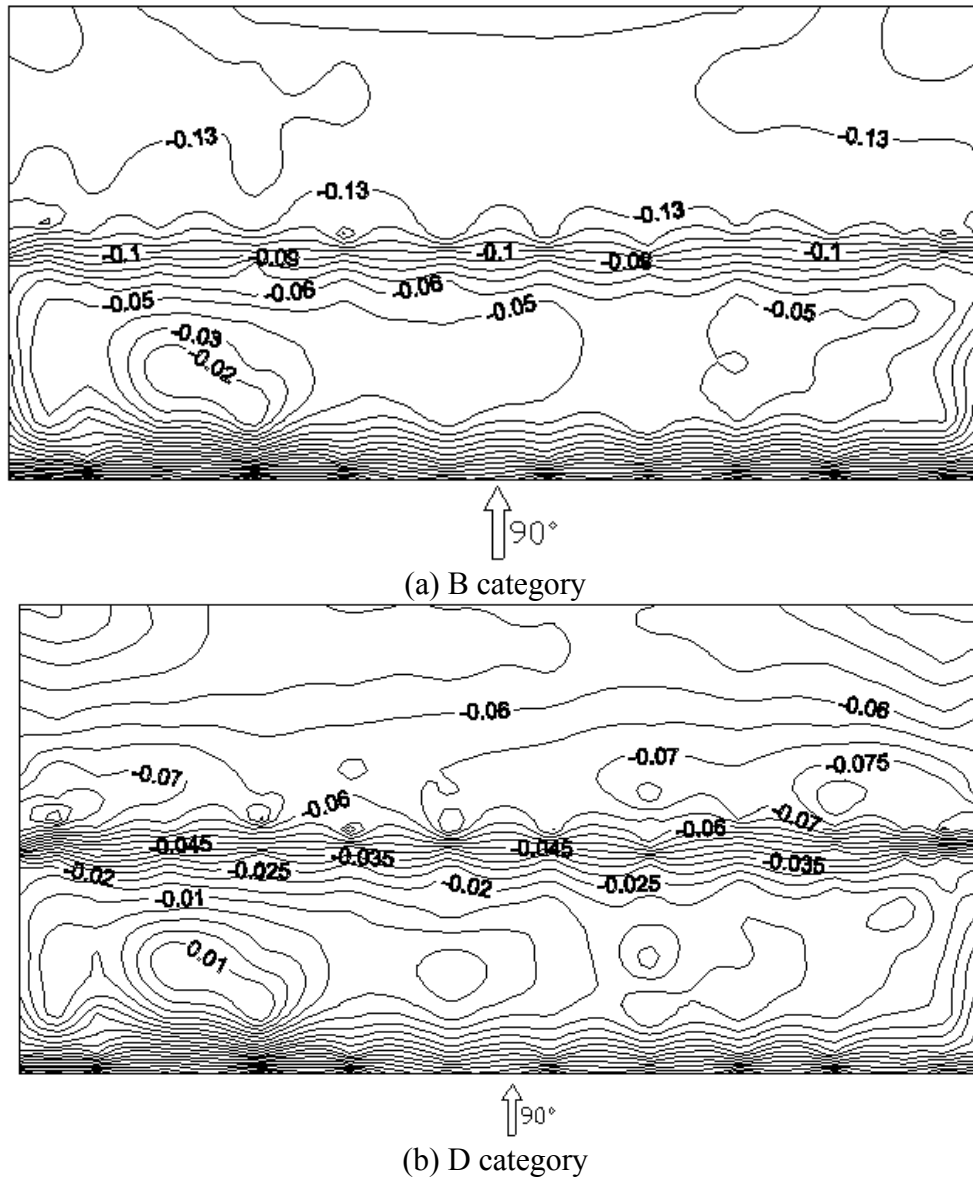


Fig.8 Distribution of mean wind coefficient for wind direction of 90° in exposure B and D categories

Table.1 Wind pressure coefficients of typical taps for 90° wind direction

Number of the tap	48	86	104	224	217	211	113	126
B category	-0.130	-0.159	-0.149	-0.224	-0.162	-0.217	-0.125	-0.097
D category	-0.059	-0.093	-0.073	-0.084	-0.060	-0.083	-0.061	-0.045

Mean wind pressure shape factors

The table 2 gives the wind pressure shape factors on typical taps which locates in the ridge and corner of pitched roof.

Table.2 Wind pressure shape factors of typical taps for 90° wind direction

The number of taps	48	86	104	224	217	211	113	126
B category	-0.405	-0.497	-0.463	-0.700	-0.506	-0.678	-0.389	-0.303
D category	-0.295	-0.470	-0.369	-0.423	-0.304	-0.417	-0.306	-0.225

The distribution of the shape factors of B category and D category for 90° wind direction can be seen in Fig.9 and Fig.10. From the comparison of the distribution of the shape factors on the different terrains, we can see, that the terrains are no directly influence to the wind pressure shape factors. The distributions of the shape factors of the domes with rise-span ratio of 0.1 and 0.2 are shown in Fig.11.

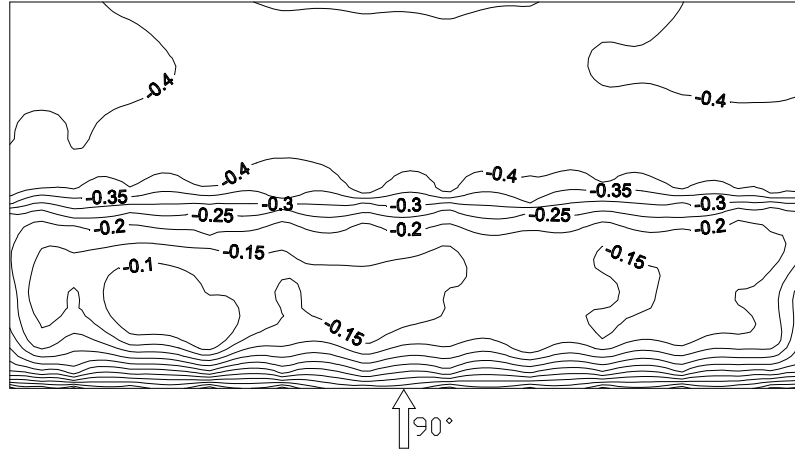


Fig.9 Distribution of the shape factors of B category

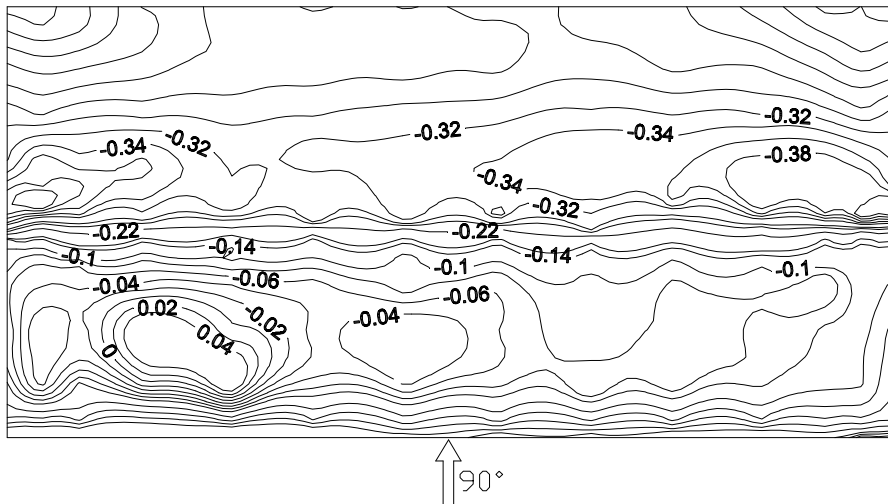
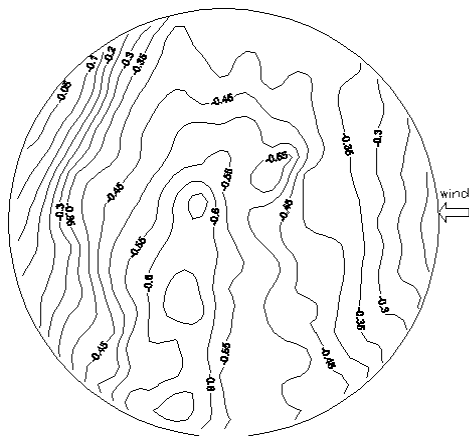
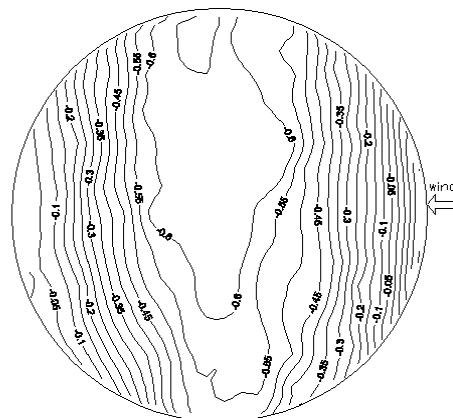


Fig.10 Distribution of the shape factors of D category



(a) Dome with 0.1 rise-span ratio



(b) Dome with 0.2 rise-span ratio

Fig.11 Distributions of the shape factors on the dome with 0.1 and 0.2 rise-span ration in exposure B category

Conclusions

The mean wind pressure field distributions of the typical roofs are investigated based on the wind pressure data obtained from the tests which can be measured simultaneously in wind tunnel. Through comparison of the wind pressure shape factors and shape factors, we can obtain the following conclusions. The wind field exposure categories don't have direct influence on the wind shape factors distribution, but the wind field category has significant effects on mean wind coefficients. From the results, we can see mean pressures of these roofs exposed to the mean pressures exposed to the suburban terrain are 2 or 3 times those exposed to the urban terrain.

Acknowledgements

The authors are grateful for the support of this research by the Foundation of Heilongjiang Province Educational Committee (11551368).

References

- [1] C. M. Cheng, C. L. Fu, Characteristic of wind loads on a hemispherical dome in smooth flow and turbulent boundary layer flow, *J. Wind Eng. Ind. Aerodyn.* 98 (2010) 328-344.
- [2] J. Marighetti, A. Wittwer, M. D. Bortoli, B. Natalini, M. Paluch, M. Natalini, Fluctuating and mean pressure measurements on a stadium covering in wind tunnel. *J. Wind Eng. Ind. Aerodyn.* 84 (2000) 321-328.
- [3] T. Stathopoulos, F. ASCE, P. Saathoff, R. Bedair, Wind pressures on parapets of flat roofs. *Journal of Architectural Engineering.* 8(2) (2002) 49-54.
- [4] H. W. Tieleman, R. E. Akins, P. R. Sparks: A Comparison of wind-tunnel and full-scale wind pressure measurements on low-rise structures. *J. Wind Eng. Ind. Aerodyn.* 8 (1981) 3-19.
- [5] J. S. Hwang, A. Kareem, H. J. Kim: Wind load identification using wind tunnel test data by Inverse analysis. *J. Wind Eng. Ind. Aerodyn.* 99 (2011) 18-26.

Explosion Resistance Investigation into Sandwich Structure of Steel Fiber Reinforced Concrete Support Plate

Wang Xinwu

Department of Civil Engineering, Luoyang College of Technology

Luoyang 471023, China

wxw197100@sina.com

Keywords: support; thin sandwich structure; penetration plate; explosion test; steel fiber reinforced concrete

Abstract. In order to avoid the damage of precision guided weapons on target, a steel fiber reinforced concrete sandwich structure with different types of support was proposed. The failure characteristics of penetration plate, steel fiber reinforced concrete plate and support beam were studied by contact explosion test. The results showed that the using of steel fiber sheet sandwich structure could increase a resistance level for the project with the same thickness of the protective layer. The failure mode of steel fiber reinforced concrete sandwich structure under partial blast loading was still the local damage mode, the strength and thickness of steel fiber laminate material, height and spacing of support beam were the main factors to control the effect of wave attenuation in steel fiber reinforced concrete sandwich structure, if some measures to prevent vibration on steel fiber sheet or under-surface of vault would enhance the resistance of structure.

Introduction

The layer structure is widely used in single building dug-type air defense projects in city, these types of structure have the advantage of less consumption of materials, strong resistance capacity on earthquake, and good effects on reduce vibration and sound, but also its have same problems on large buried deep, construction difficulties and the higher project cost [1] etc. Therefore, the optimize of the most commonly used type of layered structure in air defense works was a important issue to be solved on the basis of good protection capability, easy and economical construction type [2], etc. In this paper, a new structure type of the steel fiber reinforced concrete sheet sandwich structure was introduced, the impact factors of explosion resistance for these structures were studied, and the research results provide technical support for the application of these structures in air defense engineering

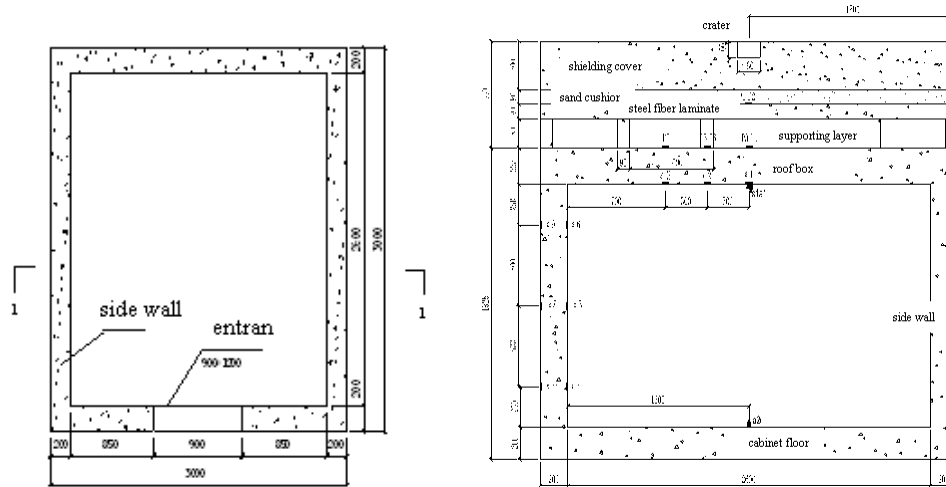
Organization of the Text

Testing Program

The main purposes of this experiment were to explore the effect of support beam in thin sandwich structure on protective performance.

In the testing, the thickness of camouflage layer, shielding cover, sand cushion, steel fiber reinforced concrete plate and enclosure roof are constant quantity, the spacing of a support beam and explosive weight can be change for a certain condition. The experiment model is composed by shelter plate, steel fiber concrete plate and roof envelope three sections, and poured with the scale of 1:4 to build test model, the plane size of the model is taken as 3m×3m, the model design as shown in Figure 1.

The camouflage layer is dry loess, and the thickness is 0.9m. The shielding cover and roof are the C50 reinforced concrete, and distribution layer is dry and loose sand. The production process of reinforced concrete is supporting the template, the preparation of steel skeleton, pouring and vibrating concrete, bedding cover and water conservation 28 days. Reinforce as shown in Table 1.



(a) The plan of enclosure box testing model (b) The profile of steel fiber reinforced concrete sandwich structure

Fig.1 The design of testing model

Table 1 Test Reinforcement

<i>components or parts</i>	<i>main reinforcement</i>	<i>stirrups or rachel bar</i>
shielding cover	HRB400 ϕ 10@190, double two-way	HPB235 ϕ 6, all nodes
steel fiber reinforced concrete sheet	HRB400 ϕ 16@105, single two-way	—
XGY arch board	HRB400 ϕ 14@115, double two-way	HPB235 ϕ 6, all nodes
XGY roof	HRB400 ϕ 14@115, double two-way	HPB235 ϕ 6, all nodes
ZGY roof	HRB400 ϕ 16@115, double two-way	HPB235 ϕ 6, all nodes
ZGY article support	HPB235 ϕ 6, always two	—
side wall of the box	HRB400 ϕ 12@230, double two-way	HPB235 ϕ 6, plum-type configuration
bottom of the box	HRB400 ϕ 12@230, double two-way	HPB235 ϕ 6, plum-type configuration

The explosive is TNT, and the weight is 9kg. The explosive was placed in the surface of pre-penetration hole, the bottom is parallel with the surface of the shelter plate, the center height of charge is 9.4cm above.

Test set up four pressure sensors measuring points (P1-P7), the stress wave spreading from shielding cover, coarse sand distribution layers, and air sandwich layer was tested on the surface of roof box. In the testing, the first testing point (P1, P2) was set on the center of steel fiber reinforced concrete structure, used to measure the maximum explosion pressure on fiber sheet sandwich structure.

Nine strain measuring points were arranged on the steel fiber sheet sandwich structure, the measuring points of ϵ_1 , ϵ_2 , ϵ_3 were arranged on the reinforcement of roof box envelope, used to measure the tensile strain of the roof. The first measuring point ϵ_1 was placed in the center of the roof, and the measuring points of ϵ_2 and ϵ_3 were placed in vertical with the spacing of 0.3m. Other measuring points of ϵ_4 to ϵ_9 were placed on side of the box with the spacing of 0.5m, used to measure pressure strain of the side wall.

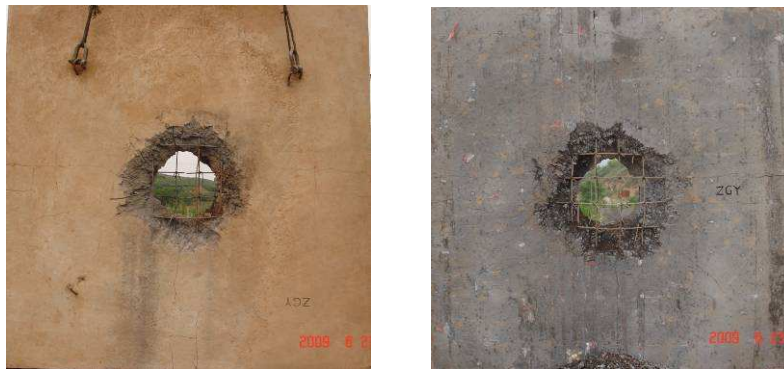
At the same times, the test arranged two acceleration sensor points a1, a2 and a relative displacement measuring point s1. The acceleration measuring point a1 and a2 were placed on the center of roof and bottom of the envelope box. The displacement measurement point s1 was placed on the center of the envelope box roof, used to measure the relative displacement of the roof envelope. Displacement sensor embedded in the box structure and fixed in the center of the steel on the floor.

The macro-damage of the structure

(1) The macro-damage of shielding cover

Shelter plate was penetrated, the diameter of positive crater was $108\text{cm} \times 100\text{cm}$, the depth of positive crater was 13cm , the through hole diameter was $55\text{cm} \times 51\text{cm}$. Many radial cracks appeared in steel fiber reinforced concrete plate with the center of crater, the maximum width of the crack reached 3mm , mostly $1\text{-}2\text{mm}$, there were four vertical and horizontal cracks extend to the entire board and the board through the side, in which two crack width of $2\text{-}3\text{mm}$, two cracks on width of $0.5\text{-}1\text{mm}$. The edge of the plate and damage the edge of the crater area appeared in two ring tensile cracks, the width of $0.1 \sim 3\text{mm}$, mostly 1mm , cracks approximately parallel with the plate edge, and crack intersected with radiation into the "turtle" shape. Cracks along the entire board, the board's size effect did not exist.

The under-surface of shelter plate was penetrated, and the crater diameter was $106\text{cm} \times 110\text{cm}$. Radial cracks distributed around the crater, the maximum crack width of 7mm , mostly 3mm , there were 2 to 3 cracks extend through the entire board, no circumferential cracks. Slabs were damaged phenomenon shown in Figure 2. After blasting a small amount of broken concrete slabs were piled on top of sand, sand pit center appears concave, diameter $90\text{cm} \times 80\text{cm}$, depth 13.6cm .



(a) The positive of clean-up shielding cover (b) The back of clean-up shielding cover

Fig.2 The damage of shielding cover

(2) The macro-damage of steel fiber plate

A damage area appeared in the center of sheet steel plate, damage range was $97\text{cm} \times 101\text{cm}$. The length direction of damage range was consistent with the support direction, and the width was limited by the support beam. Many circumferential tensile cracks appeared in sheet plate with the center of damage pit. The more damage near the hole, the more dense cracks were, there were no visibly longitudinal or transverse cracks.

The under-surface of sheet plate was damaged but not through back, the damage range were $122\text{cm} \times 100\text{cm}$, reinforced by the distribution network consisting of longitudinal bars protruding plate plane, protrusion height of 14cm , all of the concrete outside the steel fiber network were fall off, but the concrete within the network of steel fiber network did not fall off because the role of steel mesh, but the damage was obvious. The rest section of the board without any visible cracks, which as shown in Figure 3.

(3) The Damage of Support

Two concrete support beams near the explosive center damaged completely, and the reinforced barely in the air. Many cracks appear in the rest part of support beam, and four support beams far away from the center of the explosion was intact throughout, which as shown in Figure 4.



(a) Positive destruction (b) Back destruction
Fig.3 The damage situation of Steel fiber sheet plate



Fig.4 The damage of support beam

(4)The Damage of Enclosure Box

The surface of envelope box was intact, without any visible cracks. A micro-crack appeared in the under-surface of the envelope box with the north-south orientation, the width was less than 0.5mm. Some micro-cracks near the bottom of explosion appeared the phenomenon of broken. The east, south and west side walls of enclosure box internal were intact, without any visible cracks. A micro-crack appears in the north wall, the crack began to extend downward from the roof, about through the 1/4 wall height, the width less than 0.5mm.

Conclusions

In this paper, the model test of steel fiber reinforced concrete sandwich structure was carried out. From the experimental phenomena and the analysis of test results, the main conclusions were summarized as following:

- (1) For the dug-type civil air defense works, if it uses the steel fiber laminate sandwich structure, the protective layer can increase a resistance level at the uniform thickness.
- (2) The strength and thickness of steel fiber sheet material, height and spacing of support beam were the critical factors for the controlling of wave attenuation, and the determination of these parameters needs further study.
- (3) In order to avoid the damage and repeated loading on envelope roof, the deformation of steel fiber sheet plate and vault can not reach the upper surface of envelope.

References

- [1] WANG Nianqiao. *Calculation principle of protective structure*[M]. PLA Univ.of Sci.& Tech, Nanjing, 2002.
- [2] YAN Haichun, FANG Qin, CHEN Li. *Damage effect on top plate of layered structure under impact of falling mass from blast layer*[J]. *Journal of PLA University of Science and Technology (Natural Science Edition)*, 2008.9(1):52-56.

Failure-mode Based Coupled Shear Wall Optimization Design

Shan-suo Zheng^{1,a}, Qiang Xu^{1,b} and Zhi-qiang Li^{1,c}

¹School of Civil Engineering, Xi'an University of Architecture and Technology, Xi'an, Shanxi, China

^azhengshansuo@263.net, ^b538270385@163.com, ^czhiqiangli2023@163.com

Keywords: coupled shear wall; coupling beam; failure-mode; multi-objective optimization; damage grades

Abstract. Failure-mode based optimization is very effective at improving the performance of structure, therefore, a new optimal approach based on failure mode with the ability to limit the cost is proposed. Three different failure modes of the coupled wall are discussed, and then the objective function is setted up according to the expected failure mode and minimum cost. Finally, an example is cited to verify the method. It is concluded that the method can supply an effective way to reduce the cost of coupled shear wall, and the expected failure mode can be obtained.

Introduction

The earthquake has caused great economic losses and disaster to the humanity, which has drawn attraction of the worldwide seismic engineering to the existing ideas and methods for seismic design. Failure-mode based structural optimization design has been proposed in this paper, while the purpose of optimization is to achieve the best economic performance indicators in certain material and technical conditions.

Failure-mode based seismic design concept reflects the general design principles, making the structure of the system-level clear, emphasizing the designer to grasp the seismic performance of overall structure, simplifying the structural analysis and design, improving reliability of the design. Through the failure of the individual or specific components, the main structure greatly enhances the adaptability to ground motion and improves the defensive ability to unexpected catastrophic earthquakes.

Failure mode of coupled wall

The stiffness of the coupling beam decides to space stiffness of coupled shear wall, failure mechanism and ductility performance^[1-3]. According to the size of stiffness and strength of coupling beam, three different failure modes of the coupled wall structure may occur:

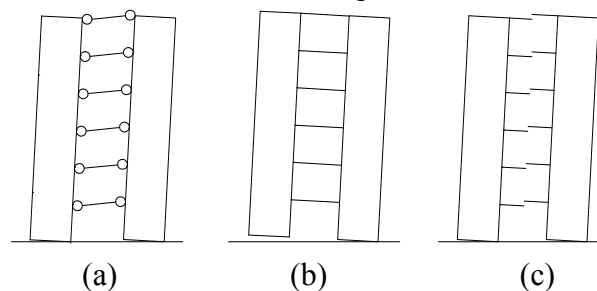


Fig. 1 Three different failure modes of the coupled wall

(1) When the coupling beams yield before the walls, the structure has sufficient ductility and plastic hinges have formed at the end of beams before the bottom of walls as shown in in Fig. 1 (a).

(2) When stiffness and flexural capacity of the coupling beam is high, the beams may not yield and plastic hinge appeared only at the bottom of the wall, just as shown in Fig. 1 (b). (3) When the shear failure of coupling beam appeared at first, the wall lost restraint of beams and formed a separate wall, as shown in Fig. 1 c).

Failure-mode based optimization design

Formulation of objective function. The design objective is to minimize the material cost and the structural failure modes. Therefore, the multi-objective function can be expressed as

$$\left. \begin{aligned} \min F(X) &= \alpha \left(\frac{C(x)}{C_0} \right) + \beta (D_S(x) + D_M(x) + D_L(x)) \\ (\alpha, \beta > 0, \alpha + \beta &= 1) \\ g_i(x) &\leq 0, i = 1, \dots, N_I \end{aligned} \right\} \quad (1)$$

Where, X is the design variable; D_S , D_M and D_L , respectively represent the damage of the structure under a small earthquake, a moderate earthquake and a large earthquake; $F(X)$ is the objective function; $C(x)$ and C_0 , respectively represent the overall cost of structure and cost of the initial value; α and β are the weight coefficient; $g_i(x)$ is deterministic constraints, including the given requirements by specification for seismic construction and so on ^[5]; N_I is the corresponding number of constraints.

$$C(x) = C_c(x) + C_s(x). \quad (2)$$

Where, C_c and C_s are the cost of concrete and steel, respectively.

$$\left. \begin{aligned} D_S(x) &= D_{SWs}(x) + D_{SBs}(x) + D_{Cs}(x) \\ D_{Cs} &< D_{SWs} < D_{SBs} \end{aligned} \right\} \quad (3)$$

Where, subscript SW , SB and C , respectively represents shear walls, coupling beams and columns; D_{SWs} , D_{SBs} and D_{Cs} , respectively, represents the maximum damage index of shear walls, coupling beams and columns under a small earthquake.

$$\left. \begin{aligned} D_M(x) &= D_{SWm}(x) + D_{SBm}(x) + D_{Cm}(x) \\ D_{Cm} &< D_{SWm} < D_{SBm} \end{aligned} \right\} \quad (4)$$

Where, D_{SWm} , D_{SBm} and D_{Cm} , respectively, represents the maximum damage index of shear walls, coupling beams and columns under a moderate earthquake.

$$\left. \begin{aligned} D_L(x) &= D_{Cl}(x) + D_{SWl}(x) + D_{SBl}(x) \\ D_{Cl} &< D_{SWl} \leq D_{SBl} \end{aligned} \right\} \quad (5)$$

Where, D_{SWl} , D_{SBl} and D_{Cl} represent the maximum damage index of shear walls, coupling beams and columns under a large earthquake, respectively.

Failure-mode based structural optimization design example

As shown in Fig. 2 and Fig. 3, a ten-story and three-bay steel reinforced concrete framework-core tube structure is considered. The design variables are 20, including 10 height variables of coupling beam and ten width variables of shear-wall. The beam and column section dimensions of the frame part and steel consumption are assumed unchanged.

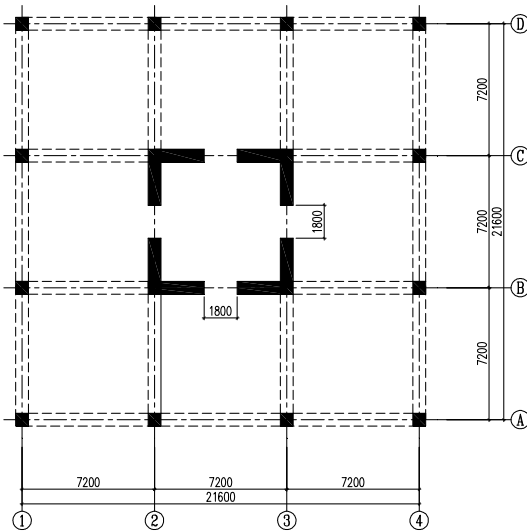


Fig. 2 Plan of structure

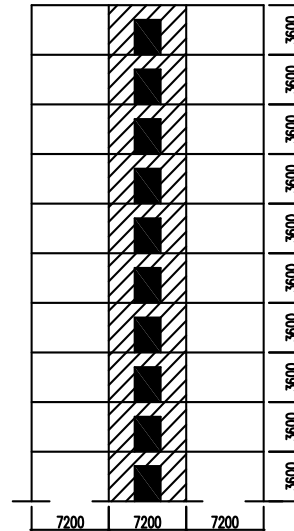


Fig. 3 Framework -core tube structure

Initial data of framework-core tube structure members were shown in table 1, and the selected cross-section of concrete by optimization were shown in table 2.

Table 1 Initial data of framework -core tube structure member

Floor	Cross-section of column /mm	Column shaped-steel cross-section /mm	Cross-section of beam /mm	Beam shaped-steel cross-section /mm	Width of shear-wall /mm	Height of coupling beam /mm
1~3	600×600	W14×455	700×400	W36×210	250	700
4~7	550×550	W14×370	700×350	W36×182	250	700
8~10	500×500	W14×311	700×300	W30×148	250	700

Table 2 The selected cross-section of concrete by optimization

Floor	1~3	4~7	8~10
The width of shear-wall /mm	300	250	200
The height of coupling beam /mm	500	450	400

Because this optimization is only for double limb wall, do not consider frame part, and the cost of coupled shear walls have a small proportion in the whole cost, so the weight coefficient of the cost of can be appropriately taken a smaller value ($\alpha=0.3$). In table 3, negative represent only operation results, does not mean that no damage or injury component value is negative.

Table 3 The contrast of cost and damage before and after optimization ($\alpha=0.3, \beta=0.7$)

Design proposal	Cost	Total damage	Damage		
			Small seisms	Middle seisms	Large seisms
Optimum design	0.33	-1.401	0.084	-0.526	-0.959
Normal design	0.30	-0.650	0.072	0.083	-0.805

Table 4 Structure period and seismic action under large seismic

Design proposal	The first 3 period of structure /s			Total seismic action /kN
Optimum design	1.21	0.43	0.28	3864.2
Normal design	0.83	0.29	0.17	5302.6

Considering the structure stiffness degradation under large seismic after optimization, natural vibration period of the structure is longer, absorbing less seismic action, and the results could be seen in table 4.

The damage of component is analyzed by finite element software in Fig. 4. Under moderate seismic, the coupling beam damages firstly, and the damage value reaches 1.0. Shear wall damage value is 0.53. Column damage value is 0.14, which can be thought do not happen damage, so as to achieve the "The structure don't damage in middle seismic ". Under large seismic in Fig. 5, both the damage value of coupling beam and Shear wall reach 1.0 while column damage value is 0.54. This means "The structure don't fall in large seismic ".

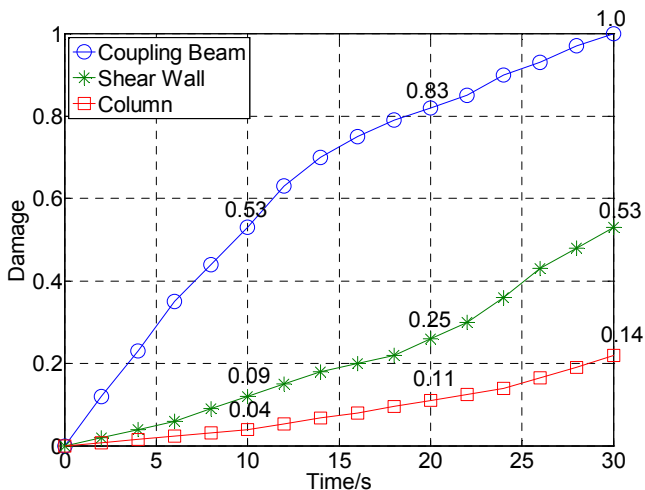


Fig. 4 Structure damage under moderate seismic

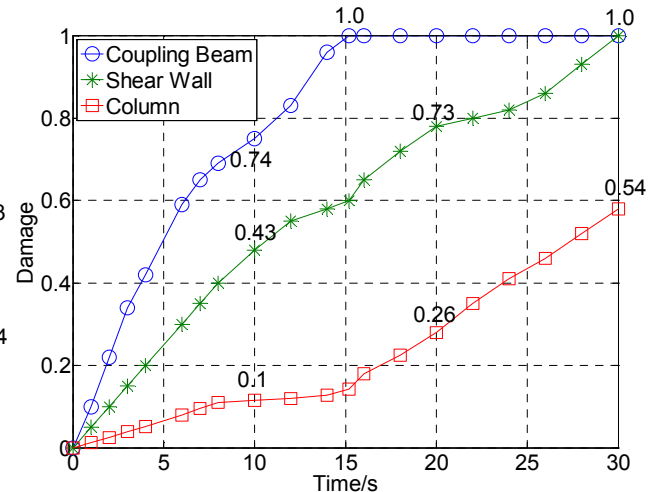


Fig. 5 Structure damage under large seismic

Conclusions

The most important conclusion that can be drawn from the study described in this paper is that, through changing the stiffness of the structure characteristics and dissipating the energy of earthquake, the proposed method can supply an effective way to reduce the cost of coupled shear wall; meanwhile, the expected failure mode can be obtained.

Acknowledgments

This project is sponsored by National Natural Science Foundation of China (Grant No. 90815005, 50978218, 51108376), Research Fund for the Doctoral Program of Higher Education of China (Grant No. 20106120110003) and the Office Educational of Shan'xi Province in China (Grant No. 2010JK633)

References

- [1] Meng Guo, Qian-feng Yao and Pei Liu: Journal of Huazhong University of Science and Technology, Vol. 37(2009), p. 102-105. (In Chinese)
- [2] Dong-sheng Huang, Wen-rang Cheng and Fei Peng: Vol. 26(2005), p. 51-56. (In Chinese)
- [3] Clarence-Cormier, J., David, R. and Peter, M: Journal of Prosthodontics, Vol. 10(2001), p. 26-36. (In Chinese)
- [4] Gang Li, Geng-dong Cheng: Journal of Dalian University of Technology, Vol. 40(2000), p. 483-488. (In Chinese)
- [5] Earthquake Resistant Design Code(GB50011 —2010). Railway Publishing House of China, 2003. (In Chinese)

Experimental Tests on Composite Beam with Various Slab Systems

Anis Saggaff^{1,a}, Mahmood Md Tahir^{2,b}, Norwati bte Jamaluddin^{3,c},
Shek Poi-Ngian^{2,d}, Tan Cher-Siang^{2,e}

¹Civil Engineering Department, Faculty of Engineering, Sriwijaya University, Indonesia

²Steel Technology Centre, Universiti Teknologi Malaysia, 81310 UTM Johor Bahru, Malaysia

³Department of Civil Engineering, Universiti Tun Hussin Onn Malaysia, 86400 Batu Pahat, Malaysia

^aanissaggaf@yahoo.com, ^bmahmoodtahir@utm.my, ^cnorwati@uthm.edu.my
^dshekpoingian@utm.my, ^etcsiang@utm.my

Keywords: composite beam, metal decking floor, pre-cast floor, solid floor

Abstract. This paper presents the structural behaviour of composite beams with various floor systems tested in full-scale arrangement. Six full-scale specimens with staggered and non-staggered arrangement of studs on the composite beams were tested until failure. The moment capacities obtained from the experiment are compared with the theoretical values established from BS 5950 and Eurocode 4. The experimental results showed good agreement with theoretical predictions while no significant influences were found between staggered and non-staggered arrangement of studs.

Introduction

The use of composite beam in buildings has known to be more economical against bare steel beams, which the composite action between steel and concrete has results in significant savings in steel weight and reduce the beam depth [1]. The advantages of composite beam contributed to the dominance of composite beam in the commercial building in steel construction industry. To date, the advantages of composite beam have been further extended with the use of pre-cast floor and metal decking floor, to minimized or eliminate the use of formwork. The performance of such floor systems depends on the interaction of the concrete slab and the steel section connected together by shear connectors. This interaction depends on the strength of the studs, the concrete strength, and the continuity preserved along the horizontal interface so that the concrete slab and the steel section respond as one unit. This paper presents the experimental investigation on composite beam with three types of slab system namely solid slab (in-situ slab), pre-cast slab (half-slab system) and profiled metal decking slab. The shear studs are 19 mm in diameter and were positioned either as staggered or non-staggered arrangement. A total of 6 full-scale composite beams were tested until failure and the performance of each floor system will be discussed based on the maximum moments and deflections.

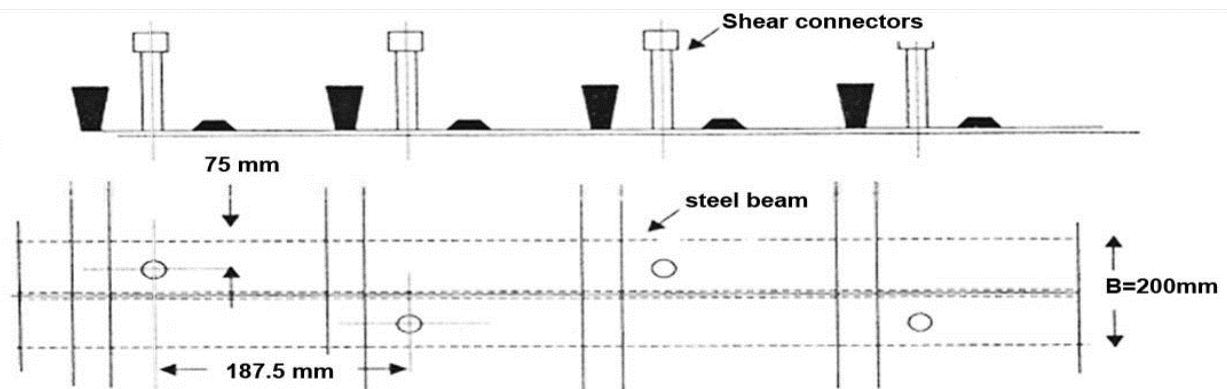
Experimental Programme

Mechanical Properties of the Materials. The concrete grade of C30 was used in the slab system throughout the specimens and 9 pieces of cubes were tested for compression to verify the concrete strength [2]. The cube tests have shown an average value of 36.78 N/mm² which has achieved the minimum requirement of 30 N/mm². A total of 12 coupon specimens were cut from the web and the flange of the steel section to obtain the mean values of yield strength (f_y), ultimate strength (f_u) and the elastic modulus (E) [3]. From the tensile test, the mean values for $f_y = 324$ N/mm²; $f_u = 392$ N/mm²; and $E = 202$ kN/mm². The values obtained from the material tests are then used to calculate the moment capacities of the composite beams in accordance to BS 5950 [4] and Eurocode 4 [5].

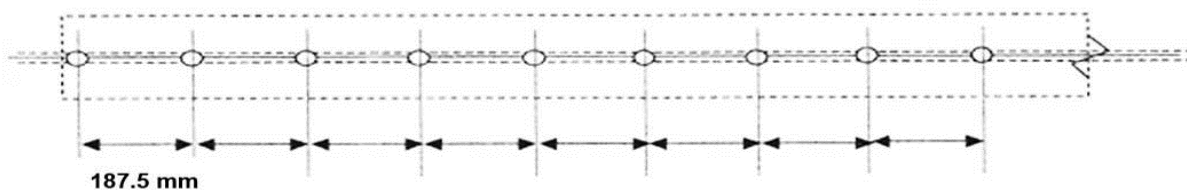
Full-Scale Bending Test. 6 full-scale composite beams consist of 3 different types of slab system and 2 types of stud arrangement were tested until failure. The slab systems used are solid slab, pre-cast slab and steel decking slab while the studs are positioned either in staggered or non-staggered arrangement. The detail dimensions of each specimen are summarized in Table 1 and Fig. 1. The arrangement of the test rig and measuring equipments are shown in Fig. 2. The DARTEC hydraulic actuator was used to exert 2 point loads on the specimen at a distance of 1 m from the mid span of the beam. This distance is to represent an area for a pure bending moment developed in the beam. The LVDTs were placed at the mid span of the beam and also the loading point. Strain gauges are also installed along the beam depth as shown in Fig. 2. An increment of 10 kN is applied to the composite beam so that a uniform data and gradual failure of the specimen can be monitored. The specimen is further loaded until substantial deflection of the beam can be observed. At this point, the loading sequence is controlled by the increment of deflection as a small increment of load has resulted to substantial increase in the deflection. The failure condition is considered to have reached when an abrupt or significantly large reduction in the applied load.

Table 1 Details of specimens full-scale bending tests

Model Name	Steel Beam Size	Slab System	Slab Dimension	Stud Arrangement
CB SSD	400x200x65.4 kg/m Length = 6 m	Steel Decking	Slab thickness = 125 mm Width of Slab = 1.5 m Length of Slab = 6 m	Staggered at 187.5 mm
CB SSS		Solid Slab		
CB SHS		Pre-cast Slab		
CB PSD		Steel Decking	Parallel along the beam at 187.5 mm	
CB PSS		Solid Slab		
CB PHS		Pre-cast Slab		



(a) : One stud on each staggered arrangement



(b) : Arrangement of studs in parallel to the central beam

Fig. 1 Arrangement of shear studs in staggered and parallel to the beam

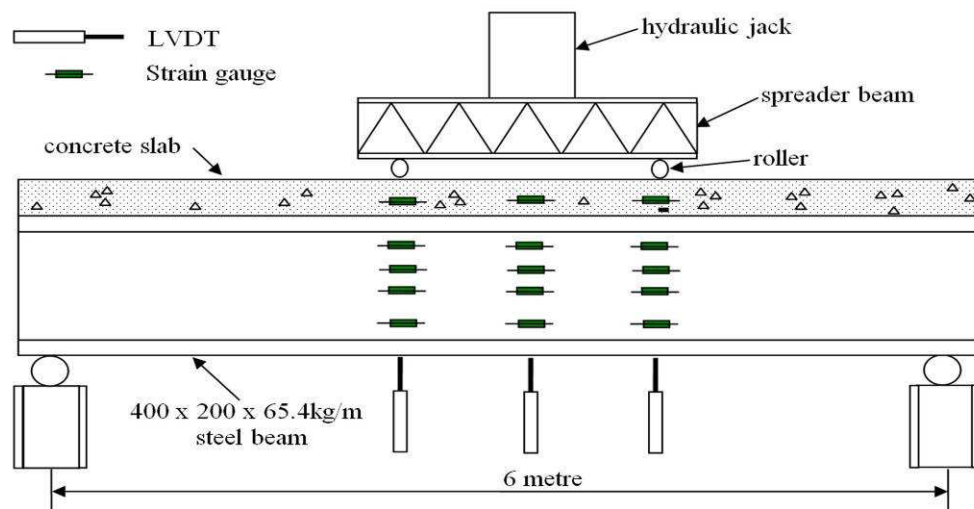


Fig. 2 Test arrangement

Results and Discussion

The test results were presented based on the ultimate moment capacity, initial stiffness and the maximum deflection, which derived from the moment-deflection curves as shown in Fig. 3. The test results were summarized in Table 2 and the ultimate moment capacities were compared to the theoretical predictions, which calculated in accordance to BS 5950: Part 1 Section 3.1 [4] and Eurocode 4: Part 1.1 [5]. The comparison shows good agreement between experimental results and theoretical predictions where the ratios are in the range of 1.05 to 1.11. The maximum deflection at mid span of the beam corresponding to the ultimate moment ($\delta_{\max, \text{exp}}$) and the initial stiffness of the beam at linear elastic region ($S_{\text{ini, exp}}$) obtained from the moment-deflection curves are also recorded in Table 2, and the values are in the range of 40.0 mm to 125.7 mm for deflections and 30.6 kNm/mm to 48.9 kNm/mm for initial stiffness.

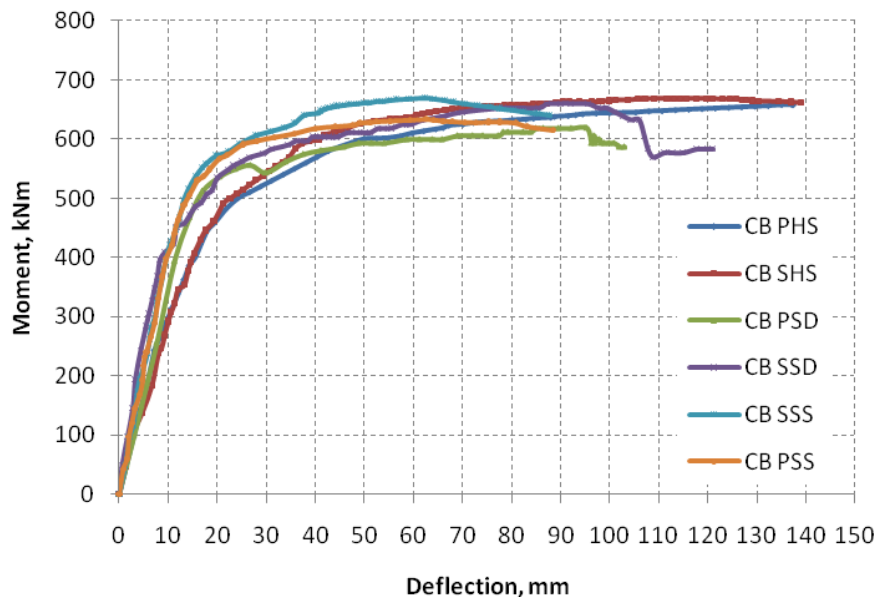


Fig. 3 Moment-deflection curves for tested composite beams

Table 2 Comparison of experimental results and theoretical predictions

Model Name	$M_{u,theo}$ (kNm)	$M_{u,exp}$ (kNm)	$M_{u,theo} / M_{u,exp}$	$\delta_{max,exp}$ (mm)	$S_{ini,exp}$ (kNm/mm)
CB SSD	587.6	650.3	1.11	93.9	48.9
CB SSS	603.0	670.1	1.11	40.0	43.8
CB SHS	630.5	677.3	1.07	122.8	32.4
CB PSD	575.2	608.8	1.06	85.2	36.0
CB PSS	601.5	633.9	1.05	45.9	41.7
CB PHS	601.8	638.3	1.06	125.7	30.6

By observing the failure modes of the specimens, shear studs are dislodged from its position on the specimen and showed significant deformation, which demonstrate the characteristics of partial shear connection between steel and concrete. Slippage between steel and concrete was recorded at about 10 mm that did not contribute significantly to the failure of the composite beam. Composite beams with staggered studs arrangement are slightly higher in both moment capacity and initial stiffness as compared to non-staggered studs. Both theoretical and experimental results showed the performance of composite beams with metal steel decking are low in moment capacity as compared to solid slab and precast slab system, while the composite beam with precast slab system showed largest values in the maximum deflection as compared to the other 2 slab system.

Conclusions

The concluding remarks from the experimental results of the composite beam with 3 different slab systems and stud arrangement are listed as follows:-

- 1) BS 5950: Part 1 Section 3.1 [4] and Eurocode 4: Part 1.1 [5] are suitable to be used to predict the moment capacity of composite beams for the tested slab systems and stud arrangement.
- 2) No significant difference in terms of moment capacity was found between staggered and non-staggered stud arrangement in a composite beam.
- 3) Composite beam with precast slab systems showed higher capacity in bending and high ductility, but relatively low in initial stiffness as compared to solid slab system and metal decking system.

Acknowledgements

The authors would like to acknowledge special thanks and gratitude to MOHE and UTM for providing the funding and facilities to this project under Vot Q.J13000.7122.00J18.

References

- [1] R.M. Lawson. SCI P055 Design of Composite Slabs and Beams with Steel Decking. The Steel Construction Institute, Berkshire, UK. (1993)
- [2] British Standards Institution, BS 8110: Structural use of concrete. Part 1: Code of practice for design and construction. (1997)
- [3] British Standards Institution BS EN 10002-1. Tensile Testing of Metallic Material, Part 1. London: British Standards Institution. (2001).
- [4] British Standard Institute, BS 5950 Structural use of steelwork in building, Part 3: Design in composite construction, Section 3.1 Code of practice for design of simple and continuous composite beams. (1990).
- [5] Eurocode 4: Design of composites steel and concrete structures Part 1.1 General rules for buildings. (1994).
- [6] N. Jamaluddin, Performance of composite beam with various slab system, M.Eng Thesis, Universiti Teknologi Malaysia (2002).

Experiment on a Concrete Filled Steel Tubular Arch with Corrugated Steel Webs Subjected to Spatial Loading

Jing Gao^{1, a}, Jia-zhan Su^{2, b} and Bao-chun Chen^{3, c}

¹ Department of Civil Engineering, Xiamen University, Xiamen, China

² Department of Civil and Structural Engineering, Hongkong Polytechnic University, Hongkong,

³ College of Civil Engineering, Fuzhou University, Fuzhou, China

^agaojing@xmu.edu.cn, ^b309065267@qq.com, ^cbaochunchen@fzu.edu.cn

Keywords: Arch, concrete filled steel tubular arch, corrugated steel web, spatial loading, test.

Abstract. To investigate the spatial performance of concrete filled steel tubular arch with corrugated steel webs, a static loading test has been conducted on an arch with a clear span of 6m subjected to in-plane and out-of-plane loading simultaneously. The structural behaviors such as load-displacement relation, ductility, distribution of strains in tubes and corrugated webs, were explored. Based on the results, it is demonstrated that the lateral deformation is the critical factor for the ultimate load-carrying capacity of the arch. In the whole process of test for the tubular arch, material non-linearity is dominant and geometrical non-linearity is subordinate. It could be concluded that the CFST-CSW arch shows good structural behavior and may be applicable in practice.

Introduction

Concrete filled steel tubular structure with corrugated steel webs (CFST-CSW) is a structure which uses both the advantages of the compressive strength of CFST and the shear strength of CSW. The circular CFST members act as key load bearing components and the CSWs connect the CFST members together. It is expected that CFST-CSW structures have higher resistance against axial compression, bending moment and shear force. It not only provides a good choice for girder which is dominant in bending and shear[1], but also for columns and arches which are dominantly subjected to compression[2, 3]. In order to study the performance of CFST-CSW system, a trial model based on the Wanxian Yangtze River Bridge, which has the longest span of 420m in concrete arch bridges in the world, was designed replacing the concrete arch by a CFST-CSW system [4]. Through this trial design, it became clear that CFST-CSW structure provides an optimized construction method, reduces the self-weight (dead load) and the requirement for substructures. These indicate that, apart from saving construction time and cost, the CFST-CSW structure has the potential to improve the seismic resistance and to allow the construction of longer span concrete arch bridges. However, arches that are subjected to in-plane loading may suddenly deflect laterally out of their plane of loading, especially in large span arches. In order to further investigate the out-of-plane behavior of CFST-CSW arch, a test on the arch subjected to both in-plane and out-of-plane load was conducted. Test results and the analysis of the arch behavior are presented in the paper.

Test Preparation

Test Specimen. The detail of the tested arch is shown in detail in Fig. 1. The tubular chord is 75mm in diameter with a 2mm thick wall. The web, 2mm thick, was welded continuously to the tubular chords from its top and bottom sides along the arch axis to combine them into a cross-section. As for the corrugated steel webs, the main geometrical parameters are shown in Fig. 1(c). Between the two panels, steel tubes with 40mm in diameter and 2mm in thickness were utilized as transverse bracings, welded at a distance of 195mm in both top and bottom chords to build a four-tube CFST-CSW arch.

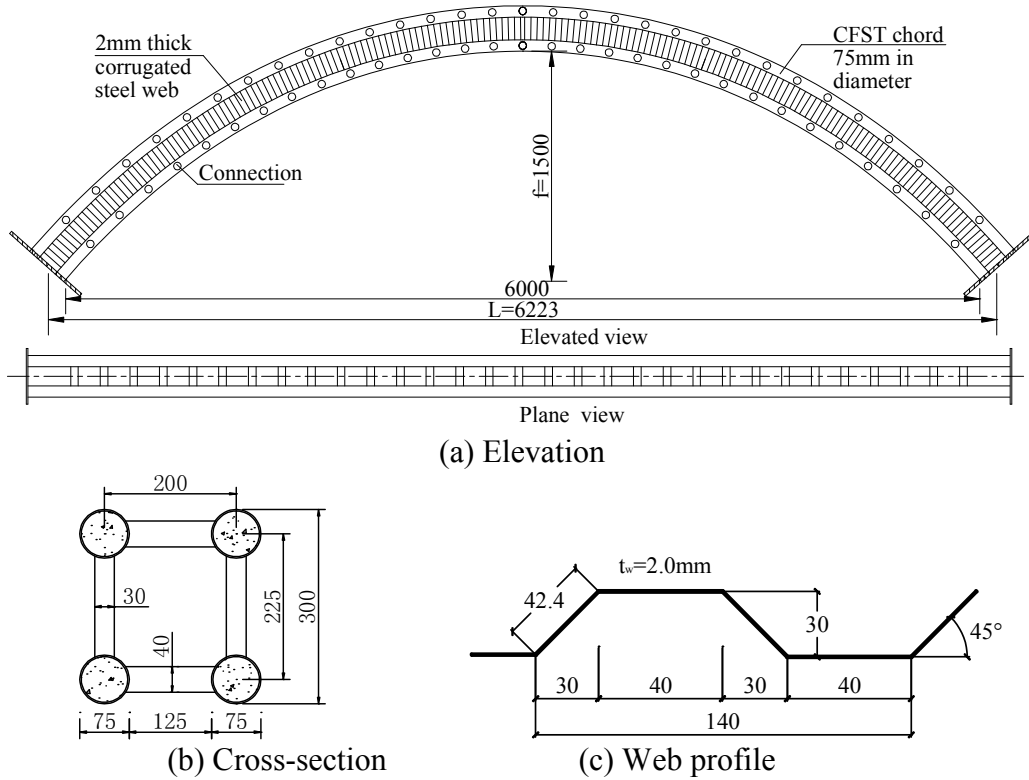


Fig. 1 : Specimen geometry (unit: mm)

Test Set-up. The arches were mounted on two stiffened steel pedestals, which were fixed at both ends. Supports were made up of triangular steel plates placed on a reinforced concrete block anchored to the ground. The supports restricted the horizontal displacement and rotation of the arch spring, thus simulating the fixed support conditions. Fig. 2 shows the configuration of the test set-up.

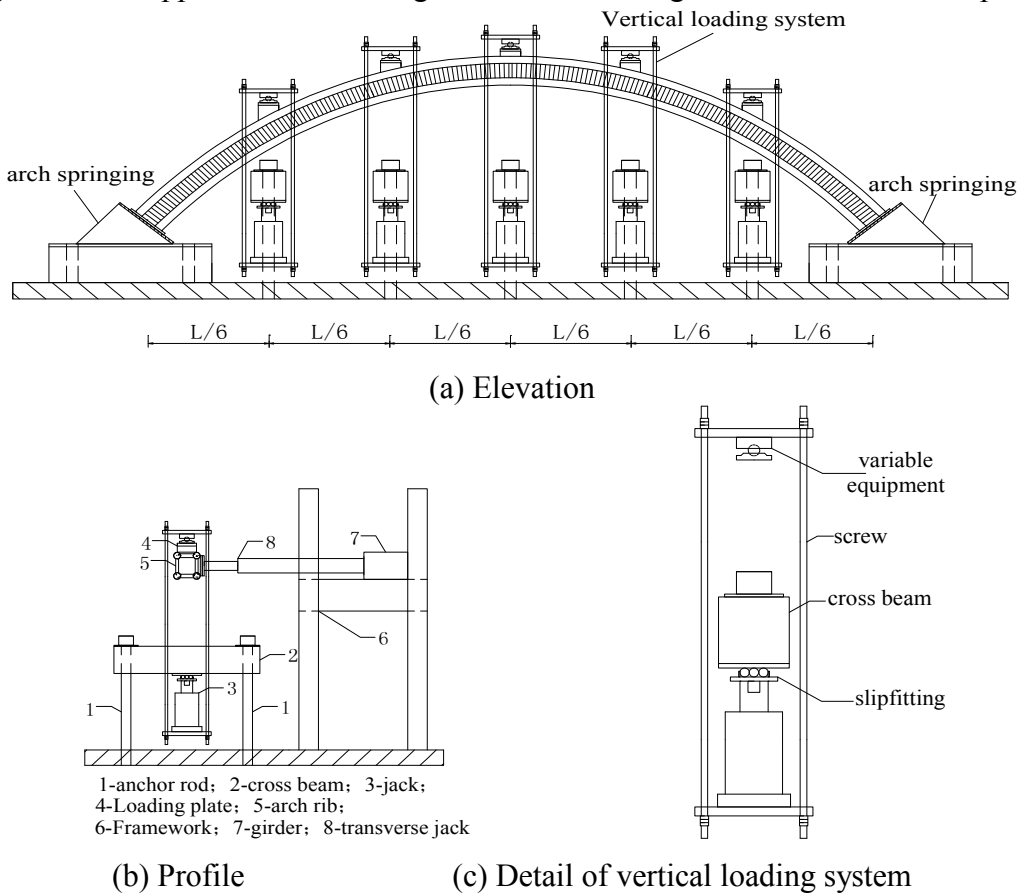


Fig. 2: Test set-up

Test Results

Test Procedure. During the test, the vertical load was applied simultaneously with the lateral load at the arch crown. The magnitude of the lateral load was 10% of the vertical load. The load step was designed before the test according to the preliminary analysis of the arch. In the first 20 steps, the loading and strain gauge data were recorded for every 10kN load increments, and the following steps were 5kN. The loading times were also collected. In each load step, the loading was kept constant for at least three minutes to obtain steady data.

It is demonstrated from the test that the vertical deflection and the lateral displacement were symmetrical, and the maximum value was located at the arch crown. With the increase of the load, the displacement developed rapidly. When the vertical load reached 302.5kN, the screw at 2L/3 and 5L/6 came in contact with the cross beam, which lead to the interruption of the test. It is shown from the load-displacement relationship that the stiffness of the arch nearly reached zero at this time, which was deduced from the slope of the load-displacement curve, and the maximum vertical deflection reached 34.2mm, and the maximum lateral displacement reached 48.2mm. Therefore, the ultimate load of the arch was defined as 302.5kN.

Displacement. Fig. 3 shows displacement distribution along the arch at specified loading step. It is shown that from the beginning, the lateral displacement is quite larger than vertical deflection although the vertical load is 10 times of the lateral load. It is obvious that the in-plane stiffness of the arch is quite larger than the out-of-plane stiffness. That is to say, the lateral load will have great effect on the load-carrying capacity of the arch.

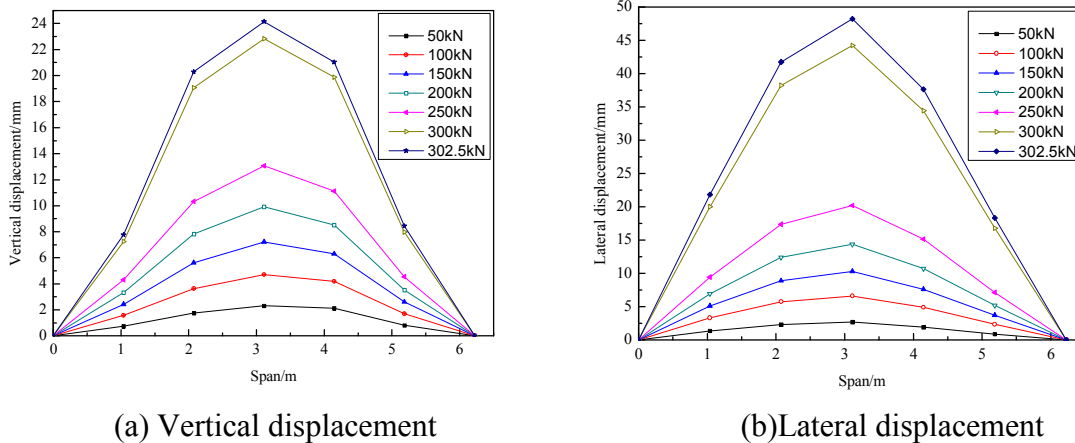


Fig. 3: Vertical and lateral displacement along the arch span

Relationship between load and displacement. The load – displacement relationship of the arch is shown in Fig. 4 and 5. It can be noted that the slope of the curve in Fig. 4 is larger than that in Fig. 5, which means that the in-plane stiffness of the arch is quite large, and the geometric nonlinearity has little effect on the load carrying capacity. Because the interaction between out-of-plane and in-plane displacement is not obvious at the beginning, the lateral displacement has little effect on the vertical displacement. When the lateral load increased to some extent, the increment of the in-plane displacement is grew rapidly. When the vertically applied load reached 260kN, there was an obvious bend in the curve, then the displacement increased quite rapidly. Therefore, the failure mode of the test arch was controlled by the lateral deformation, which is similar with the pattern of arch with singular CFST rib.

It can be noted from the Fig. 5 and 6, that before the applied load reached 170kN, the lateral displacement at each section increased linearly, with the midspan section increasing the most. After 250kN, the load vs. vertical deflection went into nonlinear development with bigger increment. At 302.5kN, the curve was horizontal, which means that the arch has reached the ultimate load. As for the lateral displacement at midspan, it entered into nonlinear development when the applied load reached 250kN. This validates the fact that under the applied load, the lateral displacement will develop nonlinearly earlier than the vertical deflection.

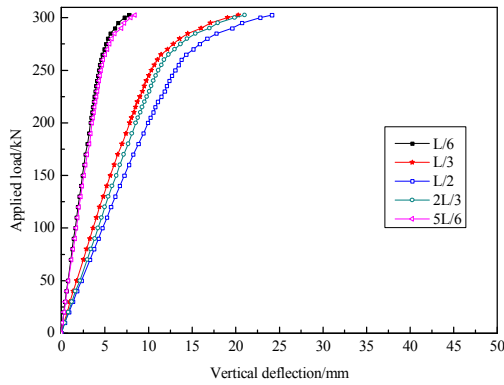


Fig.4: Load-vertical displacement curve

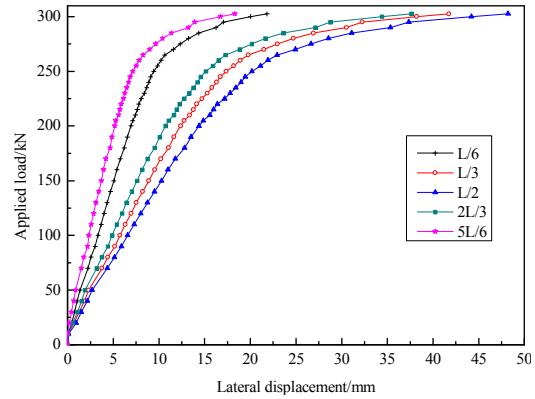


Fig.5: Load-lateral displacement curve

Strain distribution along the top and bottom chord. Fig. 6 shows the distribution of longitudinal strain of top chord and bottom chord at each section, in which the positive value denotes tension and negative value denotes compression, and the dotted line denotes the yield strain of the steel. It can be noted that distribution of the longitudinal strain at both bottom chord and top chord is toothed. Under the bending and compression, the strain distribution of the arch is symmetrical apart from the springing section. However, at the right side of the arch, after the strain reached yield strain, the distribution of the strain is not symmetrical anymore, even the strain at the springing is reversed from compression to tension. When the applied load reached 250kN, longitudinal strain at most of the section has reached yield strain in Fig. 6(a), while only the strain reached yield point at $L/12$ and $11L/12$ in Fig. 6(b) and Fig. 7. It can be noted that during the test, the arch is mainly in compression, though at some points, the tension strain appeared, but of very small magnitude and in elastic phase.

Strain distribution along the width of the section. The relationship between the longitudinal strain and applied load is plotted in Fig. 8. It is evident that the curves experienced linear and nonlinear phase nearly in the same way. However, in Fig. 8(b), the curves present reversed development when the applied load is larger than 250kN, which means that the direction of the bending moment changed at this time.

Fig. 9 and 10 show the development of strain along the width of the section during the test. Because the applied lateral load was located at the arch crown, the strains at segments between $L/12$ and $2L/3$ in Fig. 10(b), $5L/12$ and $7L/12$ in Fig. 9(a) are in tension and symmetrically distributed along the arch. It is evident that most of the section are in compression, and at the late stage, the steel chord tube yields at most sections. As a result, geometric nonlinearity has little effect on the mechanical behavior of CFST-CSW arch, which is quite different compared to that of CFST arch with singular tube[5].

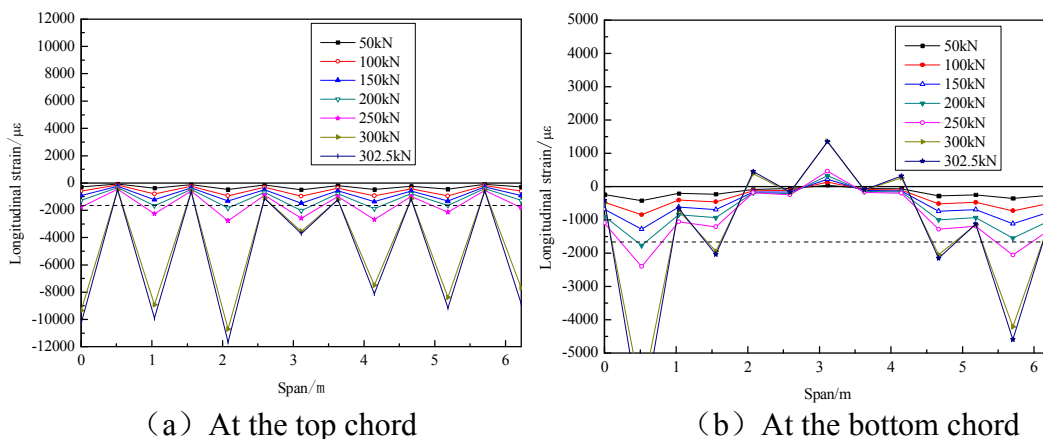
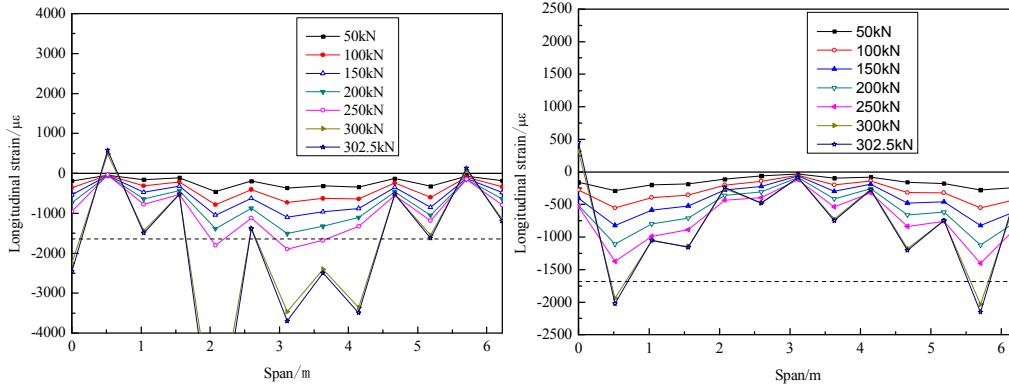


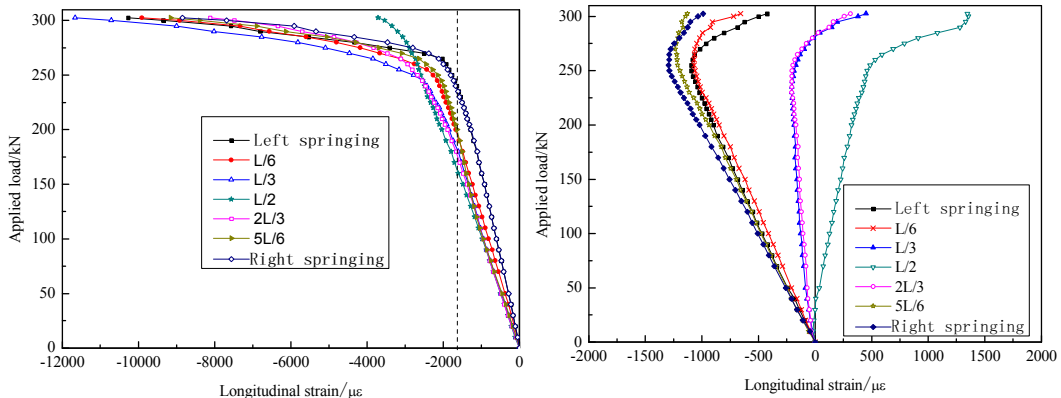
Fig. 6: Distribution of longitudinal strain at left side along the arch



(a) At the top chord

(b) At the bottom chord

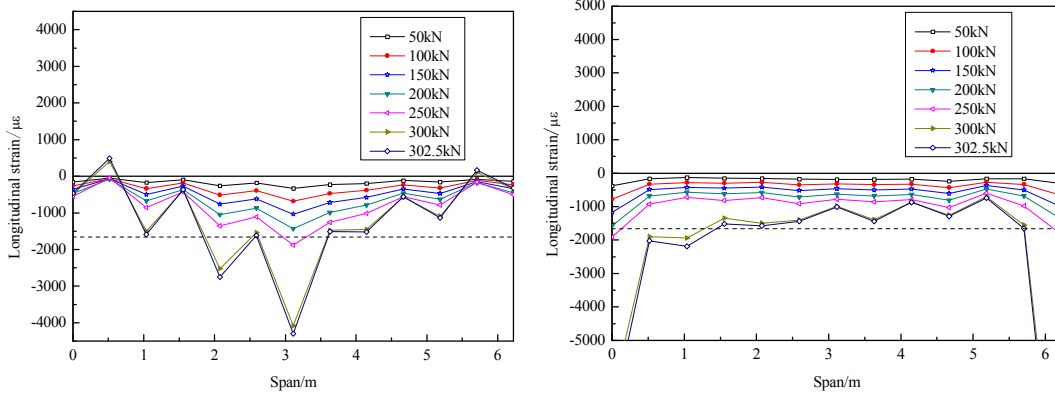
Fig. 7: Distribution of longitudinal strain at right side along the arch



(a) At the top chord

(b) At the bottom chord

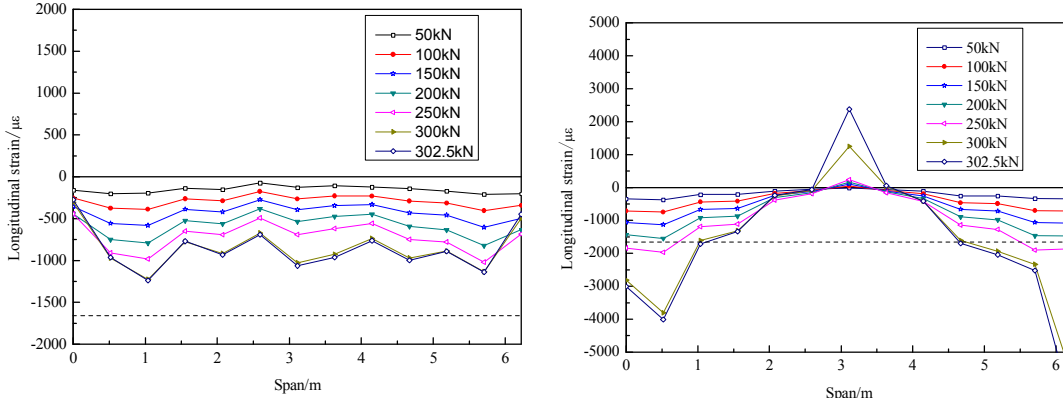
Fig. 8: Relationship between applied load and strain at left side of the section



(a) Near to the loading side

(b) Far from the loading side

Fig. 9: Longitudinal strains along the arch at top chord



(a) Near to the loading side

(b) Far from the loading side

Fig. 10: Longitudinal strains along the arch at bottom chord

Summary and Conclusions

From the results presented, the following conclusions can be drawn:

(1) During the test, although the in-plane load is 10 times of the lateral load, the lateral displacement of the arch far outweighs the vertical deflection, which demonstrates that the lateral stiffness of the arch is smaller than the in-plane stiffness. A small lateral load will lead to large lateral deformation.

(2) The strain distribution along the arch is of toothing shape, which is similar to the CFST arch with singular tube subject to spatial loading.

(3) Test results indicate that corrugated steel web has larger shear stiffness and capacity to resist local buckling. During the test, no obvious local buckling appeared. Therefore, the CFST members and corrugated steel web can work well together and make use of their advantages.

(4) In the test of CFST arch with singular tube subjected to spatial loading in literature[5], the displacement of the arch developed nonlinearly from the beginning. However, in the test reported in this paper, the tested displacement curves show obvious linear stage and nonlinear stage, and have distinct turning point. It is indicated that under the spatial load, geometric nonlinearity has less effect on the behavior of CFST-CSW arch than on a CFST arch with singular tube.

Acknowledgements

This work was financially supported by the Natural Science Foundation of Fujian Province of China (No. 2011J05138) .

Literature References

- [1] B.C. Chen & J. Gao : Journal of Building Structures Vol. 29(1) (2008),p. 75-82.
- [2] B.C. Chen & J. Gao : Journal of Building Structures Vol. 30(2)(2009), p.55-63.
- [3] J. Gao &B.C. Chen: Engineering Mechanics Vol. 27(3) (2010), p. 91-100.
- [4] B.C. Chen, Y.Y.Wang & Q.W. Huang : World Bridges (4)(2006), p.10-14.
- [5] B.C. Chen, J.G. Wei & J.Y. Lin: Engineering Mechanics Vol. 23(5)(2006), p.99-106.

Research on Steel Beam-column Joints of Concrete Filled Steel Tube

Li Ming^{1,a}, Liu Yong^{1,b}, Sun Zhezhe^{1,c} Liu Yongfang^{1,b} and and Du Jingfeng^{2,b}

¹Shenyang Jianzhu University, Shenyang, China. 110168

²Liaoning Zhujing Room Limited Company

^acemli@sjzu.edu.cn, ^bly325788781@126.com, ^chuoerzheman@126.com

Key words: CFST, steel beam-column joint (SBCJ), outer annular-stiffener type

Abstract: With the increasingly sophisticated theory of concrete filled steel tube (CFST) and its' wide application, how to make the CFST steel beam-column joints (SBCJS) becomes one of the key problems in research. According to the relevant references in and abroad, types and research done on CFST SBCJ are introduced, including outer annular-stiffener type, Inner stiffening ring type connection with anchorages type, beam integral breakthrough type etc. Finally the key problems need to be further studied are promoted.

Introduction

CFST is a component in structure that is made of steel tube filled with concrete. For the interaction of the two materials in the process of bearing, it has a series of advantages over concrete and steel structure. During the process of bearing, the steel tube will constraint the core concrete, which will greatly improve the strength plasticity and toughness of concrete, At the same time, the existence of concrete can inhibit or avoid the buckling deformation of steel tube. So it has good seismic performance, and favored by civil engineers [1-2]. But like other composite structures, the structure of SBCJ CFST are also very complex, because they are not like the reinforced concrete connection that can directly realize the transmission of tension, and also can't adopt the steel connection method. So a lot of study on them is done and a series of achievements are obtained, which will be overviewed in this paper.

Types of CFST SBCJS

CFST SBCJ is composed of the core area of the joint, the end part of the connected beam and column, It is used to transfer the loading on beam and slab to column [3]. In order to make this connection strong enough to transfer the internal forces, including shear and bending moment, and satisfy the requirement of seismic performance, different types of it are put forward.

Common Connection Types.

Outer Annular-Stiffener Type. It is one of the node types studied most maturely at present and recommended by 《Specification for design and construction of concrete-filled steel tubular structures》 (CECS28:90). This type of SBCJ is realized through two annular-stiffener rings which are welded on the column. These two rings are located at the upper and lower flange of the beam respectively and connected with the flange by weld. Then vertical plate is set between the two rings. One end of it is welded on the column and the other end is used to connect with the web of the beam by weld or bolts [4]. This connection type is reliable for force transmission and convenient in construction. Also it has good seismic performance because the ring is not only good for force

transmission between beam flange and column, but also can reduce the deformation of the column wall, which make the principle of strong column weak beam and stronger node easily achieved. But this connection type will spend more steel, and the adaptability and flexibility of it is limited in construction. So it is only adopted for small diameter column and beam connection.

Inner Stiffening Ring Type. It is realized by two stiffening rings welded in the column. They are located at the upper and lower flange of the beam. This connection type can satisfy the requirement of stiffness with less steel than the above one, but it is difficult to complete the alignment of the flange and the inner ring in height, and there will be a large welding area in the steel tube after welding which will make it easy to cracked under dynamic loads [5]. At the same time, it is difficult to deal with the condition that two beams connected with column are of different elevation while in the same direction. This type of SBCJ is generally applied to the case that the column diameter is greater than 1m.

Connection with anchorages type. It is realized by two T-shaped anchorages welded in the steel tube. These two plates were located at the upper and lower flange of the beam, which can be used to transmit the tension from the flanges of the beam to the joint. The T-shaped anchorage is made of two steel plates vertical to each other. The tensile force of the beam flange will transmit to the steel tube by welding, and then pass to the anchorage through the groove weld; finally the anchorage will extrude the core concrete. This kind of force transmission method can effectively transmit tension from beam flanges to the concrete of column, which will reduce the deformation of steel tube. The stiffness of it is less than the inner stiffening ring type, but it has its advantages, such as simple structure, steel saving is suitable for the condition that large diameter column is connected with beam bearing small tension.

Cross plate type. It uses the cross plate arranged in steel tube to improve the integral stiffness and bearing capacity of the joint. The integral stiffness of it is large, but the steel consumption is big too. And the cross plate is inconvenient to be welded. At the same time, the cross plate impacts the pouring and vibrating of the core concrete and the wall of steel tube is affected by the welding heat, which will make the joint easy cracked under cyclic load and the overall bearing capacity reduced.

Bar anchored type. It is made by the following steps: firstly two pieces of strengthening plate are welded on the tube corresponding to the position of the beam flanges; secondly a ribbed slab is welded between the two plates to connect the web of beam and column; finally a few relatively thick bars are welded on the upper and lower plates with one end welded on the beam flange and the other anchored into the column or linked with the bars on the other side by passing through the hole in the tube. This type has good bearing and hysteretic dissipation capacity [6], because the bars anchored in column will produce large frictional force with the core concrete and bear much of the tension transmitted from beam, which will reduce the local tension on the column wall and improve the transmission way of bending moment.

Beam flange breakthrough type. It refers to the beam flange passed through the column section, and the beam web directly welded on the column surface. This type of SBCJ is very good for transferring the bending moment at the beam end, but the column section is largely weakened [4, 7].

Beam web breakthrough type. It refers to the beam web passes through the column section while the beam flange weld on the column surface, this type of SBCJ can reduce the affection of beam flanges on concrete pouring and vibrating, and it is reliable for shear transferring, but the rigidity and bearing capacity decrease greatly. In addition, after the weld on the beam flange cracked, the heated-affected web which is brittle is equally susceptible to cracking [6].

Beam internal breakthrough type. shown as figure 8, which refers to the beam web and flange all passing through the column. The bending moment and shear at the beam end can be directly transmitted by the beam. This type of SBCJ is conducive to the transmission of tension and shears and reducing the local deformation of CFST under the tension from the beam flanges [4], so it has good ductility and seismic performance and is suitable for rigid frame structure. But it will largely weaken the column section at the beam breakthrough part, and the construction is complicated when the beams of different direction are intersected at the same part of column.

New Joint Types

Bolted End Plate Connection. There are lots of weld used in the above beam-column joints, which is easy to brittle failure under earthquake. In order to solve the problem, D.X.Zhang et al. proposed a new connection type. The beam end and the end plate are connected by groove weld, while the steel tube and the end plate are connected by high strength bolts, shown as figure 9. This type of connection has high rigidity and bearing capacity and can better achieve the transmission of tension in column. It can also save the stiffening ribs in column located at the upper and lower flange of the beam and avoid the local deformation of steel tube wall produced from welding. Especially, this type of connection can easily solve the problem of the equipment of beams that have different elevation. The seismic principle of strong column weak beam and stronger node can be well realized.

New Composite Stiffening Ring Type. Outer strengthening ring type has large rigidity and is convenient in construction, but it affects the service function of building. Therefore some scholars put forward this type of connection[8]. The up ring adopts outer stiffening ring to ensure the column not be broken, and it can be set in the concrete slab, which will not affect the service function of building. The lower stiffening ring adopts a new type ring. The column is discontinued at the lower ring, but was directly connected by it. The welding quality and force transition are easily ensured and the requirement of construction. It is also satisfied this type of connection has high bearing capacity, stiffness and good ductility, and the construction is not only in accordance with the requirements of architecture, but also simple and reasonable. It also can achieve the seismic principle.

Development of Experiment and Finite Element Simulation

Corresponding to different CFST SBCJ types, domestic and foreign scholars have carried out series of experiment and finite element simulation research. In the early 1992, T.Ferdinand carried out static experimental study with 18 different types of combined joints and got the corresponding moment-rotation relationship, formulated the structure measures on them [9]. In the same year, Y.M.Alostaz et al. analyzed how the different factors affect the node behavior with finite element software named Abacus, including the ratio of tube radius to thickness, axial load ratio, beam moment-shear ratio, which lay theoretical foundation for experimental research. In 1998, Schneider studied the behavior of 6 kinds of CFST SBCJS under constant axial force with pseudo-static tests The results showed that the force performance of the beam directly connected with steel tube wall type, beam web breakthrough type and steel beam flange breakthrough type were not good under the action of repeated stress, yet the beam internal breakthrough type and bar anchored type showed a good hysteretic performance [10]. In 2001, E.Ahmed et al. carried out pseudo static experimental study of on 7 CFST SBCJS [11]. It showed that the members designed according to the principle of strong column weak beam and stronger node could realize beam hinge failure mechanisms and has a good seismic performance. In the same year, S.P.Chiew et al. simulated the force performance of 51 CFST SBCJS with software MARC and put forward the

corresponding formula for calculating the yield and ultimate bending moment according to the results of analysis. He also carried out static tests with 8 specimens, 4 of which have no stiffening construction measures, the rest of which have. The result showed that the bar anchored type was an effective form of connection and the thickness of steel tube is a main parameter to determine the bending moment [12].

The domestic study on the form of CFST SBCJS started relatively late, which began after 2000 year. In 2001, D.X.Zhang et al. carried out quasi static test with 4 normally designed CFST SBCJS in order to study their dynamic properties and Shear bearing capacity [13]. The results showed that the damage of joints designed according to the principle of strong column weak beam and stronger node occurred at the beam end, and these joints have strong energy dissipation capability, which were affected little by axial compression ratio, yet the joints designed on the opposite principle showed opposite behavior. In 2003, H.Qu promoted a yield shear stress calculation formula by simulate CFST SBCJS force behavior [14]. In 2004, J.Chen et al. established entity model by ANSYS to analyze the performance of stiffening ring type connection, and conducted an experiment with six 1:3 joints accordingly. The result showed that for the Outer annular-stiffener type, the ring rotated to some extent under loading at the beam end, the ring have certain influence on the joints stiffness, and the stiffness is affected more by the height of beam than by the web[15]. In 2006, C.Y.Li et al. carried out static tests with 12 Outer annular-stiffener type CFST SBCJS and discussed their stiffness. It was pointed out that this type of connection could be used as stiffness node if its rigidity could be ensured. And the calculation formula for bending stiffness was also put forward according to the finite element analysis result [16]. In 2009, F.M.Xu analyzed how the column-beam bending strength ratio and the core concrete affect the force performance of joints with 3-D nonlinear finite element model. The result showed that the place that plastic hinge appeared was affected by the column-beam bending strength ratio, and this ratio should be controlled in order to achieve strong column weak beam.

Problems need to be studied further

From the above summary it can be seen that different CFST column-beam joints are put forward and series of achievements are also obtained through experiment and finite element simulation study, but the research done on the stress mechanism and design method are still not deep enough. Therefore, the following problem is necessary to be further studied:

- (1) More work should be done on analyzing how the different factors affect the mechanical performance of CFST SBCJS under low reversed cyclic loading through finite element simulation, and affection of the coupling action of different main factors should also be studied.
- (2) More experiment research also should be done, and it is necessary to set up simplified calculation method for design based on the results of finite element simulation and experiment. The relevant atlas are also should be worked out for convenient application.
- (3) Improve or put forward new types of connection, which have better force performance and are more convenient for construction. And further study is also should be done on the mechanical properties of these joints to establish convenient design method.

Acknowledgements

This work was financially supported by the Youth Foundation of Shenyang Jianzhu University (2011219)

References

- [1] L.L.Han: Concrete Filled Steel Tube Structure(2nd Ed)(Science Publications, Beijing 2004)
- [2] M.S.Gong,L.L.Xie,J.P.Ou: China Civil Engineering Journal Vol.43-12(2004),p.35-40
- [3] F.Q.Xu,M.Q.Xu,C.X.Xu: Journal of Yangtze University Vol.6-4(2009),p.98-101
- [4] X.Li,Y.Xiao,Y.R.Guo: Progress Building Structure Vol.7-4(2005),p.22-26
- [5] Y.M.Alostaz,S.P.Schneider: Construct.Steel Res. Vol.40-2(1996),p.95-127
- [6] X.L.Sun: Architecture and Structure Design No.2(2008),p.32-35
- [7] A.Azizinamini,S.P.Schneider: Journal of Structure Engineering Vol.130-2(2004),p.213-222
- [8] F.H.Xie,Y.S.Cao: Journal of Inner Mongolia University of TechnologyVol.30-2(2001),p.140-145
- [9] T.Ferdinand: Journal of Constructional Steel Research Vol.22(1992),p.59-70
- [10] S.P.Schneider,Y.M.Alostaz: Journal of Construction Steel Research Vol.45-3(1998),p.321-352
- [11] E. Ahmed,A.Azizinamini: Journal of Construction Steel ResearchVol.57-10(2001),p.1099-1119
- [12] S.P.Chiew,S.T.Lie,C.W.Dai: Journal of Structure Engineering Vol.127-10(2001),p.1164-1172
- [13]D.X.Zhang,S.M.Zhang: Journal of Harbin University of C.E.& Architecture Vol. 34-1 (2001),p.21-27
- [14] H.Qu,X.J.Zhou: The Third National Modern Structure Engineering Symposium 2003
- [15] J.Chen,Z.Wang: Journal of Building Structures Vol.25-4(2004),p.43-51
- [16] C.Y.Li,Y.J.Guo: Foreign Building Materials Science and Technology Vol.27-1(2006),p.21-24

Structural optimization of transmission line of steel poles

QIN Li^{1, a}, LUO Yanan^{2, b} HUANG Peng^{3, c}

^{1, 2, 3}School of Civil Engineering, Northeast Dianli University, Jilin Jilin, 132012, China

^bemail, 444503489@qq.com

Keywords: transmission line of steel pipe poles; LINGO software; mathematical modal; steel pipe pole's deflection; structural optimization;

Abstract. For the structural optimization of transmission line of steel pipe poles, the structural mass was considered the objective of the economic optimization, the taper of shaft and then the thickness of each wall with the taper of shaft were successively regarded as the design variables, established mathematical modal of transmission line of steel-pipe pole. Various conditions of load calculation were accomplished. The most unfavorable load condition founded were taken as the design load condition. And LIN-GO is introduced to solve some optimization problems about the design variables. From what has been analysed, it is proved using LINGO on structural optimization of transmission line of steel pipe poles can significantly reduce the amount of steel used.

Introduction

With China's rapid economic development, urban industrial and residential electricity consumption is growing rapidly, high-voltage transmission lines get into the city generally, the city's original feeding power road have to be modified [1], how to make a single column steel tower' technology more mature, to make more rational designing, to make its shape more perfect, is the key to make the steel pole transmission widely used to further. Because China's power transmission steel pole R & D, designing and using are relatively late, there is a big room for optimization. It has been optimized on steel pole transmission with software LINGO specially designed for the optimization. Firstly, the load is calculated, practical problem is translated into a reasonable mathematical model. Using mathematical language to describe the steel pole optimization problem, and then using the software LINGO' unique modeling language to edit mathematical model. Entering the LINGO model window this mathematical mode can be solved. Because LINGO software has its own unique functions and programming languages, it relatively increase the design efficiency.

The optimization theory of using LINGO software to optimize Steel pole transmission

Load calculation. Firstly, it should determine the steel pole transmission' designing load conditions, "Overhead transmission line steel pole design requirements" [3] provide that it should consider the load of the operation of the line, breaking the case, installation conditions and special circumstances when it do structural designing about various types of the steel pole transmission. It is complex if each design load conditions are used to do mathematical modeling. To address this theme, after each load condition is calculated, it need to do finite element modeling on steel pole which will be optimized, the finite element model is imposed by the load of each of the conditions. By finite element analysis, the most adverse conditions is used as designing conditions.

The construction of Mathematical model. Optimization goal is to make the steel pole' weight lightest in mathematical model, the objective function is the total weight of steel pole. Major constraints is to consider the strength requirements, stiffness requirements and stability requirements of steel pole. strength requirements is that maximum stress which contains Bending stress and shear stress does not exceed the allowable stress, stiffness requirements is that maximum deflection does not exceed the allowable value. Designing variables mainly consider shaft taper and each thickness, according to adjust shaft taper and each thickness, to make the minimum steel pole' shaft weight in the condition of meeting the requirements of a variety of conditions.

The objective function. When shaft taper C of Steel pole transmission is the designing variables :

$$W = n \times t \times (2r + hc) \times \sin(\pi/n) \times h \times \pi \times \rho \quad (1)$$

When shaft taper C and each thickness of Steel pole transmission is the designing variables :

$$W = \rho \times n \times \sin(\pi/n) (t_1 \times (2r + h_1c) \times h_1 + t_2 \times (2r + 2h_1c + h_2c) \times h_2 + t_3 \times (2r + 2h_1c + 2h_2c + h_3c) \times h_3 + t_4 \times (2r + 2h_1c + 2h_2c + 2h_3c + h_4c) \times h_4) \quad (2)$$

Constraints. Constraints are the same when taking shaft taper C of Steel pole transmission as the designing variables and taking shaft taper C and each thickness of Steel pole transmission as he designing variables ,It Only because each paragraph has different wall thickness In the case of variable thickness, The shaft of Steel pole to be part of different sub when do mathematical model . strength requirements : Locally stable bending, shear strength and bending strength conditions in constraints is Calculated under the requirements of "Overhead transmission line steel pole design requirements":

$$\frac{N}{Ag} + \frac{M_x}{W_x} \leq f_a \quad (\text{bent local stability condition}) \quad (3)$$

$$V \times \frac{Q}{I_t} + T \times \frac{C}{J} \leq 0.58 f_a \quad (\text{Conditions shear strength}) \quad (4)$$

$$\frac{M}{W_x} \leq f_a \quad (\text{Bending strength conditions}) \quad (5)$$

Axial force:

$$N_i(x) = \sum_{j=5-i}^4 2G_j + n \times \rho \times t \times (2 \times r + (h-x) \times c) \times \sin(\pi/n) \times (h-x) \quad (6)$$

Bending moment:

$$M_i(x) = \sum_{j=5-i}^4 2P_j(h_i - x) + \frac{(h-x)^2}{2} W_s \quad (7)$$

Shear force:

$$Q_i(x) = \sum_{j=5-i}^4 2P_j + (h-x)W_s \quad (8)$$

Calculation of deflection:

$$y \leq [y] \quad (\text{Maximum allowable deflection}) \quad (9)$$

Analysis of Cases

Example of Engineering. The angle steel tower transmission' height is 29.1 m, its Top diameter is 0.675 m, its Shaft were divided into four sections, its Wall thickness are 0.01 m, its Taper is 0.025, the maximum design wind speed is 30 m / s, we calculate the operation of its lines, broken case, and installed case of load combination (Figure 1).

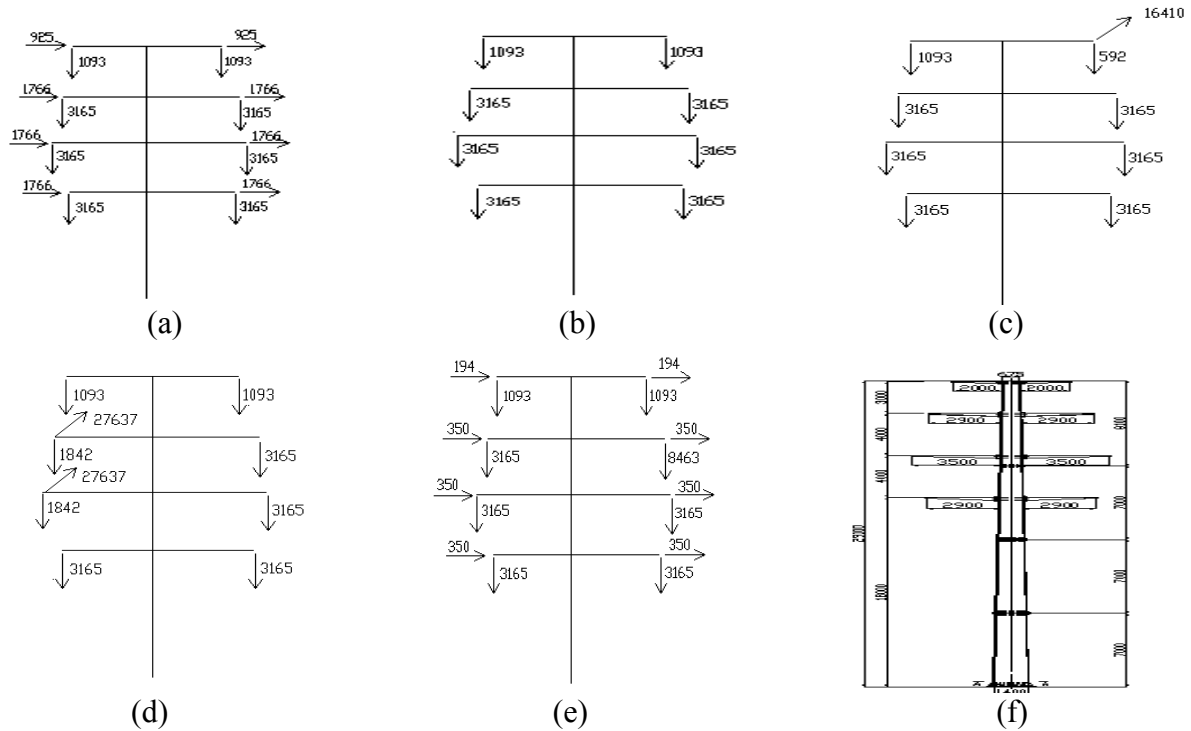


Fig. 1. a) Maximum wind speed ,not disconnect, no ice conditions; b) Lowest temperature ,calm, no ice, not disconnection second c) Broken one ground wire conditions ; d) Within the same file broken any two- phase conductor condition ; e) Installation conditions ; f) the geometry of Steel pole transmission ;

Though finite element analysis, It can be find obviously that tower stress of any two wires is big. Maximum wind speed did not break the ice-free relatively large deflection of the shaft to be, respectively, as the two conditions to optimize the design load.

Built the mathematical model . Take taper C as design variables:The establishment of four mathematical models is according to the different loads suffered, divided steel pole tower into four parts, constraints in the shear strength, bending strength, bending formula in accordance with local stability «design requirements of overhead transmission line steel pole» . According to the beam deflection differential equation theory, Solving the following equation, the analytic expression of thick steel pole tip deflection pull can be got: a mathematical model ,take maximum wind, undisconnection,no ice as the conditions,the first mathematical model is:

$$\begin{aligned} \text{Min} &= 4625.34 + 195435.018 \times c & a &= c/0.665 \\ & 1850(1/a^3 \ln(1+29.1a)/(1+0.1a)) + (1+0.1a)/(2a^3 + 58.2a^4) - 1/(2a^3 + 0.2a^4) - (1691.7la + 29.1)(1691.7la + 29.1) / (2a^2(1+29.1a)^2) + 3532(1/a^3 \ln(1+29.1a)/(1+3.1a)) + 1/a^3 \ln(1+29.1a)/(1+7.1a) + 1/a^3 \ln(1+29.1a)/(1+11.1a) + (3+21.3a)/(2a^3 + 58.2a^4) - 1/(2a^3 + 6.2a^4) - 1/(2a^3 + 14.2a^4) - 1/(2a^3 + 22.2a^4) - (4461.03 + 87.3)(2a^2(1+29.1a)^2) + 401(1/a^3(72.75 - 58.2 \ln(1+29.1a)) - 1/a^3(3 - 29.1a) \ln(1+29.1a) + 1/2a - 1/(2a + 58.2a^2) - 29.1/(1+29.1a) - 846/(2a^2 + 58.2a^3) + 29.1/(a^3 + 29.1a^4) + 846.81/(2a^3 + 58.2a^3)) + 11669.1(1/a^3 \ln(1+29.1a) - 1.5 + 2/(1+29.1a) - 1/(2(1+29.1a)^2)) \leq 1.445 \times 10^8; \\ & (4263.6 + 904.32(0.675 + 58.2c - 2cx)(29.1 - x)) / (0.0332(58.2c + 0.665 - 2cx)) + (1850(29.1 - x) + 1850(29.1 - x)^2 401)(0.491(0.675 + 2c(29.1 - x))) / (0.0411(0.665 + 2c(29.1 - x^3))) \leq 346 \times 10^6; \\ & 63.1(1850 + 802(29.1 - x)) / (0.675 + 2c(29.1 - x)) \leq 200.1 \times 10^6; \\ & 1850(29.1 - x) + 1850(29.1 - x)^2 401(0.491(0.675 + 2c(29.1 - x))) / (0.0411(0.665 + 2c(29.1 - x^3))) \leq 346 \times 10^6; \\ & x \geq 26; x \leq 29; c \geq 0; \end{aligned}$$

Edite the mathematical models of second,third,fourth parts with LINGO software, within the same schedule as any two-phase conductors are calculated design conditions,it can be found through the analysis results: By optimization,the weight of steel pole reduce from 8711 kg to 8308 kg, 4.6% reduced. The design parameters before and after optimization be showed in Tab.1.

Tab.1 Comparing Design Optimized with The Former One

	Value of C (m)	Weight of steel pole(kg)
Before optimization	0.025	8711
After optimization	0.018	8308

When Take taper C and wall thickness as design variables,The design parameters before and after optimization be showed in Tab.2.

Tab.2 Comparing Parameter Optimized with The Former One

	Thickness of the first paragraph(m)	Thickness of the second paragraph (m)	Thickness of the third paragraph (m)	Thickness of the fourth paragraph(m)	Taper C	Shaft weight (Kg)
Before optimization	0.01	0.01	0.01	0.01	0.025	8711
The optimized	0.006	0.006	0.009	0.007	0.020	5864

Through optimization, the total mass of the tower from the 8711 kg reduced to 5864kg, reduced by 32%. Optimization before and after the design parameters shown in Table 2. Optimize the effect is obvious.

Conclusion

This work was financially supported by the Shanghai Natural Science Foundation (0666666), Innovation Program of Shanghai Municipal Education Commission (060000) and Shanghai Leading Academic Discipline Project of Shanghai Municipal Education Commission (0555555).

This paper describes the use of steel pole transmission LINGO optimization software to solve the problem of basic ideas, and a specific instance of the optimization analysis, the results can be seen:

- (A)A steel pole transmission structure optimization design, by optimizing the design variables, can significantly reduce the amount of steel shaft, and thus achieve significant economic benefits.
- (B)LINGO software to address the issue of power transmission steel pole optimization is a relatively successful software, and the use of matlab for transmission steel pole structural optimization compared to significantly reduce the difficulty of programming, to improve the design efficiency should be increased in LINGO software engineering applications in the transmission line extension.

References

- [1] Xie ShanWang, Yu jiong Gu . Power transmission line steel pole tip deflection pull the analytical method and the simple method [J]. Modern Power, 2002, 19 (3) :35-40.
- [2] Chau Lu . 220 kV steel pole optimal design parameters and design features of the Red River [J]. 2007,26 (2) :17-20.
- [3] National Power Company issued. Overhead transmission line steel pole design requirements. Beijing: China Electric Power Press, 2002.
- [4] Fei xiang Luo , Xingpeng Ju, Yang and Li. LINGO optimization in engineering design applications [J]. Shan xi Architecture, 2008,34 (25) :367-368.
- [5] Timoshenko S, Gail J. Mechanics of Materials [M]. Beijing: Science Press,978.448-462.

Analysis of Storey Damage Effect Factors of SRC frame-RC Core Tube Hybrid Structure under Cyclic Loading

Shan-suo Zheng^{1,a}, Wei Yang^{1,b}, Qing-lin Tao^{1,c} and Yi Hu^{1,d}

¹School of Civil Engineering, Xi'an University of Architecture and Technology, Xi'an, Shanxi, China

^azhengshansuo@263.net, ^bbluceyang1987@163.com, ^ctl6551@163.com, ^dhuyi6570@163.com

Keywords: ABAQUS program, SRC frame-RC core tube hybrid structure, stiffness character value, shear wall depth-thickness ratio

Abstract. Based on the general finite-element software ABAQUS, the FE model of 30-story SRC frame-RC core tube hybrid structure is built up. The maximum storey drift angle of the structure under cyclic loading can effectively characterize the changes in storey damage. With the new achievements on damage effect factors, the relation between storey damage and component damage of various types and influence of the main design parameters on the storey damage law are analyzed. It is found that storey damage degree is more serious with the increase of stiffness character value and shear wall depth-thickness ratio, but the effects of both of them are gradually weakened and the change range of it is really small. Research will provide theoretical support on the building of hybrid structure damage model under earthquake excitation.

Damage index of SRC frame-RC core tube hybrid structure

In view of this particular substructure of the hybrid structure, the maximum storey drift angle of the structure is used as an index to characterize the storey damage under cyclic loading. Based on the domestic and foreign correlation research results which include the dates and conclusions got from numerical [1] and experimental methods [2], this article proposes a proper expression function to characterize the storey damage of SRC frame-RC core tube hybrid structure, by using the following equation:

$$D = \frac{\theta_{\max, \text{weakened}}}{\theta_{\max, \text{original}}} \quad (1)$$

Where, $\theta_{\max, \text{original}}$ is maximum storey drift angle in original structure; $\theta_{\max, \text{weakened}}$ is maximum storey drift angle in damaged structure.

Seven numerical calculation models [3] are built to analyze SRC frame-RC core tube hybrid structure and the numerical simulation results are regressed through a data analysis software ORIGIN8.0. The mathematic related expression between component damage value and storey damage value is expressed as follows:

$$D_s = 0.53e^{(0.12 \times D_b)} \sqrt{1.4D_c^2 + 1.7D_{sw}^2 + 0.005} \quad (2)$$

Where, D_s is storey damage value; D_b is SRC beam damage value; D_c is SRC column damage value; D_{sw} is RC shear wall damage value.

Design calculation model

Using SRC frame-RC core tube hybrid structural system, this building contains 30 storeys which are 3.6m uniform storey height), the plan size is 24.0m×18.0m with a uniform column spacing and span of the column of 6m, and the total height of the structure is 108m. The plan graph of typical floor is as shown in Figure 1. This hybrid structure is located in the region with 7 degree of seismic fortification intensity, where soil type in site is II, seismic grade is secondary, and classification of design earthquake is in the second group by the Chinese earthquake code.

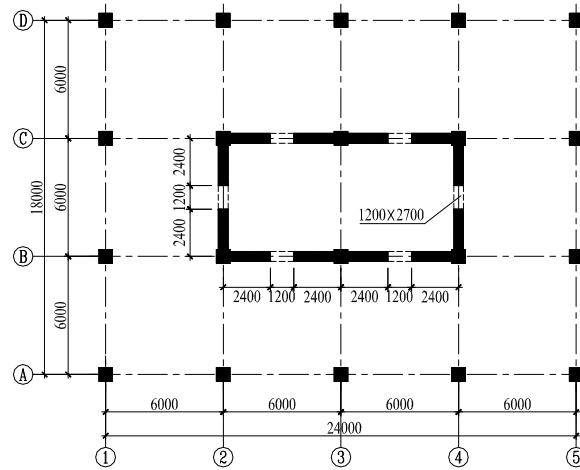


Fig.1 Plan graph of typical floor

Analysis of storey damage law

Structure stiffness character value

Structure stiffness character value (λ) reflects the ratio relation of frame stiffness and core tube stiffness, which is a very important parameter for describing the distribution of structure internal force and the displacement of structure. The λ can be calculated by the following equation [4]:

$$\lambda = H \sqrt{\frac{C_F}{E_w I_w}} \tag{3}$$

Where, C_F is shearing stiffness of frame column; $E_w I_w$ is shear-wall equivalent bending stiffness.

Due to the different degradation degree between shear-wall stiffness and frame stiffness at different cyclic loading stage and different damage accumulation degree, structure stiffness character value is the dynamic structural design parameters. Six calculation models with different stiffness character value are analyzed to study the effect of stiffness character value on the storey damage law of hybrid structure. The specific design parameters are reported in Table 1 and the numerical simulation results are reported in Table 2.

Table1 Storey design parameters corresponding with different stiffness character values

No.	SRC frame		Concrete strength grade	stiffness / $\times 10^6$	RC shear wall		Stiffness character value λ	
	Frame beam	Frame column			Wall thickness	Concrete strength grade		stiffness / $\times 10^9$
1	500×800 (H550×250×25×3)	800×800 (H500×450×40×6)	C45	4.91	400	C40	2.04	5.29
2	500×800 (H550×250×25×3)	800×800 (H500×450×40×6)	C45	4.91	350	C40	1.75	5.73
3	500×800 (H550×250×25×3)	800×800 (H500×450×40×6)	C45	4.91	350	C30	1.61	5.96
4	500×800 (H550×250×25×3)	800×800 (H500×450×40×6)	C45	4.91	300	C30	1.37	6.47
5	500×800 (H550×250×25×3)	800×800 (H500×450×40×6)	C45	4.91	250	C30	1.16	7.02
6	500×800 (H550×250×25×3)	800×800 (H500×450×40×6)	C45	4.91	200	C30	0.98	7.63

Note: (1) The data in the bracket is the section size of inserted steel, and the unit of section size is millimeter (mm); (2) The stiffness character value of the original design structure is 5.18.

Table2 Influence of stiffness character value on storey damage

No.	Stiffness character value	Storey damage value	No.	Stiffness character value	Storey damage value
1	5.29	0.043	4	6.47	0.255
2	5.73	0.080	5	7.02	0.279
3	5.96	0.131	6	7.63	0.339

Note: Storey damage value and stiffness character value can be separately calculated by Eq. (2) and Eq. (3).

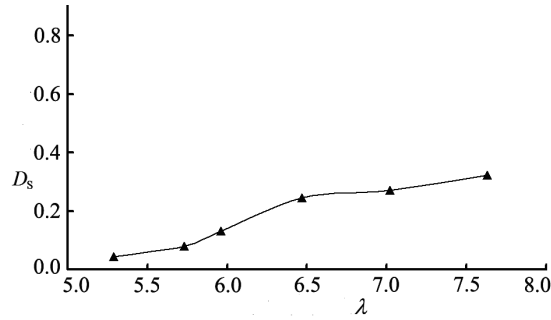


Fig.2 Influence of stiffness character value on storey damage

The relationship curve between storey damage value and stiffness character value is shown in Fig.2. With the increase of stiffness character value, storey damage degree becomes more serious, while its change range is small which is between 0.043 and 0.339. The effect of stiffness character value on storey damage value is gradually weakened with the increase of stiffness character value. Based on the numerical simulation data of six calculation models, the mathematical relationship between storey damage and stiffness character value is fitted out, and its equation is as follows:

$$D_s = 0.1\lambda^4 - 2.6\lambda^3 + 25.2\lambda^2 - 107.4\lambda + 170.3 \quad (4)$$

RC shear wall depth-thickness ratio

RC shear-wall depth is far bigger than its section thickness. Due to its large plane stiffness, shear wall bears most of the horizontal load, which decides the structure's mechanics characteristic is inclined to frame structure or core tube structure.

In order to study the effect of shear wall depth-thickness ratio which is calculated by Eq.(6) on the storey damage law of hybrid structure, the author presents numerical analysis for six calculation models with different depth-thickness ratios which is between 10.3 and 36.0. The numerical simulation result is shown in Table 3. Based on the numerical simulation data, the mathematical relationship between storey damage and stiffness character value is fitted out, and the equation is as follows:

Table 3 Influence of shear wall depth-thickness ratio on storey damage

No.	Thickness /mm	Depth-thickness ration	Storey damage value	No.	Thickness /mm	Depth-thickness ration	Storey damage value
1	350	10.3	0.042	4	200	18.0	0.247
2	300	12.0	0.111	5	150	24.0	0.312
3	250	14.4	0.153	6	100	36.0	0.367

Note: (1) Storey height is 3600 mm; (2) The depth-thickness ratio of original structure is 9.

$$D_s = 0.26\ln(\zeta) - 0.54 \quad (5)$$

$$\zeta = \frac{h}{t} \quad (6)$$

Where, h is shear-wall depth; t is shear-wall thickness.

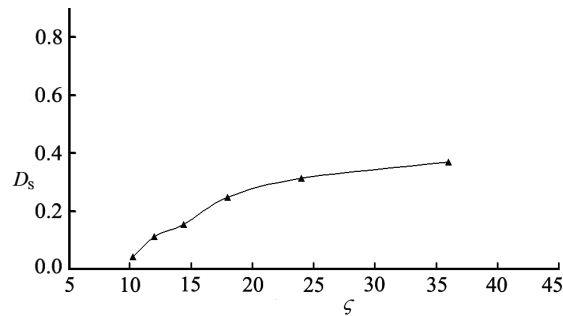


Fig.3 Influence of shear wall depth-thickness ratio on storey damage

The relationship curve between storey damage value and stiffness character value is shown in Fig.3. Storey damage degree will become increasingly serious with the increase of shear wall depth-thickness ratio, but the change range of damage value is small. When $\zeta > 18$, the effect of depth-thickness ratio on storey damage value becomes weaker where damage value changes between 0.247 and 0.367 as the impairment of shear wall plane stiffness weakens the lateral stiffness of core tube structure leading to the fact that contribution of the RC shear wall to storey damage value is also reduced.

Conclusions

Based on the above numerical simulation, the following conclusions are obtained.

(1) Storey damage degree will become more serious with the increase of structure stiffness character value, but the change range of damage value is small. The effect of stiffness character value on storey damage value is gradually weakened with the increase of stiffness character value.

(2) Storey damage degree will become increasingly serious with the increase of shear wall depth-thickness ratio, while the change range of damage value is small. When $\zeta > 18$, the effect of depth-thickness ratio on storey damage value becomes weaker as the impairment of shear wall plane stiffness weakens the lateral stiffness of core tube structure, leading to the fact that contribution of the RC shear wall to storey damage value is also reduced.

Acknowledgments

This project is sponsored by National Natural Science Foundation of China (Grant No. 50978218, 501108376, 90815005), Research Fund for the Doctoral Program of Higher Education of China (Grant No. 20106120110003), Science and Technology Co-ordinator Innovation Project of Shan'xi Province in China (Grant No. 2011KTCQ03-05) and Office Educational of Shan'xi Province in China (Grant No. 2010JK633).

References

- [1] Powell GH, Allahabadi R. Seismic damage prediction by deterministic method: concept and procedures [J]. *Earthquake Engineering and Structural Dynamics*, 1988, Vol.16: 719-734.
- [2] Wang M L, Shah S P. Reinforced concrete hysteresis model based on the damage concept [J]. *Earthquake Engineering and Structural Dynamics*, 1987, 15(8): 993-1003.
- [3] Qing-lin Tao: submitted to Xi'an University of Architecture and Technology (2011). (in Chinese)
- [4] Qing-xuan Shi. Xing-wen Lang. Tall Building Structural Design [M]. Beijing: Science Press, 2006

A Multiaxial Damage Statistic Constitutive Model for Concrete

Shan-suo Zheng^{1,a}, Wen-yong Li^{1,b}, Qing-lin Tao^{1,c}, and Yu Fan^{1,d}

¹School of Civil Engineering, Xi'an University of Architecture and Technology, Xi'an, Shanxi, China

^azhengshansuo@263.net, ^bliwenyongok@126.com, ^cql6551@163.com

^dfanyu0806@163.com

Keywords: damage evolution, SRHSHPC, damage statistic constitutive model, complete decoupling

Abstract. In order to apply the uniaxial damage evolution equation that established with the variable of strain to the multiaxial damage quantitative analysis, this paper bases on the Hsieh-Tang-Chen four-parameter failure criterion and adopts the way of making the triaxial equivalent strain combining with the uniaxial damage evolution equation to analyze and deduce the uniaxial damage evolution equation of SRHSHPC, and which is expanded to multiaxial condition as well. A function considered triaxial stress state and a related correction value are suggested, then, improving the damage evolution equation from triaxial to multiaxial form, finally proposing the multiaxial damage statistic constitutive equation for concrete, taking numerical simulation with the complete decoupling method and the result shows that the model is effective.

Introduction

The process from the generation to the development when concrete works under uniaxial stress state is described well by the uniaxial damage evolution equation. However, in contrast with uniaxial stress state, the most area of actual concrete structure or itself generally works under multiaxial stress state, when stress-strain relationship, stress characteristics and material damage development characteristics change greatly, which results in the effects of multiaxial stress state and confining pressure on strength, poisson ratio and other mechanical properties of materials are reflected with difficulties. In fact, it is found that damage evolution and damage threshold change greatly, in addition to stress-strain relationship. If the approach to measuring damage value with uniaxial damage evolution equation is still adopted, damage response obtained certainly will be different from the actual situation. Furthermore, other mechanical responses, such as stress, strain and displacement, will be difficult to accurately obtain.

Multiaxial damage statistic evolution equation for concrete

In order to apply the uniaxial damage evolution equation with the independent variable strain established to the multiaxial damage quantitative analysis, the triaxial equivalent strain combining with the uniaxial damage evolution equation is adopted to make the damage evolution process approach to actual multiaxial stress state. Eq.(1) is one of equivalent strain expressions^[1], it can be expressed as follow:

$$\varepsilon_{eq} = \frac{k-1}{2k(1-2\nu)} I_1 + \frac{1}{2k} \sqrt{\left[\frac{k-1}{(1-2\nu)} I_1 \right]^2 - \frac{12k}{(1+\nu)^2} J_2} \quad (1)$$

Where, I_1 is the first invariant of strain tensor, J_2 is the second invariant of strain deviator, ν is poisson ratio and $k = f_c/f_t$ is ratio of compressive- tensile strength.

To reflect the concrete material multiaxial stress state, considering the effects of different hydrostatic stresses on the damage evolution, this paper adopts the Hsieh-Tang-Chen four-parameter failure criterion combining with the uniaxial damage evolution equation of SRHSHPC from the above paragraphs which is expanded to multiaxial form to apply it to the analysis of multiaxial damage and failure of concrete structure. The uniaxial damage evolution equation of SRHSHPC can be given as follow [2]:

$$D = F(\varepsilon) = \int_0^\varepsilon f(x)dx = \Phi\left(\frac{(\ln \varepsilon - \lambda)d_f}{\rho}\right) \\ = \frac{1}{2} + \frac{1}{2} \tanh\left[1.12838 \frac{(\ln \varepsilon - \lambda)d_f}{\sqrt{2}\rho} + 0.10277 \left(\frac{(\ln \varepsilon - \lambda)d_f}{\sqrt{2}\rho}\right)^3\right] \quad (2)$$

Where, λ , ρ and d_f are already known.

In fact, concrete component or structure mostly works under multiaxial stress state, while uniaxial stress state is uncommon. Because it is not appropriate to describe damage development with the uniaxial damage evolution equation of concrete, this paper suggests a function considering triaxial stress state and related correction value, as well as combining with the uniaxial damage evolution equation of concrete to reflect the influence of triaxial damage evolution, and improving the transformation of damage evolution equation from triaxial to multiaxial form to express actual stress state of concrete components or structures relatively accurately.

The function $F(\sigma_{ij})$ under triaxial stress state is considered, and the concrete expression of $F(\sigma_{ij})$ based on triaxial failure criterion, such as the Hsieh-Tang-Chen four-parameter failure criterion [3], it can be given as follow:

$$F(\rho, \xi, \theta) = A\rho^2 + (B \cos \theta + C)\rho + D\xi - 1 = 0 \quad (3)$$

Where, A , B , C , and D are relational experimental parameters, these values are described in literature [4], $\rho = \sqrt{2J_2}$, $\xi = I_1/\sqrt{3}$, θ is the stress Lode's angle, $\theta = \arccos(3\sigma_1 - I_1)/2\sqrt{3J_2}$, I_1 , J_2 and σ_1 are the first invariant of strain tensor, the second invariant of strain deviator and the first main stress respectively. A correction value $r(\sigma_{ij})$ considering stress triaxiality effect is suggested as follow:

$$r(\rho, \xi, \theta) = \begin{cases} \rho(\sigma_{ij})/\rho_0 & F(\rho, \xi, \theta) < 0 \\ 1 & F(\rho, \xi, \theta) \geq 0 \end{cases} \quad (4)$$

The compression meridian plane ($\theta = 60^\circ$) is taken for instance, which is shown in Fig.1. ρ_0 is the yielding or failure radius in meridian plane corresponding to the current stress point. $\rho(\sigma_{ij})$ is the radius of current stress point. It is concluded that $r(\sigma_{ij})$ has a relatively intuitive physical meaning which is a distance ratio from the current stress state to failure state under triaxial stress state. It can also be expressed with the deviatoric plan which is shown in Fig.2.

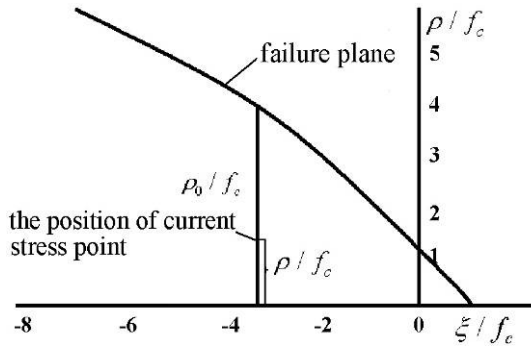


Fig.1 $\rho(\sigma_{ij})$ in the failure plane

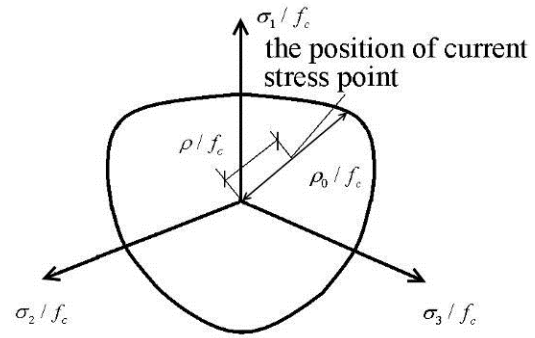


Fig.2 $\rho(\sigma_{ij})$ in the deviatoric plane

Under multiaxial stress state, when at least two stress components must be unequal to zero, the uniaxial damage evolution D can be expanded to multiaxial form, it can be given as follow:

$$D^m = D \times r(\sigma) \quad (5)$$

Where, D^m is the improved multiaxial damage evolution equation. The damage of principal axis direction $D_i (i=1\sim 3)$ is obtained by analyzing, then the second-order tensor of damage can be established.

Multiaxial damage statistic constitutive model for concrete

Based on the above analysis, the multiaxial constitutive model can be established as follow:

$$\{\sigma_i\} = \left[[I] - [D^m] \right] [K] \{\varepsilon_i\} \quad (i=1,2,3) \quad (6)$$

Where, $[K]$ is the elastic matrix of virgin material, $[I]$ is the unit matrix, $[D_m]$ is the variable matrix of equivalent damage.

$$[D^m] = \begin{pmatrix} D_1 & & 0 \\ & D_2 & \\ 0 & & D_3 \end{pmatrix} \quad (7)$$

Based on the equation (2) ~ (7), the multiaxial damage statistic constitutive model for concrete can be obtained

Numerical simulation for multiaxial damage statistic constitutive model for concrete

Finite element analysis method based on damage theory. The procedure of structural analysis including damage research, strength check, life prediction and others will be more reasonable by introducing damage variable. However, there are many disadvantages dealing with the damaged structure on fixed solution problem, for example, the number of fixed solution equations and damage evolution equations increases, which results in solving the problem with more difficulty. Because of a series of problems brought by this mean, considering the computational complexity and the precision requirement, methods which include complete decoupling, full coupling, half decoupling and local coupling etc. are generally adopted in damage mechanics. Because of the large computational complexity which results from full coupling and half decoupling, this paper adopts the complete decoupling method to take numerical simulation for the multiaxial damage model.

Numerical simulation. This paper uses the experiment data and example in the literature [4] to take numerical simulation for the model. The damage pattern under critical load for concrete is obtained, and it is shown in Fig.3. The test specimens had a rectangular cross section of $0.85\text{m}\times 0.3\text{m}\times 1.3\text{m}$, Fig.4 is the mesh and load for concrete console, the selected material property parameters is given as follow:

$$\nu = 0.2; f_t = 2.26\text{MPa}; E = 21.87\text{GPa}$$

The actual value of failure load is 740kN in the literature [4], the load-displacement obtained by using the model is close to the value above, namely 700kN. The reform was obviously different from the result in the literature, however, due to taking the complete decoupling method for damage problem, the result is a little conservative. It is concluded that the model is valid.

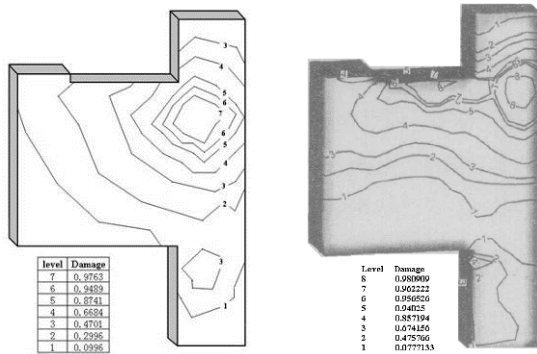


Fig.3 Damage pattern under critical load for concrete

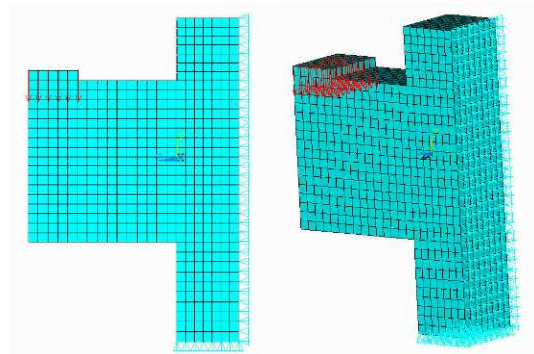


Fig.4 Mesh and load for concrete

Acknowledgments

This project is sponsored by National Natural Science Foundation of China (Grant No. 50978218, 501108376, 90815005), Research Fund for the Doctoral Program of Higher Education of China (Grant No. 20106120110003), Science and Technology Co-ordinator Innovation Project of Shan'xi Province in China (Grant No. 2011KTCQ03-05) and Office Educational of Shan'xi Province in China (Grant No. 2010JK633).

References

- [1] Simone A.,Well GN.,SluysL.J. From continuous to discontinuous failure in a gradient enhanced continuum damage model. *Compute Methods Appl. Mech. Engrg.* 2003, 192, 581-4607.
- [2] PARK H, KIM J Y. Plasticity model using multiple failure criteria for concrete in compression [J].*Int J Solids Struct*, 2005, 42:2303-232.
- [3] Jian-jing Jiang, Lie-ping Ye, Xin-zheng Lu. *Finite element analysis of concrete structures* [M]. Beijing, Tsinghua Publishing House, 2004
- [4] Rong-qiang Du, Gao Du, A multiaxial anisotropic elastoplastic damage model for concrete and its application [J] *Journal of Dalian University of Technology*, 2007,47(4):567-572

Influence of Various Inclinations of Webs on Anti-torsion Characteristic of Steel-Concrete Composite Box Girder

Xuhui Hu

Chongqing Jiaotong University, China

guyuejiu@163.com

Keywords: composite box girder, FEM, inclination of the web, anti-torsion performance

Abstract. Applying FEM Analysis Software to the analysis that under the conditions of webs with inclinations of 15°, 20°, 25°, 30°, 35°, 40°, the girders appear mid-span transformation, the concrete stress of the base plate and the stress of the steel webs at the fulcrum. The results of the research show that the increase of the inclination of the web can facilitate the anti-torsion performance of the composite box girders.

Introduction

Since the first composite box girder bridge with corrugated steel webs, namely Bridge Cognac, was constructed in France in 1986, this kind of new composite structure has been developed in many countries, among which the development in Japan is most rapid. Since 1993, Japan has constructed a large number of simple composite box girder bridges with corrugated steel webs, continuous girder bridges, continuous rigid frame bridges and cable-stayed bridges. Currently, Japan is advocating highway designer to apply this kind of composite structure.

China commenced to make a study on the composite box girder bridges with corrugated steel webs in 1990s. The composite box girder bridges with corrugated steel webs have achieved rapid development in China, including the Long March Bridge in Jiangsu and the grand bridge on the Yellow River in Juancheng City in Shandong. It is very important to further make a study on the stress characteristics of this new type composite structure and figure out the laws of its bearing capacity. This thesis takes the composite box girder with corrugated steel webs as an example, and focuses on the effect of the changes of the web inclinations on the anti-torsion performance of the steel-concrete composite girders.

Characteristics of trapezoidal girders

Under the condition of terrain limit, the trapezoidal girder shall be positioned on the skewing webs, which is not only able to reduce the width of the base plate, narrowing the breadth of the abutments, reducing the masonry and making the bridges more nice in appearance, but also to own better performance of wind resistance. However, the traditional trapezoid box girder of reinforced concrete carries no convenience in construction and is rarely applied in large-span box girder bridges. However, it is only required for the composite box girder bridge with corrugated steel webs to set the processed steel webs aslant to form the trapezoidal girders, in which the construction is rather easy. Most of the constructed composite box girder bridges with corrugated steel webs have adopted the trapezoidal girders. For example, the Singkep Bridge in Japan takes an inclination of 20°, the Tanaka Bridge is 16° in inclination, and the Cognac Bridge in France adopts an inclination of 35°. The trapezoid girders are seldom applied in China. In the previous design cases, the inclination of the webs is often achieved through the experiences or engineering simulation, which carried a great randomness. The published technical materials concerning trapezoid girder are rare, hence the results of the analysis in this article are of more instruction value.

Project profile

One of the principal advantages of the composite box girder bridge with corrugated steel webs lies in its light dead weight and convenient construction, which enjoys more competitive advantage in the mountainous areas. This project is located on a secondary road in Chongqing City. The main technical specifications include the following:

Fig.1 shown that the width of the bridge is 9m, and the height of the girder is 1.6m. The bridge is 25m in length, and the steel web is 9mm in thickness, 90mm in wave length, see Fig. 2. The girders apply C50 concrete, and the steel webs are A3 steel.

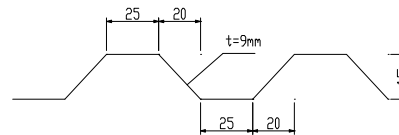
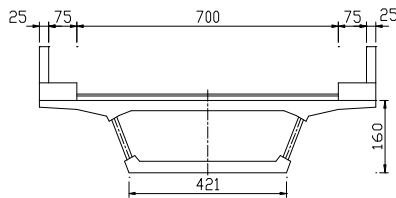


Fig. 1 Cross section view unit: (cm)

Fig. 2 Dimensional drawing of steel web unit: (cm)

Analysis of the FEM models

In the process of FEM model analysis, six cases are selected, namely: inclination of the webs of 15° , 25° , 30° , 35° , and 40° . The changes of the inclinations are to keep the axis position at the joint part of the steel webs and the roof fixed. When rotating the axis of the steel webs, the length of the cantilever beam will stay unchanged, and the height of the girder will keep stable, only the width of the bottom board will change.

Calculation hypothesis

During the analysis, it is hypothesized that the corrugated steel webs are well connected with the concrete roof and bottom board and there is no damage from relative slip or shearing linkage; the pre-stressed reinforcement is not considered into the function in the model; the corrugated steel webs are provided with enough buckling strength, thus there will be no buckling failure of any kind; there is no consideration for nonlinear effect of the reinforcing steel bars and concrete; there is no consideration for the participation of the bridge deck pavement in the function.

Modeling of FEM

Space FEM models shall be built for the dimensions of the proposed bridge. In order to simulate the corrugated steel webs more close to the actuality and with the consideration of the small span of the bridge; the selected entity element doesn't make any high standard for the computer hardware. Therefore, the Solid Element with 8 nodal points is adopted when building models. The bridge is divided into 26484 nodal points for 28726 elements in total. The boundary conditions requires the degree of freedom of u_x , u_y , u_z between two nodal points at the fixed hinged support and the degree of freedom of u_x and u_y between the nodal points at the movable hinged support. See picture 3 for the mesh of element, The element length is 25cm along the bridge length direction.

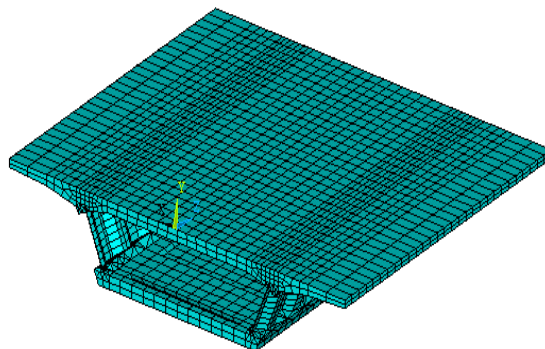


Fig. 3 Section model diagram of box girder

Operating condition of load

The effect of the dead load and car load is taken into consideration when loading. The anti-torsion and buckling performance of the corrugated steel webs shall be determined by means of the symmetry and unbalance load layout of the car load. The load falls into 3 operating conditions as follows: Operating condition I: Dead load; Operating condition II: Car load (symmetry); Operating condition III: Car load (asymmetry).

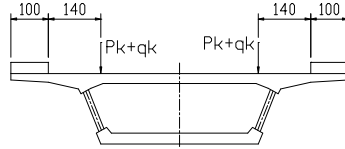


Fig. 4 Operating condition II (Unit: cm)

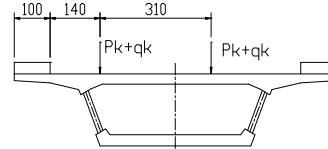


Fig. 5 Operating condition III (Unit: cm)

Operating condition I: the dead load includes dead load of phase I and phase II, which shall be achieved from the dead load of the model; operating II: on the two lanes cars shall be symmetrically laid out. Lane load consists of uniformly distributed load (q_k) and the concentrated load (P_k). The horizontal position shall be laid out as per the car load. The position of load shall take the centerline between two wheels. Therefore, the distance from position to the edge of the sidewalk shall be: $50 + 180 \times 0.5 = 140\text{cm}$, which is shown in figure 4. The stress is concentrated in the mid-span cross-section; operating III: two lanes are laid out in asymmetric way. The distances from the layout position to the edge of the sidewalk are respectively: $50 + 100 \times 0.5 = 140\text{cm}$ and $140 + 180 \times 0.5 + 130 + 180 \times 0.5 = 450\text{cm}$. Other cases are similar to operating condition II, which is shown in figure 5.

Results of analysis

The FEM software analysis can achieve the deflection of different web inclinations at the angular point of the mid-span under various operating conditions, the tensile stress of concrete and the principal tensile stress of steel webs. In order to eliminate the tangential stress and deformation of the girder bridge, the value at angular point of the bottom board of the mid-span cross section shall be taken as the analysis object in reading the data results.

Under the dead load, the deflection, axial stress and primary stress at each point are shown in table 1; under the symmetrical and asymmetric loads, the deflection and the enhanced coefficient of the unbalance load at the mid-span cross-section are shown in table 2:

Table 1 Strained condition of box girder under live load

Inclination of webs ($^{\circ}$)	Deflection cm	axial stress MPa	primary stress MPa
15	1.701	7.446	75.7
20	1.722	7.785	75.0
25	1.750	7.857	72.7
30	1.796	8.129	71.5
35	1.826	8.052	70.7
40	1.887	8.861	68.5

Table 2 Mid-span deflection of box girder under dead load

Inclination of webs ($^{\circ}$)	Deflection I cm	Deflection II cm	Unbalance loading coefficient
15	0.6968	0.7434	1.067
20	0.7106	0.7565	1.065
25	0.7279	0.7733	1.062
30	0.7499	0.7947	1.060
35	0.7697	0.8126	1.055
40	0.8083	0.8385	1.037

See table 3 for the tensile stress and the enhanced coefficient of the unbalance load of the cross-section baseboard in the box girder mid-span under the symmetrical and asymmetric loads; see table 4 for the shearing stress and the enhanced coefficient of the unbalance load of the cross-section baseboard in the steel webs under the symmetrical and asymmetric loads:

Table 3 The tensile stress of the baseboard girder mid-span under live load

Inclination of webs ($^{\circ}$)	Operating condition I MPa	Operating condition II MPa	Unbalance loading coefficient
15	3.896	4.306	1.105
20	4.076	4.468	1.096
25	4.101	4.464	1.089
30	4.203	4.541	1.080
35	4.061	4.201	1.055
40	4.679	4.811	1.028

Table 4 The shearing stress of the of the box webs near the support under live load

Inclination of webs ($^{\circ}$)	Operating condition I MPa	Operating condition II MPa	Unbalance loading coefficient
15	9.58	11.43	1.19
20	8.92	10.56	1.18
25	8.29	9.73	1.17
30	7.45	8.66	1.16
35	6.75	7.68	1.14
40	5.89	6.61	1.12

The enhanced coefficient of unbalance load of deflection of the mid-span cross section and the tensile stress of the concrete bottom board and the tensile stress of the steel webs near the support will change under different web inclination. See chart 6 for details.

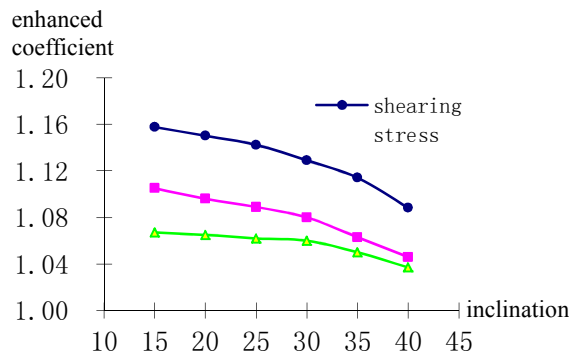


Chart 6 Enhanced coefficient curve of the unbalance loading

As per the results of the finite-element analysis, it is shown in table 1-4 that the deflection and the tensile stress of the cross-section of the mid-span increases with the increase of the inclination of the web; the enhanced coefficient of the unbalance loading of axial stress is rather small (the setting of the diaphragm plate functions well for anti-torsion); it is worth noting that the enhanced coefficient of the shearing stress is large.

Conclusions

In conclusion, the enhanced coefficient of unbalance for the composite box girder will get less with the increase of the web inclination, namely the weakening of the torsion and distortion effect, which indicates that the increase of the web inclination can facilitate the antitorque performance of the box girder. However, the moment of inertia I of the interface will be less with the increase of the web inclination, thus the whole resistance will be weakened.

Consequently, when designing the steel-concrete composite box girder bridges, if the convenient construction conditions can be met, the designers shall choose a comparatively great web inclination, which is recommended to be more than 20° , to improve the anti-torque performance of the steel-concrete box girders, save the engineering materials and reduce the construction costs as well.

Acknowledgements

This work was financially supported by the Chongqing Science Foundation (2003-7985).

References

- [1] X. Haifan: *Advanced Theory on Bridge Structure* (China Communications Press Beijing 2001).
- [2] L. Hongjiang: *Experimental Study and Analysis on Torsion and Distortion* (Jiaotong College of Southeast University, Nanjing:2003).
- [3] Konndo Shotai, Kobayasi Tutome, Simizu You: Design and Construction of 'Saitama Bridge'—composite box-grider bridge with corrugated steel webs. *Bridge and Base* vol.9 (1994),p.13-20.

Contrastive Finite Analysis of SRC Frame under Cyclic Loading Base on Macroscopic and Microscopic Element

Shan-suo Zheng^{1, a}, Wei Wang^{1, b}, Pi-ji Hou^{1, c} and Ming Xie^{1, d}

¹School of Civil Engineering, Xi'an University of Architecture and Technology, Xi'an, Shanxi, China

^azhengshansuo@263.com, ^bwangweiwei1881@126.com, ^choupiji@163.com, ^dkpptx@163.com

Keywords: steel reinforced concrete (SRC) frame, macroscopic element, microscopic element, contrastive analysis

Abstract. A macroscopic finite element model and a microscopic one were set up respectively to simulate SRC frame with two bays and three stories under cyclic loading, by comparing the simulation and test results, the authors find that the results obtained from the two finite methods have few differences, and each of them can satisfy the demands of engineering, but the principles established in simulation process were different. The macroscopic finite element model was established by very few elements and the results data were obtained easily and quickly, however, it just attain some macroscopic mechanics data (axial force, bending moment and shearing force etc.). The microscopic finite element model involves complex modeling principle, not only needs more time for dealing with the geometry model, gridding and boundary conditions and so on, but also limited by professional knowledge, which make users establish a correct model hardly. The comparison shows that macroscopic finite element method has many advantages in engineering fields.

Introduction

Steel reinforced-concrete composite structure has been used as new construction for a long time, which has a lot of features such as higher bearing capacity, outstanding durability, convenient production and usage, so this type of structure has been widely applied. The components of SRC composite structure is consisted by reinforcing, shape steel and concrete, due to the complexity section type, it is difficult to determine how the internal stress transfers. So it is difficult to get exact computation result through numerical simulate. The current SRC finite element method models can be divided into the macroscopic model and the microscopic model. It's hard to establish a microscopic model to simulate a structure without finite element knowledge and enough time, so it's limited in the practical application. For example, it is almost impossible to simulate frame structure or other structures, because it always consists of thousands microscopic elements, which lead to be difficult in calculation. When whole structure analysis is needed in practical application, the model is usually established by macroscopic model. Each finite method has its advantages and disadvantages. In this paper, a macroscopic and a microscopic finite element model were set up to simulate SRC frame with two bays and three stories under cyclic loading, the analytic processes were compared, and the differences of finite-element method principles, the constitutive relation of materials, meshing, loading control and simulation results were discussed.

Test

The SRC frame quasi-static test in this paper is referred in literature[1], the specimen is a 1:6 miniatures to a real project, the test system is shown in Fig.1, the specimen details are shown in Fig.2, the cyclic loading scheme is shown in Fig.3. The columns at two sides were loaded 520kN in vertical direction, and the middle column was loaded 1040kN in vertical direction. The horizontal load was located on the top of the specimen and the lateral face of column. The horizontal loading method use

displacement-control, take 3 loops at each loading stage, and the test stopped until specimen destroyed. The mechanical properties of steel are shown in Table1, and the test adopts C30 concrete to produce beams and columns.

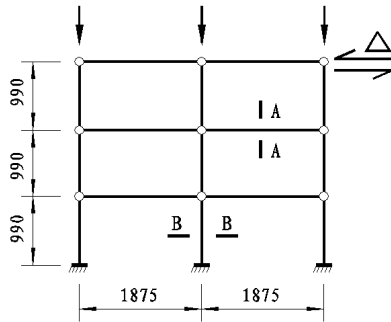


Fig.1 Dimension of SHPC frame specimen

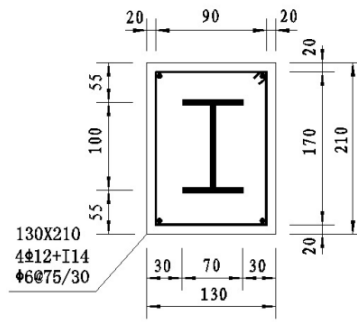


Fig.2 Details of specimen

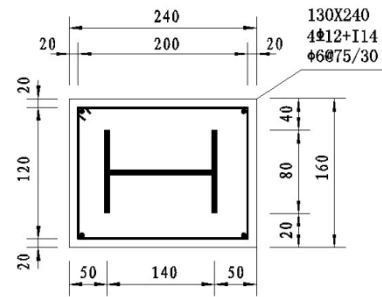


Table 1 Mechanical properties of steel of test

parameter	II0 Q235		II4 Q235		A6	B12
	flange	web	flange	web	HPB235	HRB335
f_{yk} /MPa	321.0	315.5	319.7	312.4	297.5	384.0
ε_{yk} / $\mu\varepsilon$	1540	1503	1543	1507	1447	1863
f_{uk} /MPa	509.9	494.2	491.5	502.5	438.0	557.0
Notes	f_{yk} : yield stress; ε_{yk} : yield strain; f_{uk} : ultimate strength					

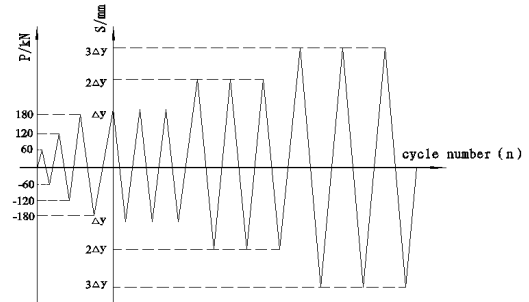


Fig.3 Load curve

Macroscopic model by OpenSEES

The Open System for Earthquake Engineering Simulation (OpenSEES) is a software framework for simulating the seismic response of structural and geotechnical systems, which is an open-source finite elements software developed by University of California, Berkeley. OpenSEES has advanced capabilities in modeling and analyzing the nonlinear response of systems with a wide range of material models, elements, and solution algorithms.

Elements. The model in this paper is established by nonlinear beam column element, this element model is based on nonlinear fiber element model, and it is widely used to simulate static and dynamic nonlinear response of component and structure.

Material models. The material models in this model contain concrete, shape steel and steel reinforcing. In order to simulate the hysteretic behavior of the test accurately, this model divide the concrete of cross section into three areas: 1. concrete without constraint 2.high constraint by shape steel 3.the area between the other two. This method is based on the theories of concrete under compression which is proposed in 1982 by Mender in literature [2]. The stress-strain curve should be defined for each area respectively. For concrete with no constraint: $f'_{cc} = K_p f'_{c0}$. For concrete under constraint: $f'_{cc} = K_h f'_{c0}$. K_p , K_h present the factor of constraint.

Shape steel and reinforcing bar use the same material model, which is proposed by Giuffr-Menegotto-Pinto in literature[3], the material model expression in equation(1):

$$\left. \begin{aligned} \sigma_{eq} &= b\varepsilon_{eq} + \frac{(1-b)\varepsilon_{eq}}{(1+\varepsilon_{eq}^R)^{1/R}}, \varepsilon_{eq} = \frac{\varepsilon_s - \varepsilon_r}{\varepsilon_0 - \varepsilon_r}, \sigma_{eq} = \frac{\sigma_s - \sigma_r}{\sigma_0 - \sigma_r} \\ R &= R_0 - \frac{a_1 \xi}{a_2 + \xi}, b = E_1 / E_0 \end{aligned} \right\} \quad (1)$$

In equation (1), σ_0 and ε_0 present the stress and strain at yield point. σ_r and ε_r mean the stress and strain at reversal point. b is the ratio of sclerosis stiffness E_1 to origin tangent modulus E_0 , R is constant which considers Baushinger effect of reinforced bar. a_1 and a_2 are material constants, ξ is absolute value of the plastic strain at last cycle.

Mesh. The section meshing type and density of fiber affect calculation precision and efficiency. In order to get results accurately and quickly, it's better to use 10mm for each fiber section side length, and it should be set 5 Gauss-Lobatto integral point for one element.

Loading and boundary condition. Like the test, the vertical load was loaded before loaded in horizontal direction, and the horizontal loading method use displacement-control, Newton's iterative method was adopted for the solution of non-line equation with using energy principle as convergence rule.

Microscopic model by ABAQUS

Element type. When building a microscopic finite model, thousands of solid element or other element are used to consist a component, different material models are used to simulate different kinds of materials. Concrete and steel are usually simulated by solid element, reinforcing bar is simulated by truss element, and loading block is simulated by solid element with high Young Modulus.

Material models. For each material, finite method under microscopic level has its own microscopic constitutive equations involving damage mechanics and mechanics of materials. So the microscopic material model can simulate microscopic mechanics properties of components, such as fracture, stress cloud chart, strain cloud chart and so on.

For concrete material model in this simulation, it not only needs to determine the elastic and plasticity data including elasticity model E_s , Poisson ν , Dilation Angle A and so on, but also needs to calculate the data of compression and tensile behavior for concrete at inelastic phase. According to code for design of concrete structures, these data are determined by equations (2) and (3):

$$\text{Compression behavior: } y = \frac{x}{\alpha_t(x-1)^{1.7} + x}, x > 1 \quad (2)$$

$$\text{Tensile behavior: } \begin{cases} y = \alpha_a x + (3 - 2\alpha_a)x^2 + (\alpha_a - 2)x^3, & x \leq 1 \\ y = \frac{x}{\alpha_d(x-1)^2 + x}, & x > 1 \end{cases} \quad (3)$$

In equation (2) (3), α_t present descend stage of tension curve. α_a and α_d present ascend and descend stage of compression curve.

The damage factor can be obtained from literature[4], express as equations (4):

$$d_k = \frac{(1-\beta)\varepsilon^m E_0}{\alpha_k + (1-\beta)\varepsilon^m E_0}, (k = t, c) \quad (4)$$

In equation(4), t represents tension and c represents compression. β is the ratio of elasticity stress and plasticity tress, the number always lies between 0.35~0.7 when compression, 0.5~0.95 when tension, ε is strain when exceeds elastic phase.

Material data of shape steel and reinforcing bar used in the model are in table2.

Table 2 Mechanical properties of steel for simulate

Steel	$f_a / (\text{N} / \text{mm}^2)$	$E_a / (\text{N} / \text{mm}^2)$	ν
Shape steel	312.4	2.07×10^5	0.3
Longitudinal bar	384.0	2.06×10^5	0.3
Stirrup	297.5	2.06×10^5	0.3

Mesh. Meshing is very important when use microscopic finite method to simulate component. If the shape of the gridding is not fit to the rules, the results will non-convergence.

Loading. Gravity load and horizontal load are added in different loading steps. Gravity load is added in first step by instantaneous loading; the horizontal loading still uses displacement-control.

Simulate results Contrastive

It is shown from the results of macroscopic and microscopic model for SRC structure: when use macroscopic model to simulate the structure, it is important to build correct mechanical model for corresponding component, and this kinds of model make the structure excess simplify, more detail information can not be got from the simulate result. The microscopic model has an unusually high degree of detail, computation results are also reliable, but it spends too much time in building a model and needs high-performance computer to calculate. Besides, it needs workers learn enough finite element knowledge. Considering this, macroscopic model is more convenience for structure design, it has great significance in structure design, but it needs to improve its theoretical system for more structure.

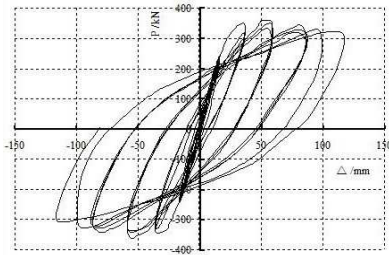


Fig.4 Hysteresis curve of test

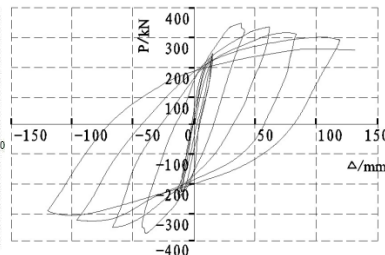


Fig.5 Simulate result of macroscopic model

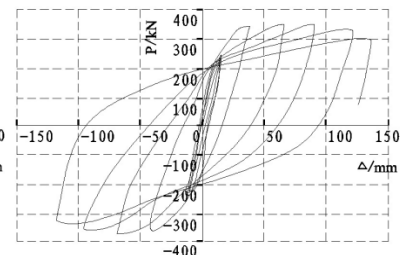


Fig.6 Simulate result of microscopic model

Conclusions

The advantage and disadvantage of the two finite element methods can be categorized as follows:

About macroscopic model:

- (1) It needs few elements to build these kinds of model, it just can express macro-mechanics behavior of the component, but the precision of the result is in tolerable range.
- (2) If the modularized program used for macroscopic model, the calculation and analysis for structure becomes more convenient, and it has great significance for structural design.
- (3) Macroscopic model can simulate regular shape of the component only, and it usually can't be qualified for simulate component with special-shaped of section.

About microscopic model:

- (1) It requires user learn some professional knowledge of microscopic finite method, and take long time to establish a model. Because of the number of the elements, it must be done right when meshing or choosing the step length of material curve, or the results will not be converged.
- (2) The stress and strain of significant details can be expressed in stress and strain curve charts. It has great importance for structure experiments research and single material structure analysis.
- (3) Microscopic model could not only simulate typical component and structure, but also could be applied to components or structure of special-shaped or under special loading.

Acknowledgments

This project is sponsored by National Natural Science Foundation of China (Grant No. 90815005, 50978218, 51108376), Research Fund for the Doctoral Program of Higher Education of China (Grant No. 20106120110003) and the Office Educational of Shan'xi Province in China (Grant No. 2010JK633).

References

- [1] Shan-suo ZHENG, Guo-zhuan DENG, Lei LI. Journal of Engineering Mechanics, Vol.26-5(2009), p.88-101.
- [2] Mander JB, Priestley MJN, Park R. Journal of Structural Engineering, Vol.114-8(1988), p.1804-26.
- [3] Menegotto M, Pinto P E. International Association for Bridge and Structural Engineering, (1973):p.15-22.
- [4] Jin Zhang, Qingyang Wang, Shouying Hu, Chuanjia Wang. Building Structure, Vol.38-8(2008), p.27-30.

A new method tracing load-deflection equilibrium path of a doubly nonlinear truss

Shutang Liu^{1,a}, Qiliang Long^{1,b}

¹School of civil engineering, Guangzhou University, Guangzhou city, China 510006

^aLQUUTH@163.com ^b275663117@qq.com

Key words: Nonlinear iteration technique, Post-buckling analysis, Truss structure

Abstract: A new method tracing the load-deflection equilibrium path of a truss with doubly nonlinearity is proposed. The total global stiffness matrix equation has been formulated in terms of nodal coordinates, iteration formulations has been written through adopting a single control coordinate, so that an new method tracing the load-deflection equilibrium path has been proposed. Analysis results of Star dome truss and Schwedeler dome truss have shown that the proposed method is stable numerically, quick in convergence, high in degree of accuracy and easy in use. The proposed method can be used for large-scale truss structure.

Introduction

For long span structures, especially trusses, how to establish and solve the nonlinear load-deflection equilibrium equation is very important. At present, the solution methods for the nonlinear equilibrium equation include the incremental iteration method[1], Newton-Raphson method, arc length method[2,3],and generalized displacement control method[4], Modified Normal Flow Algorithm[5]. Torkamani[6] pointed out that generalized displacement control method is one of the advanced nonlinear solution procedures and others have their limitations such as instability in the vicinity of critical points etc. Garcea[3] adopted a mixed formulation for tracing load-deflection equilibrium path so as to pass critical points of limit loads. In the present paper, a new method is proposed for tracing nonlinear load-deflection equilibrium path. Star dome truss and Schwedeler dome truss[7] are analyzed by the proposed method, and the results presents good agreement with that of the reference[7]. The proposed method can pass limit load points easily, quick in convergence, and high in degree of accuracy.

Nonlinear element stiffness matrix in terms of nodal coordinates

Suppose \mathbf{x} is a set of the member end nodal coordinate vectors in the deformed configuration of truss, the deformed member orientation vector can be written as: $\mathbf{l}(\mathbf{x}) = [-\mathbf{I}_3 \quad \mathbf{I}_3] \mathbf{x}$, where \mathbf{I}_3 is a unit matrix of 3 orders. The deformed member stress is denoted as $\sigma(\mathbf{x})$, and the member cross sectional area is denoted as A_x . the deformed member length is $l(\mathbf{x})$. The member end force vector under global system of coordinate is written as:

$$\mathbf{f}(\mathbf{x}) = \frac{1}{l(\mathbf{x})} \begin{Bmatrix} -\mathbf{l}(\mathbf{x}) \\ \mathbf{l}(\mathbf{x}) \end{Bmatrix} \sigma(\mathbf{x}) A_x = \frac{\sigma(\mathbf{x}) A_x}{l(\mathbf{x})} \begin{bmatrix} \mathbf{I}_3 & -\mathbf{I}_3 \\ -\mathbf{I}_3 & \mathbf{I}_3 \end{bmatrix} \mathbf{x}. \quad (1)$$

The element stiffness matrix yields:

$$\mathbf{s}_m(\mathbf{x}) = \frac{\sigma(\mathbf{x})A_x}{l(\mathbf{x})} \begin{bmatrix} \mathbf{I}_3 & -\mathbf{I}_3 \\ -\mathbf{I}_3 & \mathbf{I}_3 \end{bmatrix}. \quad (2)$$

Determination of member stress for ideal elastoplastic model

Suppose l_0 is the initial member length, ε_y and ε_{max} are yield strain and limit strain of material, respectively. The member critical lengths corresponding to ε_y and ε_{max} are:

$$l_b = (1 - \varepsilon_y)l_0, \quad l_t = (1 + \varepsilon_y)l_0, \quad l_{max} = (1 + \varepsilon_{max})l_0, \quad l_{min} = (1 - \varepsilon_{max})l_0. \quad (3)$$

The deformed member length is divided into four regions by the member critical lengths l_t, l_b, l_{max} and l_{min} the elastic, the plastic-tensile, the plastic-compressive and the failure. In fact, if a member produces plastic deformation, then the member critical lengths will change and need to be updated in iteration. In order to formulate iteration method, the member stress $\sigma(\mathbf{x})$ can be written in the difference of two parts for the ideal elastoplastic model, $\sigma(\mathbf{x}) = \sigma_s(\mathbf{x}) - \sigma_Q(\mathbf{x})$, in which, $\sigma_s(\mathbf{x})$ and $\sigma_Q(\mathbf{x})$ are as follow:

$$\left. \begin{array}{l} \text{if } l(\mathbf{x}) < l_{min} \text{ .or. if } l(\mathbf{x}) > l_{max} : \sigma_s(\mathbf{x}) = 0, \sigma_Q(\mathbf{x}) = 0 \\ \text{if } l_{min} \leq l(\mathbf{x}) < l_b : \sigma_s(\mathbf{x}) = E - \sigma_y, \sigma_Q(\mathbf{x}) = E \\ \text{if } l_b \leq l(\mathbf{x}) \leq l_t : \sigma_s(\mathbf{x}) = E + \sigma_y - E \frac{l_t - l(\mathbf{x})}{l_0}, \sigma_Q(\mathbf{x}) = E \\ \text{if } l_t < l(\mathbf{x}) \leq l_{max} : \sigma_s(\mathbf{x}) = E + \sigma_y, \sigma_Q(\mathbf{x}) = E \end{array} \right\} \quad (4)$$

Substitution of Eq.4 into Eq.2 makes $\mathbf{s}_m(\mathbf{x})$ to be form with the difference of two parts:

$$\mathbf{s}_m(\mathbf{x}) = \mathbf{s}(\mathbf{x}) - \mathbf{q}(\mathbf{x}). \quad (5)$$

The total nodal stiffness matrix equation can be expressed in the following form:

$$\mathbf{S}(\mathbf{X})\mathbf{X} - \mathbf{Q}(\mathbf{X})\mathbf{X} = \mathbf{A}. \quad (6)$$

Where \mathbf{X} is the total nodal coordinate vector for the deformed truss; \mathbf{A} is the total nodal load vector of a truss; $\mathbf{S}(\mathbf{X})$ and $\mathbf{Q}(\mathbf{X})$ are total global stiffness matrices.

Iteration technique for proposed method

The total nodal coordinate vector \mathbf{X} is classified as three subvectors: \mathbf{x}_e , \mathbf{x}_f and \mathbf{x}_r . x_f is a controlling coordinate; and \mathbf{x}_r is support restrained coordinate subvector. \mathbf{x}_e is free coordinate subvector. Through transformation, the global stiffness matrix is as follow:

$$\begin{bmatrix} \mathbf{S}_e & \mathbf{S}_{ef} & \mathbf{S}_{er} \\ \mathbf{S}_{fe} & S_f & \mathbf{S}_{fr} \\ \mathbf{S}_{re} & \mathbf{S}_{rf} & \mathbf{S}_r \end{bmatrix} \begin{Bmatrix} \mathbf{x}_e \\ x_f \\ \mathbf{x}_r \end{Bmatrix} - \begin{bmatrix} \mathbf{Q}_e & \mathbf{Q}_{ef} & \mathbf{Q}_{er} \\ \mathbf{Q}_{fe} & Q_f & \mathbf{Q}_{fr} \\ \mathbf{Q}_{re} & \mathbf{Q}_{rf} & \mathbf{Q}_r \end{bmatrix} \begin{Bmatrix} \mathbf{x}_e \\ x_f \\ \mathbf{x}_r \end{Bmatrix} = \begin{Bmatrix} \mathbf{I}_e f \\ I_f f \\ \mathbf{I}_r f \end{Bmatrix} + \begin{Bmatrix} \mathbf{0} \\ \mathbf{0} \\ \mathbf{r} \end{Bmatrix}. \quad (7)$$

From Eq.7, the iteration formulations are written as follow:

$$\mathbf{x}_e = \mathbf{S}_e^{-1} \left(\mathbf{I}_e f + [\mathbf{Q}_e \quad \mathbf{Q}_{ef} \quad \mathbf{Q}_{er}] \begin{Bmatrix} \mathbf{x}_e \\ x_f \\ \mathbf{x}_r \end{Bmatrix} - [\mathbf{S}_{ef} \quad \mathbf{S}_{er}] \begin{Bmatrix} x_f \\ \mathbf{x}_r \end{Bmatrix} \right). \quad (8)$$

$$f = \frac{1}{I_f} \left([\mathbf{S}_{fe} \quad S_f \quad \mathbf{S}_{fr}] - [\mathbf{Q}_{fe} \quad Q_f \quad \mathbf{Q}_{fr}] \begin{Bmatrix} \mathbf{x}_e \\ x_f \\ \mathbf{x}_r \end{Bmatrix} \right). \quad (9)$$

Steps for the proposed method

The iteration steps for the proposed method as follow:

1. Give initial structure coordinates, yield stress, elastic modulus, reference load vector;
- 2 Cycle start for x_f ;
- 3 Assemble $\mathbf{S}(\mathbf{X})$ and $\mathbf{Q}(\mathbf{X})$;
- 4 Perform iteration using Eq.8 and Eq.9;
- 5 $\max(\|\mathbf{x}_e^{(k)} - \mathbf{x}_e^{(k-1)}\|) \leq \varepsilon$? If yes, go step 6, else return step 3;
- 6 Record $\mathbf{x}_e^{(k)}$ and go to step 2;
- 7 Stop if all cycle for x_f is completed.

Confirmation for proposed method

Star dome truss. A star dome truss is shown in Fig.1. For all members, the section $A=3.17\text{cm}^2$, elastic modulus $E=3 \times 10^5 \text{N/m}^2$, and the yield stress $\sigma_y=200 \text{N/m}^2$. A vertical load P is applied to the central node(the node 1). The vertical coordinate of the central node is controlled ranging from 8.216cm to 3.216cm with step size of 0.2cm. The convergence tolerance $\varepsilon=10^{-5}$. Using the proposed method, relationships of Load P against the vertical displacement at the central node, are obtained for the linear elastic material(LEM), the nonlinear elastic material(NEM) and the ideal elasto-plastic material(EPM), as shown in Fig.2. Limit loads of LEM, NEM and EPM are 299.81N, 238.72N and 238.72N for the proposed method. The results of LEM and EPM are available in reference[7], and the result of EPM from ANSYS software has been given in Fig.2. The results from the proposed method are in good agreement with results of the reference[7] and ANSYS software. The relative errors of the present obtained limit loads to those of reference[7] and ANSYS software are below 0.8 percent.

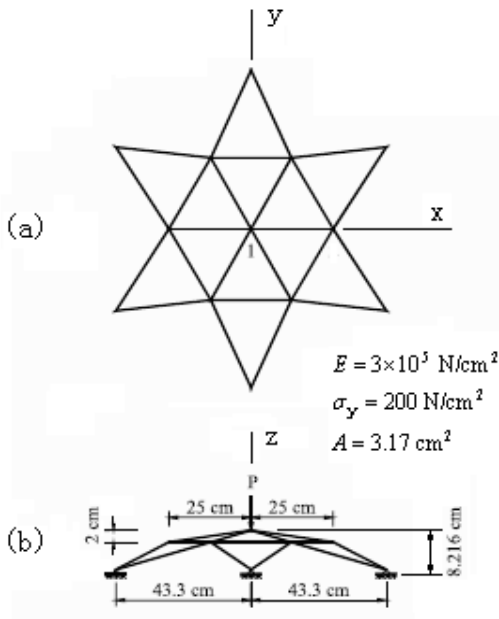


Fig.1 Star dome truss

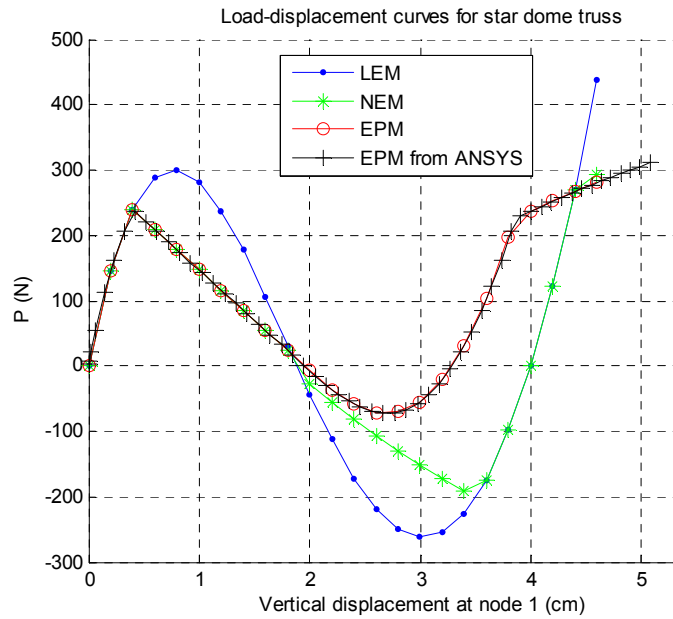


Fig.2 Load-displacement relationship for star dome truss

Schwedeler dome truss. A Schwedeler dome truss, composed of 61 nodes and 156 members, are shown in Fig.3. For all members, the sectional area $A=0.0032\text{m}^2$, the elastic modulus $E=2 \times 10^8\text{kN/m}^2$ and the yield stress $\sigma_y=2.5 \times 10^4\text{kN/m}^2$. A vertical load P is applied to the central node of the truss. All outer edge nodes of the truss are pinned. The vertical coordinate of the central node is controlled, ranging from 4.58m to 3.86m with step size of 0.02m. The convergence tolerance $\epsilon = 10^{-5}$. The relationships of the load P against the vertical displacement at the central node are shown in Fig.4 for the proposed method. Using the proposed method, limit loads of LEM, EPM and NEM are 30.58 kN, 19.51 kN and 19.51kN respectively. Curves of LEM and EPM are available reference[7], The result of EPM from ANSYS software is also plotted in Fig.4. The present obtained curves(fig.4) have shown good agreement with those. The relative error of the present limit loads to the results of reference[7] and ANSYS software are under 1 percent.

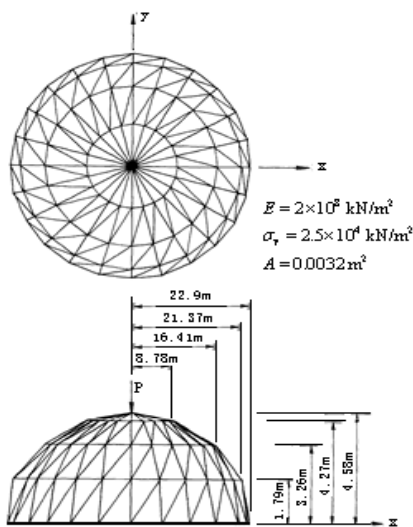


Fig.3 Schwedeler dome truss

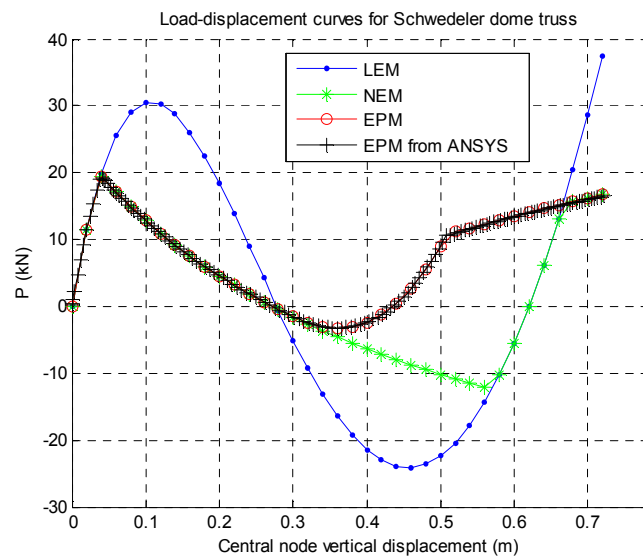


Fig.4 Load-displacement relationship for Schwedeler dome truss

Conclusions

In present paper, total global stiffness matrix equation has been established using nodal coordinates as unknowns, iteration formulations has been written through adopting a single control coordinate, so that an new method tracing the load-deflection equilibrium path has been proposed, conclusion are as follow:

(1)The proposed method is capable of solving the nonlinear problems in geometry and material, and passing limit load point easily.

(2)Aanalysis results of Star dome truss and Schwedeler dome truss have shown that the proposed method is stable numerically, quick in convergence, high in degree of accuracy and easy in use.

(3)The proposed method can be used for large-scale truss structure.

Reference

- [1] Y.B.Yang, S.P.Lin, C.S.Chen. Computer Methods in Applied Mechanics and Engineering, 196(2007).
- [2] G.E.Blandford. Computers & Structures. 58,5(1996).
- [3] Giovanni Garcea, Giuseppe A.Trunfio, Raffaele Casciaro. Computer methods in applied mechanics and engineering, 165(1998).
- [4] Huu-Tai Thai, Kim Seung-Eock.. Journal of Constructional Steel Research, 65(2009).
- [5] H.Saffari, M.J.Fadaee, and R.Tabatabaei. JOURNAL OF STRUCTURAL ENGINEERING(© ASCE), 134(2008).
- [6] Morteza A.M.Torkamani, Mustafa Sonmez. SOLUTION TECHNIQUES FOR NONLINEAR EQUILIBRIUM EQUATIONS. Proceedings of 18th Analysis and Computation Specialty Conference (© ASCE).(2008),USA.
- [7] M.Greco, F.A.R.Gesualdo,W.S.Venturini, H.B.Coda. Finite Elements in Analysis and Design, 42(2006).

Study on the Constitutive Model of Composite Materials in Elastic-Plastic Stage

Huanchao Qin^{1, a} Julin Wang^{2, b}

¹ Municipal Engineering Department, Shanxi Architectural College, 43 XueFu Street, Taiyuan
 030006, China

²Institute of Building Structures, Shanxi Architectural College, 43 XueFu Street, Taiyuan
 030006, China

^aq-huanchao98@163.com, ^bwangjl_tj@163.com

Keywords: constitutive model; composite materials; elastoplasticity

Abstract. Elastic-plastic properties of composite materials are an important part of the study on micromechanics. Based on the plastic strain of matrix, the elastic-plastic constitutive model of composite materials is presented in this paper, while considering the influence of the transient flexibility matrix on the flexibility matrix. In comparison with the experimental results, theoretical analysis of the presented model is validated.

Introduction

As we know, matrix plastic is the direct inducement of plastic deformation of composite [1-7]. On the basis of the elastic matrix [8], matrix equivalent plastic strain was selected as variable for investigating its relationship to bridging parameters, and finally determined the function expression of parameters during plastic phase. Afterwards, plastic equivalent constant of matrix was induced to determine the expression of current bridging matrix at plastic stage for establishment of composite elastic-plastic constitutive model.

The constitutive equation of matrix

Without considering ductile deformation, let's assume matrix is isotropic hardening material. The elastic-plastic problem of homogeneous matrix materials without fiber could be solved according to the classic elastic-plastic theory. Firstly, it was assumed at t moment we have known all state variables of pure matrix, such as elastic strain $(\boldsymbol{\varepsilon}^{el})_t$, plastic strain $(\boldsymbol{\varepsilon}^{pl})_t$ and equivalent plastic strain $(\bar{\varepsilon}^{eq})_t$, etc. Secondly, we would calculate all state variables under known strain increment $\Delta \boldsymbol{\varepsilon}_{ij}$. Partial strain tensor e_{ij} could be gained according to the relation between itself and strain tensor, as follows shown.

$$\boldsymbol{\varepsilon}_{ij} = e_{ij} + \frac{1}{3} \boldsymbol{\varepsilon}_{kk} \boldsymbol{\delta}_{ij} = e_{ij}^{el} + e_{ij}^{pl} + \frac{1}{3} \boldsymbol{\varepsilon}_{kk} \boldsymbol{\delta}_{ij}. \quad (1)$$

$$\Delta \boldsymbol{\varepsilon}_{ij} = \Delta e_{ij} + \frac{1}{3} \Delta \boldsymbol{\varepsilon}_{kk} \boldsymbol{\delta}_{ij} = \Delta e_{ij}^{el} + \Delta e_{ij}^{pl} + \frac{1}{3} \Delta \boldsymbol{\varepsilon}_{kk} \boldsymbol{\delta}_{ij}. \quad (2)$$

$$\boldsymbol{\varepsilon}_{ij}^{pl} = e_{ij}^{pl}, \quad \Delta \boldsymbol{\varepsilon}_{ij}^{pl} = \Delta e_{ij}^{pl}. \quad (3)$$

In the above equations, e_{ij}^{el} , e_{ij}^{pl} is partial elastic strain tensor and partial plastic strain tensor, respectively. $\boldsymbol{\delta}_{ij}$ is the symbol of Kronecker, Δ is limited incremental. The relation between partial stress tensor and partial strain tensor is

$$s_{ij} = 2G((e_{ij}^{el})_t + \Delta e_{ij}^{el}) = 2G((e_{ij}^{el})_t + \Delta e_{ij} - \Delta e_{ij}^{pl}). \quad (4)$$

Where, s_{ij} is partial strain tensor, G is shear modulus, the limited incremental of partial plastic strain tensor $\Delta \varepsilon_{ij}^{pl}$ is unknown. According to the yield condition, we can get the following equation.

$$\Delta e_{ij}^{pl} = \Delta \bar{e}^{pl} n_{ij}, \quad n_{ij} = \frac{3}{2} \frac{s_{ij}}{q}, \quad q = \sqrt{\frac{3}{2} s_{mn} s_{mn}}. \quad (5)$$

Where, $\Delta \bar{e}^{pl}$ is the equivalent plastic strain increment to be solved. Combining Equations (4) (5), we can get

$$\left(1 + \frac{3G}{q} \Delta \bar{e}^{pl}\right) s_{ij} = 2G((e_{ij}^{el})_t + \Delta e_{ij}). \quad (6)$$

In the above equation, each item multiplies itself, and let \tilde{e}_{ij} equals $(e_{ij}^{el})_t + \Delta e_{ij}$, there is

$$\left(1 + \frac{3G}{q} \Delta \bar{e}^{pl}\right) q = q + 3G \Delta \bar{e}^{pl} = \sqrt{\frac{3}{2}} 2G \sqrt{\frac{3}{2}} \sqrt{\sqrt{\frac{2}{3}} \tilde{e}_{ij} \tilde{e}_{ij}} = 3G \sqrt{\sqrt{\frac{2}{3}} \tilde{e}_{ij} \tilde{e}_{ij}}. \quad (7)$$

Tidying up Equation (7), we can obtain the following equation.

$$3G \left(\sqrt{\sqrt{\frac{2}{3}} \tilde{e}_{ij} \tilde{e}_{ij}} - \Delta \bar{e}^{pl} \right) - q = 0 \quad (8)$$

Plastic properties of matrix in unidirectional composite materials

The predictive value of strain of matrix is

$$\left\{ \varepsilon_{xx}^{m,pr}, \varepsilon_{yy}^{m,pr}, \varepsilon_{zz}^{m,pr}, \varepsilon_{xy}^{m,pr} \right\}_{n+1}^T = \left\{ \left(\varepsilon_{xx}^{m,el} \right)_n + \Delta \varepsilon_{xx}^m, \left(\varepsilon_{yy}^{m,el} \right)_n + \Delta \varepsilon_{yy}^m, f(\varepsilon_{xx}^{m,pr}, \varepsilon_{yy}^{m,pr}), \left(\varepsilon_{xy}^{m,el} \right)_n + \Delta \varepsilon_{xy}^m \right\}^T. \quad (9)$$

According to $\sigma_{zz}^m = 0$, use the constrains of plane stress as follows

$$\varepsilon_{zz}^{m,pr} = f(\varepsilon_{xx}^{m,pr}, \varepsilon_{yy}^{m,pr}) = -\frac{\nu^m}{1-\nu^m} (\varepsilon_{xx}^{m,pr} + \varepsilon_{yy}^{m,pr}). \quad (10)$$

So, the elastic stress prediction of matrix is

$$\left\{ \sigma^{m,pr} \right\} = \left[\mathbf{L}_4^m \right] \left\{ \boldsymbol{\varepsilon}^{m,pr} \right\} \quad (11)$$

According to $\bar{\sigma}^{m,pr} - 3\mu^m \Delta \bar{\varepsilon}^{m,pl} = q(\bar{\varepsilon}^{m,pl})$, we get the iterative equations.

$$\begin{cases} R = \bar{\sigma}^{m,pr} - 3G^m \Delta \bar{\varepsilon}^{m,pl} - q(\bar{\varepsilon}^{m,pl}) \\ \left(\Delta \bar{\varepsilon}^{m,pl} \right)_{n+1} = \left(\Delta \bar{\varepsilon}^{m,pl} \right)_n + R / (3G^m + h^m) \end{cases} \quad (12)$$

By calculating the above simultaneous equations, matrix equivalent plastic strain of matrix $\Delta \bar{\varepsilon}^{m,pl}$ can be obtained.

$$\text{The direction of plastic flow: } \eta_{ij} = S_{ij}^{m,pr} / \bar{\sigma}^{m,pr}. \quad (13)$$

$$\text{The plastic strain increment of matrix: } \Delta \varepsilon_{ij}^{m,pl} = \frac{3}{2} \eta_{ij} \Delta \bar{\varepsilon}^{m,pl}. \quad (14)$$

The renovated matrix strain:
$$\begin{cases} (\varepsilon_{ij}^{m,pl})_{n+1} = (\varepsilon_{ij}^{m,pl}) + \Delta\varepsilon_{ij}^{m,pl} \\ (\varepsilon_{ij}^{m,el})_{n+1} = \varepsilon_{ij}^{m,pr} - \Delta\varepsilon_{ij}^{m,pl} \end{cases} \quad (15)$$

The renovated matrix stress:
$$(\sigma_{ij}^m)_{n+1} = \eta_{ij} \bar{\sigma}_y^m + \frac{1}{3} \delta_{ij} \sigma_{kk}^{m,pr} \quad (16)$$

The strain matrix:
$$(\varepsilon_{ij}^m)_{n+1} = (\varepsilon_{ij}^{m,pl})_{n+1} + (\varepsilon_{ij}^{m,el})_{n+1} = \varepsilon_{ij}^{m,pr} \quad (17)$$

It can be seen from the above Equations (13), (14), (15), (16), (17) that in the whole calculation process the total strain remained unchanged while the proportion between the elastic strain and the plastic strain changed. Through the equivalent strain of matrix we can get hardening modulus h^m . The formulas through which Tangent modulus E_t^m , Poisson's ratio ν_m' and Shear modulus G_m' can be gotten are as follows.

$$E_t^m = \frac{h^m E^m}{h^m + E^m} \quad (18)$$

$$\nu_m' = \frac{1}{2} - \left(\frac{1}{2} - \nu^m\right) \frac{E_t^m}{E^m} \quad (19)$$

$$G_m' = \frac{E_t^m}{2(1 + \nu_m')} \quad (20)$$

The current flexibility matrix has the same form with the flexibility matrix of elastic phase, we substitute Tangent modulus, Poisson's ratio and Shear modulus with the parameters in the above three formulas.

Calculation examples and analysis

According to the above calculation model, we will calculate the shear properties of unidirectional composite materials. In the example, $E^f = 74GPa$, $\mu^f = 0.2$, the stress-strain curve is shown in Fig. 1, the equivalent stress-strain curve of plasticity is shown in Fig. 2. For convenience, eight fold lines are used to simulate this curve. The numerical values of stress, strain and hardening modulus in the endpoint of fold lines can be seen in Tab.1. The initial value of the parameters α_0 , β_0 is 0.35 and 0.45, respectively.

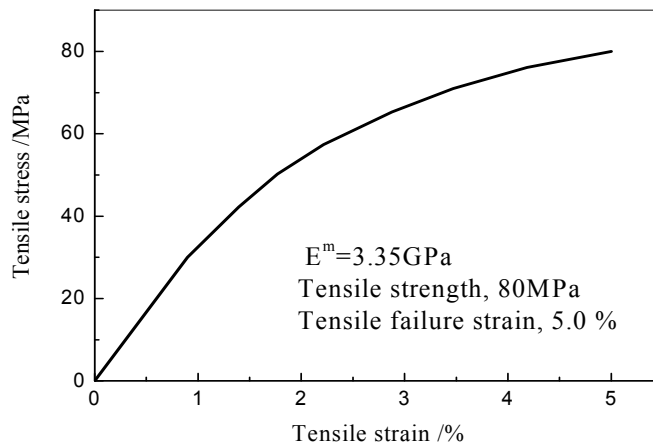


Fig.1 The stress-strain curve

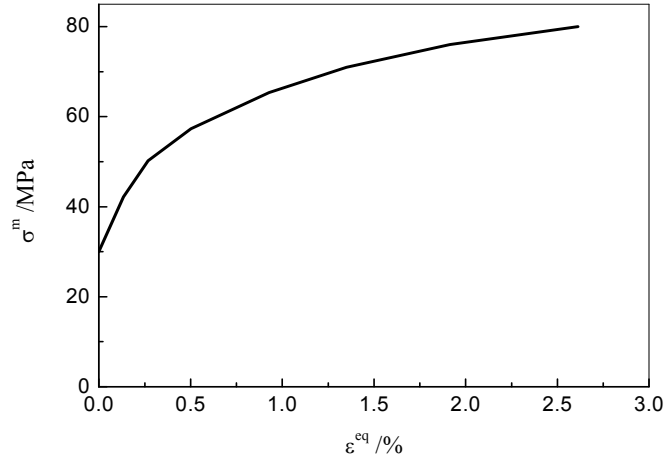


Fig. 2 The equivalent stress-strain curve

Tab.1 The elastic-plastic parameters

Break point number	1	2	3	4	5	6	7	8	9
Stress (MPa)	0.0	30.0	42.2	50.2	57.35	65.37	71.0	76.06	80.0
Strain (%)	0.0	0.898	1.394	1.768	2.214	2.879	3.471	4.184	5.0
Equivalent strain (%)	0.0	0.0	0.134	0.269	0.502	0.928	1.351	1.914	2.612
Hardening modulus (MPa)	0.0	9.104	5.926	3.069	1.883	1.331	0.899	0.564	
α_x	0.35	0.35	0.533	0.64	0.76	0.844	0.915	0.96	0.96
β_x	0.45	0.45	0.609	0.716	0.820	0.893	0.958	1.0	1.0

According to eight fold lines and nine end points of matrix, we could calculate relevant values of α_x , β_x , which are shown in Tab. 1.

The shear stress-strain curve of unidirectional composite materials is shown in Fig. 3. It could be seen that the calculation curve was roughly the same with the experiment curve. Before ϵ is equal to 1.32%, the three curves were almost in the same locus; when the shear deformation of unidirectional composite materials reached 4%, the estimated α_x and β_x changing linearly is 78.2MPa, which was 7% higher than the 73 MPa as the experimented value while the expected curves of α_x and β_x changing nonlinearly were almost the same with the experimented curves. Fig. 4 showed the crosswise s pressure tress-strain curve. From Fig. 4 it can be seen that the curve was basically the same with the experimented curve.

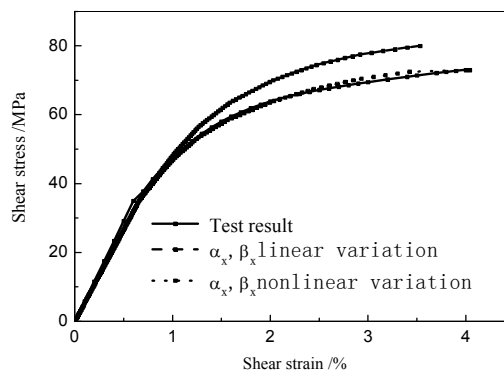


Fig. 3 The curve of shear stress-strain of unidirectional composite materials

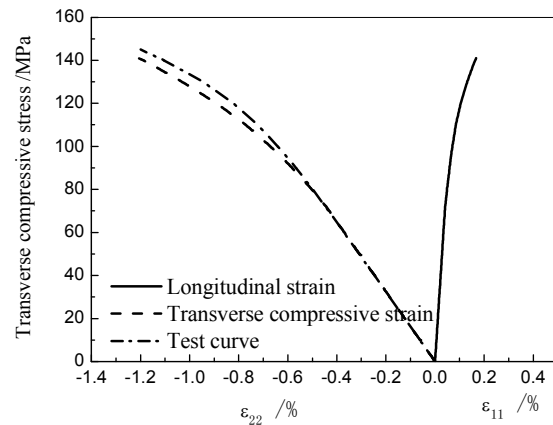


Fig. 4 The crosswise s pressure tress-strain curve

Conclusions

The paper establishes of the elastic-plastic constitutive model of composite materials. By comparison with the experimental results, it can be seen that the method which the paper presents is feasible.

References

- [1] ZhangZY, Richardson MOW. Low Velocity Impact Induced Damage Evaluation And Its Effect on the Residual Flexural Properties of Pultruded GRP Composites. *Composite Structures*, Vol. 81 (2007), p. 195-201.
- [2] BatraRC, HassanNM. Response of Fiber Reinforced Composites to Underwater Explosive Loads. *Composites: Part B* (2007), p. 448-468.
- [3] GowerHL, CroninDS, PlumtreeA. *International Journal of Impact Engineering*, 35(2008), p. 1000~1008.
- [4] AzouaouiK, Ouali N, OurouaY, MesbahA, BoukharoubaT. *Journal of Sound and Vibration*, Vol. (308) 2007, p.504-513.
- [5] PierreRossi, EdouardParant. Damage mechanisms analysis of a multi-scale fibre reinforced cement-based composite subjected to impact and fatigue loading conditions. *Cement and Concrete Research*, Vol. 38(2008), p.413-421.
- [6] VolneiTita, JonasdeCarvalho, DirkVandepitte. Failure analysis of low velocity impact on thin composite laminates: Experimental and numerical approaches. *Composite Structures*. Vol. 38(2008), p.413-428.
- [7] MichaelHebert, Carl-ErnstRousseau, ArunShukla. Shock loading and drop weight impact response of glass reinforced polymer composites. *Composite Structures*, Vol. 84(2008), p.199-208.
- [8] DhakalHN, ZhangZY, RichardsonMOW, ErrajhiOAZ. The low velocity impact response of non-woven hemp fibre reinforced unsaturated polyester composites. *Composite Structures*. Vol. 81(2007), p.559-567.

Experimental study of blind bolted joints to concrete-filled thin-walled steel tubular columns under cyclic loading

Jingfeng Wang^{1,2,a}, Xinyi Chen^{1,b}, Hetao Hou^{3,c}

¹School of Civil Engineering, Hefei University of Technology, Hefei, 230009, China

²Anhui Civil Engineering Structures and Materials Laboratory, Hefei, 230009, China

³School of Civil Engineering, Shandong University, Jinan, 250061, China

^ajfwang008@163.com, ^bchenxinyi80@hotmail.com, ^chouhetao@163.com

Keywords: Concrete-Filled Thin-Walled Steel Tubular (CFTST), Hysteretic Behaviour, Blind Bolts, joint, Cyclic loading.

Abstract. This paper discusses results of experiments on blind bolted end plate joints to concrete-filled thin-walled steel tubular (CFTST) columns. Four exterior joints to CFTST columns subjected to cyclic loadings. A feature of this novel joint is the use of the blind bolts and extensions to these bolts into the concrete-filled square steel tubular column. Failure modes, moment-rotation hysteretic curves and energy consumption of the connections were analyzed. Further, the connection rigidity and ductility were also elevated by present specifications. The test results showed that the end plate type and the steel tube thickness affect the seismic behaviour of the typed blind bolted end plate joints. The proposed joint has reasonable strength, stiffness and ductility by taking reasonable end plate type, steel tube thickness and blind bolt anchorage; its ultimate connection rotation satisfies the ductility design requirements, and could be reliably and safety used in low-layer or multi-layer composite frames

Introduction

Concrete-filled steel tubular (CFST) columns exhibit excellent structural and constructional benefits. The steel tube provides confinement and thus increases the stiffness and strength of the concrete, and eliminates the use of the framework during construction. Meanwhile, the concrete reduces the possibility of local buckling of the tube wall. Concrete-filled thin-wall steel tubular (CFTST) column, which consist of very thin steel tubes and concrete, is a novel type of structural member and was developed based on the traditional CFST columns. Due to the merits of both thin-walled steel structures and reinforced concrete structures, there has been a growing research and interest in this area.

Previous investigations on the static behaviour [1-2] and the hysteretic behaviour [3] of CFTST columns have been conducted. However, research work on the mechanical behaviour and design method of the joints to CFTST columns seems to be lacking, so that it limits application of this novel structure. After the 1994 Northridge earthquake and the 1995 Kobe earthquake, growing interests are given to semi-rigid connection which involves energy dissipation and ductility. Wang et al [4-5] proposed an innovative approach of blind bolting a flush end plate to concrete-filled circular or square hollow columns. They suggested that the blind fasteners could be used in the CFTST column connections to resolve the installation difficulty.

Scant attention has been paid to considering the seismic behaviour of the blind bolted end plate joints to CFTST columns. This paper presents an experimental study on four specimens of CFTST column connections under cycle loadings. The failure modes, hysteretic performance, ductility and energy dissipation capacity were evaluated in this paper.

Experimental Program

Specimen Design. Four test specimens were designed and fabricated to study the hysteretic performance of the CFTST column joints. Table 1 and Fig.1 provides the design details of specimens. The specimen DTE1 and DTE2 are extended end plate connections, while the specimen DTF1 and DTF2 are flush end plate connections. These square tubes were all manufactured by seam welding together four pieces of lipped angle, which made from cold rolled thin steel sheet with nominal wall thickness 1.5 mm or 3 mm. Meanwhile, the beams are commercial H-shape steel sections of a cross-section HN300×150×6×10 mm for all test specimens.

Table 1 Information of the test specimens

Specimen number	Column section	Beam section	Endplate thickness		Endplate type
	B or D mm	$h_b \times b_{fb} \times t_{wb} \times t_{fb}$ mm	t_p mm	N_0 mm	
DTE1	200×1.5	300 × 150 × 6 × 10	12	703	Flush end plate
DTE2	200×3.0	300 × 150 × 6 × 10	12	911	Flush end plate
DTF1	200×1.5	300 × 150 × 6 × 10	12	703	Extended end plate
DTF2	200×3.0	300 × 150 × 6 × 10	12	911	Extended end plate

The end plate connections were adopted by using blind bolts with extensions to connect the steel beams to CFST columns. The blind bolts used in the tests were Grade 10.9 M20, which were a nominal ultimate and yield stress of 1000 N/mm² and 900 N/mm², respectively. The extensions to the bolts were 20 mm diameter 50 mm length reinforcing bars. These reinforcing bars were welded to the head of the bolt to form a complete unit.

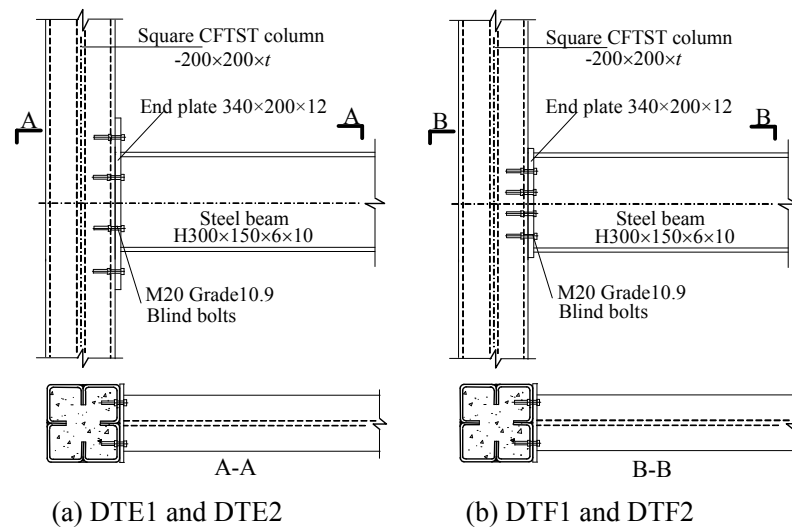


Fig.1. Details of blind bolted specimens to CFTST columns

Table 2 summarises the results of the material tests of the steel coupons used in the specimens. The compressive cube strength (f_{cu}) of the self-consolidating concrete was found to be 44.34 N/mm² at 28 days. On the day of testing, the compressive strength from cube samples was 48.27 N/mm² and the modulus of elasticity was 33,521 N/mm².

Table 2 Material properties of steel

Specimen number	Steel wall thickness (mm)	Yield stress (N/mm ²)	Ultimate stress (N/mm ²)	Elastic modulus (N/mm ²)	Elongation at fracture(%)
Steel beam flange	10	349.3	492.0	1.87×10^5	16.5
Steel beam web	6	312.5	508.3	2.16×10^5	17.4
steel tube-1	1.5	236.7	307.2	1.71×10^5	20.1
steel tube-2	3	267.2	368.3	1.86×10^5	23.4
Endplate	12	323.3	436.7	1.98×10^5	31.0

Experimental Setup and Loading History. The experimental setup photo is shown in Fig. 2. The loading history of the specimens was generally based on the ATC-24 [6] guidelines for cyclic testing of structural steel components. The adopted loading history is shown in Fig.3. The magnitude of the displacement increases gradually until the testing specimens are damaged or have larger deformations. The beam tip displacement was automatically recorded by hydraulic actuator acting on each beam tip. In addition, non-linear variable displacement transducers (LVDTs) were mounted to measure the connection rotation, shear displacement in the panel zone and side-sway of the specimens. For the composite joint specimens, a total of fifty-five strain gauges were employed in each specimen. Strain gauges were used to monitor the strains in the beam flanges and webs, end plate and the steel tube. All readings were recorded using a microcomputer.



Fig. 2. Experimental setup photograph

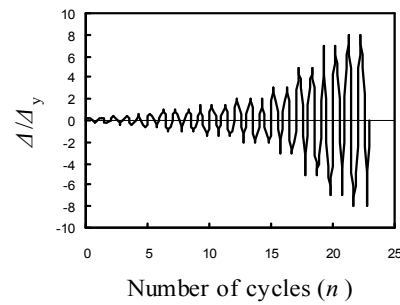


Fig. 3. Loading history

Experimental Result Analysis and Discussion

Failure Modes. In the case of the blind bolted end plate connections to CFTST columns, failure (seen in Fig.4) occurred in the following modes: (1) deformation of the end plate; (2) outward deformation of the column flange; (3) anchorage fracture of the tensile bolts with extensions in the square columns; (4) crushing of the core concrete due to the larger connection rotation.

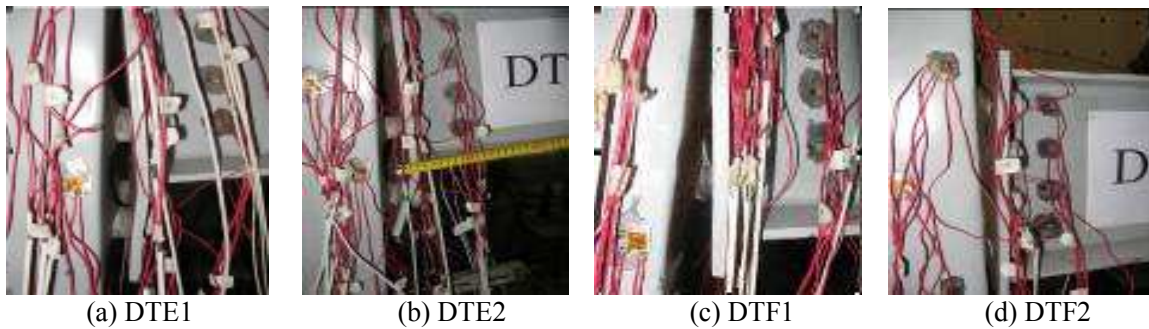


Fig.4 Failure modes of test specimens

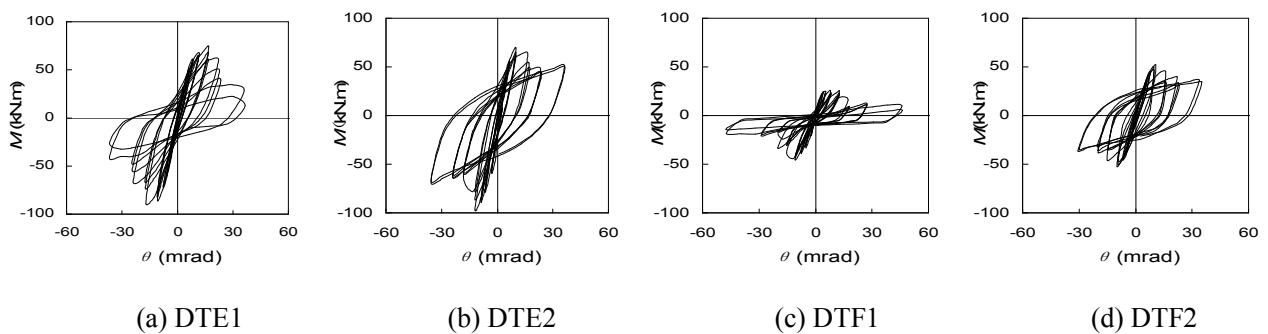


Fig.5 Moment - rotation hysteretic curves

Moment-Rotation Hysteretic Relationship. Moment-rotation hysteretic curves of all specimens are shown in Fig.5. It was demonstrated that strength and stiffness of the blind bolted end plate joints may be affected by the end plate type and the steel tube thickness. An increased the steel tube thickness enhanced stiffness and strength of nominally identical connections. Moreover, the maximum strength and initial stiffness of the extended end plate joint is more than that of the flush end plate joint.

Energy Dissipation. Table 3 illustrates the total dissipated energy capability of the CFTST column specimens. Table 43 indicates that: (1) At ultimate limit state (ULS) and failure state (FS), the dissipated energy capability E_e , the equivalent damping coefficient ξ_e and the whole dissipation energy W_{total} of specimen DTE2 are larger than those of specimen DTE1, similar with specimen DTF2 and DTF1. (2) At ultimate limit state (ULS) and failure state (FS), the dissipated energy capability E_e , the equivalent damping coefficient ξ_e and the whole dissipation energy W_{total} of extended end plate connections are larger than those of flush end plate connections.

Table 3 Energy dissipation parameters

Specimen number	Limit state	Δ / Δ_y	W_{total} (kN.mm)	ξ_e	E_e
DTE1	ULS	1.5	2759	0.175	1.097
	FS	2.	4898	0.218	1.367
DTE2	ULS	1.5	3286	0.265	1.662
	FS	3	9726	0.297	1.867
DTF1	ULS	1	388	0.096	0.601
	FS	1.5	835	0.160	1.005
DTF2	ULS	1	690	0.117	0.735
	FS	1.5	1961	0.262	1.645

Note: Ultimate Limit State and Failure State are respectively the limit state corresponding to $P=P_{max}$ and $P=0.85P_{max}$.

Ductility. The displacement ductility coefficient and angular ductility coefficient can be used to estimate the ductility of the joints in seismic loading. The displacement ductility coefficient, μ , is defined as the ratio between the failure displacement, Δ_u , and the yielding displacement, Δ_y . It can be expressed as $\mu=\Delta_u/\Delta_y$. The angular displacement ductility coefficient, μ_θ , is defined as the ratio between the failure angular displacement, θ_u , and the yielding angular displacement, θ_y . It can be expressed as $\mu_\theta=\theta_u/\theta_y$. Table 4 gives the displacement ductility coefficient and the angular ductility coefficient of the test specimens.

Table 4 Ductility coefficient of the test specimens

Specimen number	Δ_y (mm)	Δ_u (mm)	θ_y (mrad)	θ_u (mrad)	μ	μ_θ
DTE1	7.32	44.18	4.65	28.05	6.04	6.04
DTE2	8.55	51.27	5.43	32.55	6.00	6.00
DTF1	9.67	58.20	6.14	36.95	6.02	6.02
DTF2	13.47	96.09	8.55	61.01	7.13	7.13

The Chinese building seismic design code GB50011 [7] give the detail ductility regulation for the steel frame structures: the elastic layer angular displacement $[\theta_e]=1/250=0.004\text{rad}=4\text{mrad}$, and the elastic-plastic layer angular displacement $[\theta_p]=1/50=0.02\text{rad}=20\text{mrad}$. However, presently it is lack of the detail ductility regulation for the CFTST structures. From Table 4, it is concluded that the displacement ductility coefficient of the test specimens $\mu=6.00\sim 7.13$, the elastic yielding angular ductility coefficient $\theta_y=1.16[\theta_e]\sim 2.13[\theta_e]$, and the elastic-plastic angular ductility coefficient $\theta_u=1.40[\theta_p]\sim 3.05[\theta_p]$. Through comparison with the steel frame in the elastic and elastic-plastic layer angular displacements, the result showed the blind bolted end plate joints to CFTST columns have excellent ductility and can satisfy the request of the structural seismic design.

Rigidity Elevation. In order to assert the connection rigidity in the moment-rotation curves for the end plate connections to CFTST columns, the typed connection may be classified by EC3 Part 1-8[8]. The analysis results showed that the blind bolted end plate connections in the specimens presented herein may be classified as semi-rigid and partial strength, except that specimen MTF1 with 1.5 mm. It is also found that the rotation capacities of the specimens satisfy the ductility requirement of no less than 30 mrad for earthquake resistance, suggested by FEMA-350 [9].

Conclusions

The following observations and conclusions can be drawn within the limitation of the experimental research reported in this paper:

- The strength and stiffness of the blind bolted end plate joints to CFTST columns may be influenced by the end plate type and the steel tube thickness, so that they will be considered in the design of CFTST frames.
- The test results demonstrated the strength and stiffness of the connections can be improved by providing anchorage extensions to the blind bolts, according to failure modes and stain response.
- The blind bolted end plate connection to CFTST columns is classified as semi-rigid and partial strength by EC3 specification, except that the square CFST column connection with thinner steel tube behaves in a semi-rigid and simple manner.
- The proposed CFTST column joint with moderately thick steel tube exhibits reasonable strength and stiffness, while its rotation capacity satisfies the ductility requirement for earthquake resistance in seismic region.

Acknowledgements

The research reported in this paper is part of Project 51178156 and 50808062 supported by the National Natural Science Foundation of China, and the project 200803591022 supported by a grant from the Ph.D. Programs Foundation of Ministry of Education of China.

References

- [1] Z. Tao, L.H. Han, and Z.B. Wang. *Journal of Constructional Steel Research*. Vol. 61 (2005), p.962-983.
- [2] N.E. Shanmugan, B. Lakshmi, and B. Uy. *Engineering Structures*. Vol. 24 (2002), p.825-838.
- [3] Y.C. Zhang, C. Xu, and X.Z. Lu. *Journal of Constructional Steel Research*. Vol. 23 (2007), p.317-325.
- [4] Wang J F, Han L H, Uy B. *Journal of Constructional of Steel Research*, Vol. 65 (2009), p. 1644-1663.
- [5] Wang J F, Han L H, Uy B. *Journal of Constructional of Steel Research*, Vol. 65 (2009), p. 925-939.
- [6] ATC-24: *Guidelines for Cyclic Seismic Testing of Components of Steel Structures*. (Applied Technology Council, Redwood 1992).
- [7] GB50011-2010: *Specification of Structural Earthquake-Resistant Design*. (China Building Industry Press, Beijing 2002). (in Chinese)
- [8] Eurocode 3. *Design of steel structures. Part 1.8: Design of joints*. (ECCS Press, Brussels 2005).
- [9] FEMA-350, *Recommended seismic design moment-frame buildings*(Federal Emergency Management Agency Press, Washington 2000).

Frame column of the limit value of axial compression ratio of

Zhineng Tong

Jiangxi Science & Technology Normal University China

Keywords: columns, ductility, axial compression ratio, seismic design

Abstract: In the current specification of the pressure ratio limit requirement is not specific, not fully consider the impact of seismic design of frame column ductility of other factors. According to the influencing factors of column ductility analysis, reached standard of axial pressure ratio limit values in most cases are conservative, may be appropriate to do the relaxation adjustment conclusion.

Preface

General building after the first phase of seismic design can satisfy the first second standards, the requirements of seismic fortification, when more strong earthquakes, hard to avoid loss. The main goal is to prevent building collapse, must make the structure in the serious damage of the remains of a stable system, requires structural member and node has better ductility, using components of the plastic deformation of the seismic energy consumption as much as possible, so that the structure can bear large deformation and not collapse. So, in seismic design, ductility and seismic capacity of equal or greater importance. Especially for large earthquake resistance, must be taken to increase the ductility of measures, which is a reinforced concrete structure seismic design provisions relating to the starting point.

The ductility of the structure generally includes structure and ductility. The ductility of the structure is divided into general ductility ductility and floor. The ductility of the structure is realized by the ductility. Ductility requirements than the ductility of the structure to high. The relationship between the two and the structure of the plastic hinges formed after the destruction mechanism. Ductility by ductility of section to ensure. Although the ductility of many experimental studies, but it is difficult to make accurate calculation, so the standard is based on the experimental results, theoretical analysis and engineering experience from the concept of qualitative rules of various structural measures, in order to ensure the structure has enough ductility. Structure on the ductility and energy dissipation of the strict degree is divided into four levels: (1) is very strict, strict (class of two), a strict (level three) and general (four), specification called structure seismic grade. The seismic intensity is higher, the greater the structure deformation, ductility demand strict. So the structure of the fortification intensity is high, aseismatic grade is high.

Seismic design principles

According to the standard determined by the effect on the structure of the earthquake action, actually is not the biggest. Seismic and dynamic analysis calculation, structure the actual earthquake may be much larger than the standard. But the earthquake action such as too large, will increase the seismic fortification investment; too small, cannot guarantee the reliability, standard determined by the earthquake effect is often considered the two aspects of the technical policy the acceptable minimum effect. Other possibilities for some of the excess energy dissipation mechanism of some structural portion is formed to absorb and dissipate energy as compensation.

The frame structure is a statically indeterminate structure. If some parts of plastic hinge without generating member of local brittle failure, then the frame structure under strong earthquake has become a larger deformation capacity of the structure, the structure deformation to absorb and dissipate energy, thereby reducing the seismic responses of structures, the seismic control of structure subjected to strong earthquake, providing, to prevent collapse ability. Therefore, frame structure must assume in the fortification intensity of earthquake occurrence, structure in some parts of the bar will yield, can be formed with sufficient rotation capacity of the plastic hinge, to ensure that the structure has enough ductility.

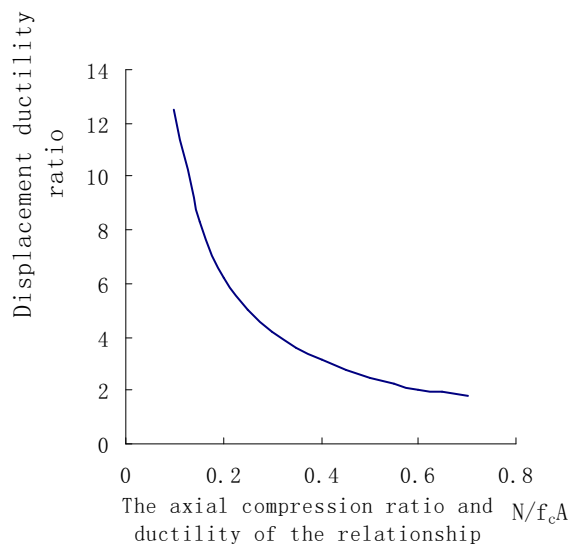
Axial compression ratio on ductility of frame column

Main beam subjected to bending moment, yield much energy dissipation, hysteresis loop and stable. To press column, less energy consumption, the hysteresis loop of narrow pillar has a high ductility, requirements are not easy to achieve. In addition, collapse of buildings is the most direct reason of vertical load force decreases with pillars. Column end plastic hinges, the vertical bearing capacity will decrease, when the bearing capacity decreased to below the column should carry axial forces will endanger the safety of the whole structure. Engineering practice shows that the earthquake damage, axial compression ratio on seismic behavior of reinforced concrete frame columns of great influence, in the framework of the numerous factors affecting the ductility of columns (longitudinal steel reinforcement ratio, stirrup reinforcement ratio, steel grade, the grade of concrete strength, axial compression ratio, shear span ratio, section shape) to axial compression ratio, distribution steel ratio and shear span ratio has the most significant effect.

Experiments show that, axial pressure ratio is directly related to the size of the failure pattern of the column. Axial compression ratio refers to the column axial force N and according to column full section concrete compressive strength design value calculation of pressure (f_{cbh}) ratio. The axial force N is considering earthquake action combination of axial force design value. Axial compression ratio is relatively small, under the horizontal earthquake action, will have large eccentric compression column of flexural failure, column section compression zone between smaller, the reinforced concrete into the stress state before, which has better ductility. Axial compression ratio, small eccentric compression column will occur the compressive failure, the column height of compression zone between large, yet yield tensile reinforcement, concrete has been crushed. The brittle failure almost no displacement ductility. As with frame deformation capacity is closely related to the column ductility along with the increase of axial compression ratio and a sharp decline (see chart), but also in high axial compression ratio of column stirrup deformation capacity influence also will be more obvious. Therefore, anti seismic frame column section size must be reasonable, to control the axial compression ratio, so that the frame column constraints in large eccentric compression range, to ensure that the column has certain ductility. Specification given in article 6.3.7 of frame column limit values of axial compression ratio, see the table below 1-1 and axial compression ratio and ductility of diagram.

Table 1-1 Limited Coefficient of Axial Compression

Aseismic grade	1	1	2
Frame column	0.7	0.8	0.9



Relationship of Axial Compression & stretch

The size of eccentric compression at the junction of the limit values of axial load ratio corresponding to I, II grade of approximately 0.8 and 0.75, taking into account the column section is the influence of architectural layout and use requirements, so the axial compression ratio and should not be too severe. So, in addition to a standard 6.3.7 seismic grade frame column strictly limited to the boundaries of axial compression ratio, level two or three earthquake resistant frame column of limit values of axial compression ratio of 0.8 and 0.9, slightly higher than the limit values of axial compression ratio. Three level earthquake intensity of frame column is mainly used for low, housing is not high and the shear wall as a first line of defense structure, it may be appropriate to increase the axial compression ratio. On the two grade earthquake grade column, should adopt strong column and weak beam, strong shear weak bending, reinforcing stirrup favorable measures.

In the actual design work, with the structure calculating software on high-rise structural seismic analysis, often appear column section consists of limit values of axial compression ratio to determine, column reinforcement for structural configuration, it is not reasonable. The column is too large, not only reducing the use of space, and decrease column shear span ratio, increased stiffness, seismic response is increased, thereby causing the brittle failure of columns, seismic unfavorable. Therefore, in aseismic design, should be integrated into the influence factors of the column ductility, should not care for this and lose that.

Impact ductility of columns of the frame structure of other factors

4.1. Shear span ratio

Shear span ratio is a reflection of the column under bending moment and shear force of the ratio of a parameter, expressed as: $\lambda = M/Vhc = Hn/2hc$

Test results show that the shear span ratio can roughly reflect the bending normal stress and shear stress ratio, is to determine the frame column is ductile failure or brittle fracture is the dominant factor, column shear span ratio is larger, better ductility. When the shear span ratio is more than 2 for the long column, column failure mode for bending type, as long as reasonable structure, generally can meet the column oblique section shear is larger than that of the normal section bearing capacity requirements, and have certain deformation capacity. When $1.5 \leq \lambda < 2$ for short column, column will produce mainly shearing destruction, when increasing concrete strength or with insufficient stirrups, may also occur with certain ductility shear compression failure. When $\lambda < 1.5$, for short columns, column failure patterns for the brittle shear failure, poor seismic performance, general design should be avoided. If unavoidable, axial pressure ratio limit should be devoted to the study and take special measures to ensure its oblique section bearing capacity. Therefore, norms of $\lambda \leq 2$ short columns axial compression ratio limit values than columns limit decrease 0.05.

4.2. Stirrup

Frame pillar damage except for bending strength caused by the lack of end column horizontal crack, damage is more common, due to lack of stirrup or unreasonable structure, body appear inclined crack, end column concrete crushed, cleft oblique or longitudinal reinforcement pop-up node. Theoretical analysis shows that, in the concrete core column of stirrups on plays an effective role in binding, can significantly improve the ultimate strain of concrete under compression, block column oblique crack development, thus greatly improving the ductility of the column. Therefore, the column of various parts of the rational allocation of the hoop is very necessary.

Experiments show that with the axial pressure increases, the ductility of the member in the fall. With the stirrup spacing decreases, the ductility increases. This shows, the axial compression ratio of high component needs to be configured in order to ensure adequate stirrup ductility. When concrete is subjected to compressive ultimate strength of pressure, the transverse deformation of concrete to increase sharply. Stirrup presence limits the transverse deformation of concrete, thus improving the ultimate deformation capacity of concrete, served to strengthen the role of ductility. Stirrup spacing

number, density, the restriction to concrete effect is big. The amount of available volume reinforcement ratio table. On the different axial compression ratio should be used in different minimum stirrup ratio. The stirrup ratio equal situation, different forms of stirrup, concrete core area constraint is not the same. Rectangular band only in the four corner areas of concrete to produce effective lateral pressure, whereas in the straight section steel hoop, or heave, constraint effect is not big. Double cross compound spiral hoop hoop, the stirrup without supporting length decreases, each in a stirrup intersection point has a longitudinal bar, longitudinal reinforcement and stirrup constitute a grid framework, greatly increase the hoop constraint, the ductility of the column profile than the ordinary rectangular stirrup is improved.

4.3. The longitudinal reinforcement ratio

Studies have shown, column longitudinal reinforcement yielding angle deformation, mainly by the longitudinal tensile reinforcement ratio, and generally along the longitudinal reinforcement ratio increased linearly increasing, in order to avoid the earthquake post prematurely enters the yield stage, as well as increasing the yield pillar deformation ability, improving column ductility and energy dissipation capacity, all longitudinal steel reinforcement ratio should not be too small. Frame column of longitudinal reinforcement of the minimum reinforcement ratio in accordance with the static calculation based on numerical be properly increased by raising the minimum reinforcement ratio, the aim is to improve the ductility of the columns of frame, the yield moment is far greater than the column of the cracking moment, assurance framework in column yield have larger deformation ability, while the maximum reinforcement ratio than the static calculation the maximum reinforcement rate to be low, this is to make the pillar has better ductility, and indirectly limit column under shear value.

4.4. Concrete strength, steel grade and column cross section shape

Concrete strength grade on the seismic behavior of members has a great influence on. Low intensity concrete, the bond between the steel and concrete strength is poor, reinforcement stress after prone slip. The strength of concrete is obviously too high, brittle, impact ductility. The present study is that, more than C50 concrete column of limit values of axial compression ratio should be more than standard corresponding limit reduction of 0.05.

Reinforced the level of structure ductility have great influence. The ductility of the member with the reinforced level decreased, the main reason is the reinforced plastic index with the reinforced level decreased. In order to make the structure satisfy certain ductility requirement, should use the hot rolled reinforced bar, namely the member in the longitudinal reinforcement should choose the II, III reinforcement, stirrups should choose I, II grade steel.

Column cross section shape, will directly affect the column cross-section balanced failure of reinforcement and concrete stress strain distribution, will seriously affect the ultimate compressive strain of concrete in compression edge test values of ε°_{cu} . The analysis shows that the circular section columns, limit value of axial compression ratio of concrete filled steel tubular column can reach more than 1.0; the compressive and shear properties, high bearing capacity, due to compression of high bearing capacity, used in high-rise building in the column can control the slenderness ratio and does not limit the axial compression ratio, thereby section can also be greatly reduced.

Conclusion

In the current code, the limit values of axial compression ratio is not specific, no comprehensive considering the effects of column ductility of other factors, in the vast majority of cases is conservative, that is to say, in the current code, the limit values of axial compression ratio, under certain conditions can be appropriately relaxed. For different stirrup ratio, different shear span ratio, different shapes, different location of the post, just take some measures, even if the column axial pressure ratio than allowable limits, its ductility and can guarantee.

Frame shear wall structure is a multi-line seismic structure, shear wall is a main lateral resisting structure, lateral stiffness greater than the pure frame structure, the deformation of the whole structure is reduced, the framework of the deformation is correspondingly reduced, also can say to frame shear wall into plastic stage and a delayed effect, so the wherein the frame ductility requirements can be reduced. Therefore the structure of axial pressure ratio limit values can be further relaxed.

In the actual design work, you can use the following method to meet the relevant provisions of the ductility of columns:

(1)Applying high strength and light weight materials reduce deadweight of the building, is to reduce the axial compression ratio of column effective method, should be used.

(2)Increase of stirrup ratio, stirrup or spiral configuration complex, using small diameter longitudinal ribs, improvement of cross section shape.

(3)Allow the limit value of axial compression ratio under certain conditions relaxed range.

(4)Using strong flexor ratio above 1.25, high ratio of less than 1.25 (I) or 1.4 (II) of steel.

(5)Appropriately increasing the strength grade of concrete, while improving the stirrup forms and column cross section shape.

Reference:

[1] Wang Qingxiang Experimental research on ductility of Building structure In China 1995.8

[2] Dong YaHong Concrete structure China Building Industry Press In China 1998.6

[3] Code for seismic design of buildings GB50011—2001 In China

Experimental Study on the Behavior of Two-way Concrete Slab under Furnace Loading

Zhinian Yang^{1, a}, Yuli Dong^{2, b}

¹P.O. Box 2554, School of Civil Engineering, Campus two, Harbin Institute of Technology, 73 Huang-he Road, Nan-Gang District, Harbin, China

²College of Civil Engineering, Huaqiao University, Quanzhou, China

^ayangzhinian213@sohu.com, ^bDongYL1965@163.com

Keywords: Two-way concrete slab, Clamped edges, Furnace test, Thermal response, structural behavior.

Abstract. This paper describes the results of a furnace test conducted on two-way concrete slab with clamped edges. The details of clamped support condition, arrangement of reinforcement, position of displacement transducers and thermocouple trees are described. Detailed experimental data in the form of describing slab cracking, the temperature distributions within the slab, vertical deflections and horizontal displacements are presented. The experimental results show that the temperature distribution along the slab depth was nonlinear and the temperature gradients in the slab were large. Extensive cracks occurred on the top surface of the slab and formed in an elliptical pattern. It is shown that two-way concrete slab with clamped edges has good fire resistance.

Introduction

The natural fire tests on the eight-storey building at Cardington show clearly that there was no sign of collapse in any of the tests, despite the fact that the temperature of unprotected steel beams exceeded 1000°C [1-4]. The analysis made after Cardington fire tests shows that this excellent fire behavior is due to both membrane and diaphragm effects of the reinforced composite slab together with steel beams once the steel beams attain temperatures at which they are no longer capable of supporting the applied load alone. However, the experimental results can be applied only to buildings of the same form as the test building. In actual engineering, there are many other types of two-way concrete slabs. How is the real behavior of two-way concrete slabs in fire? Three reinforced concrete flat slabs were tested using the BRANZ fire resistance furnace [5]. The slabs were simply supported on all four sides above the furnace. The slabs were horizontally unrestrained and were loaded with a constant uniformly distributed load. The slabs were all heated from underneath with the ISO 834 standard fire curve for three hours. In addition, small-scale tests were carried out, both at ambient and elevated temperatures [6-9]. The elevated temperature tests [6] were loaded significantly above the yield-line load, before the slabs were subjected to heating. It concluded that the failure mode witnessed from their tests did not conform to that assumed in the simplified design method comprising of fracture across the shorter span of a rectangular slab or one of the spans of a square slab. Bailey's experimental results [7] showed that for the elevated temperature tests all failure modes comprised fracture of the reinforcement, due to the reinforcement's high temperatures which reduced its strength. However, testing at small-scale will result in unrealistic temperature distributions through the thickness of the slab for the heated tests.

Most of tests of the two-way concrete slabs subjected to fire mentioned above were mainly simply-supported. Two-way concrete slabs have many different support conditions in actual construction. Only a small number of research reports on their behaviors in fire that have been presented so far. In this paper, the fire behavior of two-way concrete slab with clamped edges subjected to fire is described.

Design of the Test

Slab Properties. A flat slab with clamped edges subjected to fire, were tested at Shandong Jianzhu University, Jinan, China. The slab was measured 6060 mm wide by 9200 mm long and the thickness was 120 mm. The clear span of the slab was 4500 mm×6000 mm, giving an aspect ratio of 1.33. Commercial normal weight concrete was used for the slab and the specified compressive strength was 30 MPa. The actual cubic compressive strength was 33.5 MPa. Grade 3 hot-rolled reinforcing bars of 8 mm diameter were arranged at 200 mm spacing both along long direction and short direction. The clear concrete cover was 15 mm for reinforcement. The details of dimensions and reinforcement arrangement of the slab are shown in Fig. 1.

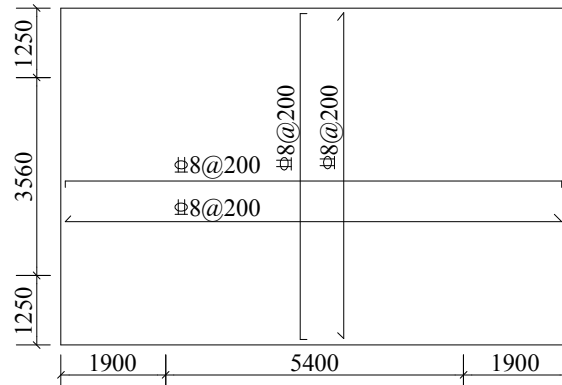


Fig. 1 Arrangement of reinforcement in slab

Support Conditions. The slab was supported with clamped edges (refer to Fig. 2). The slab was supported by long knife supports along each support axis, over the furnace on four reinforced concrete furnace walls lining the internal perimeter. The knife supports composed of angle steel of 40 mm height. There was a long 120 mm wide and 12 mm thick steel strips between concrete slab and knife supports continuously, and the same steel strip was arranged between knife supports and four reinforced concrete walls. The clamped condition was achieved by reaction space steel frame and a total of 14 screw jacks and 14 H-section steel beams. Each screw jack was applied at the mid-span of one H-section steel beam. The H-section steel beam contacted the concrete slab edge at two points with steel plate, and split one point load applied by screw jack into two equal point loads on the concrete slab. The loads were predefined and recorded by load-cell, they are shown as Fig. 2 and 3. There were 4 screw jacks and 8 point loads with spacing of 1150 mm applied on each long concrete slab edge. Meanwhile, there were 3 screw jacks and 6 point loads with spacing of 1010 mm applied on each short slab edge. The loads were arranged in order to simulate conditions close to line-distributed loading.

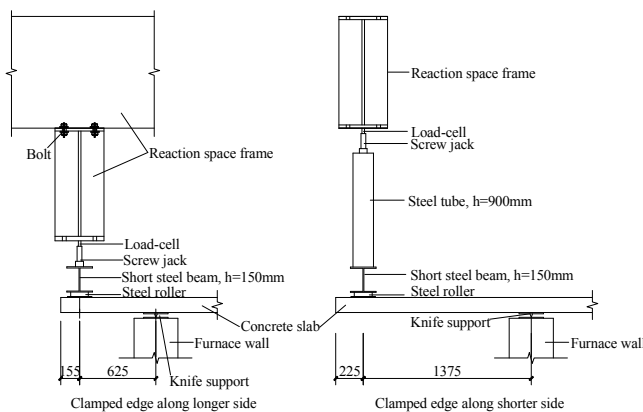


Fig. 2 Details of clamped edges



Fig. 3 View of the clamped edges

Loading of the Slab. In addition to the self weight of the slab, a uniformly distributed load was applied on the slab, to simulate live loads. Dead weights (each weighing 0.2 kN) were placed on the slab to simulate the uniformly distributed load, and the applied loads were equivalent to a uniformly distributed load of 2.0 kN/m^2 .

Instrumentation. Type K thermocouples on the thermocouple trees were used to measure the concrete temperatures across the thickness of the slab. The arrangement of thermocouple trees and its details are shown in Fig. 4. Each thermocouple tree consisted of seven thermocouples distributing vertically and the distance between them was 20 mm. The thermocouple trees were positioned at the mid-span and quarter-span of the slab. Type K thermocouples were also used to measure the reinforcing steel temperatures. Displacement transducers (LVDT) were used to measure vertical deflections and horizontal displacements of the slab. The vertical deflections were measured at the mid-span and quarter-span of the slab, and the horizontal displacements were measured at the four edges of the slab. Fig. 5 shows the positions of displacement transducers for the test.

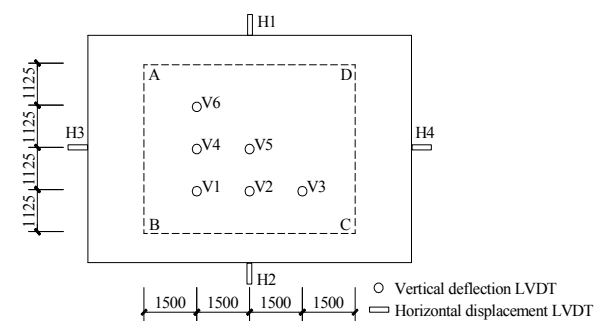
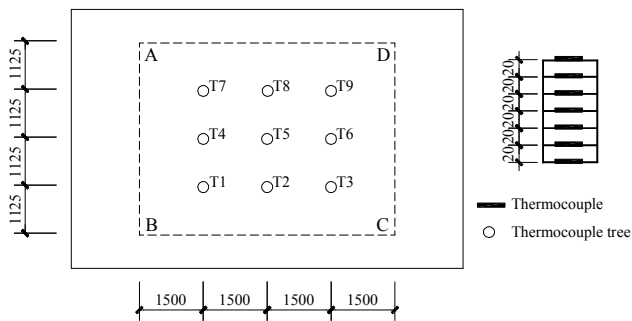


Fig. 4 Positions and details of thermocouple trees

Fig. 5 Positions of displacement transducers

Test Results

A two-way concrete slab with clamped edges was tested under furnace condition. The furnace shut-off for the Test occurred at 247 min after ignition. At the end of the test, the furnace gas temperature reached 1141°C and the central deflection of the concrete slab reached 232 mm, which was equivalent to approximately $1/20$ of the short span-length.

Cracking of the Slab. Fig. 6 shows the top view of the concrete slab after fire, the surface cracks formed in an elliptic pattern. Two large cracks spacing at 150 mm were located approximately 1250 mm from the AD axis. Five cracks spacing at 200-250 mm apart were located 1200 mm from BC line, reaching a maximum width of 8 mm. Two cracks spacing at 300 mm were located 1700 mm from AB line. Two cracks spacing at 200 mm were located 1650 mm from CD axis, and reached a maximum width of 2 mm. In addition, finer surface cracks from the corners towards the centre region of the slab and cracks along the support axis could also be seen. Fig. 7 shows the view of the bottom of the slab after fire. It shows that severe spalling occurred and large portion of reinforcing bars were exposed. Examination of the reinforcing bars showed that the bars at the bottom did not rupture.



Fig. 6 Top view of the slab after fire

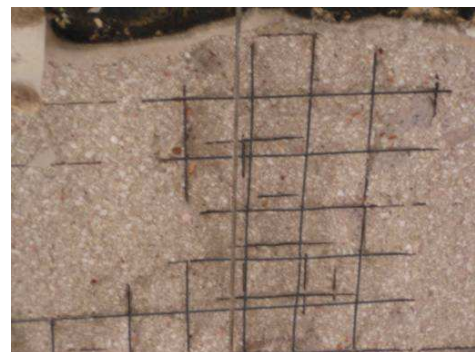


Fig. 7 Bottom view of the slab after fire

Temperature in the Slab. Fig. 8 shows the temperatures of the thermocouple tree embedded in the slab. The maximum temperature at the bottom of the slab reached 1120 °C, due to the severe concrete spalling, and the maximum temperature on the top of the slab reached 152°C by the end of test. The graph shows a clearly plateau in the temperature rise at about 100 °C level. This is attributed to evaporation of water in the concrete slab. Fig. 9 shows the temperatures of the thermocouples attached to the reinforcing mesh. There is a pronounced plateau in the temperature rise for the reinforcing bars in the graph, and it is also attributed to evaporation of water in the slab. The temperature of the bottom bar was higher than that of the top one. The maximum temperature of the bottom bar reached 1132 °C, while the maximum temperatures of the top bar was 717 °C at the shut-off point.

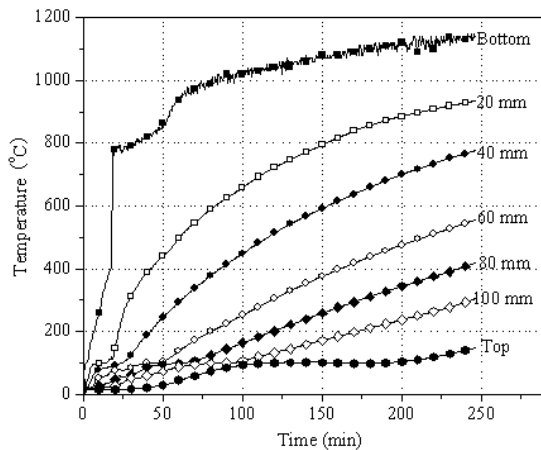


Fig. 8 Temperatures of thermocouple tree

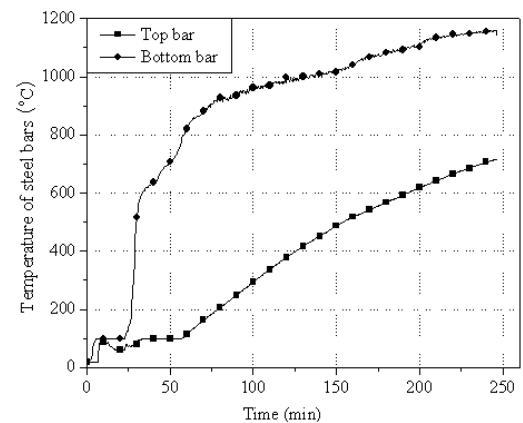


Fig. 9 Temperatures of reinforcing bars

Vertical Deflection and Horizontal Displacement. Fig. 10 shows the variation of the vertical deflections of the slab during the test. It shows that the slab deflected downwards more rapidly in 10 min after ignition, reaching 23 mm at mid-span, equal to a rate of 2.3 mm per minute. After 10 min, the deflection rate of the slab decreased and the slab deflected at a constant rate of approximately 0.88 mm per minute for the remaining duration of the test. When the test was stopped at 247 min, the mid-span deflection reached 232 mm. Fig. 11 shows the measured horizontal displacements of the slab. The horizontal displacements were due to the expansion and downward deflections in the centre region of the slab. H1 and H2 measured the horizontal displacements in the transverse direction of the slab, while H3 and H4 measured the displacements in the longitudinal direction (refer to Fig. 5). The edge connected to LVDT H1 always moved outward, and reached a minimum value of -1.38 mm. The edge connected to LVDT H2 always moved outward, and reached a minimum value of -6.28 mm. Along the long direction, the reading of H3 shows that the slab expanded at a linear rate of 0.04 mm per minute until 215 min and then malfunctioned. The reading of H4 shows that the slab expanded at a rapid rate of 0.25 mm per minute until 55 min and continued to increase at a slower rate. The outward displacement of H4 reached -11 mm at 185 min and malfunctioned until the end of the test.

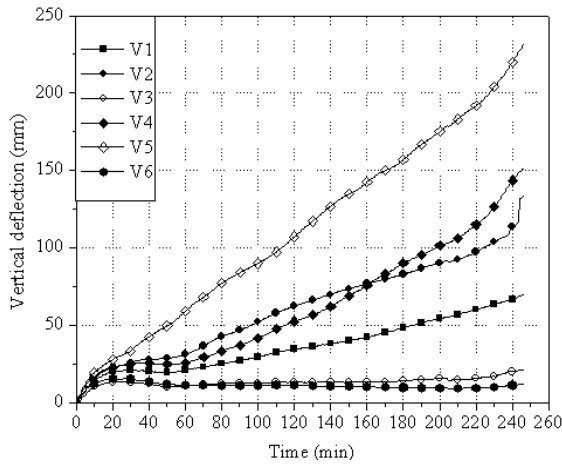


Fig. 10 Vertical deflections of the slab

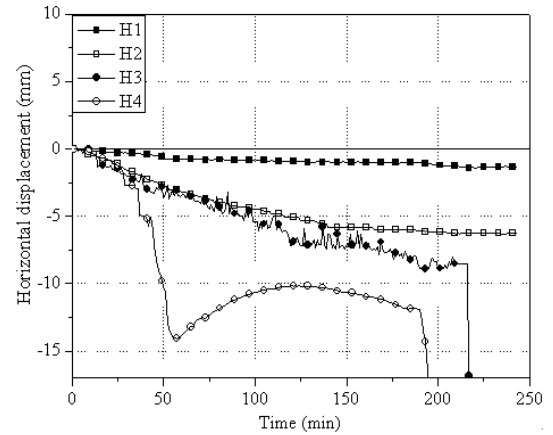


Fig. 11 Horizontal displacements of the slab

Conclusions

A furnace test was carried out on two-way concrete slab with clamped edges. Experimental results including cracking of the slab, temperature distributions within the slab, vertical deflections and horizontal displacements were presented and discussed. Extensive cracks occurred on the top of the slab during the test, and formed in an elliptical pattern. Under 247 min duration of heating, the central deflection of the concrete slab reached approximately $1/20$ of the short span-length. The test results indicate that the fire resistance of the two-way concrete slab with clamped edges is good, and the provided detailed experimental data will serve as a database for validation of numerical models.

Acknowledgements

This work was financially supported by the National Natural Science Foundation of China (51178143).

References

- [1] C.G. Bailey, T. Lennon and D.B. Moore: *The Structural Engineer*, Vol. 77 (1999) No.8, p. 15.
- [2] M.A. O'Conner, B.R. Kirby and D.M. Martin: *The Structural Engineer*, Vol. 81 (2003) No.2, p. 27.
- [3] C.G. Bailey, D.S. White and D.B. Moore: *Engineering Structures*, Vol. 22 (2000) No.12, p. 1583.
- [4] C.G. Bailey and D.B. Moore: *The Structural Engineer*, Vol. 78 (2000) No.11, p. 19.
- [3] L. Lim, A. Buchanan and P. Moss: *Engineering Structures*, Vol. 26 (2004) No.8, p. 1081.
- [6] S.J. Foster, C.G. Bailey, I.W. Burgess and R.J. Plank: *Engineering Structures*, Vol. 26 (2004) No.9, p. 1231.
- [7] C.G. Bailey and W.S. Toh: *Engineering Structures*, Vol. 29 (2007) No.10, p. 2775.
- [8] C.G. Bailey and W.S. Toh: *Fire Safety Journal*, Vol. 42 (2007) No.7, p. 425.
- [9] C.G. Bailey: *Engineering Structures*, Vol. 23 (2001) No.5, p. 470.

Natural Element Method for Material and Geometrical Bi-nonlinear Problems

Daohong Ding^{1, 2,a}, Qing Zhang^{1,2,b} and Jianqiang Xiao^{1,2,3,c}

¹ State Key Laboratory of Hydrology-Water Resources and Hydraulic Engineering, Hohai University, Nanjing, Jiangsu, 210098, China

² Department of Engineering Mechanics, Hohai University, Nanjing, Jiangsu, 210098, China

³ Department of Civil Engineering, Nanjing Institute of Technology, Nanjing, Jiangsu, 211167, China

^addh@hhu.edu.cn, ^blxzhangqing@hhu.edu.cn, ^cxiaojq7754@163.com

Keywords: Natural Element Method, Material Nonlinear Problem, Geometrical Nonlinear Problem, Natural Neighbor Interpolation, Numerical Method.

Abstract. Based on the Voronoi diagram of some nodes, the natural element method (NEM) constructs the shape functions by the natural neighbor interpolation method, and its shape functions satisfy the Kronecker delta property, which makes it impose essential boundary conditions easily. Based on the geometrical nonlinear relations and material nonlinear constitutive relations, we extend the NEM to material and geometrical bi-nonlinear problems in this paper. Numerical examples show that the NEM is effective, rational and feasible in dealing with problems of both material and geometrical bi-nonlinear.

Introduction

The natural element method (NEM) pioneered by Braun and Sambridge [1] is a popular mesh-less method. It is based on the well-known natural neighbor interpolation which uses the concepts of Voronoi diagrams and Delaunay triangulation to construct the shape functions. Now, the NEM has been widely applied to many fields [2-7]. Sukumar et al. [2-5] had applied the NEM to many problems, such as 2D small displacement elasto-statics, gradient problems and static crack problem. Through the 2D large deformation analysis of nearly incompressible bodies, Cho and Lee [6] explored the applicability of the NEM to the non-linear solid mechanics. Recently, Ding et al. [7] had researched the elasto-plastic natural element method and used this method to research the concrete filled steel tubular columns.

The characteristic of NEM

The NEM is a numerical method, which constructs shape functions based on the Voronoi diagram of a set of nodes. The Voronoi diagram and its dual Delaunay triangulation are two important concepts in the NEM. Mathematically, the Voronoi diagram can be described as follows. Set $P = \{x_1, \dots, x_n\}$ are n distinct nodes in space R^n , we can define the Voronoi diagram of node x_i as

$$T_i = \{x \in R^n : d(x, x_i) \leq d(x, x_j), \forall J \neq I\} . \quad (1)$$

where $d(x_i, x_j)$ is the Euclidean distance between the node x_i and x_j .

Set κ is Lebesgue measure (length in 1D space, area in 2D space, and volume in 3D space, respectively). Set κ_x is Lebesgue measure of the first Voronoi structure T_x (Eq.(1)) of interpolation points x' in space R^n . Set κ_{x_i} is Lebesgue measure of the second Voronoi structure T_{x_i} of interpolation points x' for node x_i , where,

$$T_{x_i} = \{x \in R^n : d(x, x') \leq d(x, x_i), \forall I\} \cap \{x \in R^n : d(x, x_i) \leq d(x, x_j), \forall J \neq I\} . \quad (2)$$

According to the Sibson interpolation[11], the shape function is the ratio of the Lebesgue measure κ_{x_l} and the Lebesgue measure κ_x , namely,

$$\phi_l(\mathbf{x}) = \frac{\kappa_{x_l}(\mathbf{x})}{\kappa_x(\mathbf{x})}. \quad (3)$$

The displacement \mathbf{u}^e of any point in the solution domain can be obtained by the following linear combination of displacement of the natural neighbor nodes,

$$\mathbf{u}^e = \sum_{l=1}^n \mathbf{u}_l \phi_l = \Phi \mathbf{u}. \quad (4)$$

where \mathbf{u}_l is the displacement vector of node x_l . n is the total number of nodes in the solution domain. ϕ_l is the shape function of the interpolation point with nodes x_l .

Governing equations

Let $\Omega \subset R^2$ be a body enclosed by boundary Γ . The static equilibrium equation can be given as

$$\sigma_{ij,j} + b_i = 0 \quad (i, j = 1, 2) \quad \text{in } \Omega, \quad (5)$$

accompanied with boundary conditions

$$\begin{cases} u_i = \bar{u}_i & \text{on } \Gamma_u \\ \sigma_{ij} n_j = \bar{t}_i & \text{on } \Gamma_t \end{cases}. \quad (6)$$

where σ_{ij} and b_j are the stress and physical stress, respectively, n_j is the cosine outside normal direction of the stress boundary, \bar{u}_i and \bar{t}_i are the boundary of displacements and tractions, respectively.

Based on the static equilibrium equation Eq. (5) and the stress boundary conditions Eq. (6), we can get the equivalent integral form of the Galerkin method

$$\int_{\Omega} \delta u_i (\sigma_{ij,j} + b_i) d\Omega - \int_{\Gamma_t} \delta u_i (\sigma_{ij} n_j - \bar{t}_i) d\Gamma = 0. \quad (7)$$

Integration by parts Eq. (7), we get

$$\int_{\Omega} (\delta \varepsilon_{ij} \sigma_{ij}) d\Omega = \int_{\Omega} \delta u_i b_i d\Omega + \int_{\Gamma_t} \delta u_i \bar{t}_i d\Gamma. \quad (8)$$

It is convenient to write the above equation into matrix form

$$\int_{\Omega} \delta \boldsymbol{\varepsilon}^T \boldsymbol{\sigma} d\Omega = \int_{\Omega} \delta \mathbf{u}^T \Phi^T \mathbf{b} d\Omega + \int_{\Gamma_t} \delta \mathbf{u}^T \Phi^T \bar{\mathbf{t}} d\Gamma. \quad (9)$$

In the 2D small deformation geometrical nonlinear problems, the geometry relation between strain and displacement can be given by Green strain theory

$$\boldsymbol{\varepsilon} = \begin{bmatrix} \frac{\partial u}{\partial x} + \frac{1}{2} \left[\left(\frac{\partial u}{\partial x} \right)^2 + \left(\frac{\partial v}{\partial x} \right)^2 \right] \\ \frac{\partial v}{\partial y} + \frac{1}{2} \left[\left(\frac{\partial u}{\partial y} \right)^2 + \left(\frac{\partial v}{\partial y} \right)^2 \right] \\ \frac{\partial u}{\partial y} + \frac{\partial v}{\partial x} + \frac{\partial u}{\partial x} \frac{\partial u}{\partial y} + \frac{\partial v}{\partial x} \frac{\partial v}{\partial y} \end{bmatrix} = \begin{bmatrix} \frac{\partial u}{\partial x} \\ \frac{\partial v}{\partial y} \\ \frac{\partial u}{\partial y} + \frac{\partial v}{\partial x} \end{bmatrix} + \frac{1}{2} \begin{bmatrix} \frac{\partial u}{\partial x} & \frac{\partial v}{\partial x} & 0 & 0 \\ 0 & 0 & \frac{\partial u}{\partial y} & \frac{\partial v}{\partial y} \\ \frac{\partial u}{\partial y} & \frac{\partial v}{\partial y} & \frac{\partial u}{\partial x} & \frac{\partial v}{\partial x} \end{bmatrix} \begin{bmatrix} \frac{\partial u}{\partial x} \\ \frac{\partial v}{\partial x} \\ \frac{\partial u}{\partial y} \\ \frac{\partial v}{\partial y} \end{bmatrix} = \mathbf{B} \mathbf{u} + \frac{1}{2} \mathbf{A} \mathbf{G} \mathbf{u} = \left(\mathbf{B} + \frac{1}{2} \mathbf{A} \mathbf{G} \right) \mathbf{u}. \quad (10)$$

where

$$\mathbf{B} = \begin{bmatrix} \phi_{1,x} & 0 & \phi_{2,x} & 0 & \cdots & \phi_{n,x} & 0 \\ 0 & \phi_{1,y} & 0 & \phi_{2,y} & \cdots & 0 & \phi_{n,y} \\ \phi_{1,y} & \phi_{1,x} & \phi_{2,y} & \phi_{2,x} & \cdots & \phi_{n,y} & \phi_{n,x} \end{bmatrix}; \quad \mathbf{A} = \begin{bmatrix} \frac{\partial u}{\partial x} & \frac{\partial v}{\partial x} & 0 & 0 \\ 0 & 0 & \frac{\partial u}{\partial y} & \frac{\partial v}{\partial y} \\ \frac{\partial u}{\partial y} & \frac{\partial v}{\partial y} & \frac{\partial u}{\partial x} & \frac{\partial v}{\partial x} \end{bmatrix}; \quad \mathbf{G} = \begin{bmatrix} \phi_{1,x} & 0 & \phi_{2,x} & 0 & \cdots & \phi_{n,x} & 0 \\ 0 & \phi_{1,x} & 0 & \phi_{2,x} & \cdots & 0 & \phi_{n,x} \\ \phi_{1,y} & 0 & \phi_{2,y} & 0 & \cdots & \phi_{n,y} & 0 \\ 0 & \phi_{1,y} & 0 & \phi_{2,y} & \cdots & 0 & \phi_{n,y} \end{bmatrix}.$$

$$d\boldsymbol{\varepsilon} = (\mathbf{B} + \mathbf{A} \mathbf{G}) d\mathbf{u}. \quad (11)$$

Substitute the geometrical relation into Eq. (9), then

$$\int_{\Omega} \delta \mathbf{u}^T (\mathbf{B} + \mathbf{A}\mathbf{G})^T \boldsymbol{\sigma} d\Omega = \int_{\Omega} \delta \mathbf{u}^T \boldsymbol{\Phi}^T \mathbf{b} d\Omega + \int_{\Gamma_i} \delta \mathbf{u}^T \boldsymbol{\Phi}^T \bar{\mathbf{t}} d\Gamma . \quad (12)$$

Since the displacement $\delta \mathbf{u}$ of any nodes varies randomly, we could get the static NEM governing equation for the problem of geometrical nonlinear as

$$\int_{\Omega} (\mathbf{B} + \mathbf{A}\mathbf{G})^T \boldsymbol{\sigma} d\Omega = \int_{\Omega} \boldsymbol{\Phi}^T \mathbf{b} d\Omega + \int_{\Gamma_i} \boldsymbol{\Phi}^T \bar{\mathbf{t}} d\Gamma . \quad (13)$$

For the material nonlinear problems, the relation between the stress and strain can be given by the constitutive relation with stress, i.e., the constitutive equation

$$d\boldsymbol{\sigma} = \mathbf{D}(\boldsymbol{\sigma}) d\boldsymbol{\varepsilon} = \mathbf{D}(\boldsymbol{\sigma}) (\mathbf{B} + \mathbf{A}\mathbf{G}) d\mathbf{u} . \quad (14)$$

where $\mathbf{D}(\boldsymbol{\sigma})$ is the constitutive matrix for an isotropic material corresponds with the stress $\boldsymbol{\sigma}$. The modulus can be represented by the tangent modulus E_t with the stress $\boldsymbol{\sigma}$. $\mathbf{D}(\boldsymbol{\sigma})$ is a matrix with the tangent modulus E_t and Poisson's ratio ν .

If the difference between the stress $\boldsymbol{\sigma}$ and $\boldsymbol{\sigma}_0$ is very small, then the difference between $\mathbf{D}(\boldsymbol{\sigma})$ and $\mathbf{D}(\boldsymbol{\sigma}_0)$ is small, and Eq. (14) can be written as

$$\boldsymbol{\sigma} = \boldsymbol{\sigma}_0 + \mathbf{D}(\boldsymbol{\sigma}) \left(\mathbf{B} + \frac{1}{2} \mathbf{A}\mathbf{G} \right) (\mathbf{u} - \mathbf{u}_0) . \quad (15)$$

By substituting constitutive relation Eq. (15) into Eq. (12), the following equations can be obtained

$$\int_{\Omega} (\mathbf{B} + \mathbf{A}_0\mathbf{G})^T \boldsymbol{\sigma}_0 d\Omega = \int_{\Omega} \boldsymbol{\Phi}^T \mathbf{b} d\Omega + \int_{\Gamma_i} \boldsymbol{\Phi}^T \bar{\mathbf{t}}_0 d\Gamma . \quad (16)$$

$$\int_{\Omega} (\mathbf{B} + \mathbf{A}\mathbf{G})^T \left[\boldsymbol{\sigma}_0 + \mathbf{D}(\boldsymbol{\sigma}) \left(\mathbf{B} + \frac{1}{2} \mathbf{A}\mathbf{G} \right) (\mathbf{u} - \mathbf{u}_0) \right] d\Omega = \int_{\Omega} \boldsymbol{\Phi}^T \mathbf{b} d\Omega + \int_{\Gamma_i} \boldsymbol{\Phi}^T \bar{\mathbf{t}} d\Gamma . \quad (17)$$

$$\int_{\Omega} (\mathbf{B} + \mathbf{A}\mathbf{G})^T \mathbf{D}(\boldsymbol{\sigma}) \left(\mathbf{B} + \frac{1}{2} \mathbf{A}\mathbf{G} \right) (\mathbf{u} - \mathbf{u}_0) d\Omega = \int_{\Gamma_i} \boldsymbol{\Phi}^T (\bar{\mathbf{t}} - \bar{\mathbf{t}}_0) d\Gamma - \int_{\Omega} \mathbf{G}^T (\mathbf{A} - \mathbf{A}_0)^T \boldsymbol{\sigma}_0 d\Omega . \quad (18)$$

where \mathbf{A}_0 equals to \mathbf{A} with $\mathbf{u} = \mathbf{u}_0$, then $\mathbf{A} - \mathbf{A}_0$ can be written as

$$\mathbf{A} - \mathbf{A}_0 = \begin{bmatrix} \frac{\partial(u-u_0)}{\partial x} & \frac{\partial(v-v_0)}{\partial x} & 0 & 0 \\ 0 & 0 & \frac{\partial(u-u_0)}{\partial y} & \frac{\partial(v-v_0)}{\partial y} \\ \frac{\partial(u-u_0)}{\partial y} & \frac{\partial(v-v_0)}{\partial y} & \frac{\partial(u-u_0)}{\partial x} & \frac{\partial(v-v_0)}{\partial x} \end{bmatrix} = \mathbf{A}(\Delta \mathbf{u}) . \quad (19)$$

It is convenient to write $\mathbf{K} = \int_{\Omega} (\mathbf{B} + \mathbf{A}\mathbf{G})^T \mathbf{D}(\boldsymbol{\sigma}) \left(\mathbf{B} + \frac{1}{2} \mathbf{A}\mathbf{G} \right) d\Omega$, $\Delta \mathbf{F} = \int_{\Gamma_i} \boldsymbol{\Phi}^T (\bar{\mathbf{t}} - \bar{\mathbf{t}}_0) d\Gamma$,

$\mathbf{S}\mathbf{F} = \int_{\Omega} \mathbf{G}^T [\mathbf{A}(\Delta \mathbf{u})]^T \boldsymbol{\sigma}_0 d\Omega$, then Eq. (19) can be written as

$$\mathbf{K} \Delta \mathbf{u} = \Delta \mathbf{F} - \mathbf{S}\mathbf{F} . \quad (20)$$

Numerical examples

Geo. nonlinear anal. We consider an unit thickness cantilever beam with uniformly distributed vertical load (as shown in Fig. 1(a)), whose length and height are $L = 100 \text{ mm}$ and $H = 10 \text{ mm}$, respectively. The Elastic modulus for this problem is $E = 1.2 \times 10^6 \text{ N/mm}^2$ and the Poisson's ratio is $\nu = 0.2$. The cantilever beam is discretized with 65 nodes as shown in Fig. 1(b). Node A is the middle point of the right edge.

Fig. 2(a) reveals the deflection results of node A for the NEM. The Holden's results [8] is provided in Fig .2(b) for comparison. We find that numerical results for the NEM with nonlinear geometrical property coincide very well with Holden's results. However, if we just consider the linear geometrical property, the NEM results differ from the Holden's results with the increasing parameter k. Thus, we will use the NEM to investigate the material and geometrical bi-nonlinear problems in the next example.

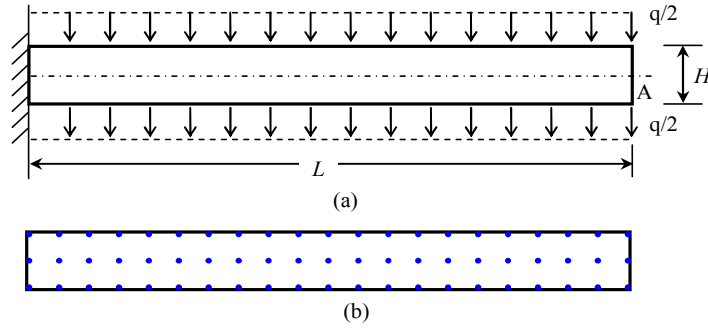


Fig. 1 Cantilever beam with uniform vertical load

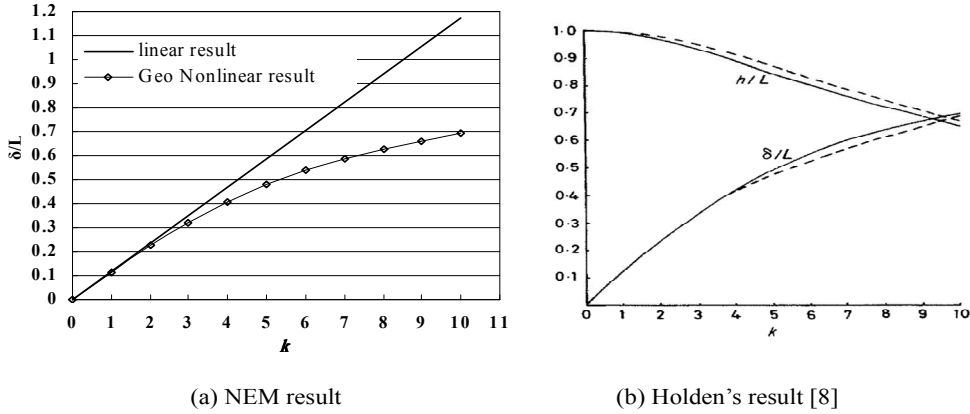


Fig. 2 Deflection results of node A

Analy. both mat.and geo. bi-nonlinear problems We consider an unit thickness cantilever beam with uniform horizontal load (as shown in Fig. 3(a)), whose length and height are $L=100\text{ mm}$ and $H=10\text{ mm}$, respectively. The constitutive relation is given in Fig. 3(c), where $E_1=1.5\times 10^6\text{ N/mm}^2$, $E_2=0.6\times 10^6\text{ N/mm}^2$, $\nu=0.2$, $\sigma_0=0.5\text{ MPa}$ is the yield stress limit. The cantilever beam is discretized with 65 nodes as shown in Fig. 3(b).

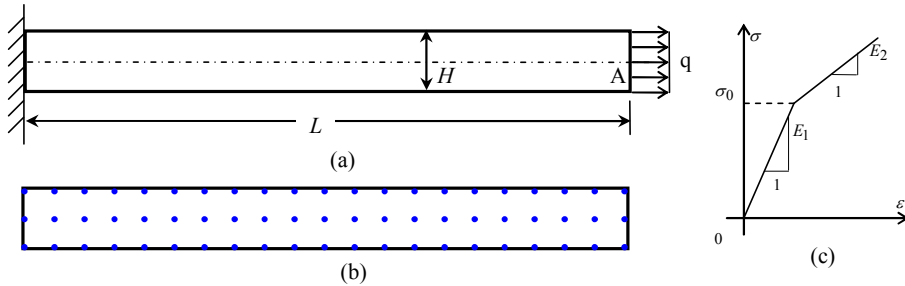


Fig. 3 Cantilever beam with material nonlinear

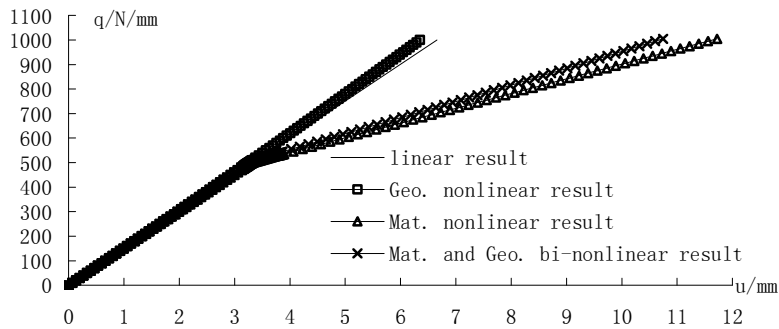


Fig. 4 Horizontal displacement - load curve of node A

Fig. 4 describes the horizontal displacement-load curve of node A. For the uniform load q between 0 and 490 N/mm , we observe that the linear results coincide very well with the material nonlinear results. For the uniform load q between 490 and 534 N/mm , the results for material nonlinear problem are a curve. This may partially due to that when $q = 490\text{ N/mm}$, parts of the yield stress is larger than the yield stress limit, and the tangent modulus for this part is $0.6 \times 10^6\text{ N/mm}^2$. For $q > 534\text{ N/mm}$, the yield stress of all regions is larger than the yield stress limit and the tangent modulus is $0.6 \times 10^6\text{ N/mm}^2$. Numerical results for the geometrical nonlinear are a curve, and it is smaller than the linear one. During the uniform load q between 0 and 490 N/mm , results for both material and geometrical bi-nonlinear coincide very well with the geometrical nonlinear solutions. Then the difference between the result for material and geometrical bi-nonlinear and the result for geometrical nonlinear is much more large. The main reason is that the region where the yield stress is larger than the yield stress limit be much more with the increasing load q .

Conclusions

An application of the NEM is extended to solve both material and geometrical bi-nonlinear problems based on the Green strain theory and material nonlinear constitutive relations. Two numerical examples are given to show the model's rationality and feasibility. Numerical results of the NEM show that the NEM is suitable for analyzing the material and geometrical bi-nonlinear problems with the merits of no need to regenerate grid, easy to impose essential boundary conditions and so on.

Acknowledgements

This work is partially supported by the National Natural Science Foundation of China (No.10972072, No.51179064, No.11132003), as well as the Special Fund of State Key Laboratory of Hydrology-Water Resources and Hydraulic Engineering of Hohai University (No.2009585912).

References

- [1] J. Braun, M. Sambridge: *Nature*, Vol.376 (1995), p. 655
- [2] E. Cueto, N. Sukumar, B. Calvo, et al.: *Arch. Comput. Method. Eng.*, Vol.10 (2003), p. 307
- [3] N. Sukumar, B. Moran, T. Belytschko: *Int. J. Numer. Meth. Engng.* Vol.43 (1998), p. 839
- [4] N. Sukumar, B. Moran, A.Y. Semenov, et al: *Int. J. Numer. Meth. Engng.* Vol.50 (2001), p. 1
- [5] D. Bueche, N. Sukumar, B. Moran: *Comput. Mech.* Vol.25 (2000), p. 207
- [6] J. R. Cho, H. W. Lee: *Comput. Struct.* Vol.84 (2006), p. 293
- [7] D. H. Ding, Q. Zhang, L. Y. Luo, in: 2011 International Conference on Remote Sensing, Environment and Transportation Engineering (RSETE) (2011).
- [8] J. T. Holden: *Int.J.Solids Struc.* Vol. 8 (1972), p. 1051

FEM Analysis on Seismic Behavior of Hybrid Coupled Wall System with Steel Boundary Elements

Shi Yun^{1,a}, Su Mingzhou^{1,b}, Song Anliang^{1,c}

¹Key Laboratory of Structural Engineering and Earthquake Resistance of China Ministry of Education,

Xi'an University of Architecture and Technology, Xi'an 710055, China

^arhyme_0305@163.com, ^bsumingzhou@163.com, ^csonganliang@sohu.com

Keywords: Steel Boundary Elements, Seismic Behavior, Hybrid Coupled Wall, Finite Element Model

Abstract. A nonlinear 3D solid model of hybrid coupled wall system with steel boundary elements has been founded by using FEM software ABAQUS to study its hysteretic behavior under cyclic loading, which considering the geometric large deformation and materials nonlinearity. To verify the efficiency of the model, two specimens with various coupling ratios of 30% and 45% are analyzed, and the results of analysis are compared with test ones. As the bearing capacities of both agree well in different loading stages, so the FEM model has enough accuracy and could be used to study the seismic behavior of hybrid coupled wall system with steel boundary elements. In addition, the results show that this new system dissipates energy by shear deformation of steel beams along and plastic hinge deformation at the bottom of wall, so it has better seismic performance.

Introduction

The concept of hybrid coupled wall system was put forward in early 90's in the United States and Canada [1]. Under the support of U.S.-Japan cooperative research program and the U.S. National Science Foundation, the researches on this system have been carried out from the properties of connection and the overall performance [2, 3, 4]. Research results show that this kind of new structural system has better energy dissipation capacity by comparing with the traditional reinforced concrete coupled wall, so it is more applicable in zones of high seismic risk. In these studies, the detail of connection adopted is that steel beam is directly embedded through reinforced boundary elements of shear walls. As a result, the detail is very complicate, and damaged seriously. In order to improve its seismic performance and simplify construction, the task groups put forward an innovative detail: arranging the shape steel column in the boundary element of shear wall, which is named as hybrid coupled wall system with steel boundary elements [5].

Previous studies have shown that coupling ratio (CR) is an important parameter and a reflection of shear wall integral working performance [6], which represents the proportion of system overturning moment resisted by the coupling action. In coupled walls, the transfer of shear forces through the coupling beams induces tensile and compressive forces between adjacent walls.

In order to study the effect of coupling ratio (CR) on hysteretic behavior of innovative hybrid coupled wall systems with shape steel boundary elements, two 1/3 scale 5 storey models with CR=30% and CR=45% have been tested under cyclic loading[7][8]. The test models are designated as CR-30 and CR-45, respectively. However, the finite element simulation is particularly important due to the limits of experimental site and equipment ability, so a nonlinear 3D solid model has been founded by using FEM software ABAQUS and verified based on the test results.

Test model descriptions

The test model, whose scale is 1:3, is selected from the tests mentioned above. The elevation view of the structure CR-30 is given in Fig.1. The structure is 5-storey, with a symmetric configuration of 100mm thick by 3,350 mm wide, 6,545mm high. Two individual shear walls are coupled in series by

steel beams, and steel columns are arranged as the boundary elements of the wall. In order to achieve different coupling ratios, CR-45 increase the size of coupling beam. Sectional dimension of members is given in table 1 and table 2. The structure is designed in terms of current Chinese code with the assumption that all coupling beams would yield in shear other than in flexure and will behave in a ductile manner through plastic hinge, and all coupling beams would yield prior to the shear walls fail. Strength grades of steel and concrete are Q235 and C35, respectively.

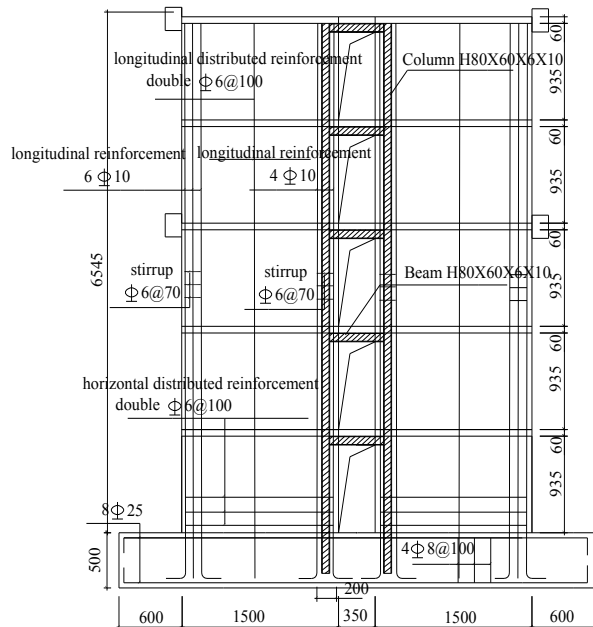


Fig.1 Main view of the structure

Table 1 Dimension of steel column

test	H	t_w	b_f	t_f
model	(mm)	(mm)	(mm)	(mm)
CR-30	80	6	60	10
CR-45	80	6	60	10

Table 2 Dimension of steel coupling beam

test	H	t_w	b_f	t_f
model	(mm)	(mm)	(mm)	(mm)
CR-30	74	3	60	12
CR-45	154	4	60	12

Finite element analysis model

The nonlinear 3D solid model which considering the geometric large deformation and materials nonlinear are founded by ABAQUS. In the model, elastic-plastic 3D solid element C3D8R in ABAQUS element library is adopted for simulating shear walls and steel coupling beams, and one-dimensional truss element T3D2 for reinforcing bars. Following criteria are assumed in the analysis:

- (1) The steel follows kinematic bilinear hardening criterion which considered Bauschinger effect and Von. Mises yield criterion.
- (2) Damaged plasticity model of William-Warnke five- parameter failure criterion for concrete is used for simulating shear walls, which takes into account the biaxial behavior of the material [9].
- (3) Material properties of steel and concrete are obtained from coupon test, as shown in table 3.
- (4) The interface slip between steel and concrete is ignored.

The finite-element models are shown in Fig.2.

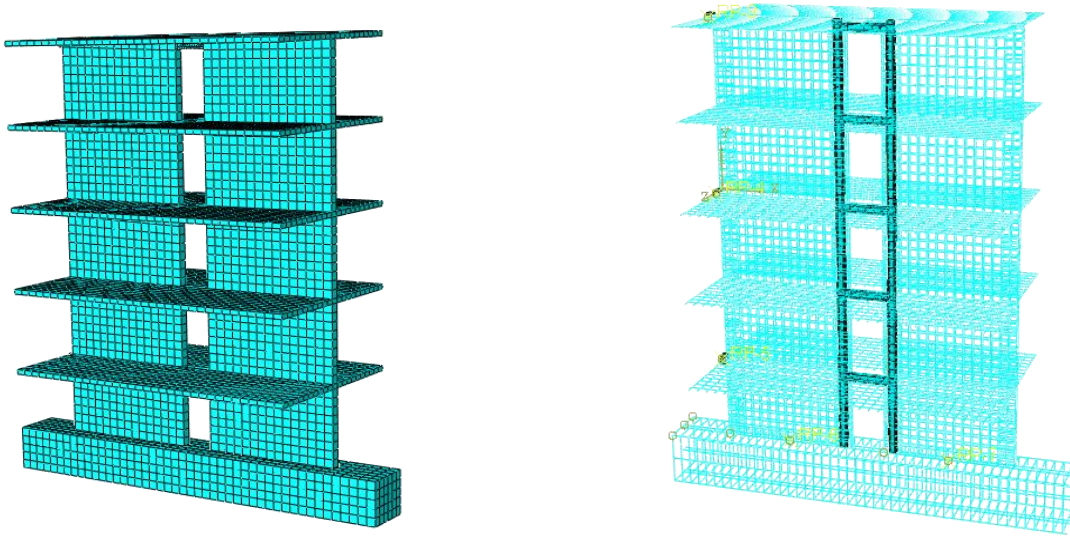


Fig.2 The FEM mesh generation

Boundary condition is set as same as in experiment, i.e., constrained all of six degrees of freedom at the bottom of the structure (U_x , U_y , U_z , UR_x , UR_y , UR_z), and three degrees of freedom out of plane at the fifth floor (U_z , UR_x , UR_y) in FEM model.

In accordance with test loading scheme, vertical load is applied in the first loading step and kept constant, and then cyclic horizontal load is added in the fifth floor till the structure fails. The loading zone of the model is defined as rigid body in order to avoid the destruction caused by stress concentration.

Table 3 Material properties

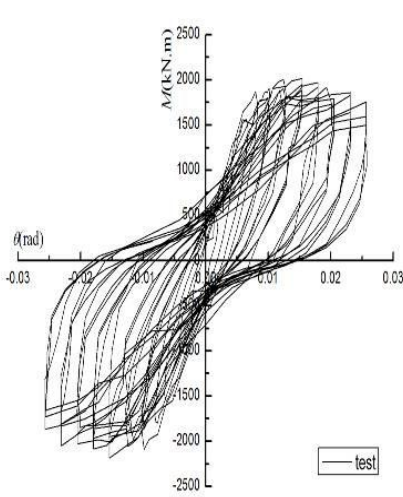
Materials	Diameter/thickness (mm)	Yield tress (MPa)	Ultimate stress(MPa)	Elongation (%)	Ultimate/ yield	Elastic modulus
Steel plate	3	353	505	34	1.43	2.1×10^5
	6	330	453	42	1.37	
	10	319	456	44	1.42	
	12	377	532	46	1.41	
Reinforced bar	6	505	605	6	1.19	2.0×10^5
	10	439	481	6	1.12	

Analysis results

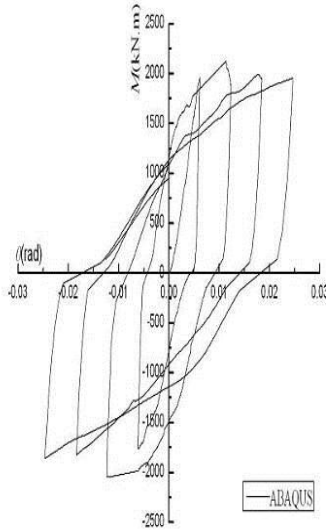
Hysteretic curves and skeleton curves. The comparison of hysteretic curves and skeleton curves of FEM analysis with test ones are shown from Fig.3. to Fig.6. Both of them exhibit excellent energy absorption and stable hysteretic response loops. The curves of CR-30 show evidence of “pinching”, while those of CR-45 appear typical stable “shuttle” form with no signs of significant “pinching”, so the latter have better energy dissipation. However, the hysteretic curve of FEM result is plumper than that of test due, in part, to neglect of the slip between the reinforcement and concrete of the former.

Comparison of loads of test with FEM at each stage is given in table 4 and table 5. It can be seen from the tables that the analytical models are able to predict the ultimate strength within an average error of 10% and the yield strength within an average error of only 5%.

In general, the results of FEM have certain accuracy and could provide a good prediction of seismic behavior.



(a) test



(b) analysis

Fig.3 Hysteretic curve of CR-30

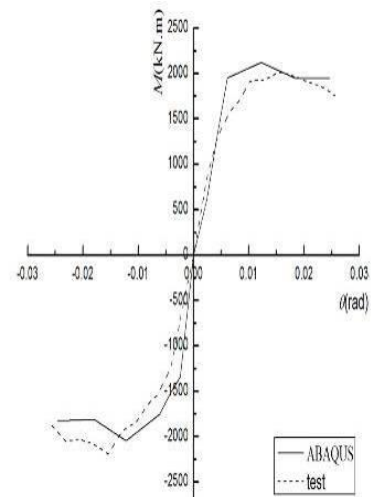
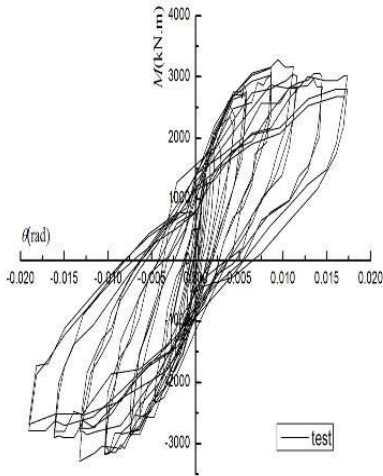
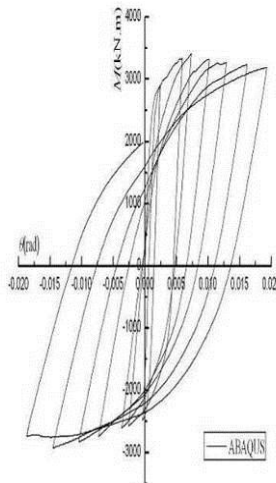


Fig.4 Skeleton curve of CR-30



(a) test



(b) analysis

Fig.5 Hysteretic curve of CR-45

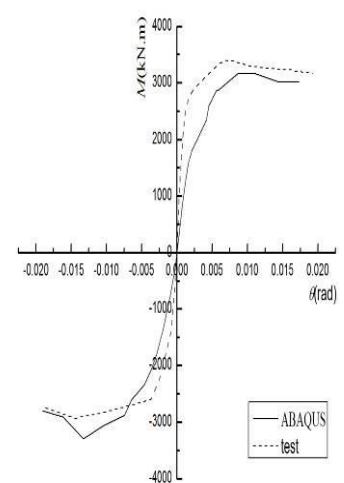


Fig.6 Skeleton curve of CR-45

Table 4 Comparison of results of CR-30 at each stage

Analysis method	Loading direction	Yield load		Ultimate load		failure load	
		M_y (kN.m)	$\theta_y(10^{-3}$ rad)	M_u (kN.m)	$\theta_u(10^{-3}$ rad)	M_f (kN.m)	$\theta_f(10^{-3}$ rad)
FEM	Forward	1988	7.49	2119	12.2	1952	18.2
	Backward	-1726	5.92	-2043	12.2	-1826	17.5
Test	Forward	1703	8.27	2017	15.4	1757	20.6
	Backward	-1832	8.45	-2187	15.4	-1869	25.6
Test/FEM	Forward	0.86	—	0.95	—	0.90	—
	Backward	1.06	—	1.07	—	1.02	—

Table 5 Comparison of results of CR-45 at each stage

Analysis method	Loading direction	Yield load		Ultimate load		failure load	
		$M_y(\text{kN.m})$	$\theta_y(10^{-3}\text{rad})$	$M_u(\text{kN.m})$	$\theta_u(10^{-3}\text{rad})$	$M_f(\text{kN.m})$	$\theta_f(10^{-3}\text{rad})$
FEM	Forward	2904	2.46	3412	7.32	3164	19.2
	Backward	-2603	4.03	-2925	14.5	-2740	18.6
Test	Forward	2722	5.01	3168	8.66	3012	17.3
	Backward	-2788	7.29	-3293	-13.2	-2799	18.9
Test/FEM	Forward	0.94	---	0.93	---	0.95	---
	Backward	1.07	---	1.12	---	1.02	---

Development of plastic hinges. Plastic hinges developed in hybrid coupled wall system during loading are shown in Fig.7. It is more intuitive and easier-to-use to analyze the development of plastic hinges by finite element analysis, making up for the deficiency of the test.

Generally speaking, the coupling ratio of the structure directly affects the plastic hinge development, for shear yield of the beam is not simultaneously. The plastic hinge formed firstly in the fifth floor for CR-30, while formed at the third floor for CR-45. Along with the increase of the lateral load, beams at other floors yielded in shear manner subsequently, and then plastic hinge formed. During strong seismic shaking, coupling beams at each layer become energy dissipating damper set along the entire height of the wall, expand the scope of the energy dissipation through the ductile deformation. At last, the bottom of wall developed plastic hinge in tensile region.

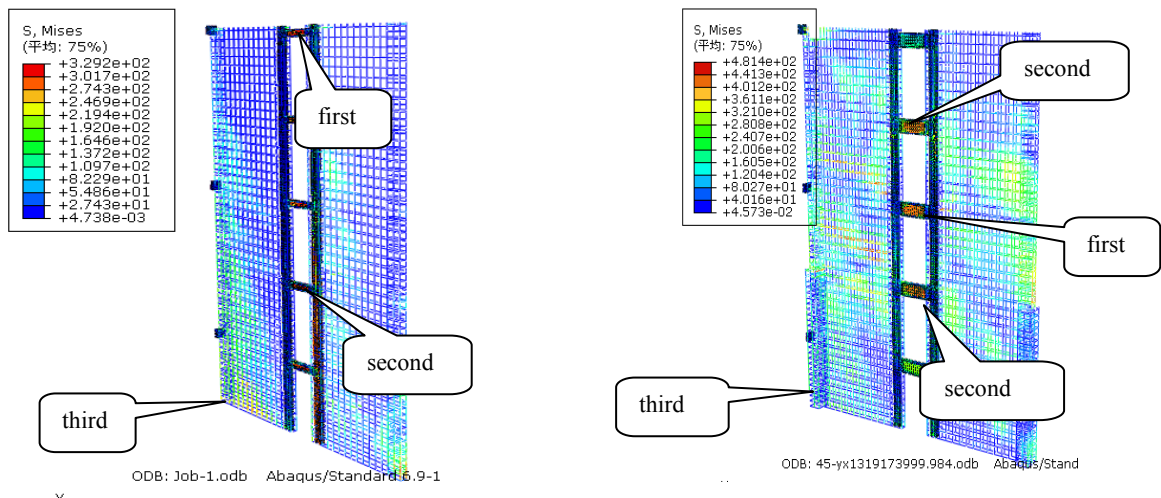


Fig.7 Sequence of plastic hinge development

Failure mechanism. As observed in FEM, destruction of model can be divided into four stages: concrete shear wall cracking, steel coupling beam at each layer yielding in shear manner, reinforcement in tension at the bottom of shear wall yielding, concrete in pressure area at the bottom of shear wall crushed.

Based on results of FEM analysis, it can be seen that failure of both specimens belongs to the beam hinge mechanism, dissipating energy by shear deformation of steel beams till plastic hinge formed at the bottom of wall, so the seismic behavior of shear walls can be significantly improved.

Conclusions

(1) The results of FEM have certain accuracy and could be used to study the seismic behavior of hybrid coupled wall system with steel boundary elements;

(2) The coupling ratio of the structure directly affects the plastic hinge development, for shear yield phenomenon on the beam is not simultaneously.

(3) Based on the sequence of plastic hinge development, it can be concluded that the structural system is a multiple anti-seismic system, dissipates energy in a ductile manner, and satisfies the demand of seismic ductility design.

(4) The hysteretic curve of CR-30 shows evidence of “pinching”, while that of CR-45 appears typical stable “shuttle” form with no signs of significant “pinching”, so the latter has better energy dissipation, and provides an efficient structural system for the resistance of seismic effects.

Acknowledgements

The work described in this paper is funded by the National Natural Science Foundation (Grant No.50878182), and by Natural Science Foundation of Shaanxi (Grant No. SJ08E209). These financial supports are greatly acknowledged.

References

- [1] Kent A. Harries, Denis Mitchell, Richard G. Redwood, William D. Cook. Nonlinear seismic response predictions of walls coupled with steel and concrete beams [J]. *Journal of Structural Engineering*, 1997, 123(12): 148-149.
- [2] Bahram M. Shahrooz, Mark E. Remmetter and Fei Qin. Seismic design and performance of composite coupled walls [J]. *Journal of Structural Engineering*, 1993, 119(11): 3291-3309.
- [3] Kent A. Harries, J. Dan'l Moulton and Robert L. Clemson. Parametric study of coupled wall behavior-implications for the design of coupling beam [J]. *Journal of Structural Engineering*, 2004, 130(3): 480-488.
- [4] Kent A. Harries, Denis Mitchell, William D. Cook etc. Seismic response of steel beams coupling concrete walls [J]. *Journal of Structural Engineering*, 1993, 119(12): 3611-3629.
- [5] Guo Feng. Hysteretic behavior of connections of steel coupling beams linking concrete shear walls with steel boundary element in hybrid coupled walls system [D]. Xi'an: Xi'an University of Architecture and Technology, 2007. (in Chinese)
- [6] Mohamed Hassan and Sherif EI-Tawil. Inelastic dynamic behavior of hybrid coupled walls [J]. *Journal of Structural Engineering*, 2004, 130(2): 285-296.
- [7] Shi Yun, Su Mingzhou. Experimental study on seismic behavior of hybrid coupled wall system with steel boundary elements [J]. *China Civil Engineering Journal* (submitted). (in Chinese)
- [8] Shi Yun, Su Mingzhou. Experimental study on hysteretic behavior of innovative hybrid coupled wall system with high coupling ratio [J]. *China Civil Engineering Journal* (submitted). (in Chinese)
- [9] Zhang Jin, Wang Qingyang. Parameters verification of concrete damaged plastic model of ABAQUS [J]. *Journal of Building Structure*, 2008, 38(8): 127-130. (in Chinese)

Dynamic Characteristic Analysis on Experiment of Suspended-span Structures in Water

Shengrong Zuo^{1, a}, Jixin Yang^{1, b}

¹School of Transportation, Wuhan University of Technology, Wuhan, 430063, China

^azola1028@sina.com, ^bwhutvses@163.com

Keywords: suspended-span structure; dynamic analysis; experiment; Additive Mass Method

Abstract. The safety of dynamic characteristics plays a very important role of underwater structures today. In this paper, in order to analyze the dynamic characteristics of structures we have done several groups of experiments and tested the dynamic characteristics of the models in air and water respectively, then we calculated the natural frequency of the suspended-span structures in water using Additive Mass Method and compared with the experimental data. The results showed that the comparison between the experimental and calculated data is accordant, contemporaneously we tested the natural frequency in water with in air to the same specimen, it shows that the frequency of structure in water is lower than in air, but only little difference.

Introduction

Along with the land and sea traffic connected more and more closely, more cross-sea bridges and the cross-harbour tunnels have achieved rapid development, especially the suspended-span structures in water such as spanning section of submarine pipeline, ocean floating structures, the mooring cable of submerged floating tunnel structures etc. These suspended-span structures are easily led to damage and even destruction under the influence of large deformation from the wave, vortex, impact, earthquake and other dynamic factors. Therefore, it is very important for the security of suspended-span structures to research the dynamic characteristics of structures.

In order to study the dynamic characteristics of suspended-span structures in water, this paper designed some different size groups of rebar instead of suspended-span structure, and we tested the dynamic characteristics of the models in air and in water respectively for comparison.

Experimental Results

The experimental condition can be seen from figure 1, it shows the condition of 2-metre-long rebar in the air and water respectively. The down deflection is not obvious when the two ends of the steel bar are fixed on the pedestal when its length is 1m and 2m respectively. After the incentive by force-hammer, the rebar vibrates in the horizontal position while the length is 4m, especially its diameter is 10mm or 16mm, the down deflection is obvious when the two ends are fixed. After the incentive, it vibrates nearly on the equilibrium position after deformation.



a) in air



b) in water

Fig.1 Dynamic experiment of 2-metre-long rebar

After repeated testing, the vibration frequency results of the rebar are relatively stable and the results of spectrum analysis are shown in table 1~table 3.

Table 1 Experimental results of 1m-long rebar in water and air

Steel Specifications	Order	Frequency in water(Hz)	Frequency in air(Hz)
Φ10	1	21.00	22.50
	2	78.00	82.50
	3	119.00	128.00
Φ16	1	31.25	32.50
	2	92.50	130.00
	3	253.53	294.35

Table 2 Experimental results of 2m-long rebar in water and air

Steel Specifications	Order	Frequency in water(Hz)	Frequency in air(Hz)
Φ10	1	5.25	5.75
	2	20.75	21.50
	3	54.30	56.35
Φ16	1	7.75	8.00
	2	30.50	32.00
	3	68.75	74.40

Table 3 Experimental results of 4m-long rebar in water and air

Steel Specifications	Order	Frequency in water(Hz)	Frequency in air(Hz)
Φ10	1	1.26	1.52
	2	5.95	6.38
	3	12.85	13.50
Φ16	1	1.95	2.12
	2	7.63	8.25
	3	17.38	18.50

A method for natural frequency of structures in water

This paper introduces a method of structure's natural frequency calculation.

Additive Mass Method

When you calculate the natural frequencies of structures in water, using the water attached to the structure surface with some mass instead of water dynamic effect, this approximate algorithm is called Additive Mass Method. This method assumes that the water is inviscid, irrotational and incompressible ideal fluids, and assuming the structure in water is rigid. Because the calculation is simple, Additive Mass Method and its application in the engineering field is also very widespread.

The key solving problems by Additive Mass Method is to calculate the mass of attached water. According to the literature[1-3], about the mass of attached water of cylinders in water, can be calculated as follows.

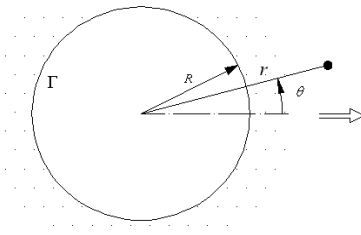


Fig.2 The infinite long cylinder submerged in water

Assuming an infinite cylinder (rigid) embedded in the whole space waters, choosing the axial direction as Z axis, supposing the speed of horizontal direction as $v(t)$, the unit long cylinder quality of attached wate is m_f , as shown in Figure 2.

Within the unit length, the fluid particles' total kinetic energy in outer domain of cylinder is

$$T = \int_{\Omega} \frac{P}{2} \left[\left(\frac{\partial \phi}{\partial x} \right)^2 + \left(\frac{\partial \phi}{\partial y} \right)^2 \right] d_{\Omega} \quad (1)$$

Since all of the physical quantity is independent of the z coordinate, this has become a two-dimensional potential flow problem. Introducing Hamilton operator ∇ (Defined as $\nabla \phi = \vec{i} \frac{\partial \phi}{\partial x} + \vec{j} \frac{\partial \phi}{\partial y}$), and we can get:

$$T = \int_{\Omega} \frac{P}{2} (\nabla \phi \cdot \nabla \phi) d_{\Omega} \quad (2)$$

According to Green's first identity and $\nabla^2 \phi = \frac{\partial^2 \phi}{\partial x^2} + \frac{\partial^2 \phi}{\partial y^2} = 0$, equation (2) can be written:

$$T = \int_{\Omega} \frac{P}{2} (\nabla \phi \cdot \nabla \phi) d_{\Omega} = \frac{P}{2} \int_{\Gamma} \frac{\partial \phi}{\partial \gamma} \phi d_{\Gamma} + \frac{P}{2} \int_{\Gamma_{\infty}} \frac{\partial \phi}{\partial r} \phi d_{\Gamma} \quad (3)$$

For (3), Γ stands for the cylindrical boundary, Γ_{∞} stands for the outside boundary of flow field Ω . In infinite distance, according to the boundary condition that the radial velocity of water particles is zero on the flow field.

$$v_r|_{r \rightarrow \infty} = \frac{\partial \phi}{\partial r}|_{r \rightarrow \infty} = 0 \quad (4)$$

$$T = -\frac{P}{2} \int_{\Gamma} \frac{\partial \phi}{\partial r} \phi d_r \quad (5)$$

Solving the two-dimensional potential flow velocity potential $\phi(r, \theta, t)$

$$\nabla^2 \phi = \frac{\partial^2 \phi}{\partial r^2} + \frac{1}{r} \frac{\partial \phi}{\partial r} \Big|_{r \rightarrow \infty} + \frac{1}{r^2} \frac{\partial^2 \phi}{\partial \theta^2} = 0 \quad (6)$$

Letbe $\phi(r, \theta, t) = \varphi(r) \cos \theta v(t)$

$$\frac{d^2 \varphi}{dr^2} + \frac{1}{r} \frac{d\varphi}{dr} - \frac{1}{r^2} \varphi = 0 \quad (7)$$

The general solution of equation (7) is

$$\varphi(r) = Ar + \frac{B}{r} \quad (A, B, \text{ are undetermined constants}) \quad (8)$$

Two given boundary conditions:

$$r \rightarrow \infty : v_r = \frac{\partial \phi}{\partial r} = \frac{d\varphi}{dr} \cos \theta v(t) = 0 \quad (9)$$

So $A=0$, by coupling conditions, namely the radial velocity (v_r) between cylindrical particles in the fluid-solid interface and water particles is equal, so

$$r=R: v_r = \frac{d\varphi}{dr} \cos \theta v(t) = v(t) \cos \theta \quad (10)$$

$$\frac{d\varphi}{dr} = -\frac{B}{R^2} = 1, B = -R^2 \quad (11)$$

Taking A, B values into (8), then the expression of velocity potential is gainable:

$$\phi(r, \theta, t) = -\frac{R^2}{r} \cos \theta v(t) \quad (12)$$

Taking (12) into the total kinetic energy of flow field (5):

$$T = -\frac{\rho}{2} \int_0^{2\pi} \left[\frac{R^2}{R^2} \cos \theta v(t) \right] \left(-\frac{R^2}{R} - \cos \theta v(t) \right) R d\theta = \frac{\rho}{2} \pi R^2 V^2 \quad (13)$$

Let be the total kinetic energy is equal to unit length quality of attached water, we can obtain equivalent quality of attached water:

$$m_f = \rho \pi R^2 \quad (14)$$

m_f is the quality of attached water, equal to the quality of discharged water by the cylinder exactly.

The results using Additive Mass Method is shown in table 4~ table 6.

Table 4 1m-long rebar's calculation results

Steel Specifications	Order	Frequency in water(Hz)	Frequency in air(Hz)
Φ10	1	19.12	20.30
	2	76.48	81.20
	3	172.08	182.71
Φ16	1	30.59	32.48
	2	122.37	129.93
	3	275.32	292.33

Table 5 2m-long rebar's calculation results

Steel Specifications	Order	Frequency in water(Hz)	Frequency in air(Hz)
Φ10	1	4.78	5.08
	2	19.12	20.30
	3	43.02	45.68
Φ16	1	7.65	8.12
	2	30.59	32.48
	3	68.83	73.08

Table 6 4m-long rebar's calculation results

Steel Specifications	Order	Frequency in water(Hz)	Frequency in air(Hz)
Φ10	1	1.19	1.27
	2	4.78	5.08
	3	10.75	11.42
Φ16	1	1.91	2.03
	2	7.65	8.12
	3	17.21	18.27

Results analysis

Under the same conditions,we compared the experiment results with Additive Mass Method,the percentage of frequency relative difference by experiment and Additive Mass Method is shown in Table 7.

Table 7 Comparison between experimental results and Additive Mass Method

Relative difference (%)	1m(the first order)		2m (the first order)		4m(the first order)	
	in water	in air	in water	in air	in water	in air
Φ10	8.95	9.78	9.29	11.65	5.56	16.4
Φ16	2.11	0.06	1.29	-1.50	2.05	4.25

We can come to the conclusion from table 7,with the increase of the rebar diameter, two curves trend the same change and the results of experimental data are close to another one using Additive Mass Method.To the specification of Φ16 rebar,the percentage of relative difference is less than 5%, only the rebar whose diameter is 10mm, the experimental result is slightly larger than another, because the experimental device is not strictly fixed as requested. The above analysis shows that Additive Mass Method is reliable and accurate, and it can be used for the analysis of structural dynamic characteristics in the water.

In order to find the vibration characteristic difference in air and in water, we compare each rebar the first order frequency of each condition, Figure 3 shows the frequency curves of the same specification rebar with different length and different media.

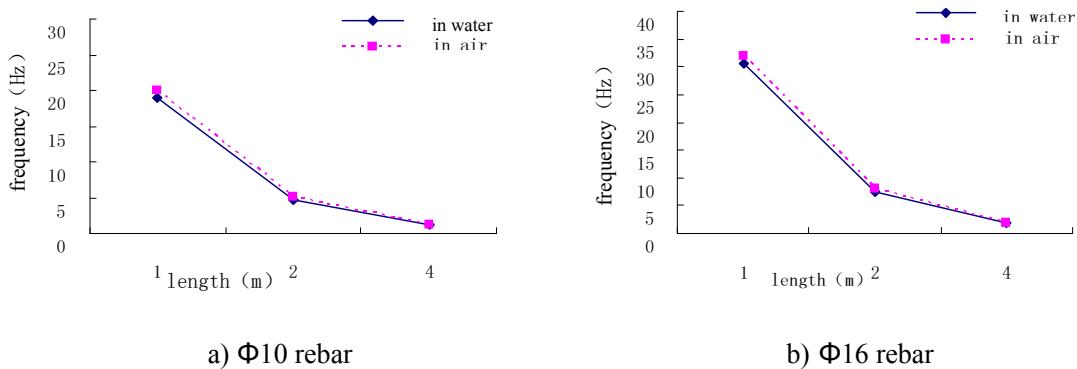


Fig.3 Comparison of rebar's first order frequency in water and in air

We can see from Figure 3,the first order frequency in air is greater than in water under various working conditions, the reason is that structural mass is increased through fluid effecting on the structure in the process of vibration,so the vibration frequency is decreased.The first order

frequency of 1m-long rebar is relatively big,so the difference of the frequency in air and water is more visible as the diagram shown. But the relative difference of vibration frequency is very close,less than 5%, when the rebar with different lengths are offered in the water and air.As structur's vibration frequency is different in water and in air, this will affect the dynamic response of structures in water,so fluid-solid coupling effect should be considered for accurate dynamic analysis of underwater structures[4-6].

Conclusions

We can come to these conclusions from the paper as follows.

(1)Experimentally measured data is compared to the results of Additive Mass Method, they are similar,so the method is reliable and accurate, and the method can be used for the analysis of structural dynamic characteristics in the water.

(2)The first frequency of rebar in air is greater than in water but the difference is small.

(3)The vibration frequency of structur is different in water and in air,and it will affect the dynamic response of structures in water,so we should consider fluid-solid coupling effect.

References

- [1]Yuying Huang. A Variational Formula for Natural Frequencies of Solid-Water Interaction System.Journal of Huazhong University of Science and Technology(Natural Science Edition). 1985.13(1): 91-96.
- [2]Qin Qian, Yuying Huang ,Zhongzu Liu. A direct method for added water mass.MECHANICS AND PRACTICE, 1996.18(5):
- [3]Haidong Su, Yuying Huang .Novel Numerical Method for Solving Added Mass of Structure Embedded in Semi-infinite Liquid Field. Journal of Huazhong University of Science and Technology(Urban Science Edition) . 2003(4): 14-16
- [4]Fan Lei,Jixin Yang,Hui Liu.Dynamic response analysis of deepwater pier with fluid-solid interaction. Guangzhou:Trans Tech Publications,2010: 161-166.

Experimental Research on Hysteretic Behavior of top-seat Angles Beam-column Connections

Wang Xinwu^{1, a}, Han Dong^{2, b}

¹ Department of Civil Engineering, Luoyang College of Technology
Luoyang 471023, China

² School of Civil Engineering And Architecture, Wuhan University of Technology
Wuhan, Hubei 430070, China

^awxw197100@sina.com, ^bhandong1851@126.com

Keywords: Semi-rigid steel joint, hysteresis cycles, top-seat angles, energy dissipation, rotational stiffness, moment-resisting force.

Abstract. Two full-scale specimens of angles steel using H-section member had been conducted. The specimens were subjected to cyclic reversal loading simulating earthquake effects on a steel moment-resisting force. The objective of the work is to determine the behavior of these connections under cyclic reversal loading well into the inelastic range and to ascertain the effect of design parameters such as column flange stiffener, pre-tension of bolts and the angles flange thickness on the overall behavior. Observations were made concerning the response of the connections and its elements in terms of strength, stiffness and energy dissipation. Information on the design of these connections is presented. The hysteretic behavior of angles beam-column connections under cyclic loading is presented in this paper. Rotational stiffness, the carrying capacity and ductility of top-seat angles connections are analyzed. It is concluded that angles connections can possess the relative high stiffness, strength and excellent ductility as moment-resisting components in the seismic design of frames. Most of the input energy was dissipated in the flange of angles while the column participated a little in the energy dissipation process in the test.

Introduction

Beam-to-column connections are integral element of a steel frame, and their behavior affects its overall performance under loading. Vulnerability of welded moment connections in steel moment-resisting frames subject to severe cyclic loading was demonstrated during the 1994 Northridge Earthquake. Since then, a lot of connections have been proposed for the retrofit and the new design of steel moment frames in high seismicity areas. Among the proposed connections are those with high strength bolts[1][2]. Top-seat angles connections is regarded as one of the most typical semi-rigid connections. This connection type offers several advantages such as low cost, simple and convenient erection procedures, and good quality control since field-welding in adverse environment is undesirable in the best of connections[3][4][5].

To obtain the data about the response of top-seat angles connection under cyclic loading, this study will be conducted. Special attention is paid to the behavior of the individual components comprising the connection and to their effect on the response. The important factors that influence the behavior of the connection, such as angle thickness, bolts' pre-tension forces, column flange thickness and column flange stiffeners, are examined. Recommendations for designing the connection's components to achieve good performance during severe earthquakes are provided. The performance of the connections under conditions of cyclic loading in terms of stiffness, ductility, strength and energy dissipation, are investigated. It is planned to assess the following:

- (1) The behavior of column flange stiffeners;
- (2) The behavior of top-seat angles connections;
- (3) The failure models of top-seat angles connections;

The energy dissipation systems and capability of top-seat angles connections.

Experiment program

In the design of moment-resisting frames under severe lateral loads, it is reasonable to assume that the points of inflection are located at the mid-span of the beams and the mid-height of the columns. A simple cantilever type beam-column connection, such as the one shown in Fig.1, was chosen as the specimen for this study. The cantilever length represents approximately one-half the length of typical beams in a moment-resisting frame. For simplicity of testing, no attempts were made to simulate axial force in the column. Attention was mainly concentrated on the study of the behavior of the connection itself.

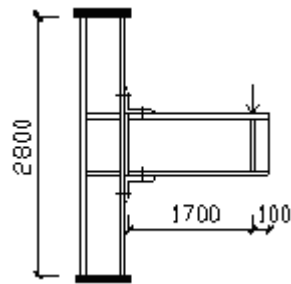


Figure1: Typical top-seat angles connection



Figure2: General view of test arrangement

The material used for two test specimens including beams, columns, continuity flange stiffeners, top-seat angles was in accordance with Q235 steel. Beams and columns were manufactured with rolling H steel. The sizes of beam and column were H300×200×8×12 and H200×200×12×12 respectively. The high tensile bolts used are specified as 20mm diameter, grade 10.9. They were full preloaded according to the China Code. The contacting surfaces between connections components were treated according to China steel design code (GB50017). An average value of the cyclic friction coefficients measured from the cyclic tested was about 0.40.

The main geometrical dimensions are indicated in the table 1.

Table1 Details of the test connection

Specimen No.	Top-seat angles Size(mm)	Column flange stiffener
JD1	110×12×12	yes
JD2	140×16×14	yes

All specimens attached through the connection to be test to a “rigid” counter-beam, as shown in Fig.2. The loads are applied to the free end of the specimen by means of a device that transfers horizontal forces only. Testing conditions hence approximate quite closely the case of beam-column joints with negligible column deformability.

For monitoring the actuator load, load transducers was loaded in the front of jack. The load transducer was calibrated after each test on a multipurpose test machine. For measuring the connections rotation, electron centigrade instrument was used. The curves of connections rotation and the load were drawn by X-Y function enregistering instrument. Strain gauges were used to monitor the onset of beam flange local bucking and to determine initial yielding of the beams.

All date from strain gauges and transducers were scanned by a multi-channel DH3815 scanner system. The readings were recorded using a microcomputer system.

To simulate seismic forces the test specimens were subject to a quasi-static cyclic loading. The loading history may be considered one of the most important factors affecting the significant of cyclic tests.

Before reaching the yield point, an individual specimen was first subjected to two load cycles of 20% the expected yield value, then the load was increased 20KN and the two load cycles was also adopted. The load was then increased until the initial beam yielding was recorded by the strain gauges or the apparent turning point was turned out in the curve of connection M- ϕ . Then for subsequent

loading cycles, the rotation of connection was incrementally increased by the yield rotation up to the failure of connections. The models of the failure of connections included top and seat angles fracturing, local flexions of column flange and the looseness of bolts. In reaching either of failure modes, the test would be terminated.

Experimental results and discussion

The connection's rotation was the result of top-seat angles and column flange deformation and bolt extension. No panel zone deformation was observed, since the column flange stiffeners were designed and the rigid of top-seat angles was very weak. Fig.3.and Fig. 4 showed the moment-rotation hysteretic curves for connection JD1 and JD2, respectively. As can be observed, all the connections showed stable hysteretic behavior up to the fracture of the connections. In the latter cases, significant degradation occurred in the connection strength after severe distortion and/or crack initiation developed. During latter cycles of the test severe distortion to the column flange was observed. It was evident that column distress could have been avoided with the use of column stiffeners. Failure of the specimen was attributed to severe distortion of the flange of top-seat angles.

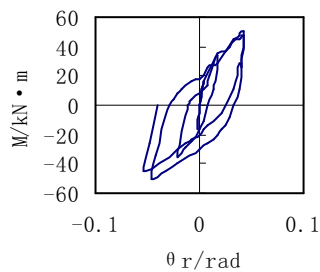


Figure3: Hysteresis curves for JD1

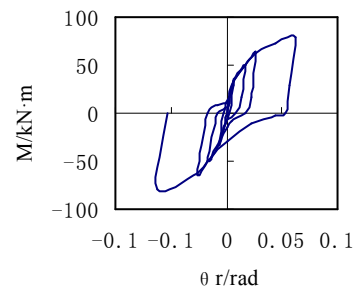


Figure4:Hysteresis curves for JD2

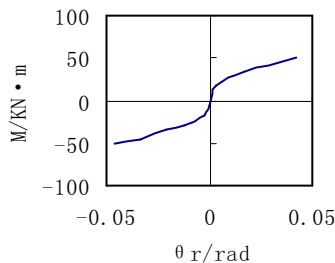


Figure5:Envelope of the cyclic response of JD1

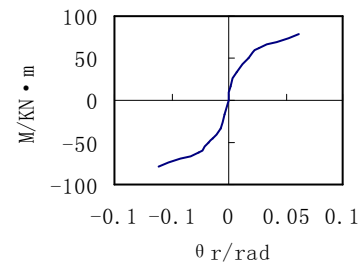


Figure6:Envelope of the cyclic response of JD2

Fig.5 and Fig.6 were the envelop of the cyclic response of JD1 and JD2 respectively. The relations of moment and rotation were outlined. The line relations of moment and rotation were showed in the initial phase and the phase was very short. With increasing the load, the non-line relations of moment and rotation became very apparent. The fluctuating phenomenon of the relations was revealed. The main reason was that the bolts lost their pretension forces significantly in the later stage of loading.

In seismic design, cyclic energy dissipation is of great important, since it expresses the ability of the members and their connections to dissipate earthquake input energy. Generally, sufficient energy dissipation without substantial loss of strength and stiffness constitutes desirable behavior for beam-column subassemblages[3][4]. It was confirmed that most of the energy was dissipated in the flange of top-seat angles while the column participated a little in the energy dissipation process in this test.

The main parameters that describe a connection's behavior are (1) the connection yield moment, M_y , (2) the initial stiffness of the connection, R_0 , (3) the connection strength, M_u and (4) the connection rotation capacity (i.e.ductility), θ_u [5]. Table 2 shows these parameters for some of the tested specimens. As expected, the initial stiffness of a connection increases as the top-seat angles

flange thicknesses increase. This is evident when connections JD1 and JD2 are compared where the column flange thickness differ, while the stiffness of JD2 is greater than that of JD1 because of the former's greater top and seat angles thickness.

Table 2 Joint capacity and ductility

Specimen	R_0	M_y	M_u	θ_u	μ_ϕ
JD1	0.58	51.01	51.01	0.0544	3.2
JD2	0.78	79.34	79.34	0.0614	4.6

R_0 the initial stiffness of connections, $10^4 KN \cdot mrad^{-1}$

M_y yield moment of connections, $KN \cdot m$

M_u maximum moment of connections, $KN \cdot m$

θ_u maximum rotation of connections, rad

μ_ϕ the ductility coefficient of connections, $\mu_\phi = \theta_u / \theta_y$

θ_y rotation corresponding to yield moment of connections, rad

Conclusions

Based on the experiment work, the following preliminary conclusions and design code implications can be made about beam-column top-seat angles connections.

(1) All two tested connections showed degradation in stiffness with load cycles due to diminished bolt pre-tension forces and inelastic deformations. Pre-tension forces in all the bolts showed degradation with repeated load cycle. The drop in the pre-tension force continues with increasing the load. To ensure that the bolts do not fail and do not lose their pre-tension forces significantly even during moderate earthquake excitation, it is suggested that the bolts be designed to sustain a force corresponding to beam moment of 1.3Mp.

(2) In all the tests, the connections were not able to sustain moment higher than the beam's nominal plastic moment capacity. The main reason was that the stiffness of top-seat angles was too weak.

(3) If the stiffeners of the column flange were designed, the most possible failure mode is the fracture of top or seat angles.

(4) Most of the energy was dissipated in the flange of top and seat angles while the column participated a little in the energy dissipation process.

(5) When properly designed and detailed, the top-seat angles connection can be considered suitable for moment-resisting frames in areas of high seismicity.

Acknowledgements

This research was supported by a grant of Ministry of Construction of China, grant No.01-2-085. The authors greatly appreciate the skillful work of all members of this project, and especially express their thanks to Pro. Peng Shaoming and Pro. Jiang Cangru for their assistance in the all process of this project.

References

- [1] Ballio, G. et al. steel beam-to-column joint under cyclic loads, experimental and analytical approach, Proc. 8th European Conference on Earthquake Eng., Lisbon, vol. 12 pp. 772~779, 1986.
- [2] C. Bernuzzi, R. Zandonini and P. Zanon. Experimental analysis and modeling of semi-rigid steel joints under cyclic reversal loading. J. Construct. Steel Research, vol. 38 pp. 95~123, February 1996.
- [3] A. Ghobarah, A. Osman and R.M. Korol, Behaviour of extended end-plate connections under cyclic loading[J], Engineering and Structure, vol. 12 pp. 15~27, January 1990.
- [4] R.M. Korol, A. Ghobarah & A. Osman, Extended End-Plate Connections Under Cyclic Loading: Behaviour and Design, J. Construct. Steel Research, vol. 16 pp. 253~280, January 1990.
- [5] J. Shen, A. Astaneh-Asl. Hysteresis model of bolted-angel connections. J. Construct. Steel. vol. 54 pp. 317~343, March 2000.

Applied Research on CL structural system in the construction of affordable housing

Hao Yunhong^{1, a}, Jin Tieshun^{1, b}, Zhao Kexing^{2, c}

¹School of Civil Engineering, Inner Mongolia University of Technology, Hohhot, Inner Mongolia, 010051, China

²JINGDA Building System Company, Wulanchabu, Inner Mongolia, 012000, China

^ahaoyunhong_hyh@163.com, ^bbuendi@126.com, ^c13947133205@163.com,

Keywords: CL building structural system; affordable housing; seismic performance; fire performance

Abstract. CL (composite light-weight) building structural system is a new composite shear wall structure, which is light, good integrity, excellent seismic performance, insulation and structure of the body of the same life, good fire performance, increased use of area, and other advantages, this paper studies the structural properties of CL on the basis of case through the construction of affordable housing in advantages in the application.

Introduction

Affordable housing and commodity housing are concept that corresponds to, affordable housing refers to the government for low-income housing for needy families provided by the limited standards, limit price or rent of housing, from low-rent housing, affordable housing and policy form of rental housing. To further improve the living conditions of people, affordable housing plays an important role. CL structural system is a set of shear wall structure with load-bearing and thermal insulation in one of the composite concrete, owing to its light weight, good integrity, seismic performance, insulation and structure with the same body of life, fire performance, increase the use of space etc., in the construction of affordable housing, with the application of CL structural system, we can better improve the quality of affordable housing and social benefits.

CL building structural system

CL building structural system belongs to composite concrete shear wall structure, for a variety of different thermal design seismic level partition of the new civil construction. Its core components - CL composite wall panels composed by CL grid (a grid of welded steel sandwich panel insulation) on both sides to form a pouring concrete and load-bearing, insulation, sound insulation in one wall. The three-dimensional diagram shown in Figure 1 (a), the cross section is shown in Figure 1 (b).



(a) three-dimensional structural

(b) cross section

Fig.1. CL system of three-dimensional structural and cross section

CL structural system is a set of shear wall structure with load-bearing and thermal insulation in one of the composite concrete, compared to the ordinary brick and shear wall structure, CL mainly has the following advantages: (1) CL building structural system's weight (average weight (800-900) kg/m^2) is less than the brick weight (average weight (1800-2000) kg/m^2) and frame weight (average weight (1300-1500) kg/m^2); (2) The integrity of CL building structures is fine, and has an Excellent mechanical properties of the structure, seismic performance is better than brick and frame structure; (3) a good solution to the current existence problem that Externally bonded insulation has a short life (≤ 10 years), poor fire performance, and achieve the same life of insulation and structure with the body; (4) increase the use area, compared with the brick, CL building structural system (the room with an area factor of 85% -90%) can be 8-10% increase in the room. Compared to the frame structure (room area index using 80% -85%), it can increased 5-8% of use area, cost-effective upgrade housing.

Performance analysis of CL building structures system

1. Analysis of the main raw material usage: Table 1 shows the main raw material of the CL building structures system and Brick architecture and shear wall structure, it can be seen from the table that the amount of CL building structural system's steel and cement is slightly lower than the wall structure, higher than the brick architecture. Amount of block is less than the brick and wall structure.

Table 1 Statistics of three structures System in the main raw material

Structure form	Steel (kg/m^2)	Cement (kg/m^2)	Block (m^3/m^2)
Brick structure	28.1	136	0.35
Shear wall structure	49.2	170	0.27
CL structural system	46.6	168	0.19

2. Analysis of the structural weight: Table 2 shows the average weight of the CL system and brick structures and shear wall structure. As can be seen from Table 2 that the weight of CL structural system weight is much smaller than brick structure, is about 45% of brick structure, while the weight is less than the shear wall structure, about 90% of its weight.

Table2. Average weight of three structures

Structure form	Average weight (kg/m^2)	Comparison Weight
Brick structure	1800-2000	2.2
Shear wall structure	850-950	1.1
CL structural system	800-900	1.0

3. Analysis of the use area: Compared to brick (with an area coefficient of 75% -80%) and framework (coefficient of 80% -85%), CL building structural system (factor of 85% -90%) has a 5-10% increased use area, greatly enhance the housing cost-effective.

4. Analysis of energy efficiency standards and operating costs: (1) CL wall's heat transfer coefficient (0.65), is less than 370 brick wall (0.9-1.0) and 300 ceramic wall filled with thick (about 0.8) overall heat transfer coefficient, building structural system insulation, heat insulation performance are better than in brick and frame structure, it can meet residential buildings' 65% energy efficiency standards. CL structural system is a composite insulation system; energy efficiency standards can reach 65%. (2) Achieve the same life of insulation and structure, 50 years without replacement.

5. Structural measures to improve the seismic performance: CL structures system consists of reinforced concrete pouring a whole, unique structure, the three-dimensional composite wall tilt steel, connect both sides of the steel welded wire mesh into the space grid, the slenderness ratio and the number on both sides concrete can pull up together into one carrying purposes. And light weight, small force by the earthquake, structural integrity is good, force structure has a good performance, and the principle is similar with ordinary reinforced concrete shear walls, seismic performance is better than brick and frame structure.

Case study

The following two examples of affordable housing, respectively, compared with CL building structural system and brick building structural system and shear wall structure.

1.Comparative analysis of CL building structural system and brick building structural system. Figure 2 shows the units of a 6-layer instance affordable housing.

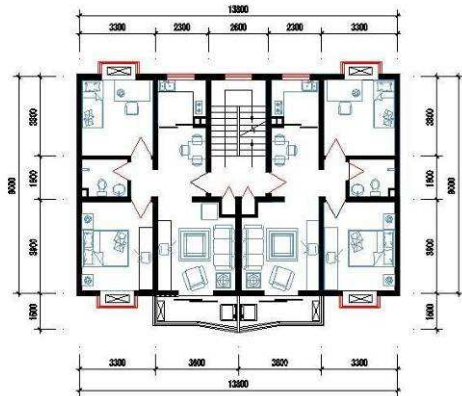


Fig.2. 6-layer instance affordable housing units

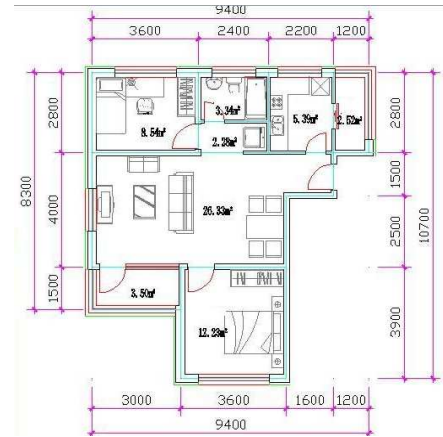


Fig.3. 12-layer affordable housing units.

Table 3 shows comparative analysis of the performance of the affordable housing showed in figure 2. which uses CL building structural system and brick building structural system.

Table 3. CL building structural system and brick structure system comparison tab (6-layer)

Structure form	Wall thickness (mm)	Building area (m^2)	Use area (m^2)	self-weight (kg)
Brick structure (6-layer)	Wall 370 (not including the insulation layer), Interior wall 240, partition120	68.6	53.17	740880-823200
CL building structural system	Wall 370 (including the insulation layer), Interior wall 240, partition120	68.6	60.72	330240-370440

(1) Comparative analysis of the main weight: Table 3 shows that, if we use brick architecture, the 6-layer self-weight goes up to 740880kg-823200kg (not including insulation). If use the CL building structural system, 6-layer weight is 330240kg-370440kg (including insulation), the weight reduced by 55% -58% than brick structural system, Savings on raw materials and building seismic performance improvement is significant.

(2) Comparative analysis of the use area: As table 3 shows, in the same premise of building area, the use area of two different structural systems will show different results, the brick structure, with the use area of 53.17, the CL architecture ,with an area of 60.72, increase the use area by 14%.

(3)Comparative analysis of energy performance standards: In CL structures system, insulation and building are of the same life, 50 years without replacement, without insulation maintenance, replacement. The potential cost of post-costly of the insulation material which has been used in China are very highly, and if use the CL structural insulation system, there is no such costs.

2. Comparative analysis of CL building structural system and shear wall structure. Figure 3 shows the units of a 12-layer instance affordable housing.

Table 4 shows comparative analysis of the performance of the affordable housing showed in figure 2 which use CL building structural system and shear wall structure.

Table 4. CL building structural system and shear wall structure comparison tab (12-layer)

Structure form	Wall thickness (mm)	Building area (m^2)	Use area (m^2)	self-weight (kg)
shear wall structure (12-layer)	Wall 370 (not including the insulation layer), Interior wall 240, partition120	70.3	59.76	717060-801420
CL building structural system	Wall 370 (including the insulation layer), Interior wall 240, partition120	70.3	62.2	674880-759240

(1) Comparative analysis of the self-weight: As table 4 shows, if we use shear wall structure, 12-layer self-weight is 717060kg-801420kg (not including insulation). If we use the CL building structural system, 12-layer self-weight is 674880kg-759240kg (including insulation), it has a 5.2% -5.8% reductions in weight. Savings on raw materials and building seismic performance improvement is significant.

(2) Comparative analysis of the use area: It Can be obtained from Table 4, in the same premise of building area, ordinary shear wall structure, with the use area of 59.76, CL building structural system with the area of 62.2, increase the use area by 4%.

(3) Comparative analysis of energy performance standards: In CL structures system, insulation and building are of the same life, 50 years without replacement, without insulation maintenance, replacement. The potential cost of post-costly of the insulation material which has been used in China are very highly, and if use the CL structural insulation system, there is no such costs.

Conclusion

CL structural system is a set of shear wall structure with load-bearing and thermal insulation in one of the composite concrete, owing to its light weight, good integrity, seismic performance, insulation and structure with the same body of life, fire performance, increase the use of space etc., in the construction of affordable housing, with the application of CL structural system, we can better improve the quality of affordable housing and social benefits.

References

- [1] China Ministry of Construction (GB50010-2011). Design Specifications of Concrete Structures, Beijing: China Building Industry Press, 2011
- [2] Liang Jian-Guo, Zhang xi-wang. Seismic performance of composite walls made of reinforced concrete and brick masonry. Journal of Building Structure, 2003,24 (3), (61 ~ 69)
- [3] Li Zhong-fu, Guan Ke. The procedure, ways and strategy to develop housing industrialization in china. Journal of Harbin University of Architecture, 2000,33 (1), (92 ~ 96)
- [4] Qian Jin, China's new wall materials (residential) building in applied research: [Master thesis]. Shanghai; Tongji University, 2004
- [5] Liu Ji -Chun. The Research of New energy-saving wall [D] . Harbin: Harbin Engineering University, 2005
- [6] Du Yi-nan, Zhang Wei -Jing, Feng Bao-Chun, Qian Jia-Ru single-layer model building big puzzle grid wall Experimental study on seismic [J]. World Earthquake Engineering, 2010,26, (2): (136~140).
- [7]China Ministry of Construction (GB50011-2011) . Seismic Design Specifications of Buildings. Beijing: China Building Industry Press, 2011
- [8] Li Yan -Bo, Zhao Ke-jian, Lin Hao-hua. Experiment on Shearing Resistance of CS Panel. Tianjin University, 2005.2 (3): (120 ~ 123)
- [9] Shi Chu-xian, Theory and Design of Masonry Structures. Beijing; China Building Industry Press, 2003-02
- [10] Hu Zhi-guang, Liu Xiu-gang, Sun xue-meng. Non-Vibro-Casting Self-compaction Concrete Moulding Test on. Building Technology. 2003,34 (7) : (534~535)
- [11] Cheng Wei -Zhi. Construction technology of CL structure of cast-in-place concrete wall. [J]. Building energy efficiency, 2008, 36 (6): (42~44).

Complex Genetic Algorithm for Structure Shape Optimization Design of Mixed Discrete Variables

Chaoyan Zhu ^{1,a} Jingyu Liu ^{1,b} Hongyan Liu ^{1,c} and Xuezhi Wang ^{1,d}

¹School of Civil Engineering, Liaoning University of Technology, Jinzhou121001, China

^azhuchaoyan0321@163.com, ^baaawater@sohu.com, ^cliu.hong.yan@163.com,

^dmyemeilwxz@163.com

Keywords: Mixed discrete variables, Shape optimization, Genetic algorithm, Complex genetic algorithm.

Abstract. Discrete complex method is used in genetic algorithm(GA) and a mixed genetic algorithm called complex genetic algorithm(CGA) is formed. The complex method used here increases the quality of species groups, and improves the searching efficiency. The mixed genetic algorithm method is used in the shape optimization for mixed discrete variables. The integration and coding of the shape variables and the cross-section variables in genetic algorithm can not only solve the coupling problem of two kinds of variables, but also avoid the partial optimum solution resulting from the separation of the two kinds of variables. The result of the exemplification indicates that the complex genetic algorithm for structure shape optimization design of mixed discrete variables is effective.

Introduction

Structure shape optimization design includes shape design variables and cross-section design variables. As shape optimization is added with shape design variables describing geometrical structure, better design results can be obtained from it than pure cross-section optimization. However, difficulty of optimization design increases accordingly. This not only increases the number of design variables, but also can result in convergence difficulty for the coupling of two kinds of variables as cross-section design variables and shape design variables have different nonlinear qualities on the part of target function and constraint function and generally different dimensions and orders. Besides, introduction of shape design variables can increase nonlinearity of constraint function and it is more difficult to structure effective algorithm [1]. In particular, it is more difficult to solve structure optimization problem of mixed discrete variables, i.e, continuation of design variables and quantization of cross-section variables. Therefore, hierarchical design optimization method [2,3] that takes shape design variables and cross-section design variables into separate consideration is adopted in shape optimization design. Although this method can reduce the difficulty in solving, optimal solution can not often be obtained owing to reduction of feasible region of solution space. In recent years, people become more and more concerned with shape optimization method taking two kinds of variables into united consideration [4,5]. This paper, taking two kinds of variables into united consideration, tries to solve structure shape optimization problem of mixed discrete variables with complex genetic algorithm (CGA) and obtains relatively satisfying results.

Mathematical Model for Structure Shape Optimization Design of Mixed Discrete Variables

Design variables of structure shape optimization design of mixed discrete variables include two kinds of variables among which cross-section design variables (viz., sectional area of member bar) are discrete variables and shape design variables (viz., coordinates of nodal points) are continuous variables. Target function is generally the overall weight of structure and constraint conditions are stress constraint, displacement constraint etc.

With the example of structure of bar system receiving both stress constraint and displacement constraint, mathematical model for structure shape optimization design of mixed discrete variables can be expressed as:

Calculate A, X

$$\min W = \sum_{i=1}^n \rho_i A_i \sum_{j \in G_i} L_j(X) \quad (1)$$

$$\text{s.t. } \mathbf{g}_i^\sigma(A, X) = [\sigma_i] - \sigma_i \geq 0 \quad (i = 1, 2, \dots, n) \quad (2)$$

$$\mathbf{g}_{jl}^u(A, X) = [u_{jl}] - u_{jl} \geq 0 \quad (j = 1, 2, \dots, m, \quad l = 1, \dots, nl) \quad (3)$$

$$A_i \in \mathcal{S} \quad (i = 1, 2, \dots, n) \quad (4)$$

$$\underline{x}_k \leq x_k \leq \bar{x}_k \quad (k = 1, 2, \dots, nk) \quad (5)$$

In the above formulas, $A = [A_1, A_2, \dots, A_n]^T$ is cross-section design variable, $X = [x_1, x_2, \dots, x_{nk}]^T$ is design variable of coordinates of nodal points after variable connection; n is class number of member bar after variable linking of cross-section design variables, nk is number of variables for coordinates of nodal points. G_i is a collection comprising member bar in Group i , $L_j(X)$ is the length of No. j member bar, A_i, ρ_i are respectively sectional area and density of member bar in Group i and W is weight of structure. $\mathbf{g}_i^\sigma(A, X)$ is stress constraint and $\mathbf{g}_{jl}^u(A, X)$ is displacement constraint. $[\sigma_i]$ and σ_i are respectively allowable stress value and most unfavorable stress value under various working conditions of member bar in Group i ; $[u_{jl}]$ and u_{jl} are respectively allowable displacement value and most unfavorable displacement value under various working conditions of specific nodal point j in the given direction l ; m is total number of nodal points and nl is number of dimensions of nodal displacement constraint; $\mathcal{S} = \{S_1, S_2, \dots, S_{nl}\}$ is cross-section discrete set, and it generally stipulates that $S_1 < S_2 < \dots < S_{nl}$, nl is number of discrete values in \mathcal{S} . Cross-section design variable A can only obtain discrete values in \mathcal{S} . \underline{x}_k and \bar{x}_k are respectively top and bottom limitation of No. k coordinate variable and coordinate variables obtain values within this range.

Complex Genetic Algorithm

Set up Optimal Individual Bank. Optimal individual of each generation group is not protected in genetic algorithm(GA) and crossover and heteromorphosis operation may cause damage to optimal individual, thus the phenomenon will appear as inferior descendants displace superior parents. Therefore, this paper specially sets up an optimal individual bank for storage of optimal individual of each generation group, but optimal individual is still put into the group for such genetic operations as crossover, heteromorphosis etc.. After completion of genetic operations, the individual in the optimal individual bank is put into next generaton group; this metod, on the one hand, enables optimal individual to participate in evolutionary process and take full advantage of its good genes; on the other hand, can avoid damage caused to optimal individual owing to crossover and heteromorphosis operation and thus missing of possible optimal solution.

Improve Group Quality with Complex Method. Species groups randomly generated by genetic algorithm contain feasible and infeasible individuals. As to feasible individuals, a part of good ones can be selected from them for optimization with discrete complex method, thus generating better ones. As to a good deal of infeasible individuals, discrete complex method is adopted to establish a mapping relationship from infeasible region to feasible region, enabling them to get closer to feasible region.

The way to improve group quality with complex method is specified as follows:

Select a part of good feasible individuals in the species groups as complex vertex, work out centre of figure X_c of these complex vertexes and first optimize it once with traditional discrete complex method so as to obtain better individuals X_L . New individuals are put into the species groups with genetic algorithm again in place of original ones if the former is superior to the latter. Then make each infeasible individual X_h move towards centre of figure X_c , which can turn them into feasible individuals or enable them to get closer to feasible region. Overall quality of the species groups is improved through the above two measures.

Structure Shape Optimization Design Method of Mixed Discrete Variables Based on Complex Genetic Algorithm

Taking shape design variables and cross-section design variables into comprehensive consideration can obtain better target function value in structure shape optimization design, but difficulty exists in coupling of two kinds of variables. Genetic algorithm conducts no direct operation towards real variable of prolem to solve in the operational process and its operation object is only bit string after coding of design variable. Therefore, this paper encodes shape design variables and cross-section design variables in the same chromosome in a united way and two kinds of variables are both expressed as operable form of bit string for genetic algorithm. Through conducting such genetic operation as replication, crossover and heteromorphosis etc. onto individual coding bit string, genetic algorithm continuously searches individuals of high fitness and finally works out optimal solution or approximate one. Hence, working out optimization design of structure shape with genetic algorithm can well solve coupling problem of two kinds of variables.

Binary coding is adopted in this paper. Binary substring of certain length stands for a design variable. There are two kinds of variables for shape optimization design; a bit string with n_1 shape design variables of m_1 substring length and n_2 cross-section variables of m_2 substring length end to end form a chromosome in coding, expressing an individual.

In decoding, dividing binary bit string expressing an individual into $m_1 n_1$ and $m_2 n_2$ according to total bit string length of shape design variables and cross-section design variables; then divide bit string expressing shape design variables into n_1 sections and that expressing cross-section design variables into n_2 sections; finally obtain decimal number from corresponding relation of binary bit string and decimal number, mapping discrete value or continuous value of variables.

Exemplification of Optimization Algorithm

This example is taken from literature [6]. Truss bridge structure receives the effect of uniformly distributed load. See Fig. 1 for initial design. Sectional areas are all 8cm^2 . Hypothesize nodal points in lower chord of the structure remain fixed with nodal load $P=10\text{kN}$. Nodal points in upper chord can move along vertical direction. Vertical displacement of nodal point 10 is restrained for less than 1cm ($1/1000$ span). Structure symmetry remains unchanged and minimal sectional area is 0.5cm^2 . Elasticity modulus of material $E=210\text{GPa}$, density $\rho =7800\text{kg/m}^3$, and admissible stress of all member bars is 240MPa .

The original question is about optimization problem of continuous variable, requiring minimal sectional area is 0.5cm^2 ; this paper selects 29 numerical values from the table of standard steel section and discrete collection composed of sectional area of each pole is $S= \{0.503, 0.636, 0.785, 0.950, 1.131, 1.327, 1.539, 1.767, 2.011, 2.270, 2.545, 2.835, 3.142, 3.464, 3.801, 4.155, 4.524, 4.909, 5.309, 5.726, 6.158, 6.605, 7.069, 7.548, 8.042, 8.553, 9.079, 9.621, 10.18\}\text{cm}^2$. Top and bottom limitations of nodal point coordinates in upper chord of the structure are 0.2m and 6.4m .

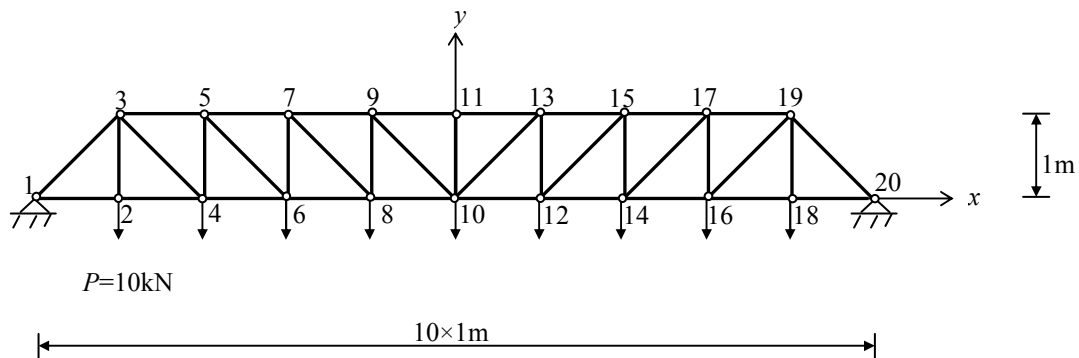


Fig.1 Truss bridge

Considering requirement for structure symmetry, divide cross-section design variables into 19 groups and coordinate design variables into 5 groups. Grouping situation is shown in Tab. 1.

Optimization results obtained from simple genetic algorithm and complex genetic algorithm are shown in Tab. 2. The unit of coordinates design variables is meter. All constraint conditions meet requirements.

It can be seen from Tab. 2 that the weight decreases by 4.05% with the method adopted in this paper compared with simple genetic algorithm; compared with the result after optimization of literature [6], the weight drops by 4.38% . Structure weight in initial design of literature [6] is 256.73kg , i.e. 2515.954N , it is 475.50N after shape optimization with complex genetic algorithm, reducing by 81.10% . Thus, it is very effective for this paper to take two kinds of variables into integral consideration for structure shape optimization design of mixed discrete variables with complex genetic algorithm.

Conclusions

This paper mixes discrete complex method and genetic algorithm combining advantages of each, improving group quality of genetic algorithm with discrete complex method, adopting the measure of setting up optimal individual bank and constituting complex genetic algorithm of better properties.

This paper applies complex genetic algorithm into structure shape optimization design of mixed discrete variables, takes shape design variables and cross-section variables into unified consideration and adopts two-step searching strategy to reduce searching space and thus to accelerate searching course. Through exemplification, optimization design method used in this paper proves to be feasible and effective.

Cross-section Variables		Coordinates Design Variables	
Number of Variable	Number of Member Bar	Number of Variable	Coordinates of Nodal Points
1	1-3, 19-20	20	y_3, y_{19}
2	2-3, 18-19	21	y_5, y_{17}
3	3-4, 16-19	22	y_7, y_{15}
4	3-5, 17-19	23	y_9, y_{13}
5	4-5, 16-17	24	y_{11}
6	5-6, 14-17		
7	5-7, 15-17		
8	6-7, 14-15		
9	7-8, 12-15		
10	7-9, 13-15		
11	8-9, 12-13		
12	9-10, 10-13		
13	9-11, 11-13		
14	10-11		
15	1-2, 18-20		
16	2-4, 16-18		
17	4-6, 14-16		
18	6-8, 12-14		
19	8-10, 10-12		

Tab. 1 Variable linking of truss bridge

Design Variable	Literature [6]	GA	CGA
1	2.128	2.545	2.27
2	0.5	0.503	0.503
3	0.5	0.503	0.503
4	1.7	1.767	1.767
5	0.5	0.503	0.503
6	0.5	0.503	0.503
7	1.515	1.767	1.767
8	0.5	0.636	0.503
9	0.5	0.503	0.503
10	1.286	1.327	1.327
11	0.523	0.636	0.636
12	0.5	0.503	0.503
13	1.078	1.327	1.131
14	0.5	0.503	0.503
15	1.007	0.503	0.503
16	1.007	0.503	0.503
17	1.090	0.636	0.503
18	1.084	0.503	0.503
19	1.058	0.503	0.503
20	1.862	1.80	1.90
21	3.059	2.90	3.00
22	4.036	4.00	4.00
23	4.727	4.70	4.70
24	4.937	4.80	4.80
$W(N)$	497.25	495.59	475.50

Acknowledgements

This paper is funded by the program of Natural Science Foundation of China (50709013).

References

[1] Huanchun Sun, Shan Chai and Yuefeng Wang: *Discrete Optimum Design of Structures* (Dalian University of Technology Publications, Dalian 1995). (In Chinese)

[2] Yunkang Sui, Zhong You: computational structural mechanics and applications, Vol. 7-4 (1990), p. 82 (In Chinese)

[3] Salajegheh E and Vanderplaats G N: *Struct. Opt.*, 6 (1993), p. 79

[4] Lianshuan Shi and Huanchun Sun: *Acta Mechanica Sinica*, Vol. 31-6 (1999), p.731 (In Chinese)

[5] Hesheng Tang, Feng Li, Yong Wang, Songtao Xue and Rong Chen: *Journal of harbin institute of technology*, Vol. 41-12 (2009), p.94 (In Chinese)

[6] Dong Wang, Weihong Zhang and Jiesheng Jiang: *Chinese Journal of Applied Mechanics*, Vol. 19-3(2002), p.72 (In Chinese)

Test Study on Anti-sliding Coefficient of Friction-type High-strength Bolt Connectors

Huainian XING^{1, a}, Xiaopeng ZHANG^{1, b}, Zengli LIU^{1, c}, Liqiang JIN^{1, d}

¹Department of Engineering Mechanics, Dalian University of Technology, China

^axinghuainian@sina.com.cn, ^bzxp@dlut.edu.cn, ^czengli@dlut.edu.cn, ^dwaitking@163.com.cn

Keywords: Friction-type high-strength bolt connection, Anti-sliding coefficient, Sand blasting, Steel structure

Abstract. Friction-type high-strength bolt connectors are widely used in steel structure. However there has only general description for connection plate surface treatment method in the current Chinese design standards. Some research tests have been designed for different connection plate surface treatment method, which include different painting thickness and different blasting method. The results show that different treatment method has different anti-sliding coefficient. The anti-sliding coefficient would decrease with the surface coating thickness increase. The anti-sliding coefficient would less than 0.50 which the Chinese design standard required when some surface treatment methods are used, such as using steel wire section or using mixture of steel wire section and steel shot to sand blasting. So procedure qualification test is necessary to guide processing in order to ensure the quality of the products. It has certain conference value for practical engineering.

Introduction

The connections of the steel structure must comply with some principles, such as safety and reliability, clear force transmission, simple construction, convenient manufacturing, steel saving and so on.

Bolt connections are one of the most commonly steel structure connections, which include ordinary bolt connection and high-strength bolt connection. The high-strength bolt connections include pressure-type bolt connections and friction-type bolt connections. Pressure-type bolt connections allow sliding of contact surface and take the ultimate bearing capacity as the design criteria. Pressure-type bolt connections have high bearing capacity but have large shear deformation. So pressure-type bolt connections are unsuitable for dynamic loading structures. Friction-type bolt connections transfer force relying on frictional resistance and take shears not more than frictions as the design criteria. Friction-type bolt connections have some advantages such as small shear deformation, good flexible performance, simple construction procedure, removable, fatigue resistance. So friction-type bolt connections are suitable for dynamic loading structures. Therefore, friction-type bolt connections are widely used in steel structures.

Normal pressures of connecting plates contact surfaces of friction-type high-strength bolt connections are provided by the tightening bolts. Prestress of bolts, anti-sliding coefficients and steel type are major factors which influence the bearing capacity.

Anti-sliding coefficients of high-strength bolt connections are relative to steel type and connecting plate surface treatment methods. Test results show that anti-sliding coefficients would decrease with prestress reducing which are different from physics friction coefficients [1,2,3].

The commonly surface treating methods include sand blasting, painting inorganic zinc after sand blasting, rusting after sand blasting, removing rust by wire brush, no treatment and so on. Anti-sliding coefficient μ design values are shown in table 1 in different processing methods according to Chinese design standard [4]. There has no more description about sand size, painting thickness and so on in Chinese design standard. Some tests have been done in order to study the influences of different sand blasting method and different painting thickness on anti-sliding coefficients.

Table 1 Anti-sliding coefficient μ values of friction-type in Chinese design standard

Processing method	Q235 steel	Q345 steel	Q390 steel	Q420 steel
Sand blasting	0.45	0.50	0.50	0.50
Painting inorganic zinc after sand blasting	0.35	0.40	0.40	0.40
Rusting after sand blasting	0.45	0.50	0.50	0.50
Removing rust by wire brush	0.30	0.35	0.35	0.40
No treatment	0.30	0.35	0.35	0.40

Test samples

Double bolts joining tension samples have been used in anti-sliding coefficient test. Sample shape is shown in figure 1. The material of the sample is Q345 steel. The sizes and quantity of samples are shown in table 2.

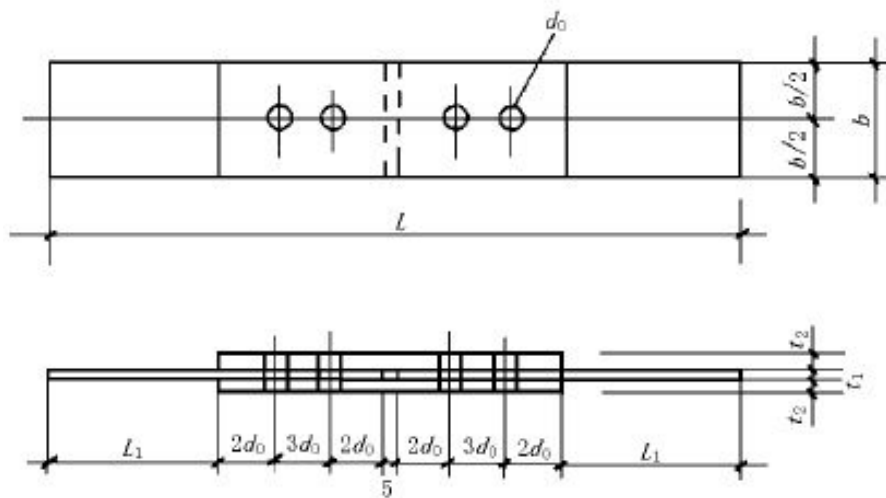


Fig.1 Test samples

Table 2 Test samples sizes and quantity

Plate thickness(mm)	$b \times L$ (mm)	Quantity	Bolts (mm)	d_0 (mm)
$t_1=16$ (core plate)	110×389	54	M24×90 10.9S	Φ26
$t_2=16$ (cover plate)	110×369	54	M24×90 10.9S	Φ26

Three treating methods S, H and D have been used to the samples.

Method S is copper ore sand blasting treating. The grain size of copper ore is less than 2.5mm and without impurities. The water ratio of copper ore is not more than 2 percent. The pressure air which is used to sand blasting is dry and non-oily by cooling devices and oil-water separator processing. The working air pressure is from 5.5 standard atmosphere pressures to 7.0 standard atmosphere pressures. The distance between nozzle and steel plate surface is from 100mm to 300mm. The included angle between spray direction and plate surface normal direction is from 15 degree to 30 degree. The coverage ratio of sand blasting is more than 200 percent.

Method D is steel wire section shot blasting treating. The grain size of steel wire sections is from 0.8mm to 1.2mm. The hardness of steel wire section with 1.0mm grain size is from 41HRC to 45HRC. The rest requirements are the same as method S.

Method H is mixture sands of steel wire sections and steel shot blasting treating. The mixing ratio of steel shot and steel wire section is one to four. The grain size of steel shots is from 0.6mm to 0.8mm. The hardness of steel shots is less than 50HRC. The grain size of steel wire sections is from 0.8mm to 1.2mm. The hardness of the steel wire sections with 1.0mm grain size is from 41HRC to 45HRC. The coverage ratio of shot blasting is more than 200 percent.

The surface dust of samples should be cleaned by vacuum cleaner or clean pressure air after sand blasting or shot blasting finished. The surface derusting grade of sample should be Sa2.5 and the surface roughness of sample should not less than Ra 50 μ m.

Inorganic zinc silicate paints (Interzinc 22 silicate QHA028/QHA027) should be painted in 2 hours after the steel surface roughness qualified.

There are three kinds of coating thickness 0 μ m, 30 μ m and 60 μ m in the test. The allow deviation of the coating thickness is plus or minus 5 μ m. Test would be done seven days later after painting finished.

Test method

Test temperature is (23 \pm 2) °C in air and the environment humidity is (60 \pm 2) percent. Strain gauges have been pasted on the high-strength bolts as force sensor which is shown in figure 2. The bolt force sensor should be calibrated by test machine before use. The bolt force can be obtained by resistance strain gauge.

The samples are assembled through drill nails first. Then those drill nails are replaced with bolt force sensors, as shown in figure 3.

There are two steps to make the bolt force sensors tightened by ND-1000 torsion testing machine. The first step should reach about half of the bolt standard tensile value P . The second step begins after all bolts finish the first step. Each bolt tensile force P_i should be equals to the bolt standard tensile value P and the allow deviation is plus or minus 5 percent. The standard tensile value P of M24 high-strength bolt is 225kN.

A line has been drawn on the sample side in order to observe the relative sliding, as shown in figure 3. UHP-1000 test machine has been used to test these samples. The loading speed is from 3kN/s to 5kN/s. The test would stop and record the sliding load value N_V when some phenomena happens such as suddenly bang noises, tensile curves mutations or the mark line distortion.



Fig.2 Bolt force sensor



Fig.3 Mark line distortion on sample side

Anti-sliding coefficient can be obtained according to formula (1).

$$\mu = N_V / (2P_1 + 2P_2) \quad (1)$$

P_1 and P_2 are bolts tensile forces on the sliding side of sample.

Conclusions

Anti-sliding coefficient test results are shown in figure 4 and table 3.

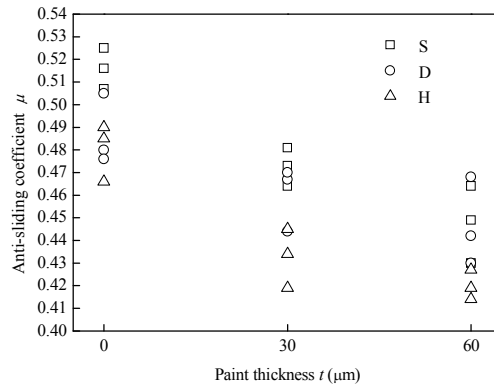


Fig.4 Anti-sliding coefficient test results

Table 3 Anti-sliding coefficient average

Plate treating method	Plate thickness(mm)	Coating thickness t (μm)	Anti-sliding coefficient average
S	16	0	0.516
		30	0.472
		60	0.448
D	16	0	0.487
		30	0.461
		60	0.446
H	16	0	0.480
		30	0.433
		60	0.420

Anti-sliding coefficient decreases with coating thickness increasing in the same surface treatment method according to table 3. And anti-sliding coefficient under method S is greater than under method D. Anti-sliding coefficient under method D is greater than under method H.

All the anti-sliding coefficient test results are greater than 0.40, and the anti-sliding coefficient test results under method S without painting are greater than 0.50, which is Chinese standard design value as shown in table 1. But the anti-sliding coefficient test results under method D without painting and method F are less than 0.50. Therefore, procedure qualification test is necessary before designing and manufacture. It has certain reference value for engineering application.

Acknowledgements

This work was financially supported by the China National Science and Technology Major Projects (2009ZX04008-011-004).

References

- [1] Wei XIE: Journal of North China Institute of Water Conservancy and Hydroelectric Power. Vol. 25(2004), p. 23.
- [2] Qicai LI: Journal of Xi'an University of Science and Technology. Vol. 27 (2007), p. 43.
- [3] Jie KANG: Journal of Kunming University of Science and Technology. Vol.33 (2008), p. 69.
- [4] China ministry of construction: *Code for Design of Steel Structures*. (Standards Press of China press, China 2003).

Projective geometry on the structure of geometric composition analysis application

Xiaozhuang Song^{1, a}, Mingliang Lu^{2, b} and Tao Qin^{3, c}

^{1,2,3} Nanjing Technical Vocational College, Nanjing, Jiangsu, 210019, China

^asonxz@163.com, ^blm15127@126.com, ^chibluetea@gmail.com

Keywords: Geometric composition analysis, Projective geometry, Infinity point, Infinity straight line.

Abstract. The analysis rule of geometry composition analysis in building structure must rely on geometry theory, while the traditional Euclidean geometry theory can not solve some building structures problems of the geometry components. This problem can be solved in the use of projective geometry theory. In this paper we introduce the proof of projective geometry in the geometry composition analysis and we discuss the application of this theory.

Introduction

When we study the geometric composition analysis of structure and if we ignore the deformation of the studied object which can be considered as a rigid body or rigid piece in the plane. Through the studying the geometric structure of the composition form, we can determine the geometry nature of stable or unstable under the action of any loads. When we study the rigid body motion, must follow the geometry principles. For example, as of a three edge of triangle length of a side once identified then the triangle is unique. That is to say, as long as the setting of a triangle of the three side of the triangle, the geometry is determined only, In turn, such as the lack of any of these conditions, the triangle cannot be uniquely determined. In the geometry structure of the composition analysis, if the three connection links which are connection each other with hinges are not on a straight line, we think it as **hinge triangle**. As the length of connection link is immutable. And therefore determine the length of triangle's three sides, then the hinged triangle is uniquely determined, so the hinged triangle is the simplest geometrically stable system with no superfluous constraint, it is known as the hinged triangle principle. This principle can be extended out several major rules of geometry composition analysis and constitute the basis for structure geometric composition analysis.

The defects of Euclidean geometry theory

Traditional Euclidean geometry can not explain several special issue of the geometry composition analysis. In the analysis of geometry composition, if we connect the two rigid pieces using two connection link and the two rigid pieces can rotate each other on the point of two extend connection link line's intersection and we can think this point as a virtual hinge. If the two parallel chains rods connecting two rigid pieces can also motion, do you think where is the virtual hinge?

In accordance with the Euclidean geometry principle, two beelines only a point of intersection, If two parallel beelines have a point of intersection, there are two opposite directions, so no point of intersection of parallel beelines. So the two parallel chains have no virtual hinge. As the two parallel connection links rods can not restrict the movement in the vertical direction, so the two rigid bodies also can do the planar motion. At this point the traditional Euclidean geometry theory shows its theoretical defect, however projective geometry makes up for the lack of Euclidean geometry.

The intersection of parallel to the line in projective geometry

Now there is a straight line named " a " and point named " O " outside the line a and if we draw a line named " p " pass through the point O , the line p and the line a intersect at the point " P " and let the line p rotate around the point O then the point P only move on the line a , so we can determine the position of the point P by the azimuth of straight line p , such as the Fig. 1. Draw a straight line named " a " pass through the point O and parallel the straight line a , when the included angle of the straight line p

with the straight line a is more and more small, the point P on the straight line a is more and more far. When the straight line p rotate to the straight line a' , the point P is at infinity; If the straight line p continues to rotate, the straight line p left the line a' , the point P is appeared in the distance at another port of the straight line a . So all the straight line pass through the point O composed of a straight line group, all the P of points of intersection of the straight line group with the line a form a set. The set and the straight line group has one by one corresponding relationship, the point corresponding the straight line which included angle with the straight line a' is zero, is named "infinity point" on the straight line a , using P_∞ express. In this way, infinite point P_∞ has a corresponding direction, thus all the infinite point P_∞ of the straight line p with all other lines of parallel the straight line a are the same point. This point is same other points to be determined by two geometry parameters, also has two degrees of freedom.

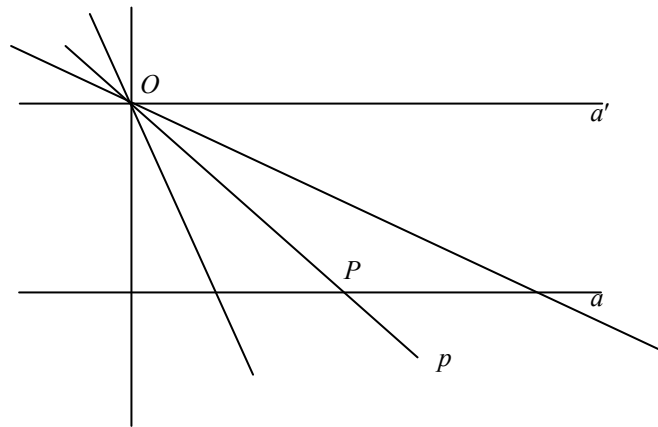


Fig. 1 Intersection point of parallel straight lines

In the same plane, each straight line on the different direction corresponds to a different infinity points and this special points have only one different parameter. The group of all the infinity points P_∞ can form the axis which is named as **infinity line- ∞ line**. It can be said that all the infinity points P_∞ of the plane are on the line - ∞ line, while all the other points with limited length are not on this line.

Summarized as follows:

- Each direction has a P_∞ point which is the intersection of all the Parallel straight lines on this direction.
- Different directions have different P_∞ points.
- All the infinity points P_∞ of the plane are on the ∞ line
- All the limited distance points are not on the ∞ line.

The application of projective geometry in the geometry composition analysis

There are two parallel connection links connecting two rigid pieces can be thought as a virtual hinge. This virtual hinge is at infinity and its azimuth has the same direction as the connection c links. Meanwhile all the infinity points of the plane are in a general straight line.

For example, Fig. 2 shows that rigid pieces II and III are connected by two parallel connection links. Four connection links forming virtual hinges A and B are parallel. Hinges A and B with the same azimuth intersect at an infinity point. This point and hinge C which connects rigid pieces II and III is in the same line meanwhile if the four connection links with different length motion a little then they will become unparallel so we think this system as an instantaneous unstable system.

Another example is shown in Fig. 3. From this Fig. we can see that rigid pieces I (1,2)II(3,5) and pieces III(4, 6) connected by two parallel and unequal length Connection links constitute three virtual hinges A , B and C at infinity of three azimuths. As we all know that all the infinity points are in the infinity straight line so point A point B and point C are in the same line. As the length of connection

links forming the virtual hinges is different if a little motion happens then the three virtual hinges will be not in the same line in the limited distance so this system is also thought as an instantaneous unstable system.

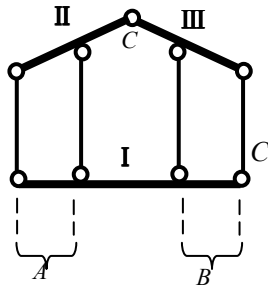


Fig. 2

Instantaneous unstable system

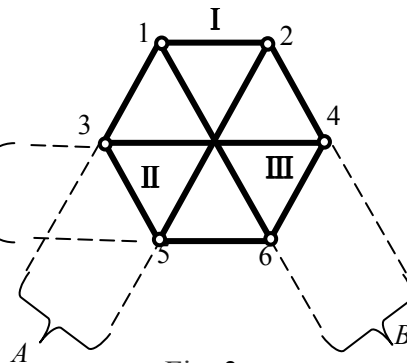


Fig. 3

Instantaneous unstable system

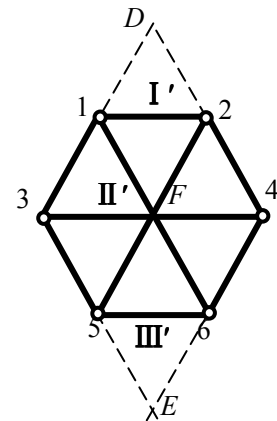


Fig. 4

Instantaneous unstable system

The same problem, if we select rigid pieces I'(1,2)II'(3,4) and piecesIII'(5,6)in Fig. 3 connecting by several connection links to constitute three virtual hinges which are in the same line in the limited distance then this system can be regard as an instantaneous unstable system. From this example we get the same conclusion as the previous example and they verify the correctness of projective geometry and the defects of Euclidean geometry theory.

There is a class of special problems in geometric composition analysis. Now two (or more) parallel connection links with the equal length connect two rigid pieces and if we connect the four hinges with straight line one by one, then we can get a parallelogram. If the length of the parallelogram is unchanged, the parallelogram always is a parallelogram in the motion process, so the virtual hinges formed by two (or more) connection links always intersect at same infinity point(same direction P_∞) .So this system can be thought as a geometric unstable system.

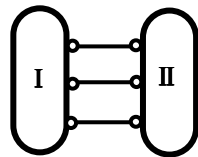


Fig. 5

Unstable system

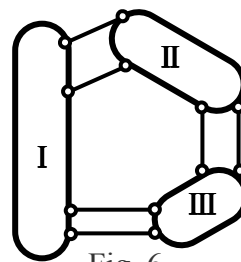


Fig. 6

Unstable system

Fig. 5 shows that tow rigid pieces connected by three parallel and equal length connection links constitute, after the tow rigid pieces is the relative moving, the three connection links is still parallel, and Intersect at the point at infinity, the motion may continue to occur. This system is a geometric unstable system.

Fig. 6 shows that rigid pieces I , II and piecesIIIconnected by two parallel and equal length connection links constitute three virtual hinges at the infinity of three different directions. Because all the infinity points are on the same infinity line so the three virtual hinges are on the same straight line. As the virtual hinge's connection links has the same length if the displacement occurs so the three virtual hinges are still at infinity and the motion can always continue. This system is also a geometric unstable system.

Conclusions

As the two parallel lines intersect at infinity and all points at infinity are on the same straight line which is a general line, however all the finite distance points are not on the line. This view is not easy to express intuitively but we can use some evidence to the contrary to prove this conclusion. Fig. 3 shows that if we use another three Connection links meanwhile (1,2),(3,4)and(5,6)are three rigid piece. We can easily determine that this three virtual hinges which connect the three rigid pieces are on the same line. If this system has a little shape change they will be not on the same line so the system is also a transient system. This conclusion is the same as the previous conclusion which is got from three virtual hinges in the infinite line. We can also use the flexibility of the system showed by Fig. 5 to prove this conclusion by contradiction.

Due to the two parallel lines intersect at P_∞ point and all P_∞ point for all in ∞ line, all limited far points are not in this ∞ line. That is not easy to intuitive expression, more abstract, and is important difference of projective geometry and the traditional Euclidean geometry. The above is to some special problems for judgment, such as not involving these particularities, the tradition Euclidean geometry analysis of the geometric composition is still correct.

References:

- [1] Department of Mathematics, Nankai University, "Introduction analytic geometry of space." 1st edition. Beijing. Higher Education Press. May 1978 In Chinese
- [2] Zhonghe Lei and Jiangai Chuan Hao Jingming. "Structural Mechanics eliminating." Beijing. Tsinghua University Press. 1995.12 In Chinese
- [3] Yuqiu Long. Shihua Bao. "Structural Mechanics tutorial" (I). Beijing. Higher Education Press. 2000 In Chinese

Research and Application of Pre-stressed Concrete Composite Slabs

Jingshu Zhang^{1, 2}, Huanhuan Nie^{1, 2}, Yuanlong Yang^{1, 2} and Yuan Yao^{1, 2}

¹Key Laboratory of Mechanics on Disaster and Environment in Western China Attached to the Ministry of Education of China, Lanzhou, Gansu, 730000, China

²School of Civil Engineering and Mechanics, Lanzhou University, Lanzhou, Gansu, 730000, China
^azjs66cn@yahoo.com.cn, ^blovelynie@sina.com, ^cyangyuanlong@lzu.edu.cn,
^dyaoyuan0106401@126.com

Keywords: the composite slab with flat bottom panel; the composite slab with bar truss reinforced precast concrete bottom panel; the concrete composite slab with precast ribbed bottom panel; the composite slab with hollow bottom panel; the composite slab with sandwich bottom panel.

Abstract. The pre-stressed concrete composite slab, which combines the advantages of cast-in-place slabs and precast slabs, has promising development prospects. In the paper, according to structural integrity, bond performance, sound insulation, thermal preservation and construction techniques, four categories composite slab, such as the composite slab with flat bottom panel (including the composite slab with bar truss reinforced precast concrete bottom panel), the concrete composite slab with precast ribbed panel, the composite slab with hollow bottom panel and the composite slab with sandwich bottom panel are studied. The composite slab with flat bottom panel has poor structural integrity, and its bond performance and crack resistance of edge joint details need to be improved; the composite slab with bar truss reinforced precast concrete bottom panel has enough bond force, but its storage and transportation are inconvenient; the concrete composite slab with precast ribbed panel has good structural integrity and convenient construction procedure; the composite slab with hollow bottom panel and the composite slab with sandwich bottom panel have functions of sound insulation and thermal preservation, however they are inadequacy to resist bending moment and have complex construction procedure. The concrete composite slab with precast ribbed panel is provided with good mechanical behavior, economy and practicability, and is worth further researching and promoting.

Introduction

In all kinds of floors, concrete slabs occupy the dominant position. Concrete slabs can be divided into two major categories, the cast-in-place slab and the precast slab. The cast-in-place slab has good structural integrity, however it needs on-site concrete pouring procedure, large concrete wet construction, instable construction quality, more scaffolding and templates, high costs and long construction period. The precast slab is produced in the factory and has advantages of less concrete wet construction, stable construction quality, less scaffolding and templates, low construction noise, reducible engineering cost and short construction period. But its structural integrity needs to be improved.

Therefore, composite slabs which combine the advantages of cast-in-place slabs and precast slabs become popular. Its bottom panel is manufactured in factory and assembled on the spot. Then the concrete is poured in place to form the composite slab. This slab is provided with advantages of good structural integrity, less scaffolding and templates, short construction period, good economical efficiency, so it has promising development prospects.

Overview of pre-stressed concrete composite plate

The composite slab with pre-stressed bottom panel is the most widely used composite slab. In China, the pre-stressed thin slab was produced up to 1957. In 1970s, the pre-stressed composite beam and slab was produced with cold-drawn low-carbon steel wires. In 1980s, the standard drawing of

pre-stressed composite slabs was compiled [1]. Nowadays, the composite slab has been widely used in the housing construction [2]. Integrated prefabricated hyperstatic structures with composite components, formed by pre-stressed composite slabs and pre-stressed hollow composite beams, have been applied in tall buildings [3].

The bottom panel of composite slabs mostly employs the first-tensioned pre-stressed panel. The bottom panel can also be used as permanent formworks. According to whether or not the braces are set under bottom panels, the composite slab can be sorted into one-stage loading composite slab and two-stage loading composite slab.

The one-stage loading composite slab has slender bottom panel, so it should be supported by temporary braces before the bottom panels are assembled. The post-poured concrete layer and bottom panel begin to work together after post-poured concrete is hardened. The one-stage loading composite slab is similar with the cast-in-place slab in mechanical behavior.

The bottom panel of two-stage composite slab has enough bending stiffness and needs no temporary braces during construction. So construction duration can be shortened and the project cost can be reduced. Different from the cast-in-place slab, the cross section dimensions and reinforcements of the composite slab is decided by construction stage, not by service stage. Before the post-poured concrete layer is hardened, it bears no loads. In the meanwhile, the bottom panel itself bears its dead weight, post-poured concrete's dead weight and construction loads. After the post-poured concrete layer is hardened, it begins to work together with bottom panel to form composite slab, which bears the dead weight of post-poured concrete layer, floor surface and ceiling and live load during service stage.

The combined interface is the interface between old and new concrete, which determines whether two concrete layers can work together. It has been specially focused on in the research and engineering application. Swallowtail grooves were used to increase bond strength between old and new concrete in England. In 1960s, artificial rough surfaces were adopted in the top surface of the bottom panel in the former Soviet Union. In 1970s, shear reinforcements were embedded in the interfaces in the France and West Germany. In 1990s, grooves were set in the top surface of hollow panel to enhance the bond strength by Wang Xizhe [4]. Mechanical behavior of smooth surfaces, indentation surfaces and binding reinforcements were researched by Hou Jianguo [5].

In addition, edge joints between the precast bottom panels may affect the integrity of composite slabs. Edge joints disposal has always been focus in the research and engineering application.

The Research and application of pre-stressed composite slabs

To take full advantage of the pre-stressed composite slab and to make up for its shortages, scholars have improved traditional composite slabs in material, bottom panel pattern and edge joint details.

To reduce slab weight, Wu Jin et al. studied the lightweight ceramic reinforced concrete composite slab and find out its shear performance [6]. Xu jien researched bearing capacity and crack resistance of pre-stressed composite slab by introducing steel fibers [7~9].

The bottom panel pattern determines the bonding behavior of the composite slab and the edge joint details influences its crack resistance.

The roughness of bottom panel surface can affect the bond force of composite slabs. According to roughness, the bottom panel can be divided into natural rough bottom panel, artificial rough bottom panel [10] and shear-resistant reinforced bottom panel [11,12].

According to cross section, the bottom panel can be classified into flat bottom panel, precast ribbed bottom panel, hollow bottom panel and sandwich bottom panel.

Concrete composite slab with flat bottom panel. The bottom panel of the composite slab with flat bottom panel is pretensioned prestressed solid slab [13], which is the earliest type of composite slab.

Its bending stiffness is inadequacy and needs temporary braces to support during construction. Additionally, the edge joint detail is main factor in crack resistance and integrity for composite slabs.

Vanke Company places steel wire gauze on the edge joint to increase the crack resistance of the composite slab [14].

Ding Yongjun [15], Xu TianShuang [16] and Shen ChunXiang [17] respectively carried out experimentally study of integral panel joint pattern (shown in figure 1). This kind of panel joint widens panel gaps and allows panel reinforcements bent and embedded into the upper post-poured concrete, in order to improve crack resistance of composite slabs.

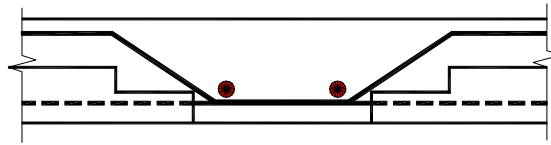
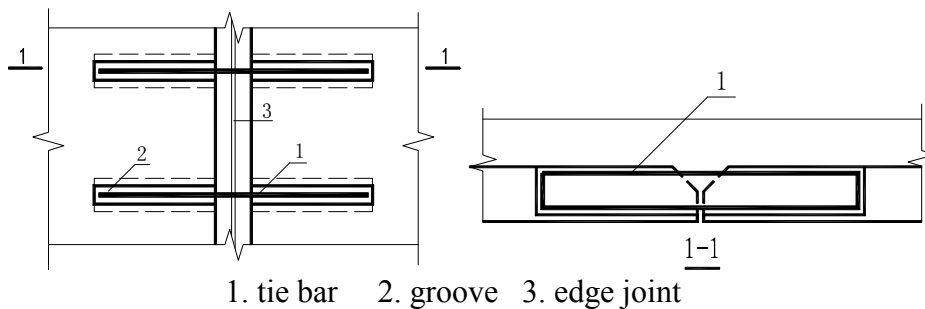


Fig. 1 The integral panel joint pattern

Xue Weichen proposed tie bars in the panel joints to increase integral mechanical behavior of the composite slab [18] (shown in Figure 2). Trapezoid grooves were designed in the bottom panel, perpendicular to panel joint direction. Closed rectangular tie bars were placed in the trapezoid grooves to connect two adjacent panels. This technical treatment enhances integrity and crack resistance of the composite slab and increases its sectional effective height where positive moment acts on.

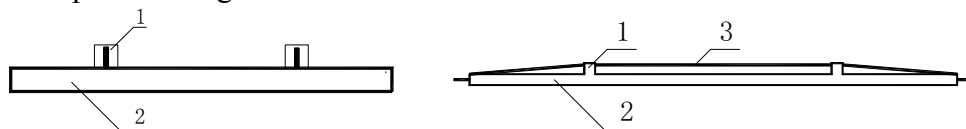


1. tie bar 2. groove 3. edge joint

Fig. 2 Arrangement of tie bars

Generally speaking, this composite slab has slender bottom panels and cracks tend to form in the panel joints. Furthermore, the bond force in concrete is small. Two concrete layers are easily uncoupled under improper construction. So application of composite slabs with flat bottom panels is seldom nowadays.

In order to increase bending stiffness of bottom panels, Liu Bin put forward fish-belly pre-stressed two-way composite slab [19], combined with the concept of beam string structure, shown in figure 3. This type of composite slab adopts pre-stressed concrete slab as bottom panel. Fish-belly bar skeletons are installed on the concrete supports which erect on the bottom panel. Pipelines can be free laid on the bottom panel during construction.



(a) along the bottom panel's short edge (b) along the bottom panel's long edge
1. concrete support 2. fish-belly pre-stressed bottom panel 3. fish-belly bar skeletons

Fig. 3 Fish-belly pre-stressed two-way composite slab

In order to enhance bond force of the composite slab and increase its bending bearing capacity, shear connector and bar truss are adopted in the bottom panels.

Wu Xiangguo employed shear connectors on the bottom panel to propose a composite slab with ultrahigh-strength ultra-thin bottom panels [20]. The bottom panel is made of fibre reinforced cement composite material and bar meshes are embedded in it.

In order to enhance bond force of composite slabs and increase bending stiffness of bottom panels, bar trusses are placed in the bottom panels to form bar truss reinforced precast concrete bottom panels. This kind of composite slab includes German composite slab [21], truss sandwich composite slab proposed by Salmon [22] and composite slab with a special bottom panel proposed by Qiu Zeyou [23].

The bar truss reinforced precast concrete bottom panels of the German composite slab is fabricated by welding elevated tie bars fixed in the bottom panel and longitudinal bars in the post-poured concrete layer (shown in figure 4). The bars form integral bearing truss and provide high bearing capacity for composite slabs.

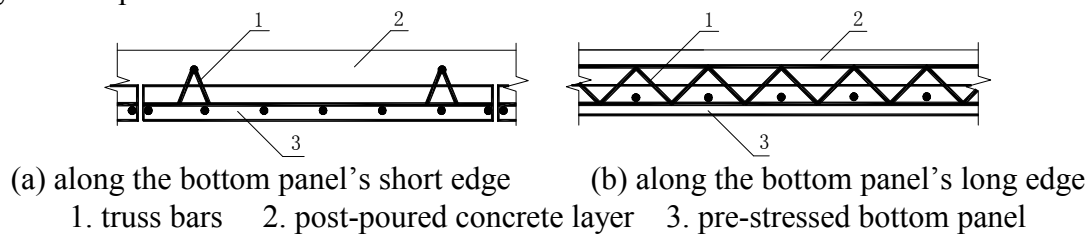


Fig. 4 Concrete composite slab with bar truss reinforced precast concrete bottom panel

Based on the German composite slab, Tong Genshu [24] and Ye Xiangguo [25] carried out experimentally research. Li Wenbin, Yang Qiangyue [26,27] and Dou Lijun [28] proposed optimal improvements. This type of composite slab has large bending stiffness and therefore can be used as long-span slab. Enough shear resistance performance in the combined interface allows the slab support vibrated loads. However, its storage and transportation are inconvenient.

The bar-truss sandwich composite slab adopts lightweight laminboard layer between pre-cast panel and post-poured concrete. The two concrete layers are connected by bar truss. Lu Fengxu conducted theoretical analysis on the bar-truss sandwich composite slab to indicate that bar truss is bearing skeleton of the composite slab and proper bar truss pattern can guarantee slab stability and force transferring uniformity [29]. Qiu Zeyou proposed a composite slab with two series of bar trusses at longitudinal edges of bottom panel, which can be applied as hollow girderless floor.

The above-mentioned fish-belly pre-stressed two-way composite slabs, composite slabs with ultrahigh-strength ultra-thin bottom panel and bar-truss sandwich composite slabs are inconvenient for storage and transportation. Therefore, the concrete composite slab with precast ribbed panel has such advantage.

Concrete composite slab with precast ribbed panel. The concrete composite slab with precast ribbed panel enhances bending stiffness by introducing ribs on the flat bottom panel. Fewer temporary braces or even no temporary braces are necessary. Therefore, it can facilitate the construction and can reduce construction period and costs.

According to the rib pattern, bottom panels can be divided into one-way rib bottom panels and two-way ribs bottom panels.

Jiang Qingqing carried out research on the inverted T-type composite plate, shown in figure 5. Ribs are installed longitudinally and have the same height with the composite slab [30~32].

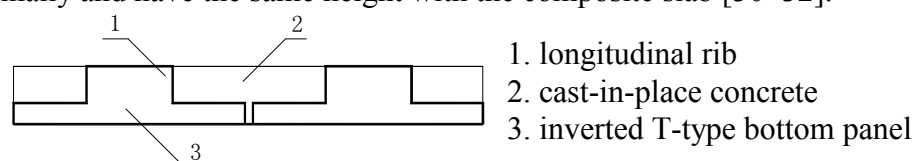


Fig. 5 Inverted T-type composite slab

The inverted T-type composite slab has enough bending stiffness in bottom panel. However, cracks tend to form in the interface of old and new concrete. In addition, the top distributing bars and fulcrum negative bars in the composite slab are inconvenient to arrange.

Zhou Xuhong, Wu Fangbo, et al. put forward one concrete composite slab with precast ribbed panel [33~38], shown in Figure 6.

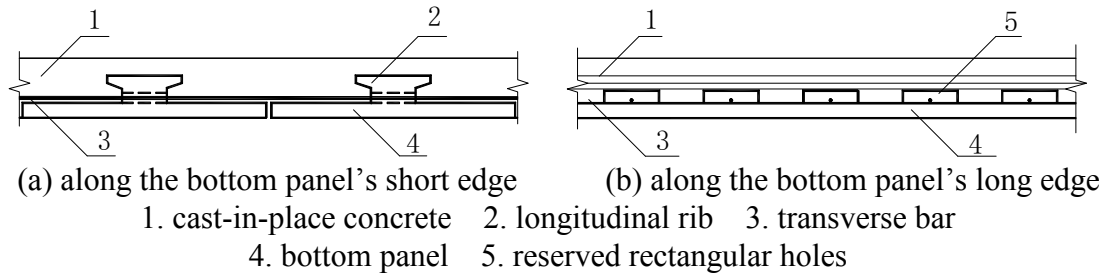


Fig. 6 Concrete composite slab with precast ribbed panel

The bottom panel of this composite slab is inverted T-type or I-type pre-stressed panel. Rectangular holes were reserved at certain intervals for transverse bars and pre-buried pipelines to pass through. Negative bars were allowed to place in the post-poured concrete layer. Two-way reinforcement arrangement and pin key function (the post-poured concrete was located and fixed in the rib holes) guarantee teamwork of old and new concrete. This concrete composite slab is provided with convenient construction method, short construction period and low engineering costs. In order to promote and popularize the concrete composite slab with precast ribbed panel, Zhou Xuhong, Wu Fangbo, Zhang Jingshu, et al. have drafted Technical Specifications for Concrete Composite Floor with Precast Ribbed Panel [39].

Qiu Zeyou proposed a composite slab with longitudinally and transversely ribbed bottom panel[40], shown in figure 7. Longitudinal ribs and transverse ribs are installed on the bottom panel. Convex panel area and concave panel area are enclosed by longitudinal ribs and transverse ribs to increase bond strength. Transverse ribs have cross sections of rectangle, taper, T type and dovetail type. Rectangular transverse ribs are showed in Figure 7. Reinforcements or steel wire mesh are placed in the concave panel area and pass through the holes in the longitudinal ribs. The composite slab has large interface area and high bond strength. However no engineering application has been promoted.

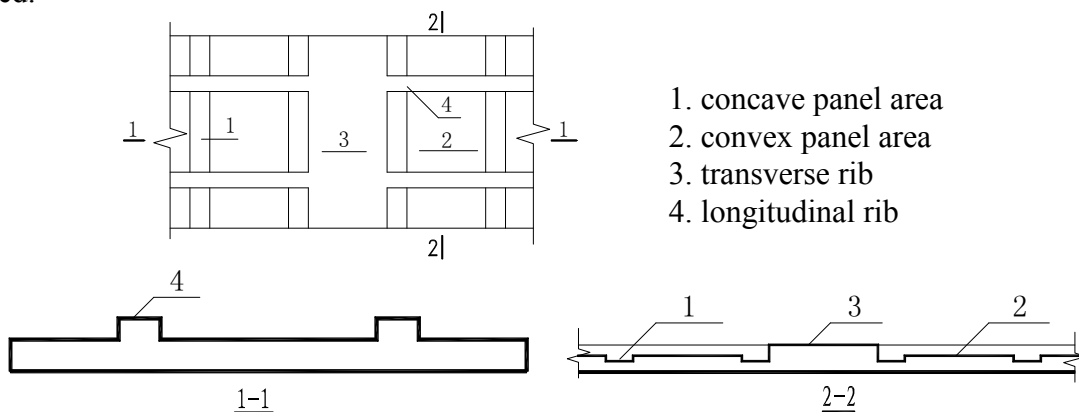


Fig. 7 Composite slab with longitudinally and transversely ribbed bottom panel

Wu Junxi proposed composite slab with dovetail-type ribs on the bottom panel [41] (shown in figure 8). The dovetail-type ribs help two concrete layers work together better. However, the bending stiffness of bottom panel is inadequacy and needs temporary braces during construction.

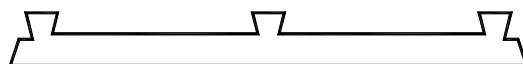


Fig. 8 Dovetail-type ribbed bottom panel

The concrete composite slab with precast ribbed panel mentioned above has solid bottom panels. It is limited within small and medium span slabs due to its large weight.

Composite slab with hollow bottom panel. The composite slab with hollow bottom panel is light enough for large span slabs. Prestressed hollow panel is usually used as bottom panel.

Wang Jun et al. carried out experimental research on the composite slab with prestressed circular-hole bottom slab [42]. The bottom panel has large bending stiffness, but increases the thickness and weight of the composite slab. Moreover, edge joint problem and bonding problem of concrete are worthy of consideration.

Wu Fangbo et al. proposed WFB integrated precast composite slab with prestressed hollow bottom panel [43~45] (shown in figure 9). The thickness of bottom panel is the final thickness of composite slab. Concrete is poured in the grooves between two adjacent bottom panels. This composite slab needs no temporary braces to support and has sound insulation function.

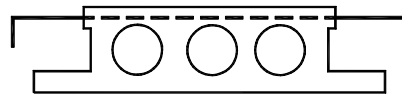
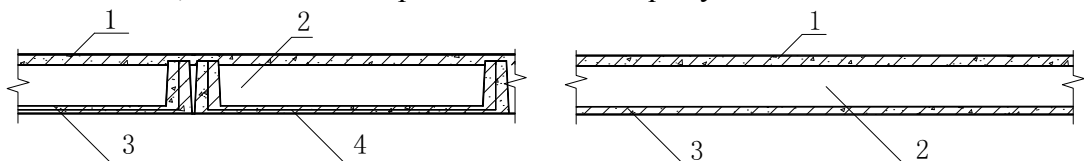


Fig. 9 WFB assembled monolithic pre-stressed hollow slab

Chen Hongliang, Zhao Chengwen et al. studied hollow composite slab with prestressed U-shaped bottom panel [46,47] (shown in figure 10). The U-shaped bottom panel facilitates pipeline installation. However, this hollow composite slab is inadequacy to resist shear load and seismic load.



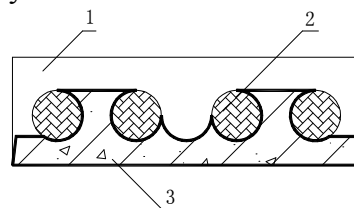
(a) along the bottom panel's short edge (b) along the bottom panel's long edge

1. cast-in-place concrete 2. hollow core
3. prestressed U-shaped bottom panel 4. pre-stressed reinforcement

Fig. 10 Hollow composite slab with prestressed U-shaped bottom panel

Composite slab with sandwich bottom panel. The composite slab with sandwich bottom panel is fabricated by filling with lightweight materials into the composite slab with hollow bottom panel. This lightweight composite slab has functions of sound insulation and thermal preservation.

Zhu Maocun, Chen Zhonghan et al. carried out study on the construction techniques and mechanical behavior of the composite slab with sandwich bottom panel [48,49] (shown in figure 11). Cylinder lightweight mandrels are buried in the bottom panel, which improved sound insulation and thermal insulation property.



1. cast-in-place concrete
2. cylinder lightweight mandrels
3. sandwich bottom panel

Fig. 11 Composite slab with sandwich bottom panel

Zhou YouXiang et al. studied RC hollow laminated slabs with two-way dense ribs [50] (in Figure 12). The bottom panel is fabricated by filling with lightweight infilled blocks into the concrete slab box. Reinforcements are installed in the grooves between two adjacent slab boxes and afterwards concrete is poured to form composite slab. The hollow laminated slab facilitates pipeline installation and has functions of sound insulation and thermal preservation. However, its bending stiffness is inadequacy and cracks are prone to emerge. Besides, its construction procedure is complex.

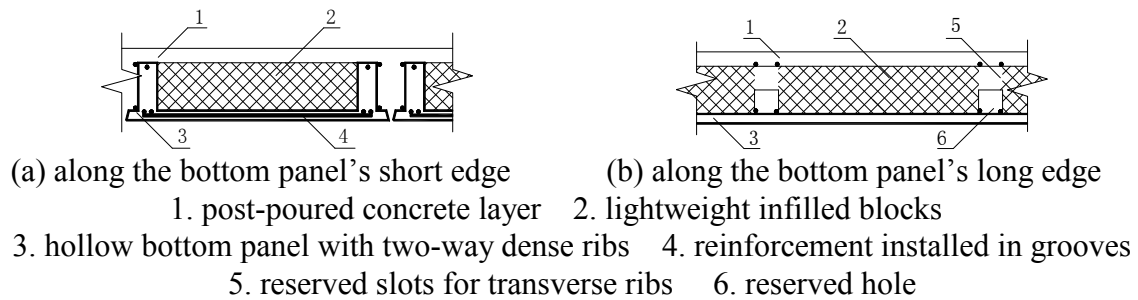


Fig. 12 RC hollow laminated slabs with two-way dense ribs

In summary, pre-stressed composite slabs have many patterns and a large number of studies have been carried out. There is still room of improvement for the majority of composite slabs. From perspective of rational mechanical behavior and convenient engineering application, the concrete composite slabs with precast ribbed panel, which is proposed by Zhou Xuhong, Wu Fangbo, shows some advantages. Up to now, technical specifications [51] and construction methods have been drafted. In Hunan, Shandong and Gansu provinces, several production bases have been established and products have been commonly applied in engineering projects. The concrete composite slabs with precast ribbed panel has not only reaped significant economic benefits, but also resulted in social benefits.

Conclusion

Review, the following conclusions can be drawn.

(1) The composite slab with flat bottom panel has inadequate structural integrity. Its bond performance and crack resistance of edge joint details need to be improved; the composite slab with bar truss reinforced precast concrete bottom panel has enough bond force, but its storage and transportation are inconvenient; the concrete composite slab with precast ribbed panel has good structural integrity and convenient construction procedure; the composite slab with hollow bottom panel and the composite slab with sandwich bottom panel have the function of sound insulation and thermal preservation, however they are inadequate to resist bending moment and have complex construction procedure. It is considered in this paper that among composite slabs mentioned above, the concrete composite slab with precast ribbed panel has more advantages for improvement.

(2) The concrete composite slabs with precast ribbed panel, which is proposed by Zhou Xuhong and Wu Fangbo, is provide with the outstanding advantages of good structural integrity, wide engineering application and economy of labor, time and money. Technical specifications have been drafted and the construction methods are completed. Production bases have been established and products have been commonly applied in engineering projects. For these reasons, it is worth further researching and promoting.

Acknowledgements

This work was financially supported by the National Natural Science Foundation of China(51078176).

References

- [1] 87SG439 (1987). *Pre-stressed Concrete Composite Slab*. (in Chinese)
- [2] W.H. Zhou: *Modern Concrete Composite Structures* (China Building Industry Press, Beijing 1998). (in Chinese)
- [3] X.F. Zhou, L.S. Zhu and H. Huang: *Building Structure Vol. 10* (1997). (in Chinese)
- [4] X.Z. Wang, M.Q. Zheng and Y.M. Wang, China Patent 99202932.5 (1999). (in Chinese)